

# **Development of the 200- $\mu\text{m}$ Photometer for Ground-Based Astronomy**

Richard J. Walker  
Astronomy Instrumentation Group  
Cardiff University

A Thesis submitted for the Degree of Doctor of Philosophy to  
Cardiff University  
2004

UMI Number: U584682

All rights reserved

INFORMATION TO ALL USERS

The quality of this reproduction is dependent upon the quality of the copy submitted.

In the unlikely event that the author did not send a complete manuscript and there are missing pages, these will be noted. Also, if material had to be removed, a note will indicate the deletion.



UMI U584682

Published by ProQuest LLC 2013. Copyright in the Dissertation held by the Author.  
Microform Edition © ProQuest LLC.

All rights reserved. This work is protected against  
unauthorized copying under Title 17, United States Code.



ProQuest LLC  
789 East Eisenhower Parkway  
P.O. Box 1346  
Ann Arbor, MI 48106-1346

## **Abstract**

The thesis presented here describes the design and construction of a 200- $\mu\text{m}$  photometer, THUMPER, a seven-element array of stressed Ge:Ga photoconductors. The photometer has been designed to observe at the James Clerk Maxwell Telescope (JCMT) in conjunction with SCUBA, with an angular resolution of 14".

A model for the expected atmospheric transmission at high-altitude, ground-based sites is developed. The model is validated through comparison with site-testing measurements of the atmosphere near to the 200- $\mu\text{m}$  window. It has been found that THUMPER will be able to undertake useful observations with levels of precipitable water vapour less than around 0.5 mm, occurring under the most favourable of weather conditions. The opportunities for THUMPER provided by the sites at Mauna Kea, Atacama and Antarctica are reviewed.

Details concerning the manufacture and testing of stressed Ge:Ga photoconductors are presented. This includes work carried out on prototypes, followed by a description of the detectors used in the THUMPER arrays. The THUMPER detectors were tested individually and found to have values of detective quantum efficiency ranging from 6 to 12%.

The basic design parameters for THUMPER are presented along with considerations for the commissioning of our instrument. In addition to plans for the integration of THUMPER at the JCMT, flux calculations have been presented indicating both Mars and Jupiter will provide sufficient fluxes for initial calibration.

## Contents

<b>Acknowledgements</b>	<b>8</b>
<b>List of Tables</b>	<b>9</b>
<b>List of Figures</b>	<b>10</b>
<b>Chapter 1 Introduction</b>	<b>15</b>
1.1. Introduction	15
1.2. Science Case	15
1.3. Other 200- $\mu\text{m}$ Observatories	18
1.4. Site and Telescope Description	20
1.5. Sources at 200 $\mu\text{m}$	23
1.5.1. Galactic	24
1.5.2. Extra-galactic	26
1.6. Outline of Thesis	27
1.7. References	27
<b>Chapter 2 The Atmosphere at 200 <math>\mu\text{m}</math></b>	<b>30</b>
2.1. Introduction	30
2.2. Atmospheric Emission/Transmission Model	31
2.2.1. Molecular Line Database	32
2.2.2. The Atmospheric Model	33
2.2.3. Line Shapes	35
2.2.4. Continuum Corrections	37
2.2.5. Scaling Profiles	40
2.3. Model Validation	46
2.3.1. Previous Measurements	46
2.3.2. Modelling Comparison with Measurements	49
2.3.3. Modelling Predictions for FIR Observing Sites	51
2.4. 220- $\mu\text{m}$ Window	52
2.5. $\tau_{225}$ Data and Instrument Usability	53



2.6.	El Niño Years	56
2.7.	Alternative Sites	58
2.7.1.	Northern Chile	58
2.7.2.	Antarctica.	59
2.8.	Summary	60
2.9.	References	61
<b>Chapter 3 Detector Theory and Construction</b>		<b>64</b>
3.1.	Introduction	64
3.2.	Photoconductive Detectors	64
3.2.1.	Intrinsic Photoconductors	65
3.2.2.	Extrinsic Photoconductors	67
3.2.3.	Stressed Photoconductors	70
3.2.4.	Detector Responsivity	71
3.2.5.	Intrinsic Noise	72
3.3.	Amplifier	77
3.3.1.	TIA Circuit	77
3.3.2.	Circuit Noise	79
3.4.	Previous Experiments Utilising Stressed Ge:Ga Photoconductors	81
3.5.	Detector Construction	84
3.5.1.	Detector Housing and the Focal Plane Array	85
3.5.2.	Crystal Preparation	86
3.5.3.	Detector Block Preparation	89
3.5.4.	Ancillary Components	90
3.5.5.	Crystal Mounting	92
3.5.6.	Crystal Stressing	96
3.6.	Summary	99
3.7.	References	99
<b>Chapter 4 Instrument Design</b>		<b>103</b>
4.1.	Introduction	103

4.2.	Instrument Requirements	103
4.3.	Optical Configuration	104
4.3.1.	Telescope and SCUBA Optics	105
4.3.2.	THUMPER Optical Configuration	106
4.4.	Optical Components	111
4.4.1.	Feedhorns	111
4.4.2.	Mirrors	112
4.4.3.	Dichroic	113
4.4.4.	Filters	114
4.4.5.	Window	115
4.4.6.	Alignment Laser	115
4.5.	Cryostat	116
4.5.1.	Location	119
4.5.2.	Cryogen Holdtime	121
4.6.	Electronic Readout	121
4.6.1.	Pinouts	123
4.7.	Calibration	124
4.8.	Summary	124
4.9.	References	127
<b>Chapter 5 Laboratory Testing and Modelling</b>		<b>129</b>
5.1	Introduction	129
5.2.	First Prototype Detector Testing	129
5.2.1.	Experimental Arrangement	129
5.2.2.	Spectral Response Measurements	131
5.2.3.	Dark Current	133
5.2.4.	Responsivity and Noise	136
5.3.	Detector Shape Optimisation	141
5.4.	The THUMPER Detectors	144
5.4.1.	Spectral Response Measurements	144
5.4.2.	Dark Current	151

5.4.3. Responsivity and Noise	153
5.4.4. Noise Performance	159
5.5. Operation of Detectors in THUMPER Cryostat	162
5.6. Detector Block Upgrades	162
5.7. Summary	163
5.8. References	164
<b>Chapter 6 THUMPER Commissioning</b>	<b>166</b>
6.1. Introduction	166
6.2. SURF and Data Analysis	166
6.3. Modelled in-the-Field Performance of THUMPER	167
6.4. Calibration	168
6.4.1. Planets as Calibrators	169
6.5. Commissioning Plan	174
6.5.1. Daytime Commissioning	175
6.5.2. Nighttime Commissioning	178
6.6. Sky Calibration	179
6.7. Previous Results	182
6.8. Decommissioning	183
6.9. Summary	183
6.10. References	184
<b>Chapter 7 Conclusions</b>	<b>187</b>
7.1 Thesis Overview	187
7.2. Instruments Improvements	188
7.3. References	189
<b>Abbreviations</b>	<b>190</b>
<b>Appendix A</b>	<b>193</b>
<b>Appendix B</b>	<b>198</b>
<b>Appendix C</b>	<b>203</b>

## Acknowledgements

I would firstly like to thank my supervisor, Peter Ade, for his help in the lab and with the atmospheric modelling. Thanks also go to Matt Griffin for acting as a deputy supervisor on many occasions.

Without the help of a great many people THUMPER would never have been built. These include Derek Ward-Thompson, the instrument PI, Henrique Araújo, Stephen Rinehart, Rhodri Evans, Sarah Leeks, Neal Potter, Bruce Sibthorpe, James Cox, Rashmi Sudiwala and Pete Hargrave, all of whom contributed to THUMPER. In addition I would like to thank, for their technical assistance and workshop expertise, Fred, Brian and Jeff.

Particular thanks go to Jeff Beeman, of Lawrence Berkeley National Labs, for his generosity in allowing me to learn the tricks of crystal mounting and stressing from him. Also for the warm welcome offered to me during my visits there.

Finally I would like to thank PPARC, without whose financial assistance I would have been extremely impoverished.

## List of Tables

1.1	Comparison of key observational parameters of 200- $\mu\text{m}$ instruments.	21
2.1	Lower quartile measurements of PWV at various FIR observing sites.	52
3.1	Stress, monitored by changes in RT resistance, of THUMPER PCs.	99
4.1	Coordinates of the external optical components used by THUMPER.	110
4.2	Mirror parameters.	112
4.3	Contributions to cryogenic boiloff.	121
4.4	Wiring for the signal chain.	125
4.5	Wiring for the housekeeping chain.	126
5.1	Prototype detector parameters.	143
5.2	Cutoff wavelengths for the THUMPER PCs as determined by FTS and by dark current measurement.	153
5.3	THUMPER PCs' performance parameters.	157
5.4	Measured and modelled noise of THUMPER PCs at optimum bias.	161
6.1	Lower quartile measurements of PWV, and estimates of NEFD for a JCMT system under conditions of that value of PWV, at various FIR observing sites.	168
6.2	Total flux and the flux in a 14" beam for each of the primary calibration sources at 200 $\mu\text{m}$ .	170
6.3	Brightness temperatures at 200 $\mu\text{m}$ for the calibrator planets.	171
6.4	Angular size and AM of five planets during a period previously given for THUMPER's commissioning. Blanks in columns indicate the planet is unavailable for observations.	174
6.5	Definition of weather bands used at the JCMT (Jenness, 1998).	181

## List of Figures

1.1	Planck function for an object of 15 K.	16
1.2	Comparison of the resolution of FIR and submillimetre instruments.	21
1.3 <i>a &amp; b</i>	L1544 at 90 $\mu\text{m}$ and 200 $\mu\text{m}$ (courtesy D. Ward-Thompson).	25
1.4 <i>a &amp; b</i>	L1544 at 200 $\mu\text{m}$ and 850 $\mu\text{m}$ (courtesy D. Ward-Thompson & J.M. Kirk).	25
2.1	The line shape used for calculation of the Clough continuum correction. The pedestal width of $\pm 25 \text{ cm}^{-1}$ is equivalent to $\pm 750 \text{ GHz}$ (from Clough <i>et al.</i> , 1989).	39
2.2	The Clough continuum correction over the frequency range 0 to 150 THz (from Clough <i>et al.</i> , 1989).	39
2.3	AFGL model profile for temperature at different locations and seasons.	41
2.4	AFGL model profile for pressure at different locations and seasons.	41
2.5	Comparison of radiosonde data with that taken from the AFGL model profile for temperature.	42
2.6	Comparison of radiosonde data with that taken from the AFGL model profile for pressure.	42
2.7	Comparison of Hilo radiosonde data with that taken from the AFGL model profile for $\text{H}_2\text{O}$ .	43
2.8	$\text{O}_3$ scaling with altitude.	45
2.9	$\text{O}_2$ scaling with altitude.	45
2.10	Comparisons of sonde and AFGL $\text{O}_3$ profiles.	46
2.11	Atmospheric transmission at Chajnantor, Chile (courtesy S. Paine).	47
2.12	FTS measurement giving transmission through the atmosphere at Pampa la Bola, Chile. PWV estimated at 252 $\mu\text{m}$ (courtesy S. Matsushita).	48

2.13	Transmission through the atmosphere from a South Pole site (from Chamberlin <i>et al.</i> , 2003).	49
2.14	Comparison of modelled and measured data for Chajnantor under 250 $\mu\text{m}$ PWV.	50
2.15	Comparison of modelled and measured data for the South Pole under 250 $\mu\text{m}$ PWV.	51
2.16	Atmospheric transmission in the FIR. Modelled for Mauna Kea, viewing zenith, for different amounts of PWV.	52
2.17	Variation of $\tau_{225}$ with date, January 1997 to December 2000 (courtesy H. Araújo).	54
2.18 <i>a to c</i>	Weather statistics. From Araújo <i>et al.</i> (2000).	55-6
2.19	Modelled atmospheric transmission (from Pardo <i>et al.</i> , 2001 <i>a</i> ).	57
3.1	Schematic of the spectral response of a PC.	66
3.2	End-fire geometry of a photoconductive crystal.	73
3.3	The TIA circuit. The dotted line marks elements placed on the cryostat cold plate.	78
3.4	Torque from a stressing screw is decoupled by use of a ball bearing.	81
3.5	Stress applied by use of lever and fulcrum.	82
3.6	Schematic of a stressed array.	83
3.7	The detector blocks used in THUMPER.	86
3.8	The focal plane array.	87
3.9	Shape of Ge:Ga crystals, with contacts, after etching.	88
3.10	The central detector stressing block.	90
3.11	Schematic of a feedthrough.	90
3.12	Contact pad and wire.	91
3.13	Photograph of the ancillary components used in the THUMPER detector blocks.	92
3.14	Detector block clamped for crystal mounting. The cavities are 3- mm diameter.	93
3.15	Detector channel identification.	93

3.16	Schematic of the electrical contact pad with anvil attached.	94
3.17	Triaxial mount and vacuum probe, used to insert crystals into detector block cavities.	95
3.18	A completed array.	96
3.19	Detector block configuration for monitoring stress applied to detectors.	97
3.20	Resistance was monitored through the feedthroughs at the back of the detector block as the stressing screw was tightened.	98
4.1	Schematic of THUMPER and SCUBA at the JCMT.	104
4.2	The optical path for the external SCUBA optics, from position approximately at top of THUMPER cryostat (from Holland <i>et al.</i> , 1999).	106
4.3	The optical path for the external THUMPER optics, as viewed from the side.	107
4.4	The optical path for the external THUMPER optics, as viewed from above.	107
4.5	The layout of the internal THUMPER optics.	109
4.6	View of the optical table used for SCUBA and THUMPER.	110
4.7	Schematic of a feedhorn.	112
4.8	The dichroic mount.	113
4.9	Transmission of THUMPER cold filters.	115
4.10	Transmission of the THUMPER window.	116
4.11	The bolthole pattern of the coldplate.	118
4.12	Internal components of THUMPER.	119
4.13	Position of the SCUBA optical bench at the JCMT showing the positions of the THUMPER (red) and SCUBA (caged) cryostats (courtesy B. Kiernan).	120
4.14	Position of the THUMPER cryostat at the JCMT.	120
4.15	Schematic of wiring within THUMPER cryostat.	124
4.16	The internal illuminator.	126
5.1	Schematic of an Infrared Labs HD-3 cryostat.	130



5.2	Schematic of the internal components of an FTS.	132
5.3	Block diagram of the FTS (courtesy C. Tucker).	132
5.4	Spectral response of test stressed Ge:Ga PC, LBL102a, at different bias.	133
5.5	Cryostat coldplate for dark current measurement.	134
5.6	Block diagram showing apparatus used in the reduction of He vapour pressure within the HD-3 cryostat.	135
5.7	Dark current falling with temperature for detector LBL102a.	135
5.8	Inside of the cryostat as set up for responsivity and noise measurements for the prototype detectors.	136
5.9	Transmission of test filters for prototype detectors.	137
5.10	Block diagram of the experimental set-up.	138
5.11	Increase of signal and noise with increasing bias for LBL102a. Detector temperature is 3.7 K.	139
5.12	DQE of detector LBL102a vs. applied bias voltage. Detector temperature is 3.7 K. Operating bias is taken at the point of maximum DQE.	140
5.13	Variation of DQE with temperature measured for LBL102a.	140
5.14	Three orientations of crystal within an integrating cavity. Viewed from above with incoming radiation shown.	141
5.15	Spectral response measurements for THUMPER prototype detectors.	142
5.16	Measured signal for THUMPER prototype detectors. Crystal shape and orientation are as given in Figure 5.15.	143
5.17	Photograph of the two THUMPER side arrays set up for spectral response measurement. Extra Cu tape limits light leaks whilst the snout, here seen on the left, provides the detectors' field of view.	145
5.18	Schematic of the front view of the 1×2 detector arrays, set up for spectral response measurement.	145
5.19	Spectral response of the THUMPER detectors.	146
5.20	Cutoff region in spectrum of detector AL, with fitted polynomial.	147

5.21	Comparison of the spectral responses of three PCs. LBL102a and LBL113c are prototypes, whereas AU is a THUMPER detector.	148
5.22	Creation of inhomogeneous stress across the cross-section of a crystal.	149
5.23	Spectral response of the THUMPER detectors as Figure 5.19. Also shown in this Figure is the model of atmospheric transmission, from Chapter 2, with low levels of PWV.	150
5.24	Spectral response of THUMPER detector CL at different bias.	151
5.25	Fall in dark current with decreasing temperature.	152
5.26	Transmission of test filters for THUMPER detectors.	154
5.27	Inside of the cryostat as set up for responsivity and noise measurements for the THUMPER detectors.	154
5.28	Noise spectral density for THUMPER PC AU. Detector temperature was 3.7 K and biased at the optimum level of 125 mV. Note the flat response at low frequency.	155
5.29	Increase of signal and noise with increasing bias for detector BL.	155
5.30	Variation of DQE with bias for detector BL.	156
5.31	Scatter graph of DQE against AC responsivity.	158
5.32	Scatter graph of DQE against dark current.	159
5.33	Pie chart of noise contributions.	162
5.34	Alternative stressing piston for THUMPER.	163
6.1	$T$ vs. $\log \lambda$ for Mars.	172
6.2	$T$ vs. $\log \lambda$ for Jupiter.	172
6.3	Schematic of THUMPER at the JCMT. Mirrors are depicted as lenses for clarity.	175
6.4	Diagram of THUMPER observations during commissioning.	182
6.5	Correlation between $\tau_{1500}$ and $\tau_{225}$ (from Matsushita <i>et al.</i> , 1999).	183

# Chapter 1 Introduction

## 1.1. Introduction

Recent technological advances have opened up the far infrared (FIR) wavelength region through the use of satellite borne instruments such as the Infrared Astronomical Satellite (IRAS) and the Infrared Space Observatory (ISO). These satellites avoid viewing through the nearly opaque terrestrial atmosphere. Data from such observatories has proven to be critical to our understanding of many astrophysical processes and has enabled many types of source to be categorized. However, the limited size of these observatories compared to both longer and shorter wavelength ground based telescope facilities has restricted our ability to determine source structure and hence the true nature of the underlying physical processes.

The work presented here describes a novel Two HUNDred Micron PhotometER (THUMPER), a ground-based seven-element array photometer for operation at the James Clerk Maxwell Telescope (JCMT) on Mauna Kea in Hawaii. It will provide critical high angular resolution data to augment that taken with other facilities. The photometer is built to observe with an angular resolution of 14", unprecedented at this wavelength. In particular this work focuses on the both the feasibility of such an instrument as well as describing its design and performance.

Before discussing the instrumental detail, the science case is reviewed and the place for a THUMPER-type instrument is considered along with other 200- $\mu\text{m}$  continuum instruments both in existence and planned. A description of the JCMT, the chosen telescope facility that will make use of THUMPER, is then described along with the types of astronomical sources that will be observed. Finally, the layout of the main body of the thesis is described.

## 1.2. Science Case

High spatial resolution observations at 200  $\mu\text{m}$  are needed to fully understand objects in the FIR. The Planck function for an object at 15 K peaks at this wavelength. When making astronomical observations of cold sources, there exists some ambiguity in determining the temperature of the source if data are only taken at two points on a

spectral energy distribution (SED). An SED plots the flux density as a function of wavelength,  $\lambda$ . This is often the case at the JCMT where observations are made using the Submillimetre Common-User Bolometer Array (SCUBA) (Holland, *et al.*, 1999). SCUBA provides high spatial resolution data at several wavelengths between 350  $\mu\text{m}$  and 2.0 mm, although 450 and 850  $\mu\text{m}$  are used predominantly. The ambiguity over temperature arises since a higher flux may be obtained from a source of high temperature, or a higher density object. For objects with a temperature of around 15 K, the flux obtained at wavelengths lower than 200  $\mu\text{m}$  is very much smaller than that at 200  $\mu\text{m}$  since the Wien regime of the SED is encroached upon and flux drops rapidly with decreasing wavelength in this regime. Figure 1.1 plots the Planck function for a temperature of 15 K.

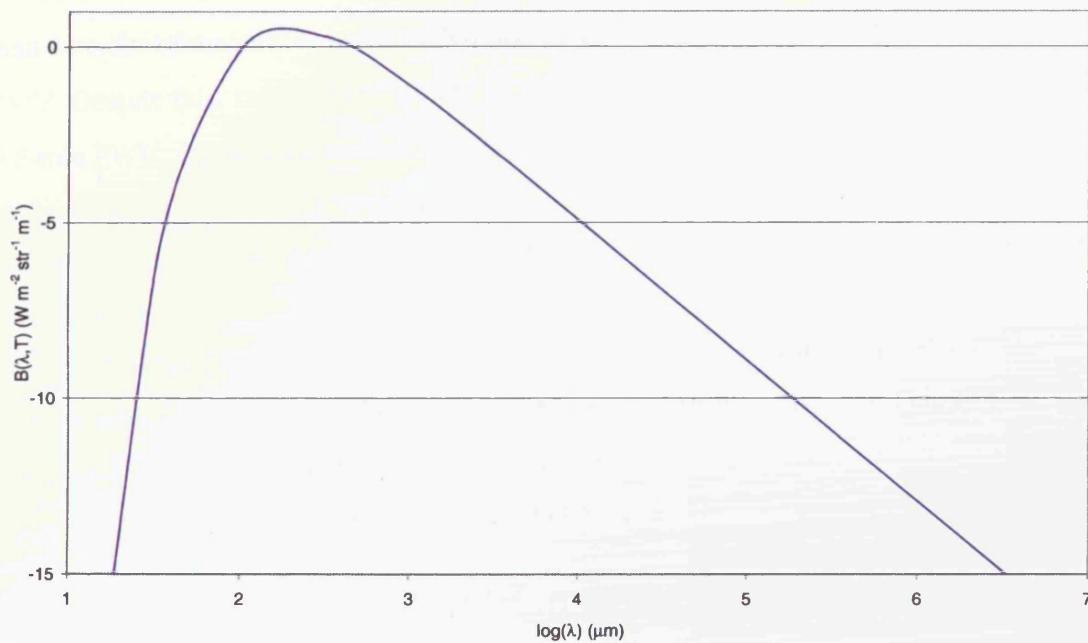


Figure 1.1. Planck function for an object of 15 K.

Although many other observatories, for example IRAS and ISO, have mapped sources at 200  $\mu\text{m}$ , none have had the high spatial resolution necessary to fully extract information on the scale that will be accomplished by THUMPER at the JCMT. Other instruments now coming into existence (e.g. Spitzer) and planned for the near future (see below) suffer the same limitations. THUMPER will be unique in that it will provide the

only high spatial resolution data points at this wavelength. Knowledge of the structure of Class 0 sources and high-mass star forming regions can then be gained from such measurements.

Analysis of weather statistics for the site of Mauna Kea estimate weather conditions to be favourable for 200- $\mu\text{m}$  observations for approximately 74 hours per year (Araújo *et al.*, 2001). For a noise equivalent flux density (NEFD) of 35 Jy/ $\sqrt{\text{Hz}}$  under a precipitable water vapour (PWV) column of 0.5 mm it was originally thought that a similar signal-to-noise ratio (SNR) could be obtained for THUMPER as with the SCUBA 450- $\mu\text{m}$  channel in approximately the same amount of integration time (Rinehart *et al.*, 1999). The Planck function gives a factor of just under 3 increase in flux at 200  $\mu\text{m}$  compared to 450  $\mu\text{m}$  for a source at 30 K. However, atmospheric transmission is more than an order of magnitude lower at 200  $\mu\text{m}$  than at 450  $\mu\text{m}$  under conditions of 1-mm PWV. Despite this, an NEFD of around 25 Jy/ $\sqrt{\text{Hz}}$  will be achievable under conditions of 0.5-mm PWV, assuming a surface accuracy for the JCMT primary of 17  $\mu\text{m}$  (see model in Appendix A). Further analysis provided in Chapter 2 of this thesis indicates that weather conditions are more favourable at the sites of Chajnantor, in Northern Chile, and the South Pole.

The flux density  $F(\nu)$ , at a frequency  $\nu$ , from an optically thin (opacity,  $\tau < 1$ ) dust cloud is proportional to the product of density and temperature. For a cloud at distance  $D$  comprised of grains each of cross-section  $\sigma$ , temperature  $T$  and emissivity  $\epsilon(\nu)$ , the flux density is given by Hildebrand (1983) as

$$F(\nu) = N \frac{\sigma}{D^2} \epsilon(\nu) B(\nu, T). \quad (1.1)$$

In Equation 1.1  $N$  is the number of dust grains and  $B(\nu, T)$  is the Planck function:

$$B(\nu, T) = \frac{2h\nu^3}{c^2 (e^{\frac{h\nu}{kT}} - 1)} \quad (1.2)$$

where  $h$  is Planck's constant,  $c$  is the speed of light and  $k$  is Boltzmann's constant. The dependence of emissivity on frequency is generally given as

$$\epsilon(\nu) \propto \nu^\beta \quad (1.3)$$

with values of  $\beta$  ranging between 1 and 2 (e.g. Harvey & Jeffries, 2000; Spinoglio *et al.*, 2002).

The temperatures of dust clouds is often assumed to be constant over the diameter of the source (e.g. André *et al.*, 2000). Such analysis allows dust masses to be estimated since variations in flux are then proportional to variations in density. However, in objects such as pre-stellar cores, where a small amount of heating occurs due to external objects (Ward-Thompson, 2002) this assumption is incorrect. In order to accurately determine the temperature, several measurements of flux at different wavelengths must be made to provide an SED of the source. The JCMT allows diffraction-limited resolution at wavelengths above 450  $\mu\text{m}$ , which is 7.3 and 14.3" at wavelengths of 450 and 850  $\mu\text{m}$  respectively. For objects such as pre-stellar cores, at a temperature of around 15 K (André *et al.*, 2000), the Planck function peaks at 200  $\mu\text{m}$ . For the SED to be accurately determined, a further data point, in addition to those of SCUBA and at the same spatial resolution, is needed.

All previous 200- $\mu\text{m}$  observations have been made using either airborne or space-based telescopes. Due to the difficulties of launching or flying large apertures, the largest telescopes which have observed at this wavelength so far have been the 90-cm Kuiper Airborne Observatory (KAO) and the 85-cm Spitzer Space Observatory. Comparison of these 200- $\mu\text{m}$  data with the 450- $\mu\text{m}$  data from SCUBA has thus required smoothing the SCUBA data to the poor spatial resolution of the available 200- $\mu\text{m}$  data whereupon detailed information on the source structure is lost. THUMPER will provide, for the first time, the capability to obtain 200- $\mu\text{m}$  data with a spatial resolution similar to that of SCUBA.

### 1.3. Other 200- $\mu\text{m}$ Observatories

A number of astronomical instruments in recent years have realised the benefits of making FIR continuum observations in the region close to 200  $\mu\text{m}$ . Due to the relatively recent technological advances that have allowed high-sensitivity instruments to be built, a large number of FIR and submillimetre observatories are still in the construction phase. A list of instruments that have taken continuum measurements at around 200  $\mu\text{m}$ , or are

currently under construction, is given here. However, all of the below-mentioned instruments suffer from the same fundamental limitation of low angular resolution.

Since 1974 the KAO (Harvey, 1979) has taken observations from an altitude of 12.5 km, well above restrictions imposed on ground-based instruments by the poor atmospheric transmission at the wavelengths of observations ranging from 35 to 300  $\mu\text{m}$ . The telescope had a primary mirror diameter of 91 cm. Although this is relatively large compared to the later space-based observatories it is still a great deal smaller than ground-based apertures.

IRAS, which used a 57-cm dish, operated for ten months during 1983 (Neugebauer *et al.*, 1984) over four wavebands centred at 12, 25, 60 and 100  $\mu\text{m}$ . The instrument scanned 96% of the sky to plot an overall map of the infrared sky, cataloguing almost 250,000 sources. The sky was mapped twice to enable subtraction of foreground objects such as comets and man-made satellites.

Following on from the successes of IRAS came ISO, which flew for three years from 1995 (Kessler *et al.*, 1996). A number of instruments useful for infrared astronomy were flown on ISO. In particular were the cameras ISOPHOT and ISOCAM optimised for use at wavelengths between 2.5 and 200  $\mu\text{m}$ . At the longest wavelength, ISO's 60-cm diameter primary mirror offered diffraction limited resolution of 84".

The InfraRed Imaging Surveyor (IRIS), also known as ASTRO-F, is dedicated to infrared sky surveys with much better sensitivity than that of IRAS. IRIS has a 70-cm telescope feeding two focal-plane instruments. The surveying instrument is the Far-Infrared Surveyor (FIS) which will survey the entire sky in the wavelength range from 50 to 200  $\mu\text{m}$  with angular resolutions of 30 to 50". It is scheduled to be launched in mid-2004.

A space based observatory recently launched and currently acquiring initial observations is the Spitzer Space Telescope (formerly the Space Infrared Telescope Facility, SIRTf). Included on the satellite is the Multiband Imaging Photometer for SIRTf (MIPS) (Heim *et al.*, 1998) which contains an array of stressed Ge:Ga photodetectors, as does THUMPER. Imaging and photometry will be possible with the instrument, at wavelengths centred at 24, 70 and 160  $\mu\text{m}$ . The observatory's angular resolution is severely hampered due to the small size of its 85-cm primary mirror.

SOFIA (Stratospheric Observatory for Infrared Astronomy) will be of the next generation of airborne observatory. It consists of a 2.5-m diameter primary mirror mounted inside a Boeing 747 aircraft. First flights are expected in 2005 (USRA, 2003). The High-resolution Airborne Wideband Camera (HAWC) is an instrument planned for use on SOFIA (Harper *et al.*, 2000) operating in the spectral region of 40 to 300  $\mu\text{m}$ . Of four bands on the instrument "Band 3" covers 155 to 258  $\mu\text{m}$ . The scientific rationale behind the instrument is fundamentally the same as for THUMPER working in conjunction with SCUBA, i.e. star formation and dust-related astronomy. However, THUMPER will benefit from the increased angular resolution afforded by the 15-m aperture.

The Herschel Space Telescope (formerly the Far InfraRed and Submillimetre Telescope, FIRST) will operate at the second Lagrangian point from 2007. The telescope primary mirror on the satellite is a 3.5-m diameter dish with a surface accuracy good enough for diffraction limited resolution at 60  $\mu\text{m}$ . It will take data over a spectral range from this wavelength up to around 700  $\mu\text{m}$  for about 4.5 years (Tofani & Natale, 2003). The Photoconductor Array Camera and Photometer (PACS) aboard Herschel covers the lower end of the wavelength range, between 60 and 210  $\mu\text{m}$  (Poglitsch *et al.*, 2001). The PACS instrument acts as a direct competitor to THUMPER, since it will also perform 200- $\mu\text{m}$  observations at the same resolution. However, THUMPER will subsequently improve on this to provide an angular resolution of 7".

All of the abovementioned instruments suffer from poor angular resolution. At the time THUMPER is commissioned it will offer a resolution of 14". Later modifications to the optics will improve this to 7", matched to the 450- $\mu\text{m}$  SCUBA channel. Table 1.1 summarises some of the instruments, and lists their angular resolution and dates of operation. Figure 1.2 summarises the resolution of some of these instruments. The high spatial resolution provided by THUMPER is obvious.

#### 1.4. Site and Telescope Description

Atmospheric transmission at FIR and submillimetre wavelengths is generally very low. This is due in the most part to absorption by water vapour. Absorption processes are



Table 1.1. Comparison of key observational parameters of 200- $\mu\text{m}$  instruments. Data are from 1: Harvey, 1979; 2: Neugebauer *et al.*, 1984; 3: Lemke *et al.*, 1996; 4: Heim *et al.*, 1998; 5: Takahashi *et al.*, 2000; 6: Harper *et al.*, 2000; 7: Poglitsch *et al.*, 2001.

Instrument	$\lambda$ ( $\mu\text{m}$ )	Telescope diameter (m)	Resolution (")	Sensitivity (mJy $1\sigma$ 1 hr)	Lifetime
KAO <sup>1</sup>	35 - 300	0.91	28 (100 $\mu\text{m}$ )	~150	1974-95
IRAS <sup>2</sup>	12 - 100	0.57	44 (100 $\mu\text{m}$ )	300	1983
ISO (ISOPHOT) <sup>3</sup>	2.5 - 200	0.60	84	45	1995-98
THUMPER	200	15	14 (later up-grade to 7)	420	2004-06
Spitzer (MIPS) <sup>4</sup>	20 - 180	0.85	50 (100 $\mu\text{m}$ )	15	2004-07
IRIS (FIS) <sup>5</sup>	20 - 200	0.7	72	5	2004
SOFIA (Band 3) <sup>6</sup>	40 - 300	2.5	30	12	2004-24
Herschel (PACS) <sup>7</sup>	60 - 210	3.5	14	0.6	2007-14

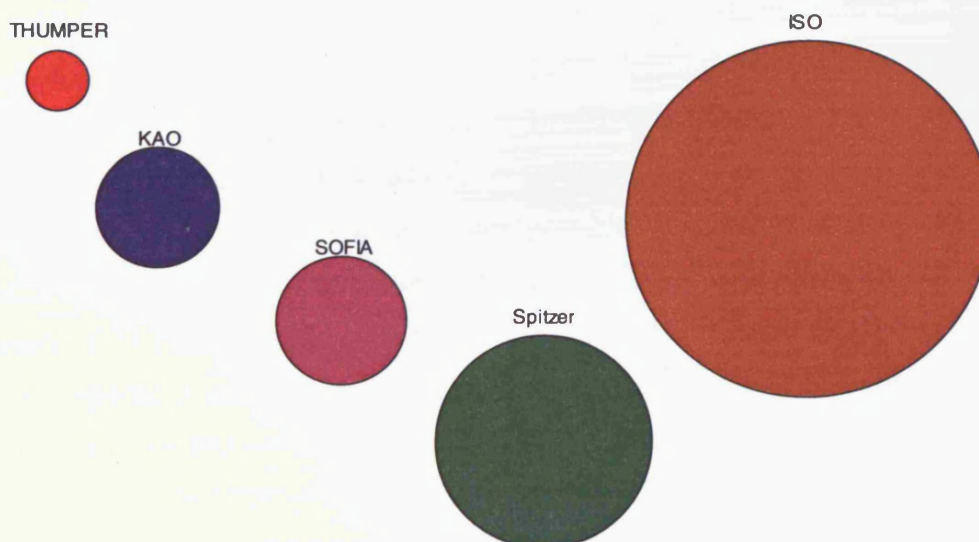


Figure 1.2. Comparison of the resolution of FIR and submillimetre instruments.

fully discussed in Chapter 2. However, a number of windows do open up under periods of extremely dry weather, especially at high-altitude sites such as Mauna Kea.

The JCMT is a Cassegrain telescope located at such a high-altitude site. It is situated near the summit of Mauna Kea, Hawaii, at an altitude of 4092 m, where observations can be made above 97% of the water vapour that exists in the atmosphere. The 15-m diameter primary mirror is the largest in the world working in the submillimetre region of the spectrum, thus enabling the highest spatial resolution measurements to be made at such wavelengths from this location. The primary dish is constructed from 276 Al panels, each of which can be adjusted by use of three motorised mounts to form a near perfect parabola. A Gore-Tex sheet, to protect against dust and wind, is attached in front of the telescope with a transmission ranging from 97% at millimetre wavelengths to around 65% at 200  $\mu\text{m}$ . The facility has been operational since 1987.

Even under good atmospheric conditions, allowing high transmission, a great deal of radiation is emitted by the atmosphere, adding photon noise to observations as well as sky noise caused by random fluctuations in the transmission of the atmosphere. In order to remove the background fluctuations of the sky emission the secondary mirror of the JCMT is modulated in a practice known as chopping. The signal flux can then be determined by the difference between the background and the signal plus background.

The beam from the telescope forms an F/12 focal ratio. However, to fit the beam through the elevation bearing to SCUBA, placed at the Nasmyth focus, the secondary mirror has been shifted slightly to provide an F/16 beam. The change in F-ratio ensures the beam to SCUBA remains unvignetted.

Under extremely good weather conditions at Mauna Kea an atmospheric window opens up at 200  $\mu\text{m}$ . Weather conditions necessary for 200- $\mu\text{m}$  astronomy are discussed in Chapter 2. THUMPER adds to the capability of the JCMT by providing the only camera to operate at this wavelength with high angular resolution. In addition to this is the benefit of simultaneous observations at three wavelengths.

However, the telescope offers many constraints to THUMPER's operation. Several of these stem from the remoteness of the observatory.

From the outset it has been envisaged that both the systems of THUMPER and SCUBA will work in conjunction with each other. This is due to ease of operation and the quality of science attainable. For this reason THUMPER has been designed to use as much as possible of the existing infrastructure at the JCMT. In addition, the design must also incorporate as little effort from JCMT staff as possible. THUMPER's dependence on SCUBA comes in part from the need to share SCUBA's unused pre-amplifier channels. Additional reliance is due to the sharing of common optical components. Because of this dependency there exists a requirement to place the THUMPER cryostat as near to SCUBA as possible.

Observations at an angular resolution higher than that possible at 450  $\mu\text{m}$  are rendered impossible at the JCMT due to surface inaccuracies of the telescope primary mirror. The Ruze efficiency, which is the efficiency of an aperture of rms optical surface accuracy  $\epsilon$ , can be given by

$$\eta_R = e^{-\left(\frac{4\pi\epsilon}{\lambda}\right)^2} \quad (1.4)$$

where  $\lambda$  is the wavelength of radiation in  $\mu\text{m}$ . For an optimistic surface accuracy of 17  $\mu\text{m}$  rms (Richer, 2003) the efficiency at 200  $\mu\text{m}$  is 32%, rising to 80% at 450  $\mu\text{m}$ .

Other considerations arising from instrument integration must be taken into account. Maximising SCUBA's SNR is of most concern to the astronomical community, due to its wide wavelength coverage and operation in atmospheric windows of higher transmission than that existing at 200  $\mu\text{m}$ . Because of this THUMPER's performance must have as little an impact on SCUBA's performance as possible.

In the absence of El Niño events discussed in Chapter 2, weather conditions at Mauna Kea, in terms of predicting the amount of PWV present, are generally unpredictable. Since THUMPER can only observe under conditions of very low PWV it is imperative that the instrument has the minimum of start up procedures: if the weather is conducive to 200- $\mu\text{m}$  astronomy it must be taken advantage of immediately.

### 1.5. Sources at 200 $\mu\text{m}$

Continuum observations of dust thermal emission are required for a wide range of sources. In many astronomical processes optical and ultraviolet light generated by stars is

absorbed by interstellar dust and then re-radiated in the FIR. Often a great deal of the total flux is emitted at wavelengths greater than about 10  $\mu\text{m}$ . Many regions of interest have multiple heating sources, for example perhaps most famously in M16. FIR observations at the highest possible angular resolution are essential for understanding the morphology of these dust-obscured sources.

#### 1.5.1. Galactic

Studying the formation of stars is currently undergoing an intense period of research within the astronomical community. In order to satisfactorily explain processes behind stellar formation, new observations are required. THUMPER offers the advantage of high angular resolution at a wavelength that has never been previously achieved from the ground. THUMPER will therefore image protostars from their earliest stages to that of a main sequence star, possibly with a protoplanetary disk.

A pre-stellar stage of star formation is defined by André *et al.* (2000) as the phase when a gravitationally bound core has formed in a molecular cloud but no central protostar yet exists. The youngest stellar class is termed the Class 0 protostar. Since they are of a temperature less than around 30 K (Ward-Thompson *et al.*, 2002), the Planck function falls away rapidly at wavelengths greater than around 100  $\mu\text{m}$ . Hence the majority of their flux is emitted in the FIR and submillimetre region of the spectrum.

A case in point is provided by the pre-stellar core L1544, shown in Figures 1.3 *a* and *b*. The images, taken by ISO, clearly show the central source at 200  $\mu\text{m}$  in Figure 1.3 *a*, whilst at a wavelength of 90  $\mu\text{m}$  the flux is severely diminished.

ISO data can be compared with that from SCUBA to determine the SED of such sources. However, due to the poor angular resolution of ISO only a mean temperature across the entire source can be inferred. A SCUBA-resolution point at the wavelength of ISO will allow a true inference of the variation of temperature to be disentangled from changes in the density profile.

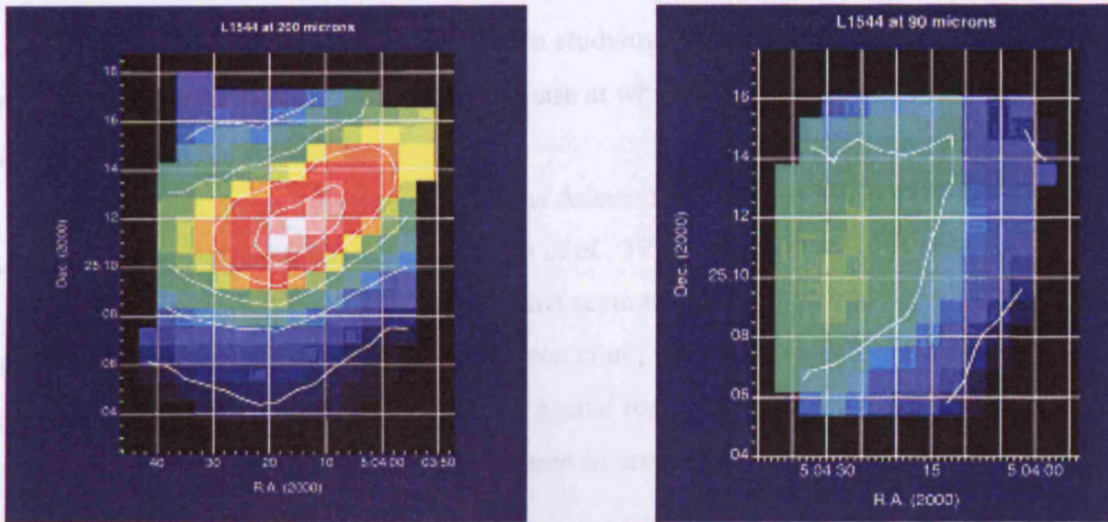


Figure 1.3 *a* and *b*. L1544 at 200  $\mu\text{m}$  and 90  $\mu\text{m}$  (courtesy D. Ward-Thompson).

Figure 1.4 shows images of the pre-stellar core L1544 at the different spatial resolutions provided by ISO and by SCUBA. The ISO image, at 200  $\mu\text{m}$ , is shown in Figure 1.4 *a* whilst the SCUBA image at 850  $\mu\text{m}$  is shown in Figure 1.4 *b*. The difference in resolution can be noted by the fact that the image at 850  $\mu\text{m}$  fits inside the central contour of the 200- $\mu\text{m}$  image. The 850- $\mu\text{m}$  image suggests L1544 contains two central cores, which are smoothed out when viewed at 200  $\mu\text{m}$ . Data taken at the same spatial resolution as SCUBA would allow separation of the multiple sources, and hence show how many central objects are actually contained within this region.

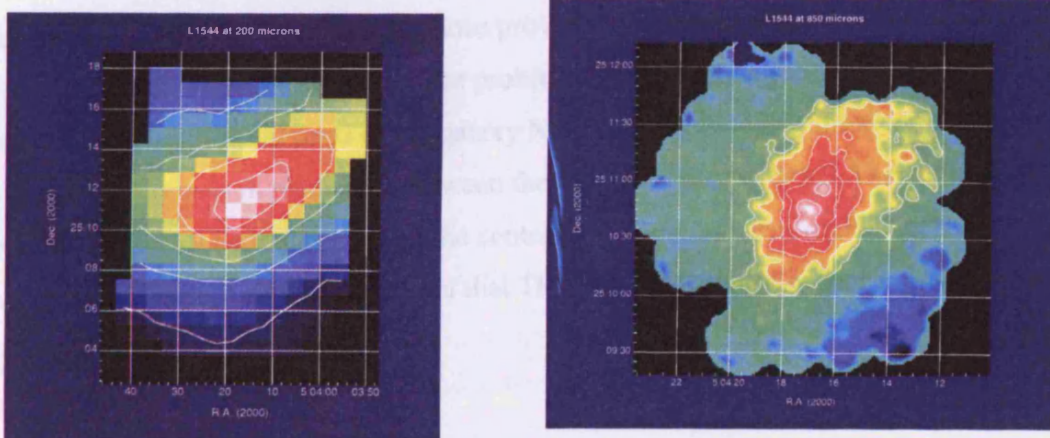


Figure 1.4 *a* and *b*. L1544 at 200  $\mu\text{m}$  and 850  $\mu\text{m}$  (courtesy D. Ward-Thompson & J.M. Kirk).

200- $\mu\text{m}$  observations are also of use in studying stars at the end of their lifetime. Many late-type stars are observed during a phase at which they are losing mass in the form of cool dust.

Imaging in the mid-infrared (MIR) has determined that dust shells exist around Asymptotic Giant Branch stars (e.g. Rinehart *et al.*, 1998). Combining MIR data with submillimetre data from the JCMT has enabled accurate SEDs to be built up of these objects (e.g. Marshall *et al.*, 1992; van der Veen *et al.*, 1995). However, as with star formation regions, there exists a gap of high spatial resolution data around wavelengths of 200  $\mu\text{m}$ . Such observations will be important in accurately determining the mass-loss histories of these objects.

#### 1.5.2. Extra-galactic

IRAS showed that a significant number of galaxies emit the bulk of their energy at infrared wavelengths (Sanders *et al.*, 1988). The majority of this is due to dust, which absorbs starlight and re-emits the energy at longer wavelengths. IRAS was only sensitive to "warm" dust of a temperature around 30 K. SCUBA showed that there also exists a cool component (e.g. Stevens & Gear, 2000). The total emission from extra-galactic objects can be measured using IRAS, ISO and SCUBA. However, to separate out the temperature variations within the central active star-formation region, and the extended, less active, disk region, higher spatial resolution measurements are needed. Higher spatial resolution measurements will be provided by Herschel, but not until its launch in 2007, and these will still not be as high as those provided by THUMPER.

Klaas & Walker (2002) note the problems incurred trying to fit different temperatures to different parts of the galaxy NGC3079. Although a three-temperature fit is likely, differences in resolution between the data obtained by IRAS, IRAM, ISO and SCUBA prevent a differentiation of the central and circumnuclear regions being performed. The high spatial resolution that THUMPER provides will be able to rectify these problems.



## 1.6. Outline of Thesis

Chapter 2 describes the atmosphere in the FIR, paying particular detail to the 200- $\mu\text{m}$  window. The background to the process which underlies absorption at these wavelengths is given, which leads to the development of a model of atmospheric transmission (Ade, 2003). The usefulness of THUMPER at different locations on Earth is summarised, through interpretation of results of this model.

Since THUMPER utilises photoconductive detectors, an introduction to the physics of these devices is given in Chapter 3. After a brief review of the experiments over the past three decades that have used detectors similar to those in THUMPER, a description is presented of the manufacture of the detector arrays.

Requirements placed upon the design of the instrument are given in Chapter 4. Key elements of the instrument are then described. It should be noted that the design of THUMPER, and hence material included within this Chapter, is the result of effort from several members of the THUMPER team, over many years.

The results of tests carried out on the THUMPER detectors, as described in Chapter 3, are provided in Chapter 5. The interpretation of these results is performed in conjunction with the results of modelling, also based on material from Chapter 3.

Chapter 6 highlights methods by which commissioning will take place. The availability of appropriate calibration sources is discussed. Mention is made of a previous attempt to correlate atmospheric opacity at 1500 GHz with that at 225 GHz.

Finally, Chapter 7 concludes the thesis by summarising the results of the constituent Chapters. Improvements that could be implemented for THUMPER to improve detector performance are given.

## 1.7. References

Ade, P.A.R., 2003, Private Communication.

André, P., Ward-Thompson, D. & Barsony, M., 2000, *From Pre-Stellar Cores to Protostars: the initial Conditions of Star Formation*, Protostars and Planets IV, Mannings, V., Boss, A.P. & Russell, S.S. (eds), p. 59, University of Arizona Press, Tucson, 2000.

- Graue, R., Kampf, D., Poglitsch, A. & Geis, N., 2000, *FIRST PACS Focal Plane Unit*, Proc. SPIE UV, Optical, and IR Space Telescopes and Instruments, **4013**, 109-118.
- Harper, D.A. *et al.*, 2000, *HAWC: a Far-Infrared Camera for SOFIA*, Proc. SPIE Airborne Telescope Systems, **4014**, 43-53.
- Harvey, P.M., 1979, *A Far-Infrared Photometer for the Kuiper Airborne Observatory*, Pub. A.S.P., **91**, 143-148.
- Harvey, P.M. & Jeffries, W.H., 2000, *A Bayesian Analysis of Models for the Dust Cloud around Fomalhaut*, *Astrophys. J.*, **538**, (2), 783-792.
- Heim, G.B. *et al.*, 1998, *Multiband Imaging Photometer for SIRTf*, Proc. SPIE Space Telescopes and Instruments, **3356**, 985-1000.
- Hildebrand, R.H., 1983, *The Determination of Cloud Masses and Dust Characteristics from Submillimetre Thermal Emission*, *Quart. J. Royal Astron. Soc.*, **24**, (3), 267-282.
- Holland, W.S., Robson, E.I., Gear, W.K., Cunningham, C.R., Lightfoot, J.F., Jenness, T., Ivison, R.J., Stevens, J.A., Ade, P.A.R., Griffin, M.J., Duncan, W.D., Murphy, J.A. & Naylor, D.A., 1999, *SCUBA: a Common-User Submillimetre Camera Operating on the James Clerk Maxwell Telescope*, *Mon. Not. R. Astron. Soc.*, **303**, (4), 659-672.
- Kessler, M.F., Steinz, J.A., Anderegg, M. E., Clavel, J., Drechsel, G., Estaria, P., Faelker, J., Riedinger, J.R., Robson, A., Taylor, B.G. & Ximenez de Ferran, S., 1996, *The Infrared Space Observatory (ISO) mission*, *Astron. Astrophys.* **315**, (2), L27-L31, 1996.
- Klaas, U. & Walker, H.J., 2002, *ISOPHOT Far-Infrared Photometry of NGC 3079*, *Astron. Astrophys.*, **391**, (3), 911-915.
- Lemke, D. *et al.*, 1996, *ISOPHOT - Capabilities and Performance*, *Astron. Astrophys.*, **315**, (2), L64-L70.
- Marshall, C.R., Leahy, D.A. & Kwok, S., 1992, *Submillimeter Observations of Circumstellar Dust*, *Publ. Astron. Soc. Pacific*, **104**, (676), 397-401.
- Neugebauer, G. *et al.*, 1984, *The Infrared Astronomical Satellite (IRAS) Mission*, *Astrophys. J.*, **278**, (1), L1-L6.



- Poglitsch, A., Waelkens, C. & Geis, N., 2001, *The Photodetector Array Camera & Spectrometer (PACS) for Herschel*, Proc. Symposium: The Promise of the Herschel Space Observatory, **ESA SP-460**, 29-36.
- Rinehart, S.A., Hayward, T.L. & Houck, J. R., 1998, *Midinfrared Imaging of  $\alpha$  Orionis*, *Astrophys. J.*, **503**, (1), 415-421.
- Sanders, D.B., Soifer, B.T., Elias, J.H., Madore, B.F., Matthews, K., Neugebauer, G. & Scoville, N. Z., 1988, *Ultraluminous Infrared Galaxies and the Origin of Quasars*, *Astrophys. J.*, **325**, (1), 74-91.
- Spinoglio, L., Andreani, P. & Malkan, M.A., 2002, *The Far-Infrared Energy Distributions of Seyfert and Starburst Galaxies in the Local Universe: Infrared Space Observatory Photometry of the 12 Micron Active Galaxy Sample*, *Astrophys. J.*, **572**, (1), 105-123.
- Stevens, J.A. & Gear, W.K., 2000, *Submillimetre Imaging of NGC3079*, *Mon. Not. R. Astron. Soc.*, **312**, (1), L5-L8.
- Takahashi, H. *et al.*, 2000, *FIS: Far-Infrared Surveyor Onboard ASTRO-F (IRIS)*, Proc. SPIE UV, Optical, and IR Space Telescopes and Instruments, **4013**, 47-58.
- Tofani, G. & Natale, V., 2003, *Herschel Space Observatory*, *Mem. S. A. It.*, **74**, 219.
- USRA, 2003, SOFIA website: <http://www.sofia.usra.edu/Sofia/sofia.html>
- van der Veen, W.E.C.J., Omont, A., Habing, H.J. & Matthews, H.E., 1995, *The Distribution of Dust Around Asymptotic Giant Branch Stars*, **295**, (2), 445-458.
- Ward-Thompson, D., André, P. & Kirk, J. M., 2002, *The Initial Conditions of Isolated Star Formation - V. ISOPHOT Imaging and the Temperature and Energy Balance of Pre-Stellar Cores*, *Mon. Not. R. Astron. Soc.*, **329**, (2), 257-276.
- Ward-Thompson, D., 2002, *Isolated Star Formation: From Cloud Formation to Core Collapse*, *Science*, **295**, (5552), 76-81.

## Chapter 2 The Atmosphere at 200 $\mu\text{m}$

### 2.1. Introduction

The Earth's atmosphere in the FIR is generally opaque to extraterrestrial radiation. There are however a few "window" regions between the intense absorption lines of  $\text{H}_2\text{O}$ ,  $\text{O}_2$  and  $\text{O}_3$  which allow observations from high and dry sites to be made. SCUBA at the JCMT takes advantage of two such submillimetre windows, primarily those at 450 and 850  $\mu\text{m}$  (670 and 350 GHz respectively). In periods of extremely dry weather many other windows of transmission open up especially at the highest, driest sites. Atmospheric modelling presented here shows that one of these windows at 200  $\mu\text{m}$  (1.5 THz) should become available for limited astronomical observations from the JCMT. Modelling is important in this respect as it shows the likelihood, and frequency, of making observations from an astronomical observing site of interest. In addition, knowledge of the exact wavelength and spectral bandwidth of any atmospheric window are parameters of paramount importance. Although other atmospheric models exist (e.g. Pardo *et al.*, 2001*b*; Lis, 2003) there is a certain amount of ambiguity over the accuracy of model parameters such as line shapes, concentration profiles and continua.

The major limitation on the use of THUMPER is provided by the weather: THUMPER will only be able to observe through periods of extreme dryness. The minimum transmission through the atmosphere for which THUMPER is still able to operate with sufficient sensitivity is around 5%. The other constraint the atmosphere plays upon the design requirement for THUMPER concerns the width of the atmospheric window. The lines defining the window are very strong  $\text{H}_2\text{O}$  and  $\text{O}_3$  lines. In order to minimise unwanted background radiation from a completely opaque atmosphere, the flux reaching the THUMPER detectors must be limited to that portion of the spectrum the atmosphere is transmitting through. This limits photon noise and hence increases sensitivity. Such a situation can only be realised with closely matched optical filtering, requiring accurate knowledge of the width of the atmospheric window.

The dominant absorption process in the 200- $\mu\text{m}$  wavelength region is due to the rotational transitions of the water molecule. Other contributions also arise, such as that

from O<sub>3</sub> and O<sub>2</sub>, but unlike the water contribution they are fairly constant under varying atmospheric conditions. Here a model for the expected atmospheric emission at high-altitude, ground-based sites is developed and used to predict the likely transmission at a selection of possible observatories. The model is validated through comparison with site-testing measurements of the transmission through the 200- $\mu$ m window. The feasibility of using a 200- $\mu$ m photometer at Mauna Kea is discussed. El Niño events and their implications for FIR astronomy are considered before the opportunities for THUMPER provided by the sites at Atacama and Antarctica are reviewed.

## 2.2. Atmospheric Emission/Transmission Model

Atmospheric modelling is essential to determine the best available atmospheric windows, the optimum profile for band-selection filters and the transmission expected under a selection of atmospheric conditions encountered at the chosen observatory site. It is this study that shows that an instrument such as THUMPER can undertake useful astronomical measurements. Here the atmospheric modelling is limited to the existing observatory sites at Mauna Kea, Chajnantor and the South Pole, which are those most likely to have the extremely dry conditions necessary for 200- $\mu$ m observations.

In principle an atmospheric model is straightforward to construct. Databases of all known lines exist for all the major species in the Earth's atmosphere. These databases contain the line strength, frequency, and temperature and pressure dependences. The addition of a selected line shape function allows, for a given path, the absorption loss to be determined in a line-by-line calculation. Summing for all the lines gives the total extinction expected and hence allows both the transmission through this atmospheric path or the emission from it to be determined. To construct a complete model this calculation must be modified to allow for the pressure, temperature and species concentration variation as a function of altitude and latitude in the Earth's atmosphere. By dividing the atmosphere into many plane-parallel layers the loss/emission for each layer can be computed and summed to give the total extinction/emission in a path of observation. It is apparent that such calculations are intensive on computing power as there are approximately 10,000 rotation lines for water alone for which there is a need to calculate the effective extinction from, for example, up to 30 THz with a spectral resolution of

around 3 GHz (10,000 points) over a 50 layer model of the atmosphere in a line-by-line calculation ( $5 \times 10^9$  calculations). As will be shown from the limited spectral measurements available, such models, although accurately replicating the spectral line features of the atmospheric emission and absorption, need adjustment to account for an ill-determined continuum absorption component that is added to give a more realistic estimate of observing conditions. In the next few sections the model used here is explained in more detail.

### 2.2.1. Molecular Line Database

HITRAN (High-resolution TRANsmission) provides a compilation of spectroscopic parameters that can be utilised to determine the emission and transmission of radiation through the atmosphere. These parameters include the frequency and intensity of each molecular transition along with the foreign and self-broadened line widths and their pressure and temperature dependencies. The latest edition (2000, version 11.0) contains 1,080,000 spectral lines and has been used in the work described in this Chapter. The software package HAWKS (HITRAN Atmospheric WorkStation) is used to extract from the HITRAN database only those molecules of sufficient strength to be important for the frequency range of interest. The line parameters in HITRAN are a mixture of direct observations and theoretical calculations. The goal of HITRAN is to have a theoretically self-consistent set of line parameters, while at the same time attempting to maximise their accuracy (HITRAN website).

In order to limit computing time the database was filtered down to the seven major absorbing molecules (HITRAN website; Anderson, *et al.*, 1986). These molecules are H<sub>2</sub>O, CO<sub>2</sub>, O<sub>3</sub>, N<sub>2</sub>O, CO, CH<sub>4</sub> and O<sub>2</sub>. All significant isotopes are included for each molecule species. Each molecule is assigned a reference number to aid the programming code: for the molecules listed above these numbers run consecutively from 1 to 7 respectively. For the calculations performed here the spectral region of the database was limited to frequencies between 0 and 3 THz (100  $\mu$ m and above), although the window is near 1.5 THz. Such a large frequency range is necessary to ensure that the far wing absorption of intense lines far from the 1.5-THz region are accounted for. Clough *et al.* (1989) take water vapour data in the spectral region 0 to 300 THz into account when

deriving the far-wing contribution of water vapour to the wet continuum when modelling frequencies up to 150 THz. A filter was applied to the molecular database, limiting the cutoff in molecular line strength to  $>10^{-26} \text{ cm}^{-1} / (\text{molecule cm}^{-2})$  resulting in a total of almost 34,000 lines. The wide frequency range studied in this Chapter also enabled comparisons to be drawn with previously published submillimetre transmission measurements (e.g. Paine *et al.*, 2000) thus allowing for empirical verification of the model. There are also a large number of ground-based astronomical instruments, existing and planned, observing in this region that can be used to further verify the model.

### 2.2.2. The Atmospheric Model

The model used here was written in Fortran code by Rice & Ade (1979) and subsequently modified by Hazell (1992) then Ade (2003). It determines the expected transmission and emission along a particular observation path. The two parameters are related by Kirchoff's law which states that, for a specific wavelength, the absorption by the atmosphere will equal its emission. Other parameters, such as temperature and pressure, can be easily adjusted to suit observing conditions and locations as needed. It uses the HITRAN molecular line database and vertical concentration profiles for all the major absorbing species in the line of sight determined from radiosonde or a model atmosphere.

The expression for the absorption of radiation occurring when a molecule undergoes a transition from energy state  $E_l$  to  $E_m$  can be given by (Hazel, 1992)

$$\sigma(\nu)_{lm} = S_{lm}(T)nl(\nu, \nu_{lm}). \quad (2.1)$$

$S_{lm}(T)$  is the integrated line strength from the HITRAN database at a temperature  $T$  for a species of number density  $n$ . The absorption at any arbitrary frequency  $\nu$  from a transition at frequency  $\nu_{lm}$ , is determined from the line shape function  $l(\nu, \nu_{lm})$ , which is discussed in the following section.

HITRAN provides line strengths at a standard temperature of 296 K. For other temperatures more appropriate to the atmosphere a correction must be made of the form

$$S_{lm}(T) = S_{lm}(296)e^{\frac{hc E_l (T-296)}{k 100 296T}}. \quad (2.2)$$

Stimulated emission must also be taken into account. It is accommodated by inclusion of the term:

$$\frac{1 - e^{-\frac{h \cdot c \cdot \nu_{lm}}{k \cdot T}}}{1 - e^{-\frac{h \cdot c \cdot \nu_{lm}}{k \cdot 296}}} \quad (2.3)$$

Finally, the rotational partition function has a power law dependence on temperature. Since HITRAN gives parameters at 296 K, this is corrected by the term

$$\left( \frac{296}{T} \right)^K \quad (2.4)$$

where  $K$  has a value 1.5 for non-linear molecules, and unity for linear molecules.

The above expressions lead to an overall equation for the absorption coefficient as (Hazell, 1992)

$$\sigma(\nu)_{lm} = \frac{1 - e^{-\frac{h \cdot c \cdot \nu_{lm}}{k \cdot T}}}{1 - e^{-\frac{h \cdot c \cdot \nu_{lm}}{k \cdot 296}}} \left( \frac{296}{T} \right)^K S_{lm}(296) e^{-\frac{1.439 E_1(T-296)}{296T}} nl(\nu, \nu_{lm}) \quad (2.5)$$

Equation 2.5 is then summed over all lines  $i$  in the frequency range  $\nu_1$  to  $\nu_2$  of interest to produce

$$\sigma(\nu) = \sum_{i=\nu_1}^{\nu_2} \sigma_i(\nu) \quad (2.6)$$

The optical depth,  $\tau(\nu)$ , at zenith angle  $z$  is given by integrating the absorption coefficient from the height of the observer,  $O$ , to the top of the atmosphere at height  $h$

$$\tau(\nu) = \int_0^h \sigma(\nu, l) dl \sec z \quad (2.7)$$

Transmission,  $t(\nu)$ , through the atmosphere can then be given by

$$t(\nu) = e^{-\tau(\nu)} \quad (2.8)$$

For a non-scattering, non-refractive atmosphere in thermal equilibrium, the equation of radiative transfer is

$$I_G(\nu) = I_0(\nu)t(\nu) + \int_0^h B(\nu, T)(1 - t(\nu)) dh \quad (2.9)$$

where  $I_G(\nu)$  is the intensity of radiation at the ground,  $I_0(\nu)$  is the intensity of radiation at the top of the atmosphere and  $B(\nu, T)$  is Planck's function. The first term on the right-hand

side of Equation 2.9 accounts for atmospheric absorption, whilst the second term accounts for atmospheric emission. Therefore to model atmospheric emission only,  $I_0(\nu)$  must be set equal to zero:

$$I'_G(\nu) = \int_0^h B(\nu, T)(1 - t(\nu))dh \quad (2.10)$$

where the prime over  $I_G(\nu)$  denotes emission only.

When measurements of atmospheric temperature are taken using a Fourier transform spectrometer (FTS), it is the brightness temperature,  $T_b$ , of the atmosphere that is measured. Brightness temperature is the temperature a blackbody would need to attain in order to produce that flux observed.

### 2.2.3. Line Shapes

Although transitions are predicted to occur at a given frequency, physical mechanisms exist which affect a broadening of these discrete frequencies. Depending upon the physical phenomena of interest, different equations describe the different mechanisms. Historically many different line shapes have been used, especially within certain spectral regions. Below, some of these shapes are described.

Due to the lifetime of the excited state a natural broadening occurs (Salby, 1996). Known as the Lorentz line shape it has the form

$$I_L(\nu, \nu_{lm}) = \frac{\alpha_L}{\pi(\nu - \nu_{lm})^2 + \alpha_L^2}. \quad (2.11)$$

$\alpha_L$  is the half-width at half-power of the self broadened line, and is a function of the mean lifetime of the excited state,  $\bar{t}$  :

$$\alpha_L = \frac{1}{2\pi\bar{t}}. \quad (2.12)$$

In the low density of space, molecular absorption and emission would be expected to exhibit these very narrow line widths. However, in the terrestrial atmosphere it is expected that the state lifetime would be limited through collisions. Decreasing  $\bar{t}$  in Equation 2.12 will increase the line half-width: a phenomenon known as pressure broadening. This can also be described by a Lorentz line shape, Equation 2.11, with  $\alpha_L$  then becoming the foreign broadened half-width,  $\alpha_c$

$$\alpha_c = \alpha_0 \left( \frac{P}{P_0} \right) \sqrt{\left( \frac{T_0}{T} \right)} \quad (2.13)$$

where  $\alpha_0$  is the half-width at HITRAN standard temperature,  $T_0$  and pressure,  $P_0$  of 296 K and 1013 mB. The root dependence on temperature is approximate, and is empirically determined (Hazell, 1992).

In the microwave region of the spectrum the van Vleck and Weisskopf (VW) line shape agrees well with measured values. This can be expressed as

$$I_{VW}(\nu, \nu_{lm}) = \frac{1}{\pi} \left( \frac{\nu}{\nu_{lm}} \right)^2 \left[ \frac{\alpha_c}{(\nu_{lm} - \nu)^2 + \alpha_c^2} + \frac{\alpha_c}{(\nu_{lm} + \nu)^2 + \alpha_c^2} \right]. \quad (2.14)$$

However, at low altitudes the line shape is well described by the Zhevakin-Naumov (ZN), or kinetic, function given by

$$I_{ZN}(\nu, \nu_{lm}) = \frac{1}{\pi} \frac{4\nu^2 \alpha_c}{(\nu^2 - \nu_{lm}^2)^2 + 4\nu^2 \alpha_c^2}. \quad (2.15)$$

The final broadening term considered here is that due to the distribution of velocities of the atmospheric molecules. For a molecule at velocity  $\nu$  the equation describing the Doppler frequency shift  $\Delta\nu$  is

$$\frac{\Delta\nu}{\nu} = \frac{\nu}{c}. \quad (2.16)$$

Derived from the Boltzmann probability distribution, the line shape function for Doppler broadening is Gaussian and can be given by (Salby, 1996)

$$I_D(\nu, \nu_{lm}) = \frac{1}{\alpha_D \sqrt{\pi}} \exp \left[ - \left( \frac{\nu - \nu_{lm}}{\alpha_D} \right)^2 \right] \quad (2.17)$$

where the Doppler half-width is

$$\alpha_D = \sqrt{\ln 2} \frac{\nu_{lm}}{c} \sqrt{\frac{2kT}{m}} \quad (2.18)$$

for an particle with molecular mass  $m$ .

In the lower atmosphere, less than about 30 km, pressure broadening dominates. At higher altitudes, as the pressure decreases exponentially, the pressure broadening term decreases. At around 70 km Doppler broadening becomes the dominant term.



When collisional broadening becomes comparable to natural broadening it becomes appropriate to use a convolution of the Lorentzian and the Gaussian profiles. This convolution is known as the Voigt profile (Pardo *et al.*, 2001*b*):

$$I_V(\nu, \nu_{lm}) = \int_{-\infty}^{\infty} I_L(\nu', \nu_{lm}) I_D(\nu', \nu_{lm}) d\nu'. \quad (2.19)$$

The atmospheric modelling code used here utilises the Voigt profile for all lines with the exception of water. The water lines were modelled by a Voigt profile with a truncation applied to the far-wings. The reason for this will become more apparent in the next section, after discussion of the continuum correction terms.

#### 2.2.4. Continuum Corrections

It has long been known (Rice & Ade, 1979; refs. therein) that line-by-line absorption calculations fail to account for all the absorption loss in the terrestrial atmosphere. An excess absorption exists which became most notable in the window regions, and which does not appear to be associated with either missing lines or species in the database. It could however be linked to using an incorrect line shape function. It has become a standard practice to add a continuum term to the absorption coefficient that has been determined empirically through comparisons between models and transmission data. A Rice-Ade type continuum correction, (Zammit & Ade, 1981), which has dependences on the water concentration, temperature and pressure, has traditionally been applied to ensure that realistic estimates are made for the atmospheric transmission. The correction term has the form:

$$\kappa_{RA} = 0.012 \cdot \text{PWV} \left( \frac{280}{T} \right)^{2.1} \left( \frac{P}{850} \right) \nu^{1.22} \quad (2.20)$$

where  $\nu$  is the frequency in GHz. It should be noted that all the correction terms become much less significant for high altitude sites with low H<sub>2</sub>O concentrations.

This correction term was improved on by Pardo *et al.* (2001*a*) who noted that there are really two correction terms. Each relates to whether the collisions are dominated by interactions involving H<sub>2</sub>O, named a wet correction, or those involving N<sub>2</sub>-O<sub>2</sub> and O<sub>2</sub>-O<sub>2</sub> interactions, named a dry correction. The effects of the dry continuum are clearly visible in the various papers of Chamberlin, and others, as a zero-PWV opacity. Pardo *et*

*al.* (2001a) then determine expressions for both dry and wet continuum opacity terms. The dry term is determined by measurement of atmospheric emission during an extremely dry period at Mauna Kea and compared with an FTS scan taken under very similar temperature and pressure conditions, but differing amounts of water vapour. Best fits to their data yield absorption coefficients for the wet and dry continuum terms, respectively

$$\kappa_{\text{wet}} = 0.0315 \left( \frac{\nu}{225} \right)^2 \left( \frac{P_w}{1013} \cdot \frac{P}{1013} \right) \left( \frac{300}{T} \right)^3 \quad (2.21)$$

$$\kappa_{\text{dry}} = 2.612 \cdot 10^{-6} \left( \frac{\nu}{225} \right)^2 \left( \frac{P}{1013} \right)^2 \left( \frac{300}{T} \right)^{3.5} \quad (2.22)$$

where  $P_w$  is the pressure exerted by H<sub>2</sub>O molecules alone.

The water lines are broadened by both self and foreign collisions, involving N<sub>2</sub> and O<sub>2</sub>. The dry continuum opacity term is around an order of magnitude lower than that for the wet for a PWV of 1 mm. At lower PWV levels its relative contribution to the overall opacity increases. Pardo *et al.* (2001b) point out that the frequency dependence changes away from the quadratic form at frequencies above about 1 THz since the centre of the strong water absorption band at 2.4 THz is approached, losing the validity of this continuum correction at higher frequencies.

A more simple method for determining the continuum correction was devised by Clough *et al.* (1989). They take into account only the far-wing line absorption of features due to water. In this method the strength of the water line within  $\pm 750$  GHz of the line centre is made equal to the value at that frequency, as shown in Figure 2.1. The continuum is then calculated by summing all far-wing contributions from all water lines in the frequency range under consideration. The Clough continuum has the benefit over other continuum terms in that it is appropriate for all frequencies, not only that region that can be fitted by a  $\nu^{1.22}$  or  $\nu^2$  term. Since the far wings are removed and added into a slowly varying continuum term, which is then added with the summed line opacity data but with the addition of an applied scaling constant, the Voigt profile can be used for all frequency regions. Note that the line opacity near the line centres is the same for all the profiles given in Section 2.2.3. For computational purposes the continuum term can be

stored as a fixed data array and not calculated for each comparison fit to the data. The Clough continuum correction is shown in Figure 2.2.

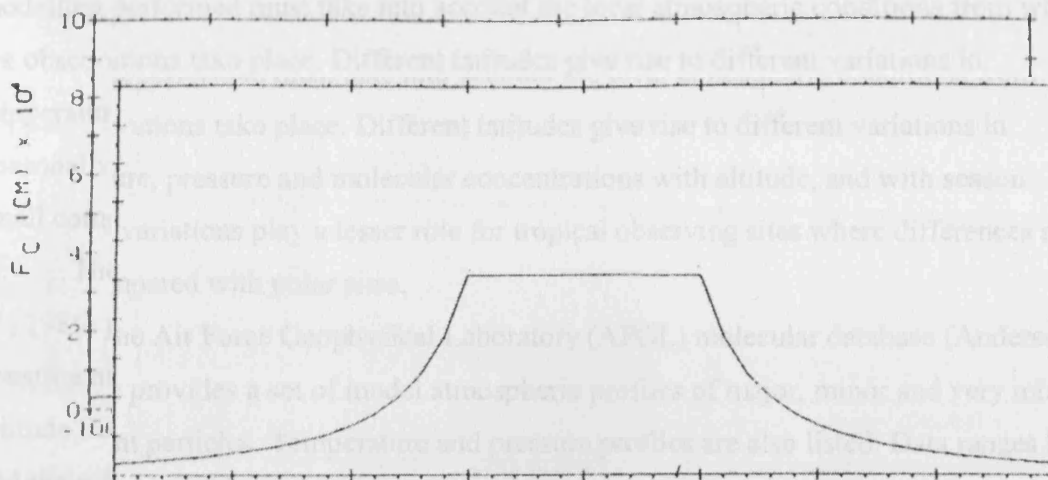


Figure 2.1. The line shape used for calculation of the Clough continuum correction. The pedestal width of  $\pm 25 \text{ cm}^{-1}$  is equivalent to  $\pm 750 \text{ GHz}$  (from Clough *et al.*, 1989).

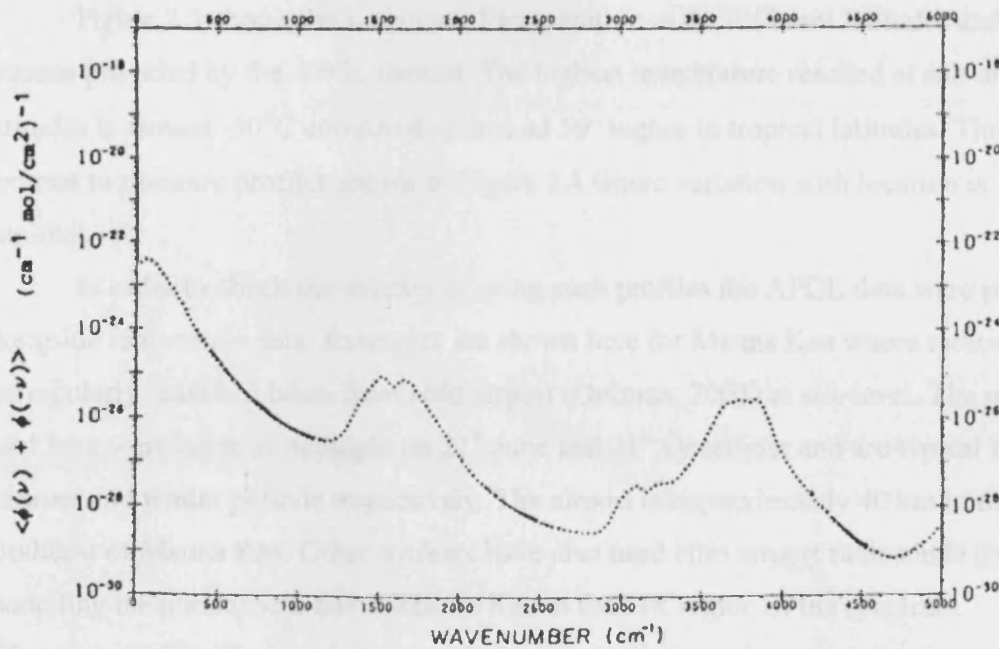


Figure 2.2. The Clough continuum correction over the frequency range 0 to 150 THz (from Clough *et al.*, 1989).

### 2.2.5. Scaling Profiles

In order to identify and compare different sites for THUMPER, any atmospheric modelling performed must take into account the local atmospheric conditions from which the observations take place. Different latitudes give rise to different variations in temperature, pressure and molecular concentrations with altitude, and with season. Seasonal variations play a lesser role for tropical observing sites where differences are small compared with polar sites.

The Air Force Geophysical Laboratory (AFGL) molecular database (Anderson *et al.*, 1986) provides a set of model atmospheric profiles of major, minor and very minor constituent particles. Temperature and pressure profiles are also listed. Data ranges in altitude from sea level to 120 km and are given for latitudes at the tropics, mid-latitudes and the sub-arctic as well as a US standard atmosphere. These designations refer to latitudes of 15°, 45°, 60° and 45.5° respectively. Sub-arctic and mid-latitudes are given for both summer and winter.

Figure 2.3 shows the variation of temperature at the different latitudes and seasons provided by the AFGL dataset. The highest temperature reached at sub-arctic latitudes is around -30°C compared to around 50° higher in tropical latitudes. This is in contrast to pressure profiles shown in Figure 2.4 where variation with location is minimal.

In order to check the validity of using such profiles the AFGL data were plotted alongside radiosonde data. Examples are shown here for Mauna Kea where radiosonde are regularly launched taken from Hilo airport (Oolman, 2003) at sea-level. The profiles used here were taken at midnight on 21<sup>st</sup> June and 21<sup>st</sup> December and are typical for summer and winter periods respectively. The airport is approximately 40 km to the southeast of Mauna Kea. Other workers have also used Hilo airport radiosonde data when modelling the atmosphere above Mauna Kea in the FIR region of the spectrum (Chapman, 2002). The South Pole has had radiosonde data taken regularly since 1961 (Chamberlin, 2003) whilst data for Chajnantor has been taken since 1998 as part of a site-testing program (Radford, 2003). Figures 2.5 and 2.6 show the temperature and pressure profiles for both the radiosonde from Hilo and tropical AFGL model datasets. As

expected, the variation of the data base average pressure profile as a function altitude is small compared to individual radiosonde data.

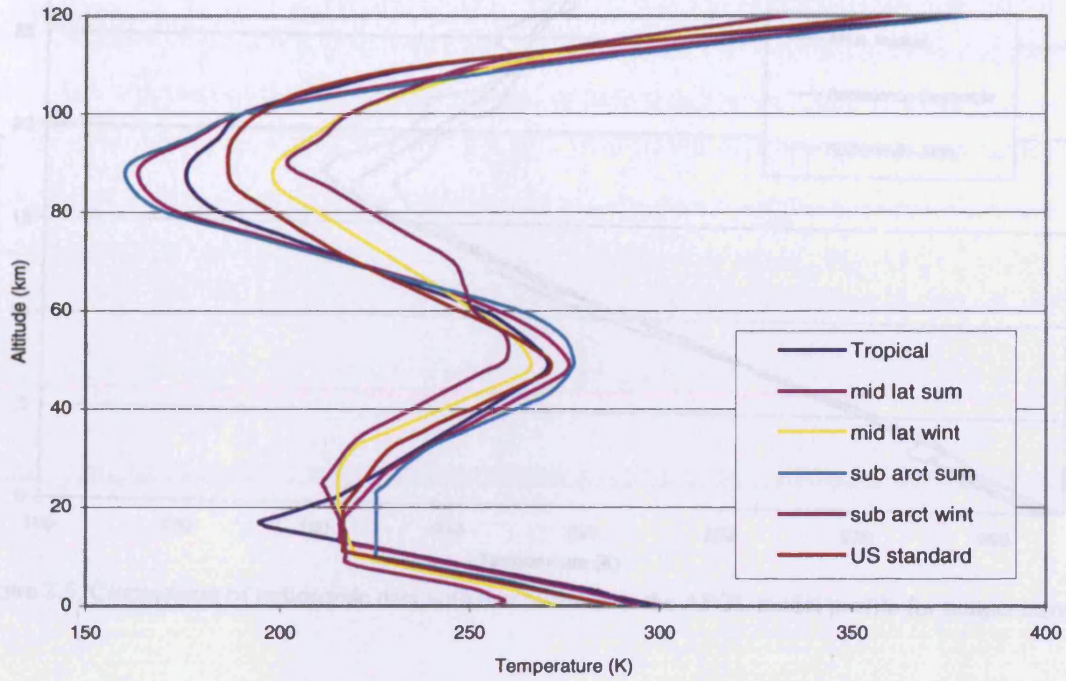


Figure 2.3. AFGL model profile for temperature at different locations and seasons.

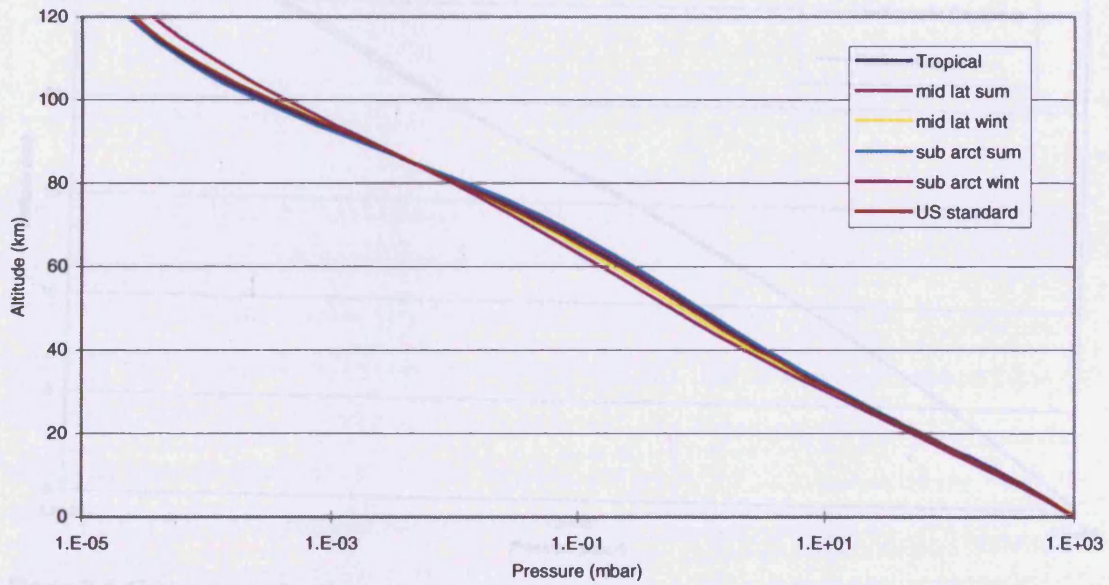


Figure 2.4. AFGL model profile for pressure at different locations and seasons.



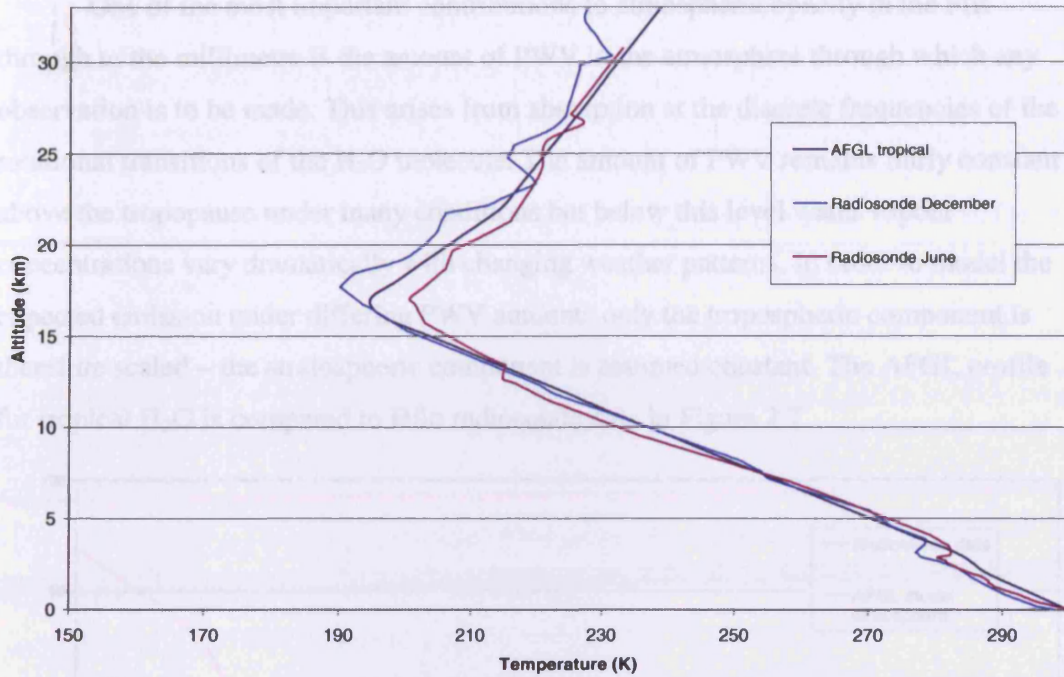


Figure 2.5. Comparison of radiosonde data with that taken from the AFGL model profile for temperature.

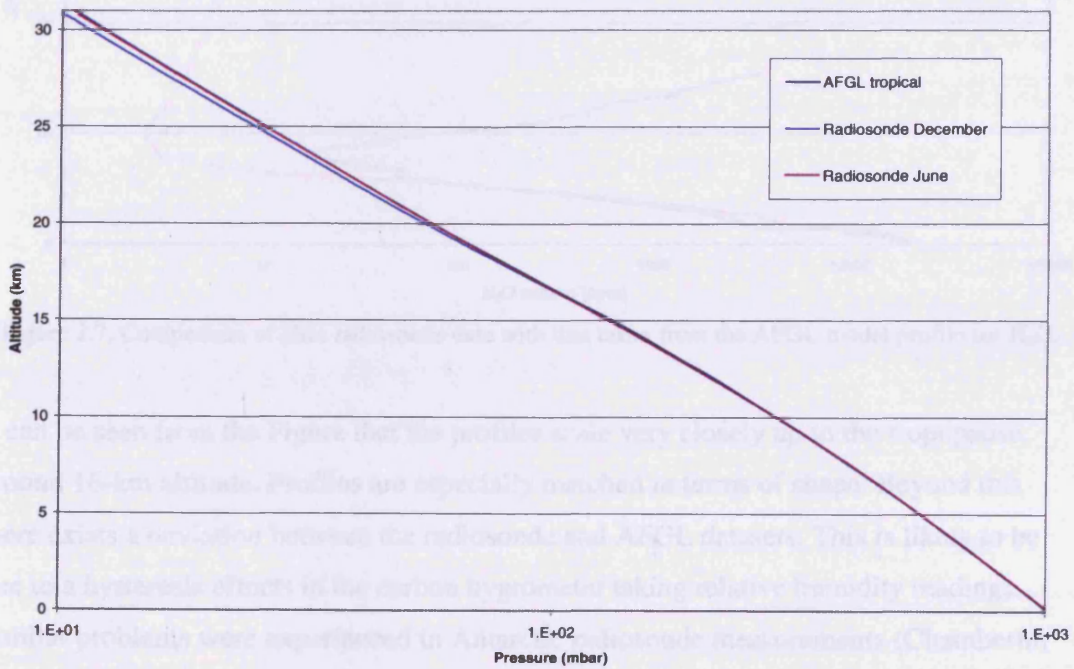


Figure 2.6. Comparison of radiosonde data with that taken from the AFGL model profile for pressure.

One of the most important contributions to atmospheric opacity in the FIR through to the millimetre is the amount of PWV in the atmosphere through which any observation is to be made. This arises from absorption at the discrete frequencies of the rotational transitions of the H<sub>2</sub>O molecule. The amount of PWV remains fairly constant above the tropopause under many conditions but below this level water vapour concentrations vary dramatically with changing weather patterns. In order to model the expected emission under differing PWV amounts only the tropospheric component is therefore scaled – the stratospheric component is assumed constant. The AFGL profile for tropical H<sub>2</sub>O is compared to Hilo radiosonde data in Figure 2.7.

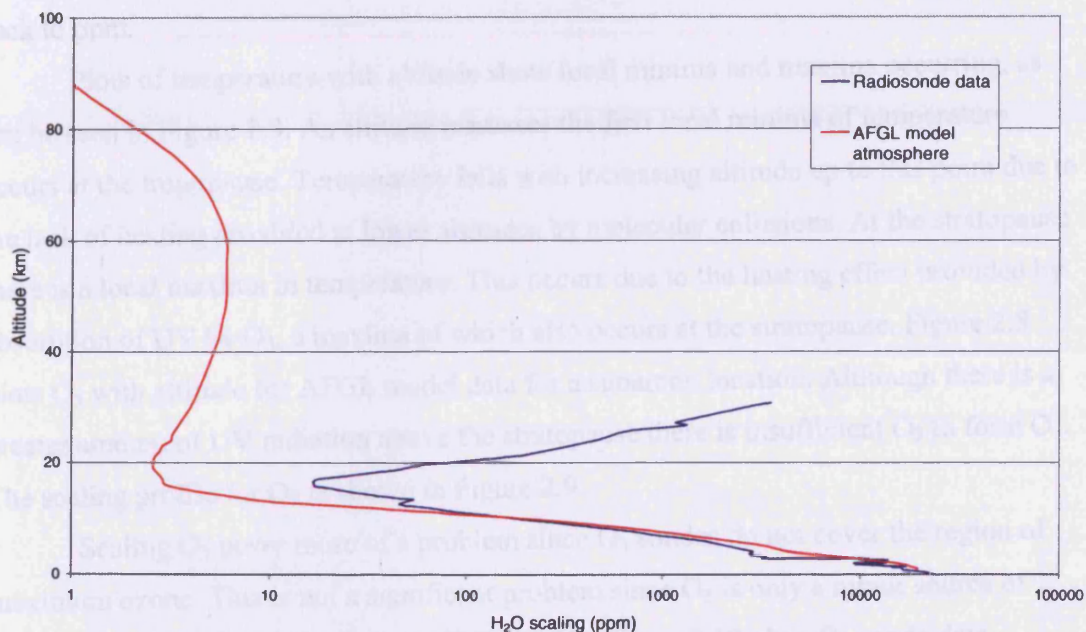


Figure 2.7. Comparison of Hilo radiosonde data with that taken from the AFGL model profile for H<sub>2</sub>O.

It can be seen from the Figure that the profiles scale very closely up to the tropopause, around 16-km altitude. Profiles are especially matched in terms of shape. Beyond this there exists a deviation between the radiosonde and AFGL datasets. This is likely to be due to a hysteresis effects in the carbon hygrometer taking relative humidity readings. Similar problems were experienced in Antarctic radiosonde measurements (Chamberlin & Bally, 1995). Because of this radiosonde data can only considered well calibrated below the tropopause. Model H<sub>2</sub>O concentration profiles (Anderson *et al.*, 1986) predict very small water vapour concentrations above the tropopause. For example, it was found

that above 9.5 km there exists an addition of a further 6% to the PWV for a level of 0.27 mm PWV at the South Pole integrated from ground to 9.5 km. However, within these small concentrations there still exists a factor of up to two difference in the amount of water vapour between different latitudes in the stratosphere.

Using the AFGL PWV concentration, the lower altitude component can be scaled using an algorithm similar to that listed in Appendix B. Lower-altitude-only variations were used to mimic true atmospheric conditions whereby only the tropospheric water vapour content varies. The concentration profile, in parts (molecules) per million (ppm) is read in, scaled to a particular value of PWV above an observer's altitude, then converted back to ppm.

Plots of temperature with altitude show local minima and maxima occurring, as can be seen in Figure 2.3. As altitude increases the first local minima of temperature occurs at the tropopause. Temperature falls with increasing altitude up to this point due to the lack of heating provided at lower altitudes by molecular collisions. At the stratopause there is a local maxima in temperature. This occurs due to the heating effect provided by absorption of UV by  $O_3$ , a maxima of which also occurs at the stratopause. Figure 2.8 plots  $O_3$  with altitude for AFGL model data for a subarctic location. Although there is a greater amount of UV radiation above the stratopause there is insufficient  $O_2$  to form  $O_3$ . The scaling profile for  $O_2$  is shown in Figure 2.9.

Scaling  $O_3$  poses more of a problem since  $O_3$  sondes do not cover the region of maximum ozone. This is not a significant problem since  $O_3$  is only a minor source of opacity in the window of interest for THUMPER. Figure 2.10 plots  $O_3$  sonde data alongside that for the AFGL model atmosphere.



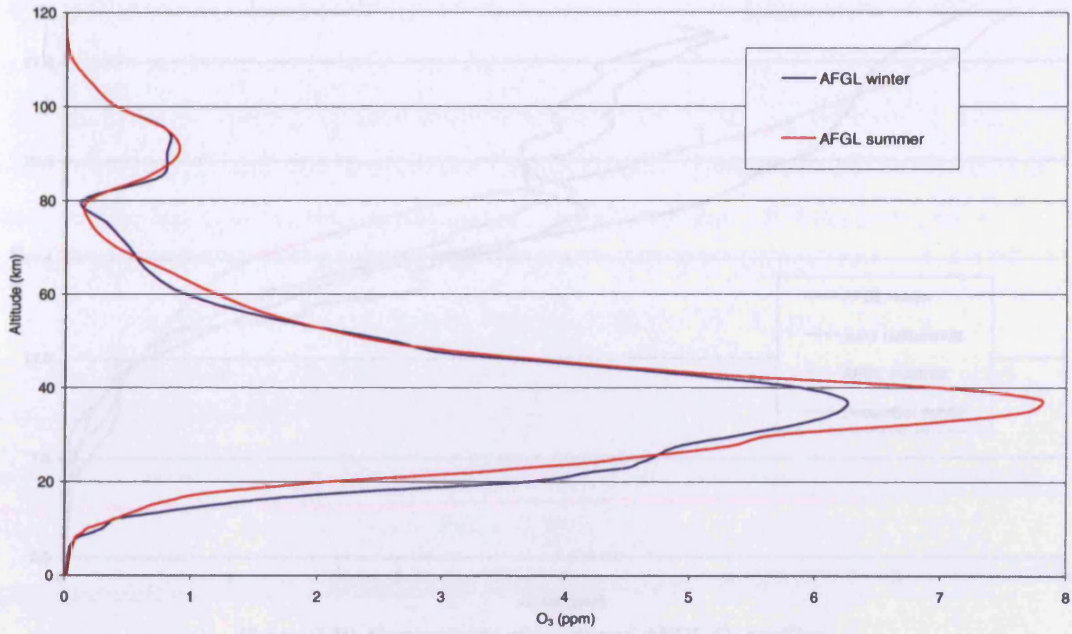


Figure 2.8. O<sub>3</sub> scaling with altitude.

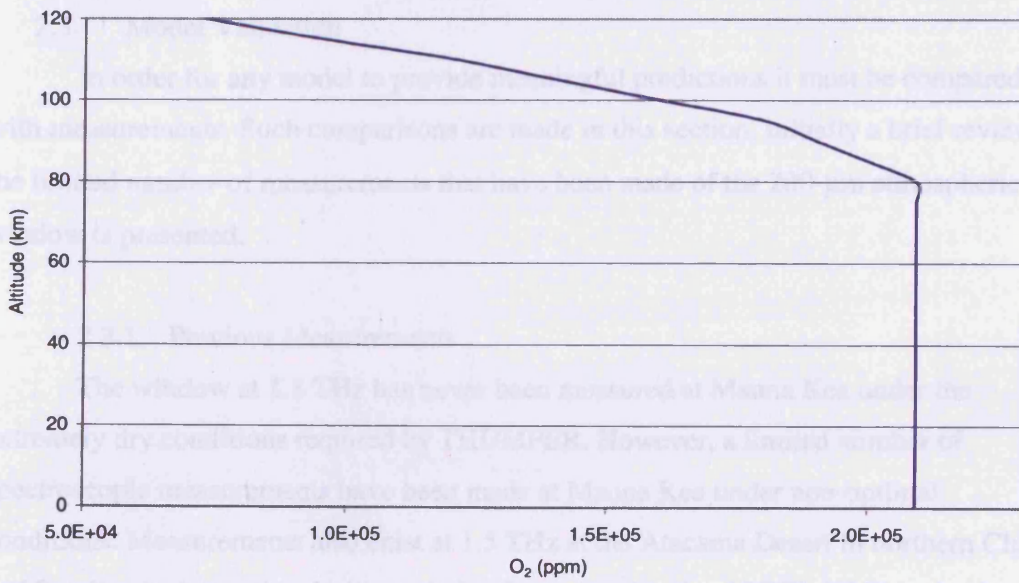


Figure 2.9. O<sub>2</sub> scaling with altitude.

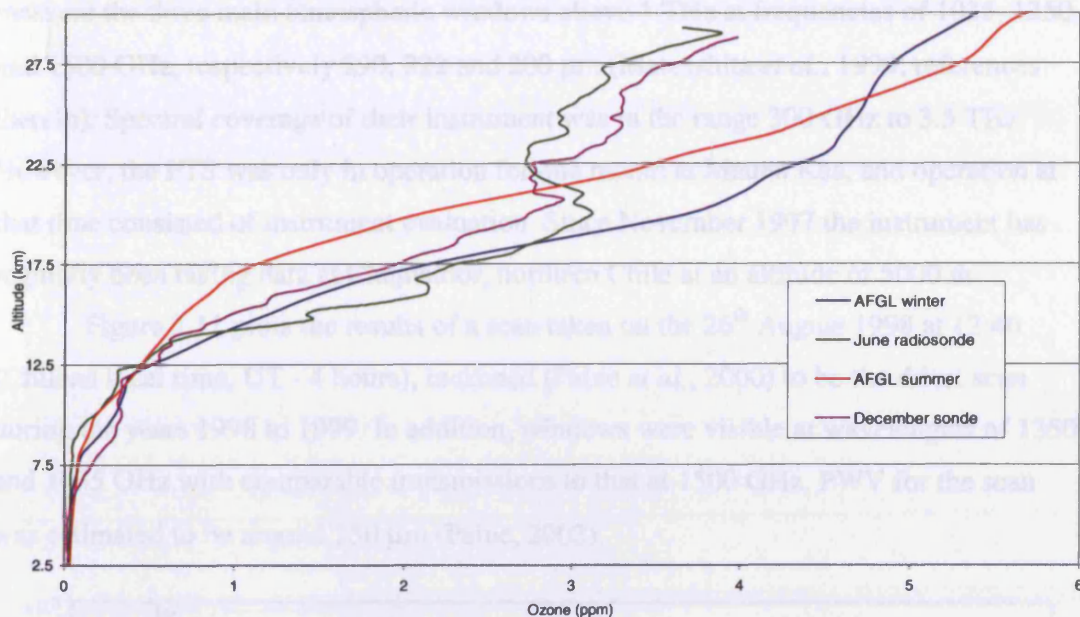


Figure 2.10. Comparisons of sonde and AFGL O<sub>3</sub> profiles.

### 2.3. Model Validation

In order for any model to provide meaningful predictions it must be compared with measurements. Such comparisons are made in this section. Initially a brief review of the limited number of measurements that have been made of the 200- $\mu\text{m}$  atmospheric window is presented.

#### 2.3.1. Previous Measurements

The window at 1.5 THz has never been measured at Mauna Kea under the extremely dry conditions required by THUMPER. However, a limited number of spectroscopic measurements have been made at Mauna Kea under non-optimal conditions. Measurements also exist at 1.5 THz at the Atacama Desert in northern Chile and for sites in Antarctica during periods of very low levels of PWV. PWV is the depth of liquid that would exist if all the water vapour in a column above a given location were condensed into liquid water and standard temperature and pressure. The development of Antarctica and the Atacama Desert for use as FIR observatory sites is discussed below.

Paine *et al.* (2000) were the first to deploy an FTS measuring atmospheric emission for continuous use at frequencies above 1 THz. They were therefore the first to

measure the three main atmospheric windows above 1 THz at frequencies of 1035, 1350 and 1500 GHz, respectively 290, 222 and 200  $\mu\text{m}$  (Matsushita *et al.*, 1999; references therein). Spectral coverage of their instrument was in the range 300 GHz to 3.5 THz. However, the FTS was only in operation for one month at Mauna Kea, and operation at that time consisted of instrument evaluation. Since November 1997 the instrument has regularly been taking data at Chajnantor, northern Chile at an altitude of 5000 m.

Figure 2.11 plots the results of a scan taken on the 26<sup>th</sup> August 1998 at 12:40 (Chilean local time, UT - 4 hours), reckoned (Paine *et al.*, 2000) to be the driest scan during the years 1998 to 1999. In addition, windows were visible at wavelengths of 1350 and 1035 GHz with comparable transmissions to that at 1500 GHz. PWV for the scan was estimated to be around 250  $\mu\text{m}$  (Paine, 2002).

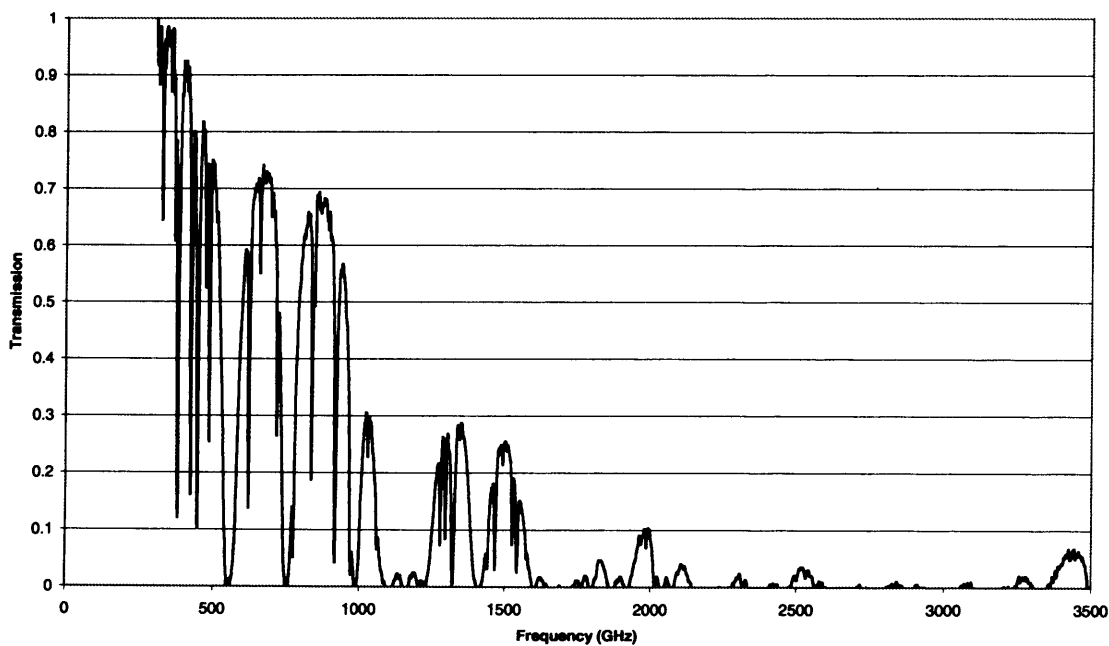


Figure 2.11. Atmospheric transmission at Chajnantor, Chile (courtesy S. Paine).

Matsushita *et al.* (1999) describe measurements carried out in the 150 to 1600-GHz spectral region at Pampa la Bola, northern Chile. Pampa la Bola is at an altitude of 4800 m and around 10 km from Chajnantor. Their results show a number of supra-THz windows opening up during the extremely dry conditions under which the FTS measurements were taken, at 10:25 (local time) 17<sup>th</sup> June 1998. Along with the windows

centred on 1035 and 1350 GHz, the 1500 GHz window was measured with all three windows having transmission of around 20%. However Matsushita *et al.* point out that due to systematic errors in the spectrum the 1500 GHz window could have transmission as low as 10%. The transmission spectrum they obtained is shown in Figure 2.12.

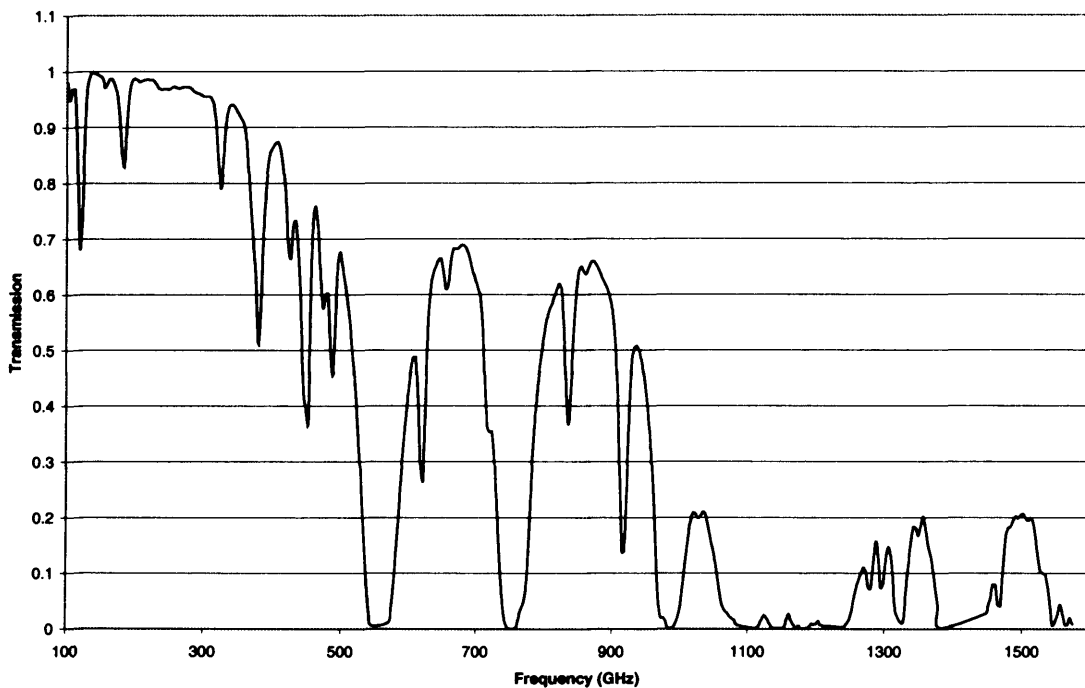


Figure 2.12. FTS measurement giving transmission through the atmosphere at Pampa la Bola, Chile. PWV estimated at 252  $\mu\text{m}$  (courtesy S. Matsushita).

Using the Atmospheric Transmission at Microwaves (ATM) modelling code developed by Pardo *et al.* (2001b) Matsushita *et al.* estimate a PWV of 252  $\mu\text{m}$  at the time their spectra were taken. Modelling in the paper seems to overestimate transmission by only a few per cent. Such an anomaly is likely caused by poor fitting of the continuum terms, which are frequency dependent, since agreement between modelled and measured transmission is good at low frequencies.

Although the continent of Antarctica may be the most logistically challenging site for the development of FIR instrumentation, it does offer the driest sky conditions for ground-based receivers. Chamberlin *et al.* (2003) describe an FTS that was deployed at the geographical South Pole during 2001 operating in the spectral region of 3 GHz to just under 2 THz. Although presenting only preliminary results, scans clearly show the 1500-



GHz window. By comparison with atmospheric models, estimates give a PWV value of a little greater than  $250 \mu\text{m}$ . The result of the FTS scan is shown in Figure 2.13.

Transmission through the 1035 and 1350-GHz windows are similar to that at 1500 GHz, in agreement with Paine *et al.* (2000) and Matsushita *et al.* (1999), above.

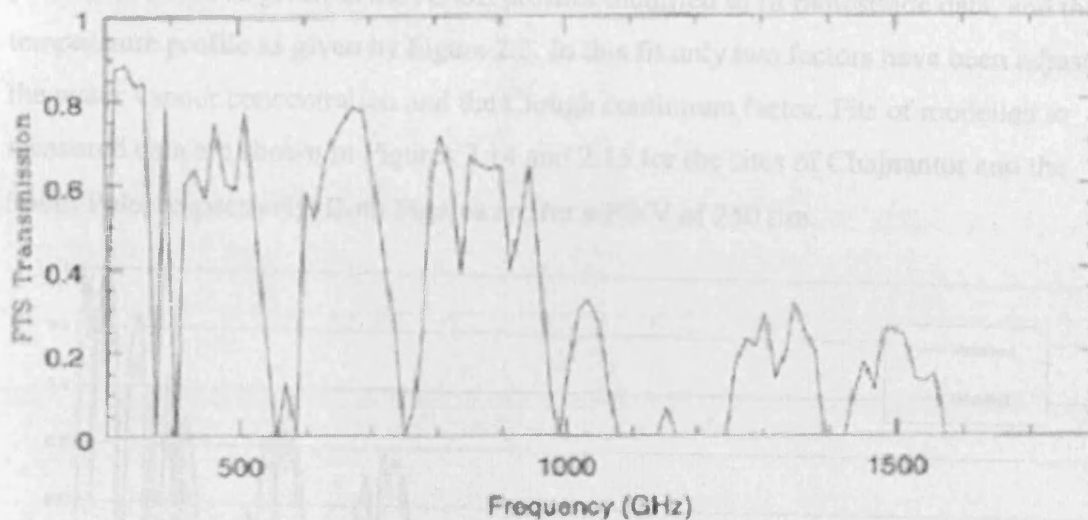


Figure 2.13. Transmission through the atmosphere from a South Pole site (from Chamberlin *et al.*, 2003).

Occurrences of extremely dry weather are generally dependent on location. Section 2.7 discusses the locations for performing astronomy with THUMPER in more detail.

### 2.3.2. Modelling Comparison with Measurements

The data taken at Chile with the FTS makes a direct measure of the atmospheric emission and is calibrated by using hot (ambient temperature) and cold (liquid nitrogen,  $\text{LN}_2$ ) sources. The resultant spectrum is then a plot of the brightness temperature as a function of wavenumber. Conversion to atmospheric transmission requires knowledge of the base temperature of the atmosphere. For a single layer plane-parallel model containing only one species this is easy to define and good estimates of the absorption can be determined from the emission. However, for the real atmosphere there are three main species with different scale heights which, given the atmospheric temperature profile, therefore have different base temperatures. Serabyn *et al.* (1998) have attempted to empirically account for this by applying a correction term to their atmospheric

transmission spectra. Although providing a good estimate of the transmission this may not be the most realistic approach to take.

Since emission spectra are measured, modelling presented here initially replicates atmospheric emission. The model is then adjusted to return values of transmission. The profiles used are as given in the AFGL profiles modified to fit radiosonde data, and the temperature profile as given by Figure 2.3. In this fit only two factors have been adjusted: the water vapour concentration and the Clough continuum factor. Fits of modelled to measured data are shown in Figures 2.14 and 2.15 for the sites of Chajnantor and the South Pole, respectively. Both Figures are for a PWV of 250  $\mu\text{m}$ .

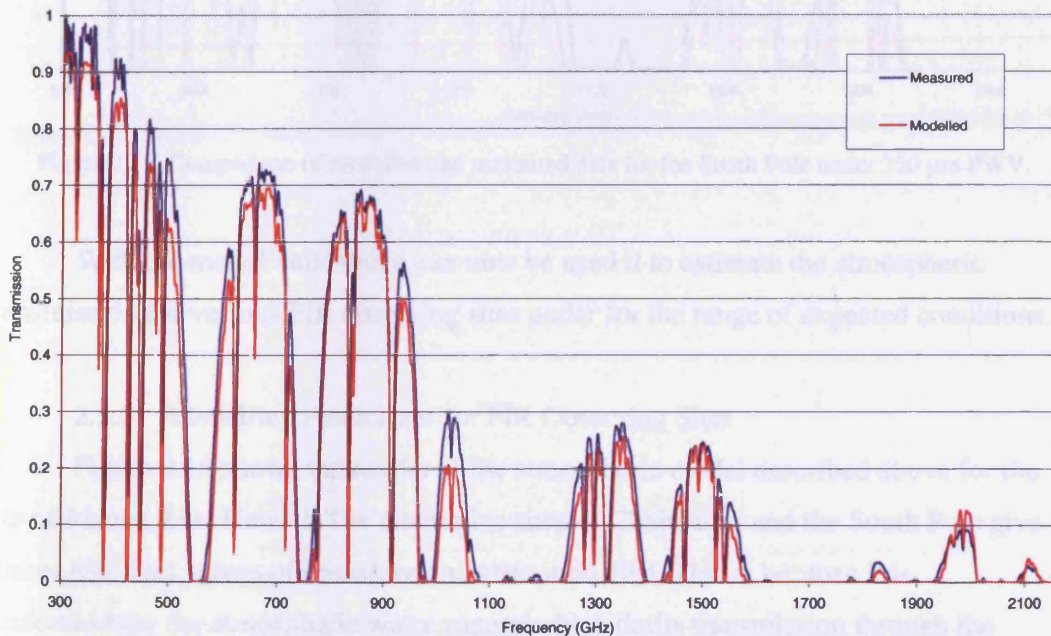


Figure 2.14. Comparison of modelled and measured data for Chajnantor under 250  $\mu\text{m}$  PWV.

Having fitted the atmospheric emission with high accuracy the model can now be used to determine the true transmission through the atmosphere by application of Equation 2.9. The good fit over all the submillimetre window regions is encouraging as it demonstrates that if there exists a measure of the emission in any one waveband it can be used to predict the transmission for all the window regions.



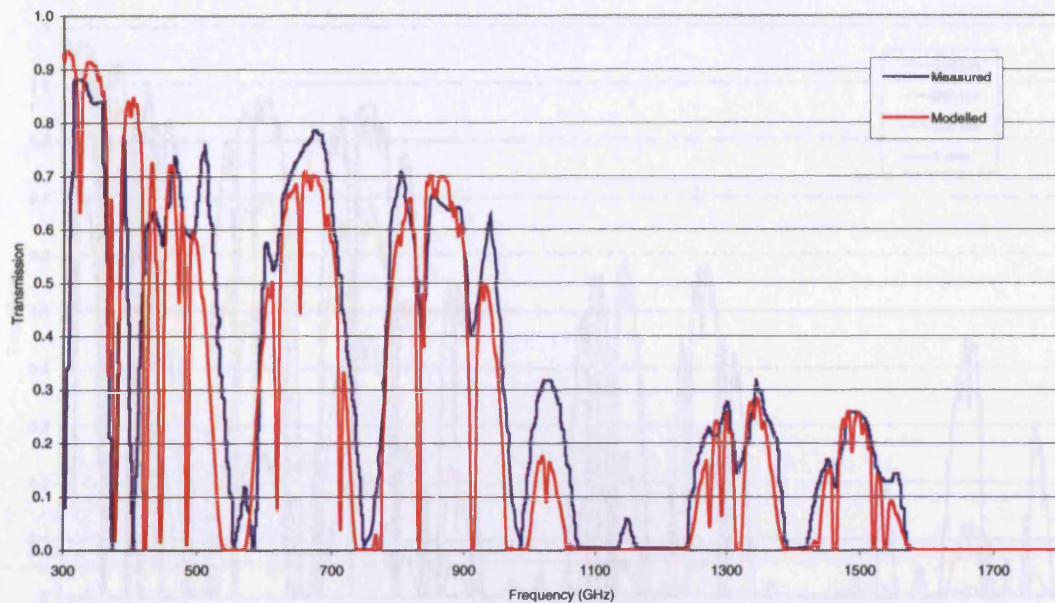


Figure 2.15. Comparison of modelled and measured data for the South Pole under 250  $\mu\text{m}$  PWV.

With the model validated it can now be used to estimate the atmospheric transmission for various FIR observing sites under for the range of expected conditions.

### 2.3.3. Modelling Predictions for FIR Observing Sites

Figure 2.16 shows the results of the atmospheric model described above for the site of Mauna Kea, Hawaii. The alternative sites of Chajnantor and the South Pole give almost identical values of transmission, when modelled. This is because it is predominantly the atmospheric water vapour which limits transmission through the atmosphere, so for a given value of PWV above a given altitude transmission is independent of location.

Lower-quartile measurements of PWV at the three optimum FIR observing sites are summarised in Table 2.1. These are further discussed in Chapter 6. It should be noted that the relatively large lower-quartile quoted for Mauna Kea does not take account of the El Niño conditions which have the effect of reducing PWV over the mid-Pacific. For example the 185  $\mu\text{m}$  PWV inferred during 1998 (Pardo *et al.*, 2001a). AM in Table 2.1 refers to airmass and is related to zenith angle  $z$  by

$$\text{AM} = \sec z \quad (2.23)$$

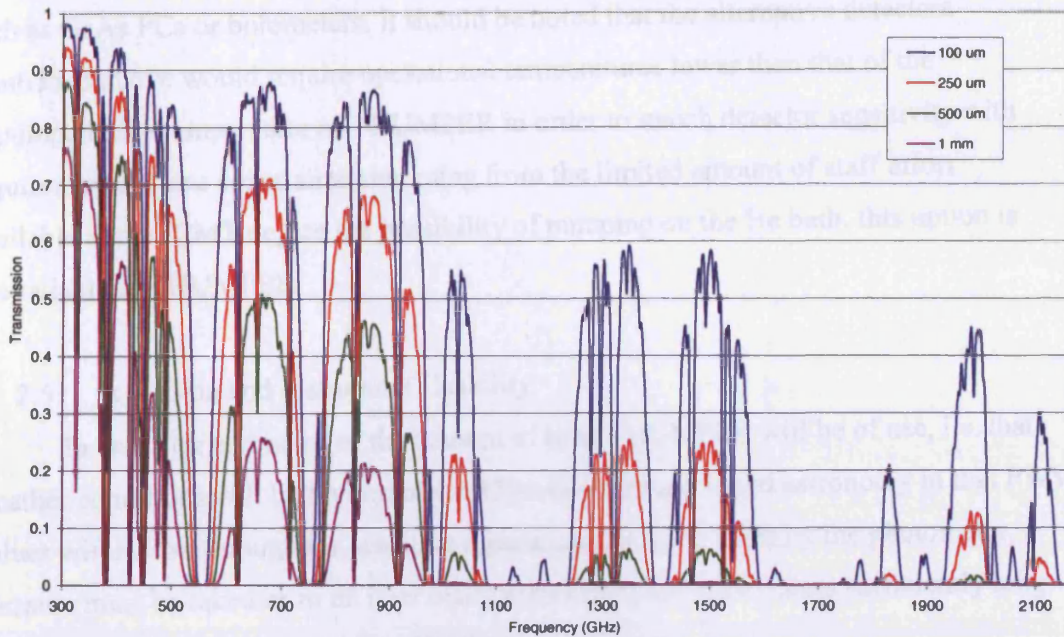


Figure 2.16. Atmospheric transmission in the FIR. Modelled for Mauna Kea, viewing zenith, for different amounts of PWV.

Table 2.1. Lower quartile measurements of PWV at various FIR observing sites.

Site	PWV (mm)	1500 GHz (200 $\mu\text{m}$ ) transmission	
		Zenith	1.3 AM
Mauna Kea	1.05	< 1%	< 1%
Chajnantor	0.68	2%	1%
South Pole	0.19	45%	36%

#### 2.4. 220- $\mu\text{m}$ Window

It can be seen though both the modelling and measurements undertaken and presented above that an atmospheric window exists centred around 1350 GHz (220  $\mu\text{m}$ ). This window appears to have transmission superior to that window centred around 1500 GHz. There exists the option of making simultaneous observations through both windows by use of optical filtering along with highly stressed Ge:Ga PCs, or alternative detectors



such as GaAs PCs or bolometers. It should be noted that the alternative detectors mentioned above would require operational temperatures lower than that of the unpumped LHe temperature of THUMPER in order to match detector sensitivity with requirements. Since constraints stemming from the limited amount of staff effort available at the JCMT negate the possibility of pumping on the He bath, this option is unavailable to THUMPER.

## 2.5. $\tau_{225}$ Data and Instrument Usability

In order for estimates of the amount of time THUMPER will be of use, i.e. that weather conditions will be favourable to 1500-GHz ground based astronomy in that PWV values will be low enough for sensitive measurements to be taken by the photometer, a measure must be taken as to on how many nights per year there occurs sufficiently long periods of sufficiently low levels of PWV.

The Caltech Submillimeter Observatory (CSO) is located about 160 m from the JCMT. Zenith measurements of the opacity at 225 GHz ( $\tau_{225}$ ) have been taken at the CSO for several years. Davis *et al.* (1997) provide a plot of 225-GHz opacity against mm of PWV. By applying a least squares fit to their data they arrive at an equation relating the two variables as:

$$\tau_{225} = 0.05 \times \text{PWV (mm)} + 0.016. \quad (2.24)$$

PWV values were calculated using atmospheric modelling. Such a correlation is important for viewing the amount of time PWV has been less than, for example, 1 mm over certain periods of time.

The weather statistics for Mauna Kea have been analysed by Araújo *et al.* (2001) for the purpose of establishing the suitability of a THUMPER-type photometer to work in conjunction with SCUBA. The key results of that analysis is summarised here. Analysis of the CSO  $\tau_{225}$  data during the period 1997 to 2000 was performed. Figure 2.17 plots  $\tau_{225}$  as a function of date during this four year period. An El Niño season (see Section 2.6 below) occurred during early 1998 and its effects can clearly be seen. Neglecting the most extreme values in Figure 2.17, the upper and lower bounds of 0.05 and 0.2 correspond to PWV values of 0.68 and 3.68 mm respectively, using Equation 2.24.

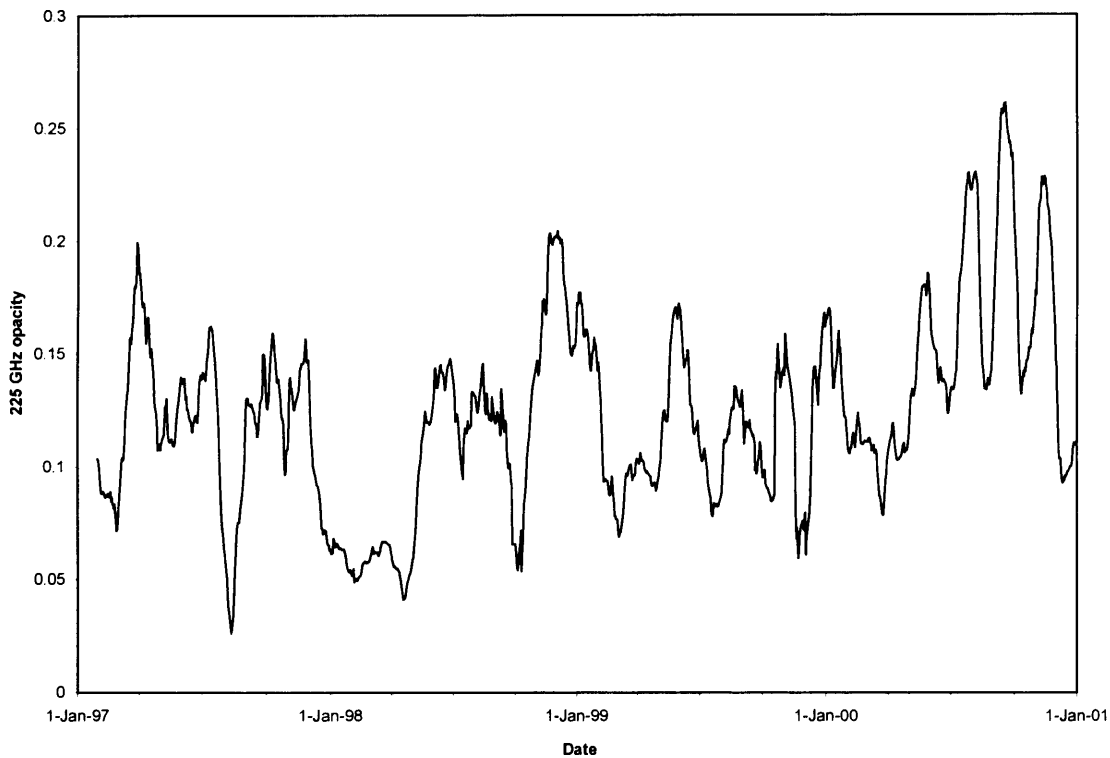
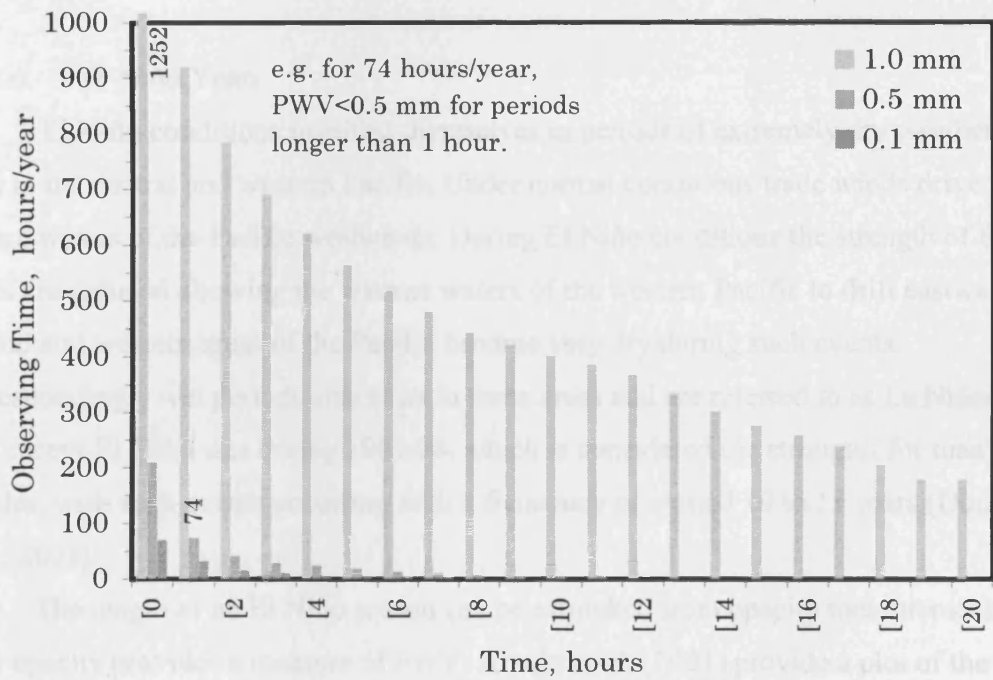
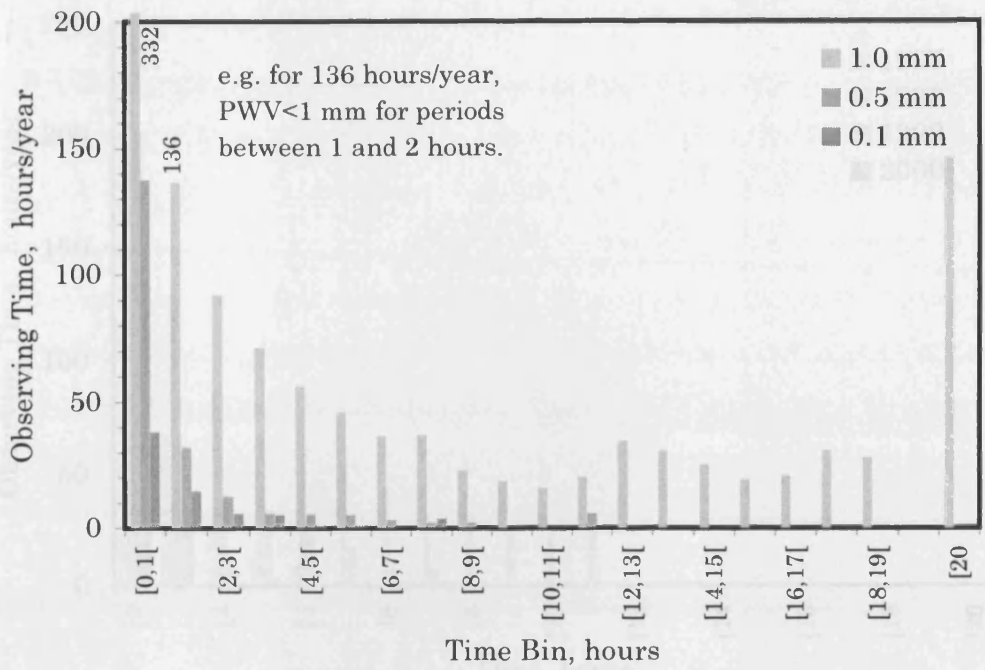


Figure 2.17. Variation of  $\tau_{225}$  with date, January 1997 to December 2000 (courtesy H. Araújo).

Araújo *et al.* also presented statistics detailing how often weather conditions were nominal for 1500-GHz observations according to the length of time taken for observations. Figures 2.18 *a* to *c* show the results of this analysis. Figure 2.18 *a* shows the distribution of how long the weather will be dry enough for observations in a one hour interval, for intervals of increasing duration. Figure 2.18 *b* gives the cumulative total of these results. Figure 2.18 *c* shows the length of time for which PWV is less than 0.5 mm for a given duration.

Since 1996 (although not continuously) there has existed a 183-GHz water vapour monitor (WVM) working along the line of site at the JCMT (Wiedner, 1998). The 183-GHz line saturates for greater than about 2 mm PWV. This is far in excess of PWV conditions under which THUMPER will operate. The 183-GHz WVM is of more use than  $\tau_{225}$  data since it does not rely on any cross-correlation, is always viewing where the JCMT is pointing, and is located at the JCMT as opposed to 160 m away.



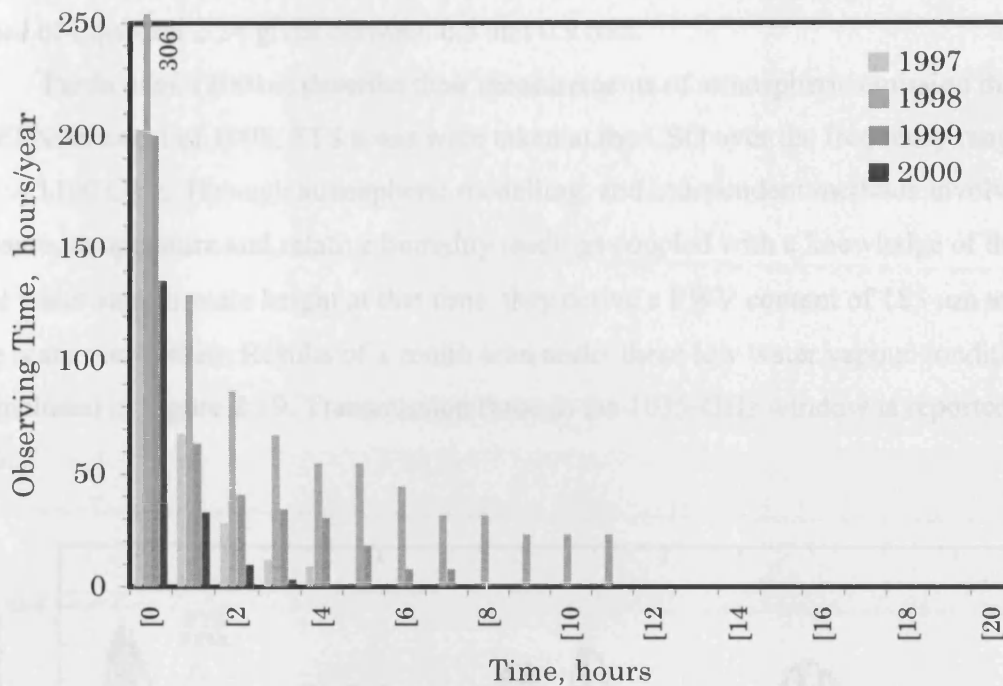


Figure 2.18 a to c. Weather statistics. From Araújo *et al.* (2000).

## 2.6. El Niño Years

El Niño conditions manifest themselves in periods of extremely dry weather over areas in the central and western Pacific. Under normal conditions trade winds drive the surface waters of the Pacific westwards. During El Niño conditions the strength of these winds are reduced allowing the warmer waters of the western Pacific to drift eastwards. Central and western areas of the Pacific become very dry during such events. Correspondingly wet periods also exist in these areas and are referred to as La Niñas. The most recent El Niño was during 1997-98, which is considered the strongest for many decades, with such events occurring with a frequency of around 10 to 15 years (Douglass *et al.*, 2002).

The length of an El Niño season can be estimated from opacity measurements, since opacity provides a measure of PWV. Araújo *et al.* (2001) provide a plot of the daily averaged  $\tau_{225}$  taken at the CSO at Mauna Kea, as a function of date. The graph is reproduced in Figure 2.17 above. The first four months of 1998 can be seen to have a

daily averaged opacity at this frequency of between 0.04 and 0.06. Converting to PWV by use of Equation 2.24 gives between 0.5 and 0.9 mm.

Pardo *et al.* (2001a) describe their measurements of atmospheric emission during the El Niño event of 1998. FTS scans were taken at the CSO over the frequency range 350 to 1100 GHz. Through atmospheric modelling, and independent methods involving pressure, temperature and relative humidity readings coupled with a knowledge of the local water vapour scale height at that time, they derive a PWV content of 185  $\mu\text{m}$  at the time scans were taken. Results of a zenith scan under these low water vapour conditions are included in Figure 2.19. Transmission through the 1035-GHz window is reported as 35%.

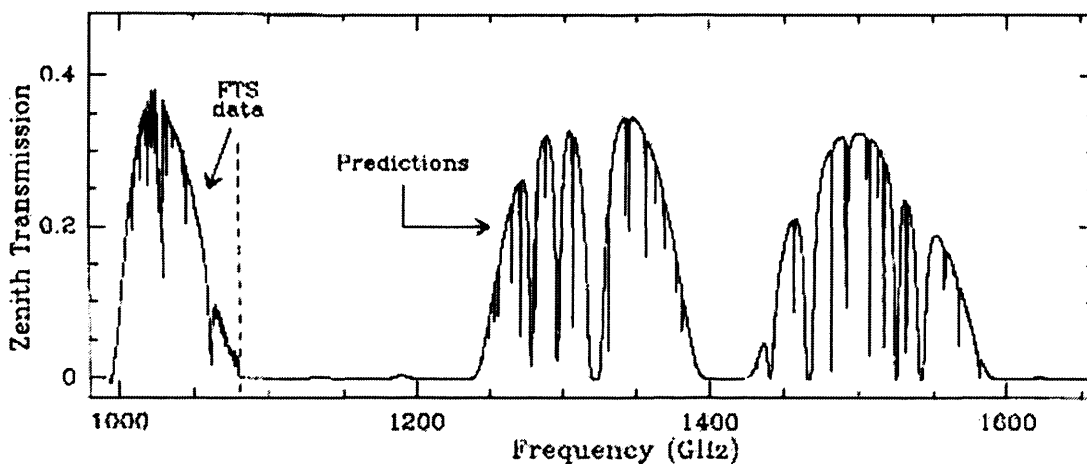


Figure 2.19. Modelled atmospheric transmission (from Pardo *et al.*, 2001a).

Although the scans stop short of the 1500-GHz window, Pardo *et al.* (2001a) use their ATM model to predict estimates of transmission through the 1350 and 1500-GHz windows under such PWV levels. The results of their modelling are shown in Figure 2.19 along with the measured transmission of the 1035-GHz window. Transmission at 1500 GHz is almost 35%, in good agreement with the 36% obtained using the model described in Section 2.2.

## 2.7. Alternative Sites

Whilst THUMPER has been designed to operate at the JCMT, this location is merely the instrument's initial location. A site description for the JCMT has been provided in Section 1.4. With an adjustment to the optics THUMPER could operate at other facilities using the data acquisition software written for laboratory testing. Possibilities provided by other sites are discussed here.

### 2.7.1. Northern Chile

A site currently under development for FIR astronomical observations is located at the Atacama Plain in northern Chile at an altitude of 5000 m. The Plain consists of a large area of desert and is considered one of the driest places on Earth (Radford & Holdaway, 1998). Throughout summer and winter of 1995/96 the opacity at 225 GHz was measured by Radford & Holdaway (1998) and found to vary between median values of 0.087 and 0.042 respectively. Opacities of these values imply PWV columns of between 2.1 and 1.2 mm respectively using Equation 2.24 for conversion. During November 1997, the lowest  $\tau_{225}$  value of 0.02 was measured, equating to 0.7 mm PWV. However, differences in empirically derived terms may exist for different sites. An example is provided by Chamberlin & Bally (1995) who derived a PWV- $\tau$  relationship empirically for the South Pole, discussed in more detail in the following section.

Measurements of atmospheric emission have been taken as a function of frequency, at the Atacama Plain. These are at Chajnantor (Paine *et al.*, 2000) and neighbouring Pampa La Bola (Matsushita *et al.*, 1999). Their results have already been discussed above, in Section 2.2.

Recently constructed at the Chajnantor site is a 12-m dish for use with the Atacama Pathfinder Experiment (APEX). Surface accuracy of the dish is expected to be good to 18  $\mu\text{m}$  (APEX website), almost as good as the JCMT primary mirror. Such a site, where liquid helium (LHe) is not readily available, would be well matched to THUMPER's long cryogenic holdtime. The telescope is currently undergoing performance verification (Kreysa *et al.*, 2004).

### 2.7.2. Antarctica

There exist a number of possible sites on the continent of Antarctica at which conditions would be favourable for FIR astronomy. Whilst the geographical South Pole (3280 m altitude) and Dome C (Concordia) (3280 m altitude, 75° S) have had a variety of site testing measurements made, those of Dome A (Argus) (4200 m altitude, 81° S) and Dome B (3600 m altitude, 77° S) are yet to be tested. The benefits of the South Pole as an infrared observing site, due to the low PWV columns there, have long been known (Smythe & Jackson, 1977).

Richard Chamberlin has studied South Pole observing conditions for more than the last decade. Measurements of opacity at 225 GHz were taken by Chamberlin & Bally (1994) and found to be less than 0.055 for 75% of the time between early March and the end of June 1992. Chamberlin & Bally (1995) report the relationship between 225-GHz opacity and PWV at the South Pole as

$$\tau_{225} = 0.069 \times \text{PWV (mm)} + 0.028 \quad (2.25)$$

which result in a PWV of 0.4 mm for  $\tau_{225}$  of 0.055. PWV values were calculated from radiosonde data. Recent results from FTS scans taken at the site are presented above (Figure 2.13).

The empirical relationship found in Equation 2.25 differs significantly to that found by Davis *et al.* (1997) of Equation 2.24. For example, an opacity of 0.08 would give a PWV of 0.78 mm for the South Pole but 1.28 mm at Mauna Kea. Such a variation may be explained by a different form for the continuum absorption between the different sites, as pointed out by Chamberlin & Bally (1995). Equations 2.24 and 2.25 lead to a zero-PWV opacity at 225 GHz of 0.016 and 0.028, at Mauna Kea and the South Pole respectively.

One cause of this discrepancy may lie in the calculation of PWV by Chamberlin & Bally: in calculating amounts of PWV, the amount of H<sub>2</sub>O is summed from ground to the tropopause. This is, amongst other reasons, because the tropopause is relatively dry. However for the extremely low values of PWV for which they are calculating their correlation it may play a part. However this turns out to be an excess of just over 6%.

Another solution to the problem may lie in the continuum correction terms. Both wet and dry corrections are functions of temperature and pressure. Temperature and

pressure are both functions of latitude. The dry opacity term increases by 20% for the South Pole compared to that for Mauna Kea for a typical set of parameters for each site. Although this does not completely eliminate the discrepancy arising between Equations 2.24 and 2.25 it does provide a partial explanation. Pardo *et al.* (2001a) point out that their measured dry opacities give an excess over that expected through their ATM modelling.

Sites at high latitude, however, offer limitations in terms of sky coverage. Radford & Holdaway (1998) point out that for latitudes less than 30° the view of sky is three times greater for an airmass < 2 compared to polar sites. Median airmass is also less at lower latitudes compared to the Poles: 1.1 compared to 1.35 respectively (Radford & Holdaway, 1998).

The advantages the South Pole site holds for FIR astronomy have only been widely recognised comparatively recently when compared to Atacama or Mauna Kea. The site is therefore under developed in terms of hardware located there. However there does exist a 1.7-m dish as part of the Antarctic Submillimetre Telescope and Remote Observatory (AST/RO), with a surface accuracy of 9  $\mu\text{m}$  (Stark *et al.*, 2001). Such a diameter of dish negates the benefits of ground based observations since, for example, SOFIA, discussed in more detail in Chapter 1, will have a diameter of 2.5 m.

A telescope currently in the design stage is the South Pole Submillimetre Telescope (SPST) (NRC, 2001), of diameter 7 to 10 m. Minimum wavelength observations are 300  $\mu\text{m}$ , assumed due to surface accuracy, which would provide diffraction limited resolution of 8".

## 2.8. Summary

Limited numbers of spectroscopic measurements have been taken at various sites under conditions of low PWV. Although none of these are from Mauna Kea, they are useful for THUMPER in that they provide an indication of atmospheric emission and transmission under certain conditions. In addition, with knowledge of such conditions the atmosphere can be accurately modelled in order to predict transmission at Mauna Kea under varying amounts of PWV.



Mauna Kea does not provide the only site suitable for 1500-GHz astronomical observations. Chajnantor and the South Pole provide superior transmission due to low amounts of PWV at these locations.

## 2.9. References

Ade, P.A.R., 2003, Private Communication.

Anderson, G.P., Clough, S.A., Kneizys, F.X., Chetwynd, J.H. and Shettle, E.P. AFGL atmospheric concentration profiles (0-120 km). Tech. Rep. AFGL-TR-86-0110, AFGL (OPI), Hanscom Air Force Base, Mass., 1987. Anderson, *et al.*, 1986, *AFGL Atmospheric Constituent Profiles*, located at <http://glacier.ssec.wisc.edu/~davet/mfiles/html/19.correlatedk/glatm.html>

APEX website: <http://www.mpifr-bonn.mpg.de/div/mm/apex/>

Araújo, H.M., Walker, R.J., Rinehart, S.A., Griffin, M.J. & Ade, P.A.R., 2001, *Assessment of the 200- $\mu$ m Atmospheric Window for Ground-Based Astronomy*, *Internat. J. Infrared Millimeter Waves*, **22**, (7), 965-982.

Chamberlin, R.A. & Bally, J., 1994, *225-GHz Atmospheric Opacity of the South Pole Sky derived from Continual Radiometric Measurements of the Sky-Brightness Temperature*, *Appl. Opt.*, **33**, (6), 1095-1099.

Chamberlin, R.A. & Bally, J., 1995, *The Observed Relationship between the South-Pole 225-GHz Atmospheric Opacity and the Water-Vapor Column Density*, *Internat. J. Infrared Millimeter Waves*, **16**, (5), 907-920.

Chamberlin, R.A., Martin, R.N., Martin, C.L. & Stark, A.A., 2003, *Submillimeter Atmospheric FTS at the Geographic South Pole*, *Proc. SPIE, Millimeter and Submillimeter Detectors for Astronomy*, **4855**, 609-620.

Chapman, I.M., 2002, Private Communication.

Clough, S.A., Kneizys, F.X. & Davies, R.W., 1989, *Line Shape and the Water Vapor Continuum*, *Atmos. Res.*, **23**, (3-4), 229-241.

Davis, G.R., Naylor, D.A., Griffin, M.J., Clark, T.A. & Holland, W. S., 1997, *Broadband Submillimeter Spectroscopy of HCN, NH<sub>3</sub>, and PH<sub>3</sub> in the Troposphere of Jupiter*, *Icarus*, **130**, (2), 387-403.

- Douglass, D.H., Abrams, D.R., Baranson, D.M. & Clader, B.D., 2002, *On the Nature of the El Nino/La Nina Events*, eprint arXiv:physics/0203016.
- Hazell, A.S., 1992, *Measurement of Submillimetre Atmospheric Emission for the Optimisation of Photometric Bands*, PhD Thesis, Queen Mary & Westfield College, University of London.
- HITRAN website: <http://www.hitran.com/>
- Kreysa, E., Bertoldi, F., Gemuend, H.-P., Menten, K.M., Muders, D., Reichertz, L.A., Schilke, P., Chini, R., Lemke, R., May, T., Meyer, H.-G., Zakosarenko, V., 2003, *LABOCA: A First Generation Bolometer Camera for APEX*, Proc. SPIE, Millimeter and Submillimeter Detectors for Astronomy, **4855**, 41-48.
- Lis, D., 2003, CSO Atmospheric Transmission Interactive Plotter found at <http://www.submm.caltech.edu/cso/weather/atplot.shtml>
- Matsushita, S., Matsuo, H., Pardo, J.R. & Radford, S.J.E., 1999, *FTS Measurements of Submillimeter-Wave Atmospheric Opacity at Pampa la Bola II: Supra-Terahertz Windows and Model Fitting*, Publ. Astron. Soc. Japan, **51**, (5), 603-610 and Plate 24.
- NRC, 2001, *Astronomy and Astrophysics in the New Millennium*, p131 (National Academic Press): <http://books.nap.edu/books/0309070317/html/131.html>
- Oolman, L., 2003, <http://weather.uwyo.edu/upperair/sounding.html>
- Paine, S., Blundell, R., Papa, D.C., Barrett, J.W. & Radford, S.J.E., 2000, *A Fourier Transform Spectrometer for Measurement of Atmospheric Transmission at Submillimeter Wavelengths*, Publ. Astron. Soc. Pacific, **112**, (767), 108-118.
- Paine, S., 2002, Private Communication.
- Pardo, J.R., Serabyn, E. & Cernicharo, J., 2001a, *Submillimeter Atmospheric Transmission Measurements on Mauna Kea during Extremely Dry El Niño Conditions: Implications for Broadband Opacity Contributions*, J. Quant. Spectrosc. Radiat. Transfer, **68**, (4), 419-433.
- Pardo, J.R., Cernicharo, J. & Serabyn, E., 2001b, *Atmospheric Transmission at Microwaves (ATM): An Improved Model for Millimeter/Submillimeter Applications*, IEEE Trans. Antennas Propagation, **49**, (12), 1683-1694.

- Radford, S.J.E. & Holdaway, M.A., 1998, *Atmospheric Conditions at a Site for Submillimeter-Wavelength Astronomy*, Proc. SPIE, Advanced Technology MMW, Radio, and Terahertz Telescopes, **3357**, 486-494.
- Radford, S.J.E. ., 2003, <http://www.tuc.nrao.edu/alma/sites/Chajnantor/instruments/radiosonde/>
- Rice, D.P. & Ade, P.A.R., 1979, *Absolute Measurements of the Atmospheric Transparency at Short Millimetre Wavelengths*, Infrared Phys., **19**, (5), 575-584.
- Salby, M.L., 1996, *Fundamentals of Atmospheric Physics*, (Academic Press, San Diego).
- Serabyn, E., Weisstein, E.W., Lis, D.C. & Pardo, J.R., 1998, *Submillimeter Fourier Transform Spectrometer Measurements of Atmospheric Opacity Above Mauna Kea*, Appl. Opt., **37**, (12), 2185-2198.
- Stark, A.A. *et al.*, 2001, *The Antarctic Submillimeter Telescope and Remote Observatory (AST/RO)*, Publ. Astron. Soc. Pacific, **113**, (783), 567-585.
- Smythe, W.D., & Jackson, B.V., 1977, *Atmospheric Water Vapor at the South Pole*, Appl. Opt., **16**, (8), 2041-2042.
- Wiedner, M.C., 1998, *Atmospheric Water Vapour and Astronomical Millimetre Interferometry*, PhD Thesis, Mullard Radio Astronomy Observatory and Gonville & Caius College, Cambridge.
- Zammit, C.C. & Ade, P.A.R., 1981, *Zenith Atmospheric Attenuation Measurements at Millimetre and Sub-Millimetre Wavelengths*, Nature, **293**, (5833), 550-552.

## Chapter 3 Detector Theory and Construction

### 3.1. Introduction

There are two types of detector that are capable of meeting with the sensitivity requirements of THUMPER. They are the bolometric detectors and the extrinsic photoconductors (PCs). Although the bolometric detectors are ideally capable of higher sensitivity (a factor of  $\sqrt{2}$  because of the absence of carrier recombination noise) their thermal mode of detection requires a lower temperature of operation, about 1.5 K compared to around 4 K for equivalent sensitivity with the PC. This may seem small but unpumped He at a high altitude site boils at approximately 3.7 K whereas to achieve 1.5 K the He vapour pressure would need to be lowered. Pumping on the LHe bath takes time and significantly reduces the hold time of the cryostat thus increasing the frequency for cryogen servicing. THUMPER, as indicated in the previous chapter, will be an opportunistic instrument and therefore needs to be readily available when the weather turns favourable. Hence it is proposed that the system is always kept cold at 3.7 K and is simply switched on when required. Operationally the PCs are therefore a better choice and will be shown to meet with the sensitivities referred to in Chapter 1.

It is useful to review here the basic physics of how the PC devices work so that the parameters that need optimising for the high photon background environment of THUMPER are identified. Particular emphasis is placed upon uniaxially stressed Ge:Ga detectors which is the choice material for the THUMPER PCs. This is followed by a description of the figures of merit used to describe the performance of such devices. After a brief review of experiments that have used stressed Ge:Ga detectors over the past three decades, a detailed description of the manufacture of the stressed arrays used in THUMPER is given.

### 3.2. Photoconductive Detectors

PC detectors can be broadly classified into two groups: the intrinsic, where the crystal comprises one type of semiconductor material; and the extrinsic, where a small amount of a dopant material is introduced. Further, the long wavelength cutoff of

diamond lattice extrinsic PCs can be further extended by use of uniaxial stress. Extensive reviews on PCs exist by Bratt (1977) and Sibille (1986), amongst others.

### 3.2.1. Intrinsic Photoconductors

The highest energy band in a PC is the conduction band where electrons are free to move about in the crystal lattice. Each electron in this band has left behind a positive ion attached to the crystal lattice. All ions in the lattice share all electrons in the conduction band. The lower energy band is the valence band, where electrons are attached to atoms. The valence and conduction bands are separated from each other by a bandgap of the order of 1 eV known as the forbidden band, since electrons cannot remain in this gap in a stable state.

The basic condition for a semiconductor to function as a photoconductive detector is that an incident photon's energy must be greater than, or equal to, the energy gap  $\Delta E_g$  within the semiconductor. If this is the case the photon can be absorbed and create a free charge carrier. For this reason, the spectral range is limited to wavelengths  $\lambda$  less than a cutoff wavelength  $\lambda_c$ :

$$\lambda \leq \lambda_c = \frac{hc}{\Delta E_g}. \quad (3.1)$$

The energy gap of intrinsic Si and Ge is relatively large. This makes them ideal to use for near infrared radiation detection. Ge has a bandgap of 0.67 eV and cutoff wavelength of 1.9  $\mu\text{m}$  whilst Si has a bandgap of 1.11 eV and cutoff wavelength of 1.1  $\mu\text{m}$ . However, some binary and ternary crystals have slightly narrower gaps. For example InSb and HgCdTe have energy bandgaps of 0.18 eV and 0.08 eV leading to cutoff wavelengths of 7  $\mu\text{m}$  and 16  $\mu\text{m}$  respectively (all values from Rieke, 1996). The energy gap can be given in terms of the cutoff wavelength by

$$\Delta E_g \text{ (eV)} = \frac{1.24}{\lambda_c \text{ (\mu m)}}. \quad (3.2)$$

The spectral response of a PC is shown schematically in Figure 3.1, indicating the cutoff wavelength.

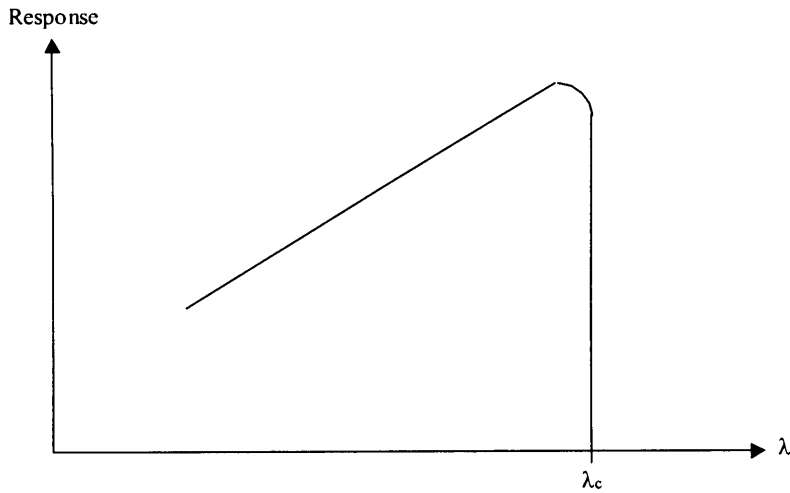


Figure 3.1. Schematic of the spectral response of a PC.

At room temperature there are too many thermally generated free carriers in the conduction band for semiconductors to work effectively as PCs. The increase in carrier energy from the absorption of signal photons results in an insignificant change in conductivity. Infrared detectors therefore have to be cooled to a temperature at which photon generated carriers can be detected against the background of thermally generated carriers. The number of carriers,  $n$ , in a material of temperature  $T$  with bandgap of  $\Delta E_g$  follows Boltzmann statistics:

$$n \propto e^{-\frac{\Delta E_g}{kT}} \quad (3.3)$$

Equation 3.3 indicates that detectors with large bandgaps can work at the relatively warm temperature of LN<sub>2</sub>, whereas smaller bandgap devices need LHe temperatures of operation.

If an electric field  $E$  is applied across a crystal of intrinsic material, a current is obtained from the drift of free electrons in the conduction band. A flow of holes also contributes to the current. The hole flow arises due to the positive ions capturing a valence electron from a neighbour, which itself becomes a positive ion. The net current density is  $i = qE(n\mu_n + p\mu_p)$  where  $n$  and  $p$  are the numbers of electrons and holes per unit volume, and  $\mu_n$  and  $\mu_p$  are the mobilities of those electrons and holes respectively.  $q$  is the charge on a free charge carrier. At high field strengths carriers attain sufficient kinetic energy to ionise neutral atoms causing an avalanching effect - impact ionisation.

Such a field strength is known as the breakdown point and manifests itself as a highly unresponsive detector with low resistance.

### 3.2.2. Extrinsic Photoconductors

When impurities are added to Si or Ge, impurity levels are introduced between the conduction and valence bands such that ionisation energies are decreased to a level of between 0.01 and 0.35 eV. When used as photodetectors this reduction corresponds to cutoff wavelengths in the detector crystal ranging from 4 to 120  $\mu\text{m}$ . The first photoconductive detectors for the 50 to 120  $\mu\text{m}$  range consisted of the host crystal of Ge, along with a moderate amount of a dopant, such as the double acceptor Be or the hydrogenic acceptor Ga as the impurity atom. These were initially made in the mid-1960s (Bratt, 1977). The shape of the spectral response curve near to the long wavelength cutoff has been found to vary with different amounts of impurity and applied electric field (Bratt, 1977). This effect is due to the width of the wavefunction, and tunnelling properties of free charge carriers, varying with impurity concentration and field.

If the dopant is a group V element of the periodic table, of the five electrons in the valence shell one is donated for conduction. Hence group V dopants are termed donors and the material is termed an *n*-type semiconductor since electrical conductivity is dominated by the concentration, *n*, of conduction electrons. The remaining four electrons then bond with the host crystal. The donated electrons introduce an electron energy level in the forbidden band close to the conduction band energy level. The bandgap between the new electron energy level and conduction band energy level is smaller than the previously forbidden band.

Dopants from group III of the periodic table are known as acceptor atoms since they capture a valence electron from a nearby host crystal atom. Materials constructed with acceptor atoms are termed *p*-type semiconductors since electrical conduction is dominated by the hole concentration, *p*. The capture of a valence electron creates a hole which moves in the crystal, the acceptor becoming a negative ion. Their presence introduces an energy level in the forbidden band close to the valence band energy level. In the case of Ge:Ga, an electron from a Ge atom can be passed to the Ga atom which creates a hole loosely bound by the Coulomb force of attraction.

High field strengths cannot be applied to Ge:Ga crystals to obtain a high photoconductive gain because impact ionisation will occur. Photoconductive gain is defined below. Because of the lack of high field strengths, materials with a minimum of compensating impurities must be constructed so as to maximise the free carrier lifetimes. For a *p*-type semiconductor, the compensation ratio is given by

$$\kappa = \frac{N_d}{N_a} \quad (3.4)$$

where  $N_d$  is the concentration of donor impurities (the subscript *d* is for donors) and  $N_a$  is the concentration of acceptor impurities.

Whether or not a photon is absorbed by the crystal depends on the absorption coefficient,  $a(\lambda)$ . This is defined to be

$$a(\lambda) = \sigma_i(\lambda)N_a \quad (3.5)$$

where  $\sigma_i(\lambda)$  is the photo-ionisation cross-section. An approximation for the photo-ionisation cross-section, based on experimentally acquired data, is (Bratt, 1977)

$$\sigma_i = \frac{2.5 \cdot 10^{-18}}{E_i^2}, \quad (3.6)$$

for  $\sigma_i$  in  $\text{cm}^2$  and the ionisation energy,  $E_i$  in eV. By increasing the amount of the dopant,  $a(\lambda)$  is increased, but the amount of the dopant that can be introduced has an upper limit (see below). Detectors working at low-light levels need low levels of dark current, which in turn negates high doping levels.

The absorption coefficient  $a(\lambda)$  is proportional to the volume density of ionisable sites. This is approximately  $10^{22} \text{ cm}^{-3}$  for intrinsic germanium (Sibille, 1986), but for extrinsic germanium Moore & Shenker (1965) found that doping levels of Ga in Ge of around  $10^{14} \text{ cm}^{-3}$  gave maximum speed of response and sensitivity.  $a(\lambda)$  is therefore much larger for intrinsic than for extrinsic material since all atoms of an intrinsic crystal are ionisable whereas only impurity sites are ionisable for an extrinsic crystal. For this reason, intrinsic material PCs can be of much smaller geometry.

The responsive quantum efficiency (RQE) is that fraction of photons absorbed that create free charge carriers. It is also known as the detective absorption  $\alpha$  (Bratt, 1977) and can be expressed as



$$\alpha = 1 - e^{-a(\lambda)z} \quad (3.7)$$

where  $z$  is the typical photon path length through the material.

In order that the RQE should be maximised, the absorption coefficient must also be maximised. To do this, the number of free charge carriers must be made as large as possible. There does exist a limit to the maximum number of impurity atoms that can be placed in the host lattice. This limit is created by the maximum solid solubility of the impurity in the host, and by impurity conduction. Taking the first of these: when the impurity concentration reaches the solubility limit, crystalline imperfections, such as dislocations, begin to occur. However before this limit is reached a practical limit to the impurity concentration of approximately one half of the maximum solubility exists (Bratt, 1977) due to detector performance being so strongly curtailed by such imperfections. Secondly, the impurity conduction limit arises since too many impurity atoms lead to the electron orbits of neighbouring impurity atoms overlapping. Before this limit is reached, hopping conduction arises, giving a drop in detector resistance and a large boost in detector dark current. Hopping conduction occurs when a loosely bound charge carrier tunnels to an adjacent empty impurity site. This form of conduction is dependent on temperature in addition to impurity concentrations.

It is inevitable that small concentrations of other minority dopants are also present. As an example, for Ge:Ga the minority dopants are often As or Pb. These compensate the majority dopants giving an equal concentration of ionised majority and compensating impurity sites. The minority dopant acts to stop the dark current, a source of noise, by decreasing the number of free charge carriers, and to stop the conductance of the crystal becoming overly large. An overly large conductance leads to an insensitive detector, although the speed of response would be improved. A dark current element also arises, due to thermal excitation leading to generation of charge carriers. Cooling a detector to lower temperatures can eliminate this, as shown in Section 3.2.5. However, when operating broadband detectors the dark current is often negligible due to the higher photon noise.

After growth of the Ge:Ga crystals, electrical contacts are required on two opposing faces. The contacts should be Ohmic, non-noisy, mechanically stable and act as a metallic conducting reservoir of free carriers down to the lowest temperatures. Ions of

an acceptor-type metal, such as  $B^+$ , are used with  $p$ -type crystals. The contact depth is at most about  $30\ \mu\text{m}$  into the crystal (Haller, 1994). For crystals with an inter-electrode spacing of over  $500\ \mu\text{m}$  this causes no problems. However, for thinner crystals with low minority dopant concentrations, it becomes possible that free carriers can spill right across the device. This results a photoconductive detector that would be highly conductive in the absence of illumination, due to a large dark current component, adding excess noise. Low-noise contacts are difficult to achieve due to sporadic impact ionisation breakdown in localised regions near to the contacts. This is because of non-uniform electric fields (Bratt, 1977).

Impurity Ge and Si are generally non-Ohmic. In such cases the current flowing through the device is not proportional to the applied voltage across it. This is because both the concentration of free carriers and the free carrier mobility are dependent on the applied field. Carrier concentration is affected by electric field since there exists an amount of carrier heating which gradually lengthens the electron or hole lifetime (Hiromoto *et al.*, 1990). Very high electric fields result in impact ionisation of atoms, causing avalanching and a high degree of non-Ohmic behaviour. An increase in the applied voltage across a device will cause a higher carrier mobility and hence a decrease in resistance.

### 3.2.3. Stressed Photoconductors

Uniaxial stress applied to  $p$ -type diamond lattice semiconductors narrows the bandgap between acceptor and valence band levels. A lower energy is then needed to ionise a neutral acceptor atom. Application of stress along the  $[100]$  crystallographic axis of Ge:Ga extends the long wavelength cutoff from around  $120\ \mu\text{m}$  to beyond  $200\ \mu\text{m}$ , when Ge:Ga is used as a PC. The reason for this is that an unstressed Ge:Ga detector has a four-fold degenerate valence band. When stress is applied the degeneracy is split into two doubly degenerate bands.

Large stresses on the crystal are involved in this application with different authors quoting different values, the largest value seemingly around  $1\ \text{GPa}$  (Laverny *et al.*, 1987). A common value appears to be around  $0.7\ \text{GPa}$  (e.g. Kazanskii *et al.*, 1977). At too high a value of stress the crystal will shatter.

Large increases in responsivity have been found after the application of stress, both in the literature and in THUMPER test crystals. An increase by a factor of two is expected due to the decrease in individual photon energy at longer wavelengths, but increases by factors of up to 10 have been found (Haller, 1994). This has been attributed to the increases in free carrier lifetime and mobility after stress has been applied.

As stress is applied the carrier wavefunction is elongated (Pollak, 1965) such that the overlap between neighbouring impurity atoms is increased. This increases the chance of carrier tunnelling and leads to an increase in the dark current of the PC that manifests itself as an increase in noise. Thermally produced carriers contribute additional dark current: since acceptor energy has decreased, a lower amount of thermal energy is needed to ionise further carriers thus increasing dark current.

An effect that provides a small extension to the spectral response can also be provided by the applied electric field, known as the Franz-Keldysh effect (Pankove, 1971). A photon with energy less than the acceptor energy gap will liberate a free charge-carrier only part-way across the energy gap of a semiconductor. In high electric fields there exists a finite probability of the carrier tunnelling from that point in the bandgap into the valence band.

### 3.2.4. Detector Responsivity

The responsivity of a PC provides a measure of the output signal obtained for a given input power. An equation is derived here for responsivity in terms of basic PC parameters.

The average distance,  $l$ , moved by a free carrier in an electric field can be expressed as

$$l = \mu E \tau. \quad (3.8)$$

where  $\mu$  is the carrier mobility and  $\tau$  is carrier lifetime. The signal current  $I_s$  from  $\dot{N}$  photons per second incident on the detector crystal is

$$I_s = \frac{q \dot{N} \eta l}{L} \quad (3.9)$$

where  $\eta$  is the RQE and  $L$  is the inter-electrode distance. The ratio of the average distance moved by the free charge carrier to the inter-electrode spacing is known as the

photoconductive gain:  $G = \frac{l}{L} \cdot l$ , and hence  $G$ , is a strong function of bias. For a PC it is only possible to measure directly the product of photoconductive gain and  $\eta$ , inferring  $G$  requires knowledge of carrier mobility.

Along with  $G$  and  $\eta$ , another important figure of merit is the current responsivity,  $R_I$ . This is the ratio of the signal current to the input power and is given by

$$R_I = \frac{I_s}{P_{sig}} = \frac{q\dot{N}\eta G}{\dot{N}h\nu} = \frac{q\eta G}{h\nu}. \quad (3.10)$$

In Equation 3.10,  $P_{sig}$  represents the signal power, and the product  $h\nu$  gives the energy of an individual incident photon of frequency  $\nu$ .

A drop in the current responsivity can be caused by reflection of radiation from the crystal face forcing incident photons back out towards the photon source. A fraction,  $r$ , of the photons are reflected from the front surface where

$$r = \left( \frac{n-1}{n+1} \right)^2 \quad (3.11)$$

for a material of refractive index  $n$ . For Ge,  $n = 4$  and so  $r = 0.36$ . However, by use of integrating cavities or rooftop shaped crystals a higher responsivity can be gained. Integrating cavities provide further chances of photon absorption by the crystal due to mounting the crystal surrounded by a highly reflective surface, with a cavity geometry designed to reflect photons towards the position of the crystal. Rooftop crystals (also known as end-fire, flat-roofed or bevel-ended crystals) increase the chance of absorption by total internal reflection. Figure 3.2 shows the shape of the rooftop geometry. The average internal path length was found to increase by a factor of 4.1 (Wang *et al.*, 1986) for a bevel of 20°.

### 3.2.5. Intrinsic Noise

Detector performance is degraded by noise arising from various sources. The most important sources in PCs are photon, Johnson, generation-recombination (g-r) and

$\frac{1}{f}$  noise. Each of these is discussed in this Section.

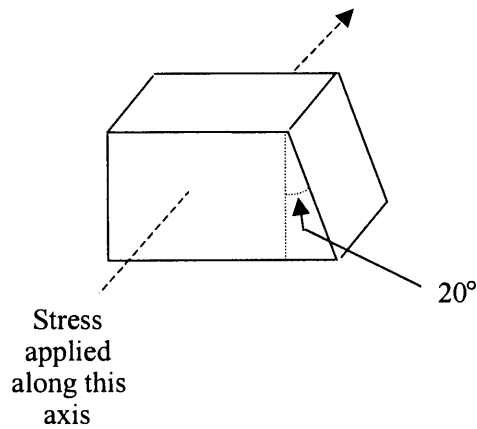


Figure 3.2. End-fire geometry of a photoconductive crystal.

When considering the arrival rate of photons, deviations from the mean rate must also be considered. The random fluctuations in the arrival rate of photons gives rise to the phenomenon of photon noise. From Poisson statistics the standard deviation from the mean is its square root. Thus if a mean number of photons are measured, constituting a signal, then the error in this measurement is the standard deviation, or the square root, of the mean, giving the noise contribution due to the random arrival rate of photons. A background photon-limited noise case is common in high background or wide spectral pass band experiments due to the large number of photons present. Hence photon noise totally outweighs other noise sources.

In an ideal situation, the only noise source will come from photons. What has to be aspired to is for the dominant noise source to be photon noise, and other noise sources are negligible in comparison. Since other noise contributions occur, the best figure of merit, which includes both the RQE and the other noise mechanisms, is the detective quantum efficiency (DQE), defined as (e.g. Haller, 1994)

$$DQE = \left( \frac{NEP_{BLIP}}{NEP_{meas}} \right)^2. \quad (3.12)$$

The NEP is the signal power that gives a signal to noise ratio of one in a 1-Hz post-detection bandwidth (PDBW).  $NEP_{BLIP}$  is the background limited NEP (BLIP is the acronym for Background Limited Infrared Photoconductor). The photon-limited NEP,

$NEP_{ph}$ , is the ultimate noise limit a detector can achieve, i.e. its only noise source is from the random arrival rate of the photons.  $NEP_{ph}$  is derived by Boyd (1982) as

$$NEP_{ph}^2 = \frac{4A_{det}\Omega(kT)^5 x_s^2}{c^2 h^3} \int_{x_1}^{x_2} \frac{\varepsilon t_{fil} x^2}{e^x - 1} \left( 1 + \frac{\varepsilon t_{fil}}{e^x - 1} \right) dx \quad (3.13)$$

where  $A_{det}$  is the area of the detector;  $\Omega$  is the solid angle of the background, as seen by the detector;  $\varepsilon$  is the emissivity of the background;  $t_{fil}$  is the transmission of the optical filters;  $x$  is the Bose factor  $\frac{h\nu}{kT}$ ; and  $x_s$  corresponds to the Bose factor with signal

frequency  $\nu_s$  incident on the detector. The term in parenthesis in Equation 3.13 is due to photon shot and wave noise. Wave noise arises in photon detectors due to the fact that photons obey Bose-Einstein statistics. Taking photon noise merely as the shot noise component treats the arrival rate of photons as random whereas in reality there exists some correlation in their arrival rate. This can be considered as photons arriving at the time of arrival of each wave crest. Such a treatment leads to an additional noise term, that of the Bose factor  $\frac{1}{e^{\frac{h\nu}{kT}} - 1}$  (Bratt, 1977), with the efficiencies of the optical filtering

included. If  $h\nu \gg kT$  shot noise will dominate. Conversely if  $h\nu \ll kT$  then shot noise is negligible and wave noise dominates. For a 200- $\mu\text{m}$  detection system viewing a room temperature background both photon and wave noise terms are significant.

The ideal NEP for PCs includes an additional component of  $\sqrt{2}$ , which must be factored into Equation 3.13, to account for g-r noise. g-r noise arises from fluctuations in the number of free charge carriers comprising the detector current, due to the random generation and recombination of the carriers. The additional factor is of the value  $\sqrt{2}$  since g-r noise occurs by the same random process as does the arrival rate of photons, and that the two noise sources add together in quadrature. The equation for the  $NEP_{BLIP}$  is then

$$NEP_{BLIP}^2 = \frac{8A_{det}\Omega_s(kT)^5 x_s^2}{c^2 h^3} \int_{x_1}^{x_2} \frac{\varepsilon t_{fil} x^2}{e^x - 1} \left( 1 + \frac{\varepsilon t_{fil}}{e^x - 1} \right) dx . \quad (3.14)$$

A simplified, and more frequently quoted (e.g. Wolf, 1994), version of Equation 3.14 can be given as

$$\text{NEP}_{BLIP} = 2 \sqrt{h \nu P_{back} \left( 1 + \frac{t_{fil}}{e^{kT} - 1} \right)} \quad (3.15)$$

and agrees with Equation 3.14 to within 1%. In Equation 3.15  $P_{back}$ , the background power incident on the detector, is given by

$$P_{back} = A_{det} \Omega_{def} \int_{\nu_1}^{\nu_2} t_{fil} B(\nu, T_{back}) d\nu \quad (3.16)$$

where the integral is taken as being between the filter defining frequency limits.

The measured NEP ( $\text{NEP}_{meas}$ ) is obtained by dividing the signal power,  $P_{sig}$ , incident on the detector by the measured signal-to-noise ratio,  $\text{SNR}_{meas}$ , in a 1-Hz PDBW  $\Delta f$ :

$$\text{NEP}_{meas} = \frac{P_{sig}}{\text{SNR}_{meas} \sqrt{\Delta f}}. \quad (3.17)$$

Haller (1994) states that DQEs can reach 40% or higher for state-of-art unstressed extrinsic germanium PC systems.

Whilst  $\text{SNR}_{meas}$  is the measured quantity, the signal power from a chopped blackbody source of temperature  $T_{bb}$  can be determined by integrating the difference between the blackbody and background Planck functions over the frequency limits provided by the optical filtering of the detection system:

$$P_{sig} = \frac{\sqrt{2}}{\pi} \frac{A_{det} A_s}{D^2} \int_{\nu_1}^{\nu_2} t_{win} t_{fil} [B(\nu, T_{bb}) - B(\nu, T_{back})] d\nu. \quad (3.18)$$

The factor of  $\frac{\sqrt{2}}{\pi}$  is the signal chopping efficiency,  $A_s$  is the area of the source,  $D$  is the detector to source distance ( $A_s/D^2$  gives the solid angle of the source,  $\Omega_s$  as seen by the detector), and  $t_{win}$  is the transmission of the window.

The spectral density of photon noise can be expressed as (Luinge *et al.*, 1980)

$$i_{n,ph} = 2R_l \sqrt{\frac{P_{back} h \nu}{\eta}}. \quad (3.19)$$

However, this fails to take account of any form of wave noise. Such a treatment leads to an additional noise term that amends Equation 3.19 to

$$i_{n,ph} = 2R_l \sqrt{\frac{P_{back} h\nu}{\eta} \left( 1 + \frac{\eta t_{fil}}{e^{\frac{h\nu}{kT}} - 1} \right)}. \quad (3.20)$$

This is similar to Equation 3.15, where responsivity is related to the noise current spectral density by

$$\text{NEP} = \frac{i_{n,ph}}{R_l} \quad (3.21)$$

In Equations 3.19 and 3.20 the value of 2 appears outside of the square root. This introduces the extra factor of  $\sqrt{2}$  to the photon noise to account for the g-r contribution.

Dark current is often the dominant noise source for stressed PCs at unpumped LHe temperatures. This is ultimately linked to the finite temperature of the semiconductor. In the absence of illumination the number of free charge carriers can be given by

$$p = \frac{(N_d - N_a)}{N_a} \frac{2}{\delta} \left( \frac{2\pi m^* kT}{h^2} \right)^{\frac{3}{2}} \exp\left(\frac{-E_i}{kT}\right) \quad (3.22)$$

where  $\delta$  is the ground state degeneracy of the donor impurity,  $m^*$  is the effective mass of the hole and  $E_i$  is the impurity binding energy. The equation, derived by Bratt (1977), provides the dependence of charge carriers on temperature. Taking logs gives

$$\log p = \log N_0 + \frac{3}{2} \log T - \log e \cdot \frac{E_i}{k} \frac{1}{T}. \quad (3.23)$$

The  $\log e \cdot \frac{E_i}{k} \frac{1}{T}$  term dominates over  $\frac{3}{2} \log T$  in the temperature range of 1.5 to 4.5 K.

Therefore from a plot of  $\log p$  against reciprocal temperature the ionisation energy can be recovered, as by Church *et al.* (1993).

The noise spectral density of dark current is given by Hiromoto *et al.* (1990) as

$$i_{n,g-r} = \sqrt{4qI_d G} \quad (3.24)$$

where  $I_d$  is the dark current flowing in the detector. The physical mechanism behind this form of noise is g-r events.

Another unavoidable noise source is that due to the random flow of charge carriers through any resistive element in a circuit. This is Johnson-Nyquist noise named



after the engineer who first measured it (Johnson) and the physicist who originally derived the equation describing it (Nyquist). Its ultimate source is from the finite temperature of the resistor. For a resistive element of resistance  $R$  at temperature  $T$ , the spectral density of thermal noise current is

$$i_{n,th} = \sqrt{\frac{4kT}{R}} . \quad (3.25)$$

There exists a noise component known as  $\frac{1}{f}$  noise, referring to the shape of its spectrum. The physical mechanisms behind  $\frac{1}{f}$  noise are somewhat uncertain.

Arutyunyan *et al.* (1989) consider it to arise from fluctuations in carrier mobility whereas Vincent (1990) provides an explanation for its origin in the generation and recombination of charge carriers. Its current spectral density can be expressed as (Arutyunyan *et al.*, 1989)

$$i_{\frac{1}{f}} = \sqrt{\frac{KI^2}{Nf^\gamma}} \quad (3.26)$$

where  $K$  is an empirically determined constant,  $N$  is the total number of charge carriers in the sample and  $\gamma \approx 1$ .

### 3.3. Amplifier

Conversion of the signal current into a measurable voltage can be performed a number of ways. One such method utilises the Trans-Impedance Amplifier (TIA). Here a description of the TIA is given and its benefits over other circuits discussed. The noise sources inherent in the TIA are presented before detector and amplifier noise sources are summed to construct a meaningful noise model.

#### 3.3.1. TIA Circuit

Figure 3.3 shows the schematic of a TIA circuit. Rieke (1996) provides a basic description of the circuit operation. An electric field is applied across the detector. The detector is connected to the inverting input of an operational amplifier (op-amp) through a Si,  $n$ -type, junction field effect transistor (JFET). The JFET input stage serves to

provide the op-amp with a relatively low impedance input at a point close to the detector. This has been proven to be beneficial in limiting microphonic noise, which can arise from the changing capacitance of the TIA input wire as it flexes with respect to the cryostat ground produce a fluctuating voltage at the high impedance input. The output of the op-amp is connected through a feedback loop to the same input. The non-inverting op-amp input is tied to ground, through a further JFET closely matched to the first. Suitable JFET pairs are provided commercially (IR Labs). Since the op-amp will produce an output to drive the two input voltages to be equal, any change in the input will cause a corresponding change in output. For a detector with impedance  $Z_d$  biased with a voltage  $V_b$ , the output voltage  $V_o$  can be expressed as

$$V_o = \frac{-V_b Z_f}{Z_d} \tag{3.27}$$

where  $Z_f$  is the impedance of the feedback resistor and capacitor in parallel. The voltage output provides a measure of the current flowing through the detector  $I_{det}$ :

$$V_o = -I_{det} Z_f \tag{3.28}$$

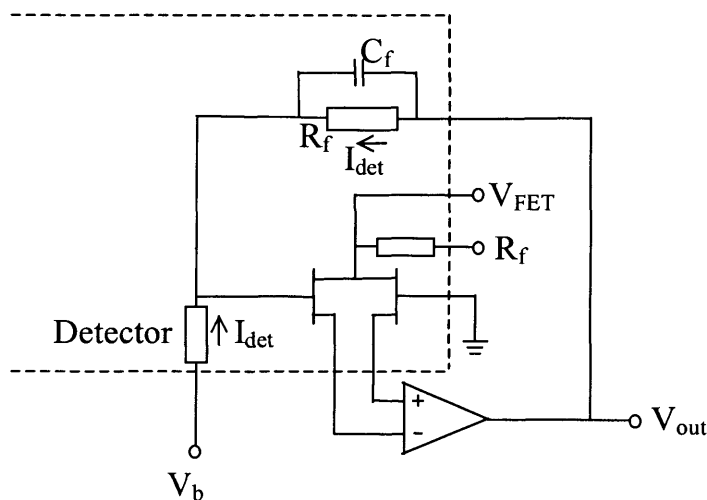


Figure 3.3. The TIA circuit. The dotted line marks elements placed on the cryostat cold plate.

It is beneficial to place the feedback resistor and capacitor as close as possible to the detector again to limit microphonic and Johnson noise contributions. The location of the JFET pairs must also be in close proximity to the detector and feedback resistor. This

is due to the very small current flowing in that part of the TIA circuit, which makes the high impedance points more susceptible to microphonic pickup. Feedback capacitors are not usually used in the feedback loop of a TIA circuit (e.g. IBEX (Lee, 1997), IRAS (Luinge *et al.*, 1980)), although some stray capacitance will exist in reality. Their introduction filters out higher frequency noise. The JFET pairs are constructed with a small internal heater supplying the necessary power to the JFETs to keep them at their operating temperature of around 100 K.

A number of benefits are gained with a TIA circuit over alternatives such as the integrating amplifier or operation with a voltage divider-type circuit. Integrating amplifiers are unsuitable for measuring large currents ( $> 10^7$  e<sup>-</sup>/s) (Price, 1994) so are not ideal for high background, or for the high dark current present in stressed PCs at unpumped LHe temperature. In a TIA circuit under conditions of high photon flux the Johnson-Nyquist noise of the feedback resistor becomes negligible due to the dominant effect of photon noise. The TIA also provides a high degree of linearity. This is due to its virtual ground: bias voltage across the detector is held constant regardless of background loading.

### 3.3.2. Circuit Noise

IR Labs-supplied JFET units are of low noise, measured to be around 20 nV/ $\sqrt{\text{Hz}}$ . This noise arises from the resistive nature of their operation, causing a Johnson-Nyquist term to ensue. The feedback resistor causes an additional source of thermal noise.

In order to evaluate detector performance it is necessary to model the noise of the detector and amplifier system. Following the analysis of Luinge *et al.* (1980), a model has been produced to calculate the contribution of the various terms presented in Section 3.2.5 to the total noise of the system.

Luinge *et al.* (1980) give the following equation for the total noise,  $i_{n,T}$ , of a TIA and detector system in a 1-Hz bandwidth:

$$i_{n,T} = \sqrt{\left\{ \frac{e_{n(\text{FET})} \left[ 1 + j\omega R_f (C_f + C_d) \right]}{R_f} \right\}^2 + i_n^2 + \frac{4kT}{R_f} + \frac{4R_f^2 P_{back} h\nu}{\eta}} \quad (3.29)$$

where  $e_{n(\text{FET})}$  is the noise of the JFETs,  $R_f$  is the value of feedback resistance,  $C_f$  and  $C_d$  are the feedback capacitance and detector capacitance respectively and  $i_n$  represents the

current noise of the detectors. The equation is composed of four terms that relate to the noise of the FETs, current noise, thermal noise of the feedback resistor and photon noise respectively. However, the above expression fails to take into account the wave noise component in the photon noise term  $i_{n,\gamma}$ . The last term in Equation 3.29 then becomes, as Equation 3.20

$$i_{n,ph}^2 = \frac{4R_f^2 Ph\nu}{\eta} \left( 1 + \frac{\eta t_{fil}}{e^{\frac{h\nu}{kT}} - 1} \right). \quad (3.20)$$

Inclusion of a Johnson-Nyquist term to account for the thermal noise of the detector's resistance should also be included. The expression for Johnson-Nyquist detector noise is  $\frac{4kT}{R_d}$  which is merely the same as the Johnson-Nyquist noise term for the feedback resistor, the third term in Equation 3.29, with detector resistance  $R_d$  replacing the feedback resistance.

When quantitative comparisons are drawn between modelled and measured noise, due to the spectral shape of  $\frac{1}{f}$  noise a measured value of the noise is often taken at a higher frequency where the  $\frac{1}{f}$  component has fallen to negligible values. This is typically between 50 and 100 Hz.

The final expression for the total noise of the system must also take into account the TIA transfer function in order for a value comparable to the measured value to be derived, i.e. a noise voltage. Luinge *et al.* quote the transfer function for current noise as

$$H(\omega) = \frac{-R_f}{\left( \frac{R_f}{R_d A_o} + \frac{1}{A_o} + 1 \right) + j\omega \left[ \frac{R_f(\tau_2 + \tau_1)}{R_d A_o} + \frac{\tau_1 + \tau_3(1 + A_o)}{A_o} \right] + (j\omega)^2 \left( \frac{R_f \tau_1 \tau_2}{R_d A_o} + \frac{\tau_1 \tau_3}{A_o} \right)} \quad (3.30)$$

where  $\tau_2 = R_d C_d$  and  $\tau_1 = \tau_3 = R_f C_f$ . Equation 3.30 simplifies to

$$H(\omega) \approx \frac{-R_f}{1 + j\omega\tau_3} \quad (3.31)$$

for large amplifier gain and low frequencies.

### 3.4. Previous Experiments Utilising Stressed Ge:Ga Photoconductors

THUMPER is built around an array of seven stressed Ge:Ga PCs. Stressed Ge:Ga has been in use for several decades in providing access for astronomical detection in the wavelength range 120 to 200  $\mu\text{m}$ . A brief review of these detectors is therefore included here.

The first stressed Ge:Ga devices for astronomical detectors were constructed by Kazanskii *et al.* (1977). By applying  $66 \text{ kg/mm}^2$  along the [100] crystallographic axis the long-wavelength cutoff was extended from 114  $\mu\text{m}$  to 200  $\mu\text{m}$ . The same group report a minimum NEP under low infrared backgrounds of  $5.7 \times 10^{-17} \text{ W}/\sqrt{\text{Hz}}$  at 150  $\mu\text{m}$ . Stress for these devices employs a ball bearing to decouple the torque from the stress-applying screw before the force is transmitted to the crystal. Figure 3.4 presents a schematic of this arrangement. Photoconductive gain for their stressed samples was 0.22 whilst absorption was 0.73, assuming a photon-noise dominated background.

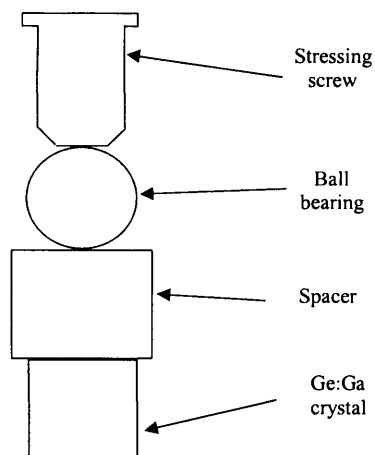


Figure 3.4. Torque from a stressing screw is decoupled by use of a ball bearing.

Léotin *et al.* (1985) examined the effect of a gradual increase of stress on a sample of Ge:Ga. Parameters such as dark current and relative photoconductive response were investigated. Their experimental arrangement used the novel approach of stressing the Ge:Ga whilst the sample was at LHe temperature, within a closed dewar, by use of a retractable key. Stress was passed along a stainless steel spring. The group found that the response increased by a factor of around 50 for a range of stress values varying from 0.1 GPa to 1.0 GPa, at the constant temperature of unpumped LHe. This is attributed to

responsivity having a dependence on more than one variable, all of which increase with increasing stress. The theory for this is discussed in more detail above in Section 3.2.3.

Another approach to torque decoupling was pioneered by Wang *et al.* (1987), at the University of California, Berkeley. Stress was applied by use of the leaf-spring to an end-fire crystal. The leaf-spring apparatus works by the principle of leverage. Figure 3.5 shows the basic mechanical set-up for the approach. As the stressing screw is tightened, the piston is forced down and transmits stress to the sample beneath it. The group quote a high responsivity of 102 A/W at 77% of the breakdown field, with an  $\eta G$  product of 0.70 at 2 K.

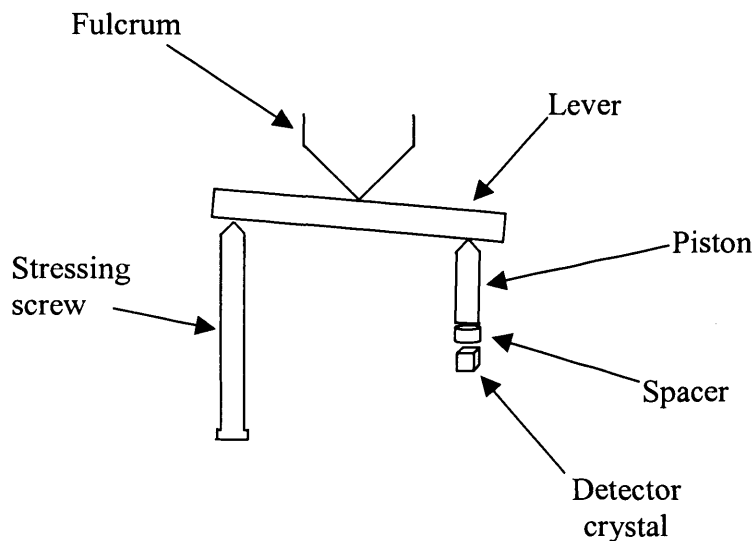


Figure 3.5. Stress applied by use of lever and fulcrum.

The ball bearing approach to decouple torque was adopted for use with the ISOPHOT (Lutz *et al.*, 1986) and LWS (Church *et al.*, 1993) detectors aboard the ISO satellite. Such detector systems operated under the extremely low backgrounds of the order  $10^{-16}$  to  $10^{-17}$  W, typical for satellite observatories. Readout for these detectors was by use of integrating amplifiers: a TIA with infinite feedback resistance. The most highly stressed of the ISOPHOT detectors obtained an NEP of less than  $10^{-17}$  W/ $\sqrt{\text{Hz}}$  and responsivity of 10 A/W at a temperature between 1.6 and 1.7 K (Lemke *et al.*, 1994; Wolf *et al.*, 1994). For the ISO LWS highly stressed detectors DQEs of 40% and

responsivities of between 4 and 8 A/W were measured at just under 1.8 K (Church *et al.*, 1993).

Stacey *et al.* (1991) developed the first stressed array. Figure 3.6 shows a schematic of the stressed array, developed for the KAO. All elements have stress derived from the same source and stress is applied along the length of the array. An electric field was applied to the detector housing such that all elements of the array were biased at the same potential. NEPs obtained were of the order  $10^{-15}$  W/ $\sqrt{\text{Hz}}$  with responsivities between 4 and 5 A/W for elements of the array at the operating temperature of 2.2 K. Stacey *et al.* (1992) went on to develop a larger array of 5 $\times$ 5 elements, as an extension of the initial KAO array, for the Far-Infrared Imaging Fabry-Perot Interferometer (FIFI). FIFI achieved similar values of NEP but an increased responsivity of between 14 and 26 A/W.

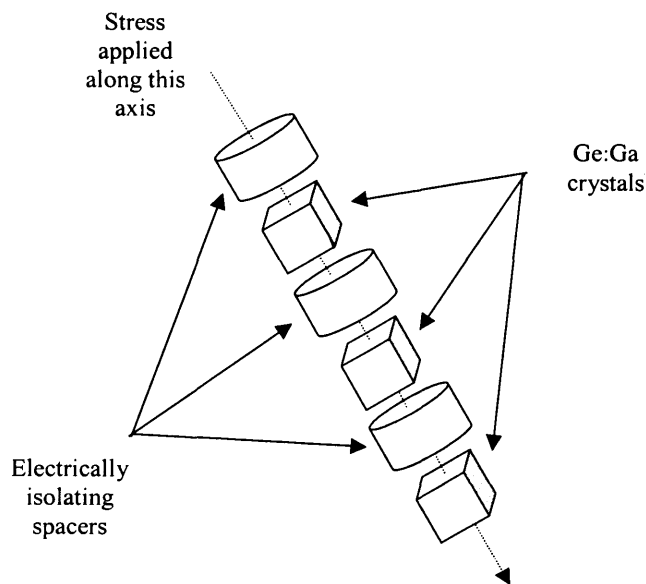


Figure 3.6. Schematic of a stressed array.

Hiromoto *et al.* (1989, 1992) describe their development of stressed Ge:Ga for use in an astronomical Balloon borne Infrared Telescope (BIRT), followed by a linear array for the Japanese InfraRed Telescope in Space (IRTS). The array is constructed from three PCs again using the ball bearing approach. Responsivity for the detectors is quoted at being around 100 A/W with NEPs of less than  $5 \times 10^{-18}$  W/ $\sqrt{\text{Hz}}$  for a detector at 2 K under

a background of the order of  $10^{-15}$  W. The  $\eta G$  products for each of the detectors in the array were of the value 0.9 to 1.0.

Wolf *et al.* (1996) described the development of a 16×16-pixel array as a prototype for the Herschel (the satellite formerly known as FIRST) Space Observatory. The stressing mechanism employed follows that of Wang *et al.* (1987) by providing a force on the crystals by use of a lever and fulcrum. The lever forces down a plunger into a line of crystals mounted in integrating cavities and separated by ceramic chips for electrical isolation. The preferred way of stressing this array was at LHe temperatures in a specially adapted cryostat, following Léotin *et al.* (1985).

An enlarged array size of 16×25 pixels introduced no further complications in terms of designing a large array, since stress was still applied along the length of the 16 elements of the array. Kraft *et al.* (2000) describe the 25 linear modules known as PACS, the design of which developed away from the lever and fulcrum approach into technique where stress is applied by a screw mounted at one end of the detector housing. Early test results for these types of array have shown responsivities of between 15 and 40 A/W at 1.7 K with a stress uniformity which leads to cutoff wavelengths varying between only 193 and 202  $\mu\text{m}$ . DQEs are quoted at values up to 48% under a high background power loading of  $10^{-8}$  W. Two instruments aboard the Stratospheric Observatory For Infrared Astronomy (SOFIA): AIREs (Rabanus *et al.*, 2000) and FIFI LS (Rosenthal *et al.*, 2000) follow the design of PACS very closely and testing of these is ongoing.

Whilst the current generation of astronomical instruments under construction, such as Herschel and SOFIA, rely in part on stressed Ge:Ga technology, the need for ever larger arrays is problematic. Since such arrays must be manually constructed, assembling anything larger than the 16×25 pixel arrays currently undergoing testing must be considered most unenviable. However, these arrays offer state of the art performance for stressed Ge:Ga.

### 3.5. Detector Construction

The original THUMPER design planned to utilise seven singly mounted and stressed Ge:Ga PCs. However in late-2000 the design was changed to a set of linearly stressed arrays. Because of this, initially two single elements had been mounted as



prototypes in mid-2000, whilst the actual  $1 \times 2$  and  $1 \times 3$  arrays were mounted in mid-2002. The difference in mounting procedure between single and multi-element arrays only becomes apparent when attempting to stack the latter type, since movement in one cavity can cause movement of a crystal in the cavity either immediately above or below. Hence the procedure set out below is relevant for the mounting of Ge:Ga chips in cavities for use in either single or multi-element arrays, although the description given is specific to the arrays.

A microscope set up to view horizontally was used for crystal mounting. The procedure was carried out in a laminar flow cabinet to minimise dust or other particulates becoming lodged either on the crystal faces thus lowering the RQE, or on the contact pads, which may lead to inhomogeneous stress. The procedure adopted here was optimised by J.W. Beeman at the Lawrence Berkeley National Laboratories (LBNL), and performed by the author at Cardiff University.

Before construction of the detector array is given, a brief description of the detector housing is provided. The focal plane array (FPA) in which the blocks form a part, is also described.

### 3.5.1. Detector Housing and the Focal Plane Array

Detector blocks for THUMPER have been constructed from BeCu. BeCu is a more robust material than Cu and was chosen as the detector block material due to the large stresses on the detector blocks.

The Ge:Ga crystals have been stressed in two  $2 \times 1$  arrays and one central  $3 \times 1$  array. The three arrays are then screwed together. A dowel pin provides the accurate positioning of each block relative to its neighbour. Once the blocks are aligned with each other the seven element, close packed hexagonal pattern is formed. The design of the detector blocks, based on the leaf-spring approach pioneered by Wang, *et al.* (1987), is shown in Figure 3.7. The design offers the benefits of a torque free stress acting on the crystal, and provides a more compact overall size than the belleville spring used in a SAFIRE-A prototype block, an airborne Earth observing experiment (see Dickinson, *et al.*, 1995, for a description of SAFIRE-A). The need for a compact array is necessary due to the narrow feedhorn diameter.

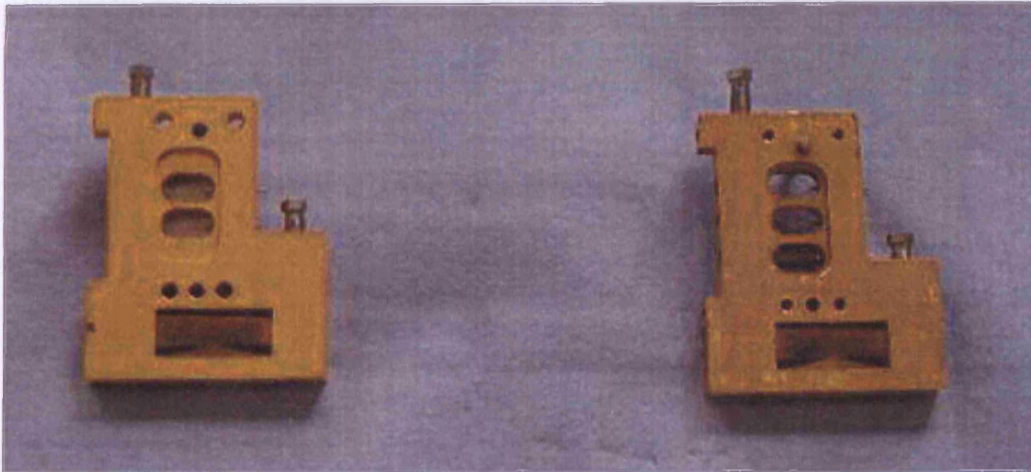


Figure 3.7. The detector blocks used in THUMPER.

The stress is applied along the long axis of each detector block. Stress is derived by turning a screw through the rear of the block, which causes the leaf spring to act downwards on the photoconductive crystals. The height of the crystals can be altered by turning a screw in the base of the stressing block, placing the crystals in the centre of their cavities prior to the application of stress.

The FPA is then formed by the detector blocks, feedhorns and an optical filter assembly. The feedhorns and optical filtering are discussed in greater detail in Chapter 4. The FPA components are held together by the mounting assembly. Figure 3.8 shows the FPA prior to mounting on the cryostat coldplate.

### 3.5.2. Crystal Preparation

Before mounting the crystals of Ge:Ga into detector blocks, the crystals were first prepared. The preparation involved transforming a block of Ge:Ga of approximately 20-cm length by 4-cm diameter into the required 1-mm<sup>3</sup> cubes. This process was carried out by J.W. Beeman, at the LBNL, prior to shipment of the crystals to Cardiff University.

Many samples of crystals have been grown at the LBNL Material Science Department since the 1960s. The material chosen for the THUMPER detectors was grown in February 1970. Named 102-10.0 the first number represents the ordinal of which the material was grown, the second number provides the distance from the head of



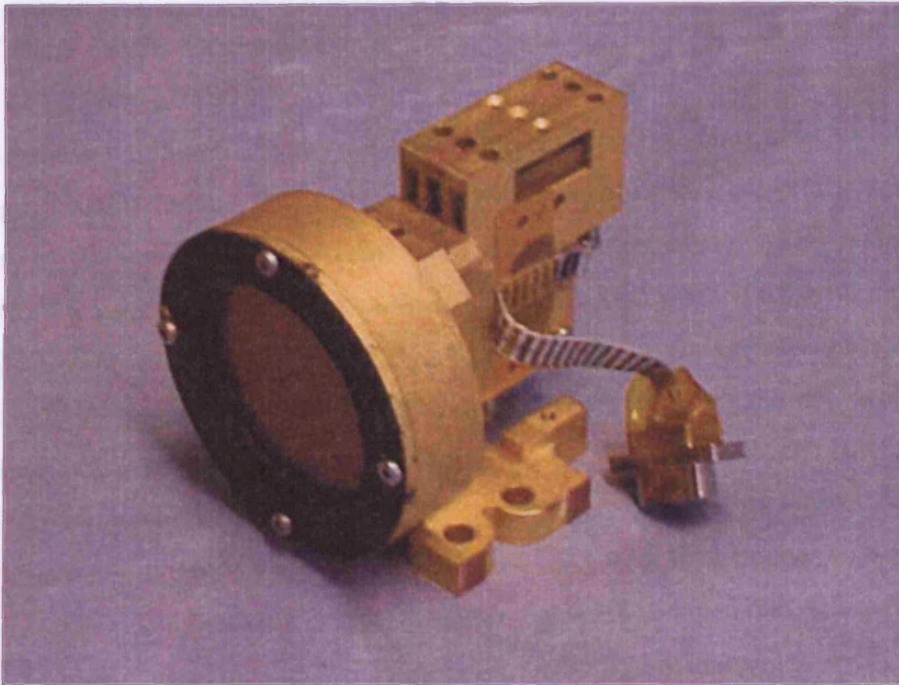


Figure 3.8. The focal plane array.

the crystal to the wafer from which the Ge:Ga chips are taken. As the crystal of Ge grows, Ga and As concentrations increase due to impurity segregation as the amount of the melt diminishes. This results in a crystal doped more lightly at the head end than the tail end (Stacey *et al.*, 1992). Crystals were Czochralski grown in the  $\langle 111 \rangle$  orientation in a hydrogen atmosphere. Doping levels have been estimated to be  $1.7 \times 10^{14}$  Ga atoms per  $\text{cm}^3$  with compensating donors (probably P) around  $2.0 \times 10^{12} \text{ cm}^{-3}$  (Beeman, 2002). The choice of crystal was governed by previous, prototype samples. The dark current in the prototypes was very high, leading to a situation where the dominant noise source was not photon noise under background conditions of about 1 nW. Since background at the JCMT is expected to be around 2 nW, crystals of a higher compensation were chosen to limit the dark current component.

1-mm wide wafers had been cut from the crystal using a diamond saw. The wafers had been polished several times with silicon carbide powder of an increasingly finer grade. After polishing, the wafers were ion implanted with  $\text{B}^+$  and RF sputtered with Pd and Au of thickness 20 and 400 nm respectively to provide electrical contacts. These were cut into 1-mm strips to be stored until needed. The strips were then cut into cubes,

providing 1-mm<sup>3</sup> Ge:Ga chips plated on opposing faces with a conductive layer of Pd and Au.

To remove damage caused by the sawing process the crystals must be etched: After being washed in xylene, they were rinsed with methanol and dried gently by blowing dry N<sub>2</sub> gas onto them. They were then left in a mixture of HNO<sub>3</sub>, HF and red fuming HNO<sub>3</sub> in a 7:2:1 ratio for forty seconds before this was washed off with methanol. Fuming HNO<sub>3</sub> is formed by dissolving NO<sub>2</sub> into HNO<sub>3</sub>. The crystals were again gently blown dry with N<sub>2</sub> gas. A 4:1 mixture of HNO<sub>3</sub>:HF can be used as an alternative to the 7:2:1 mixture, however the ratio including fuming HNO<sub>3</sub> gives an even etch rate since Ge initiates a run-away reaction. Scratches on the crystal can be a source of noise so it is important to remove them. While the Ge:Ga crystals are harder than stainless steel, small pieces of the crystal can break off during the cutting process and then abrade the crystal face. Therefore great care must be taken whenever manipulating them.

Before etching, the crystals are near-perfect cubes. Etching has the effect of removing a small amount of the Ge:Ga but leaves the metalised contact pad unaffected. A rounding effect is also introduced near the boundary where the Ge:Ga crystal comes into contact with the metallised contact pad. This is caused by the Au in the contact mixing with the Ge semiconductor and acid, causing a faster reaction rate. This leaves the chips with a shape approximated by the sketch shown in Figure 3.9.

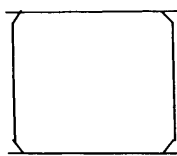


Figure 3.9. Shape of Ge:Ga crystals, with contacts, after etching.

Care must then be taken during the mounting process to ensure that no traces of Au come off the crystals and cause short circuits or an inhomogeneous stress. For this reason the overhanging parts of the contact pads were removed by holding the crystal with a very small, fine paintbrush on a piece of clean filter paper, and the offending overhang pulled off with a pair of fine-point tweezers.

The final checks on the crystals' surfaces were carried out visually under a microscope. Checks were made to ensure crystal surfaces were good, and that no cracks existed in the contacts. Cracks in the contacts could be indicative of surface defects in the Ge:Ga material underneath, which could cause a fracture when stress is applied.

### 3.5.3. Detector Block Preparation

As returned from the manufacturers (Thomas Keating Ltd, UK), the detector blocks consisted of little more than a shape of BeCu with holes in. A CAD drawing of the central block is shown in Figure 3.10. All three blocks were initially soaked in acetone to remove any fragments or oil left on the surface. To prevent light leakage between channels, and from outside the block, a light tight cavity is included just to the rear of the detector crystals' cavities and marked on Figure 3.10. The cavities include holes originally made for Eltec feedthroughs (part no. 901) to be placed within these. Figure 3.11 shows a schematic of the feedthrough. It was suggested (Beeman, 2002) that a better use of the hole between crystal cavity and light-leak-preventing cavity would be to have a wire from the contact pad passing directly through this hole, since any arrangement of securing wire to a feedthrough behind the crystal would be very troublesome. Feedthroughs were attached to the back of the detector blocks with Epotek H70E non-conductive epoxy. The epoxy was spread around the cylindrical hole using a thin piece of brass wire. The feedthrough was then passed into this cavity followed by a further addition of epoxy between the block and one leg of the feedthrough. Application of too much epoxy to these parts can lead to trapped air inside the epoxy, causing the epoxy to flow out of the cavity during curing.

In addition to the Eltec feedthroughs, BeCu pivots were epoxied into the blocks. These were placed such that the centre of the leaf spring would act on the pivotal point, causing the amount of stress applied to the crystal to be equal to that of the force caused by the turn of the stressing screw.

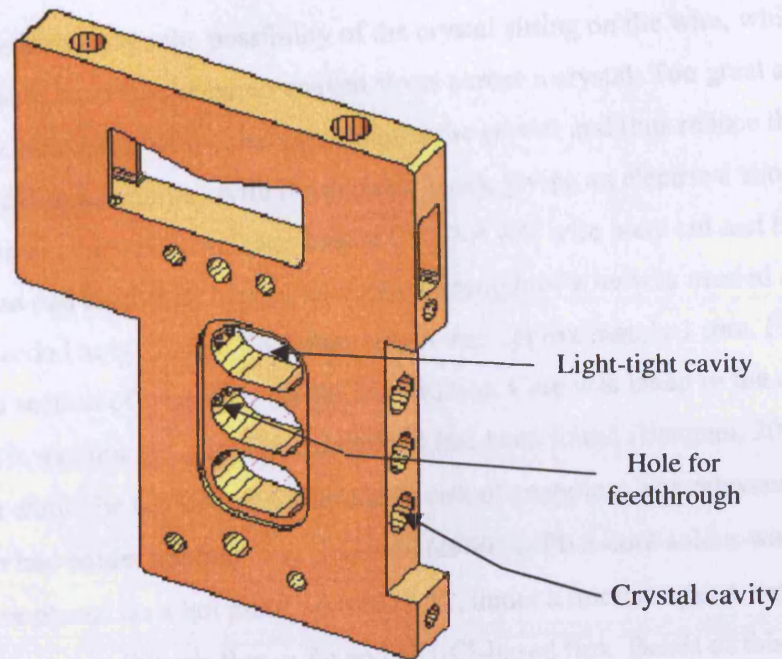


Figure 3.10. The central detector stressing block.

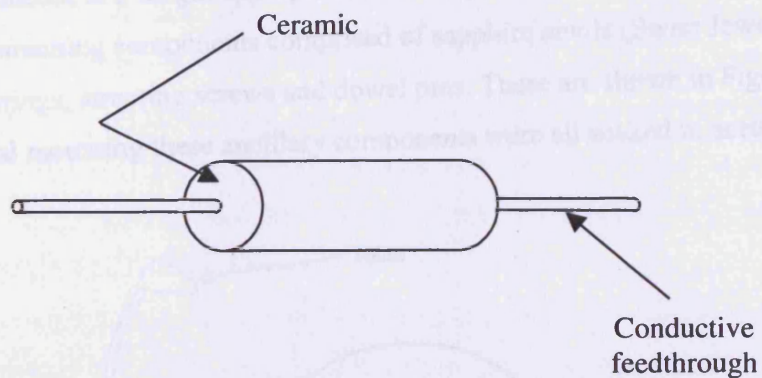


Figure 3.11. Schematic of a feedthrough.

#### 3.5.4. Ancillary Components

To provide the electric field necessary to bias the detectors, electrical contact pads were fabricated from brass sheets of approximately 35- $\mu\text{m}$  thickness. Shims of diameter 2 mm were cut from the sheet and soaked in acetone for cleaning. The particular diameter used was chosen to ensure enough room for the mounting of a wire around the crystal.



Too small a diameter leaves the possibility of the crystal sitting on the wire, which is clearly undesirable, as it would create uneven stress across a crystal. Too great a diameter would leave the possibility of the pad overhanging the crystal and thus reduce the throughput, or causing a contact with the detector block giving an electrical short.

Sections of single polyurethane-coated Cu 37 AWG wire were cut and held against the brass pad to give an idea of how much a length of wire was needed and how much of this needed to be tinned. The latter length was approximately 1 mm. Figure 3.12 is a sketch of a section of wire after the tinning process. Care was taken in the choice of wire to ensure it was not too thin. For example, it had been found (Beeman, 2000) that wire of 50  $\mu\text{m}$  would be too thin and introduce a risk of snapping. The relevant section of each wire then had solder applied to it. Standard 60/40 Sn/Pb 5-core solder was used. The brass pads were placed on a hot plate, set at 225 °C, under a microscope. A small splint of wood was dipped in Baker's flux, a Zn and  $\text{NH}_4\text{Cl}$ -based flux. Beads of this liquid were then carefully dropped on to the wire and the wetted wire held onto the brass pad. After about a second the pad could then be lifted from the hot plate by the wire. The wires were trimmed to a length appropriate to the detector cavity.

The remaining components comprised of sapphire anvils (Swiss Jewel Co., PA, USA), leaf springs, stressing screws and dowel pins. These are shown in Figure 3.13. Prior to crystal mounting these ancillary components were all soaked in acetone for cleaning.

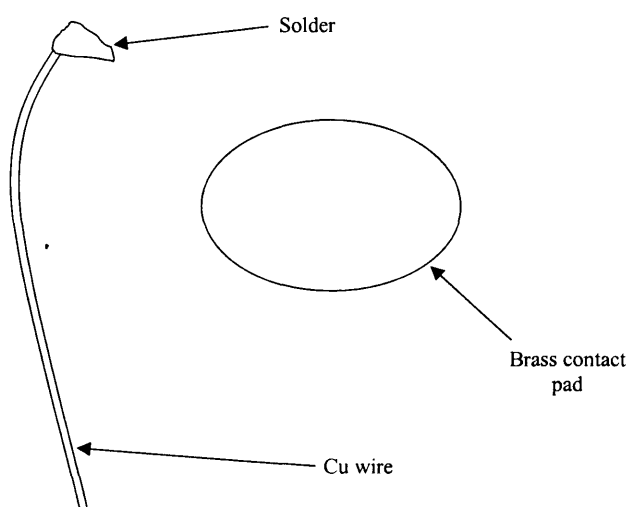


Figure 3.12. Contact pad and wire.

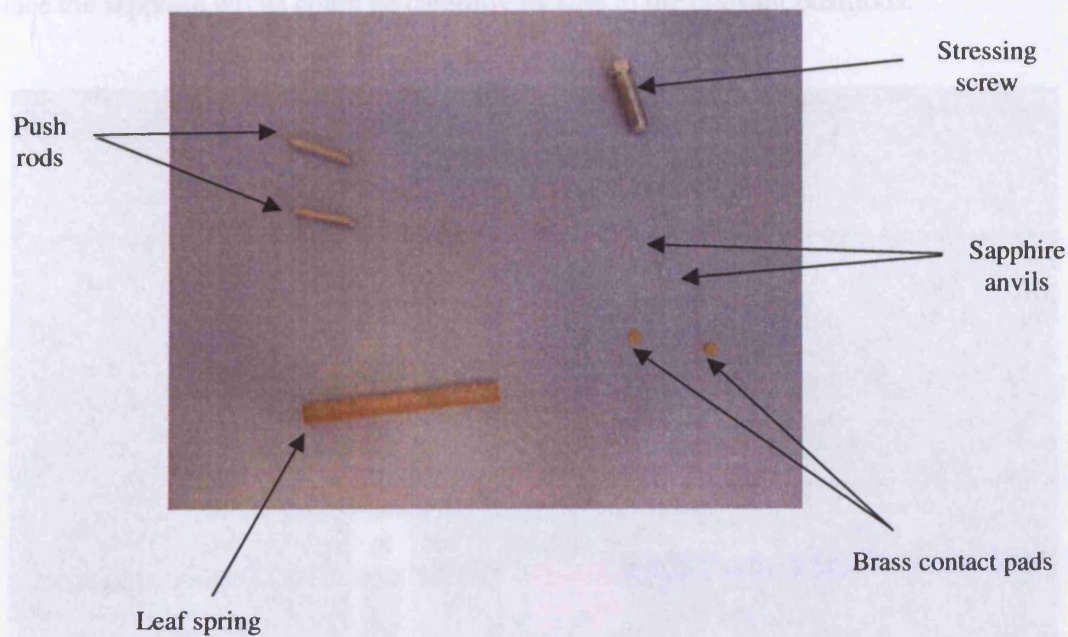


Figure 3.13. Photograph of the ancillary components used in the THUMPER detector blocks.

### 3.5.5. Crystal Mounting

The detector blocks were clamped vertically to the top of a lab-jack, in view of a microscope, as seen in Figure 3.14. This orientation of the block allowed components to be balanced more easily during the mounting process. The leaf spring-end of the block was placed lowermost since once the crystals had been mounted and centred application of stress could then be activated with the minimum of disruption to the crystals and the least possibility of the crystals moving off centre. Detectors were then assigned a two-character designation in each of the three blocks as shown in Figure 3.15. Block C is centrally placed. The latter alphabetic character refers to upper, middle or lower placement within the block.

A small amount of adhesive was taken from the back of some standard insulating tape and placed around the edge of the middle of the dowel push-rods. This process enabled the rods to be inserted into the detector-stressing block and left without slipping out. The inter-cavity rods were placed through the front of the cavities and manoeuvred either up or down into their appropriate positions. End rods were inserted through the



openings left for this purpose in either end of the stressing blocks. With these parts in place the sapphire anvils could be carefully located to the relevant positions.

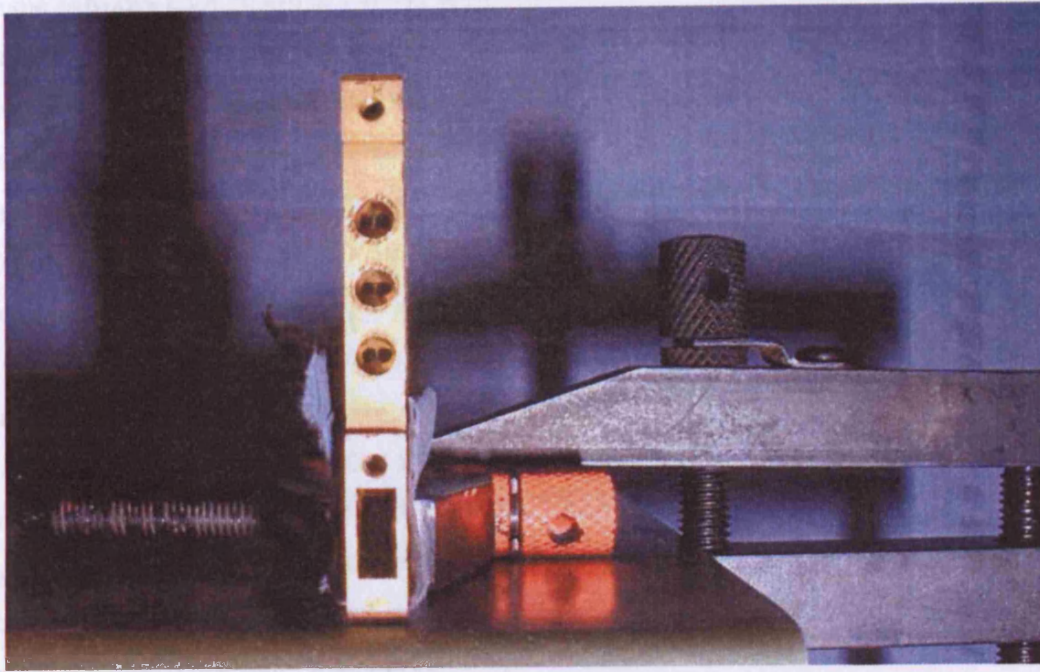


Figure 3.14. Detector block clamped for crystal mounting. The cavities are 3-mm diameter.

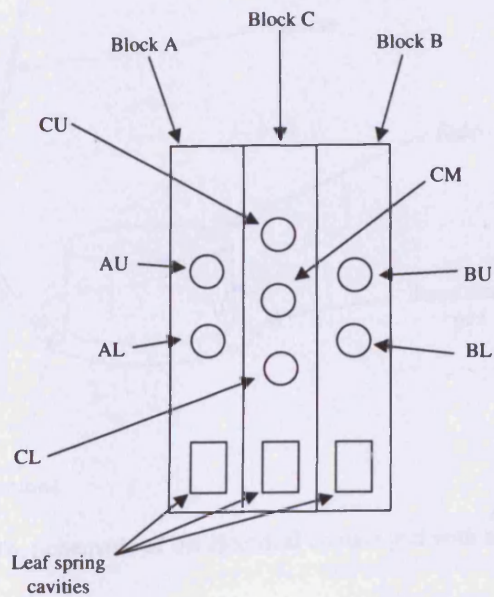


Figure 3.15. Detector channel identification.

Further small pieces of adhesive were rubbed onto one side of the sapphire anvils in a circular manner. It was found that a scalpel was ideal for this task. The adhesive from the tape extrudes enough not to put any differential pressure on the crystal. The anvils were then placed on the brass electrical contact pads such that the wire was on the side facing away from the anvil and toward the detector. The wire was placed in this direction to ensure the crystal did not sit directly on the solder. Adhesive was placed on the remaining sides of the anvils. The whole contact pad-anvil assembly could then be lifted into the detector cavity and placed against the push rod. Figure 3.16 shows the pad-anvil assembly ready for mounting. This was done by initially feeding the wire through the hole to the rear of the crystal cavity, then pulling the wire from the rear of the cavity. The small amount of adhesive, coupled with the lightweight of the anvil, held the contact pad-anvil assembly in place. Pads were placed on both sides of the cavity such that the crystal could then be placed directly in between them. The wire-solder joint was orientated slightly away from the cavity entrance to avoid the vignetting of incoming radiation. If the brass pad overhangs the anvil in any way, it is of greater benefit to have the overhang toward the rear. This helps with the centring of the crystal, making it easier to observe where the crystal is in relation to the anvil, and avoids reflection of incident radiation.

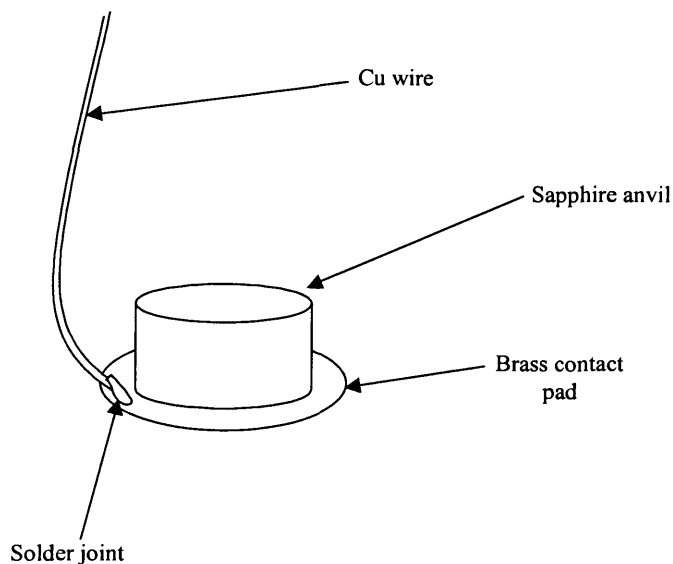


Figure 3.16. Schematic of the electrical contact pad with anvil attached.

A vacuum probe, held in a triaxial mount, was used to mount the crystal in the cavity. Figure 3.17 shows this apparatus. The probe consisted of a hollow length of stainless steel with a bend in one end. The other end was placed inside a piece of rubber tubing, which was connected to a small vacuum pump. The stainless steel section was clamped in the mount, and upon its open end was placed a thin piece of rubber tubing, located thus to minimise crystal surface damage. The crystal was placed on a piece of filter paper and this was held up to the probe with the vacuum applied. The crystal was positioned using the knobs on the mount before the vacuum pump was disconnected allowing the crystal to detach itself from the probe. The crystal was then aligned centrally with respect to the central axis of the anvils and push rods, orientated such that incident radiation from the feedhorn's exit would strike a corner of the Ge:Ga chip.

Once all crystals in a stack had been sufficiently centred, the stressing screw was tightened until the crystals were held tight. Great care was taken since this process can often cause crystals to become uncentred, necessitating a repeat of the centring process. The loose end of the wires, connected to the electrical contact shims, could then be soldered to the Eltec feedthroughs, and a multimeter used to measure resistance falling with applied stress. Figure 3.18 shows a completed array.

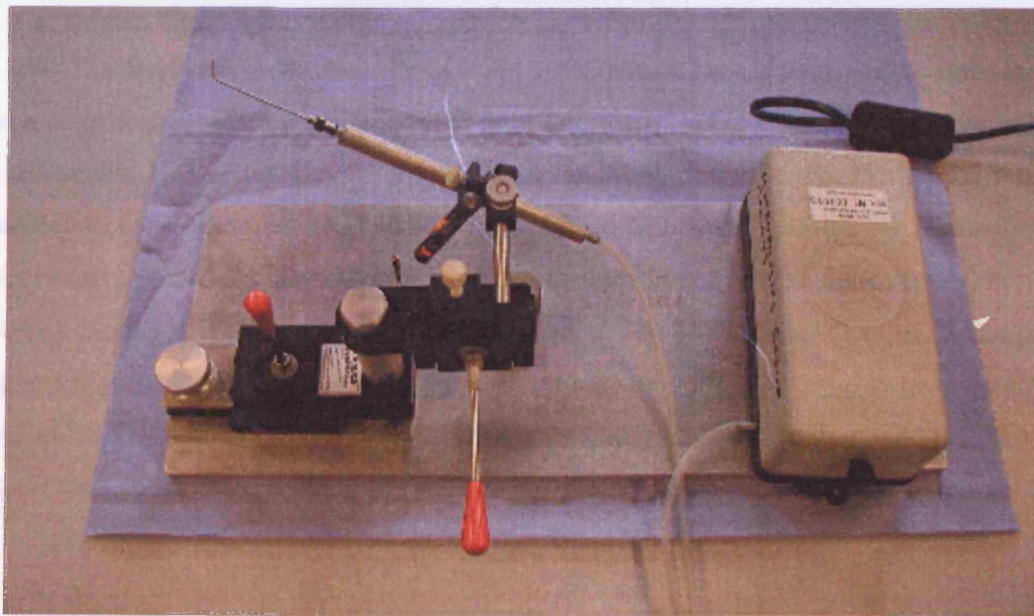


Figure 3.17. Triaxial mount and vacuum probe, used to insert crystals into detector block cavities.



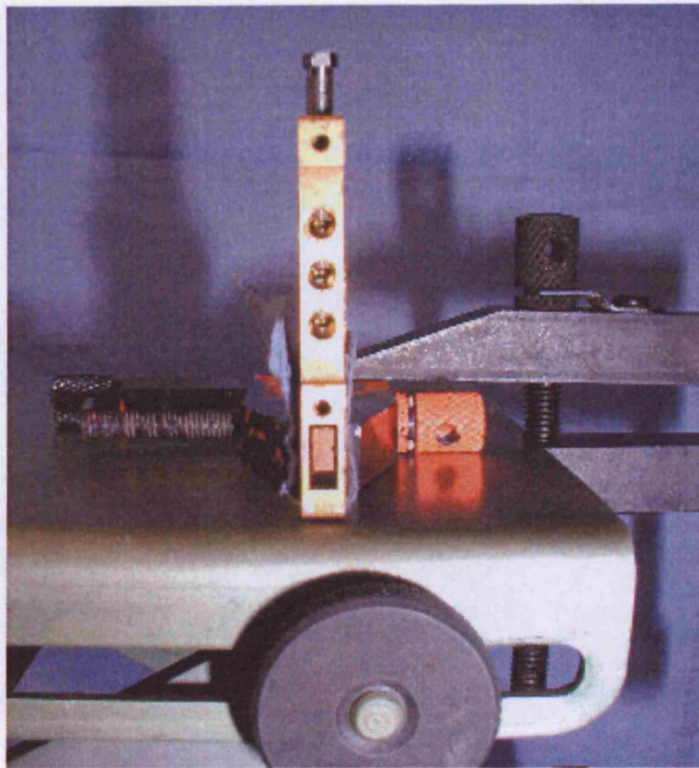


Figure 3.18. A completed array.

Mechanical stress is applied by following the set-up shown in Figure 3.20. The

### 3.5.6. Crystal Stressing

The application of stress is measured by monitoring room temperature resistance. Even at room temperature the amount of light falling on Ge:Ga PCs can cause a variation in resistance. This is due to non-ionised carriers in the intrinsic Ge. For this reason the entrance to the detector cavities was masked with Al tape whilst monitoring resistance of the crystals. Coated Cu wire was soldered between the feedthroughs at the rear of the detector blocks to a set of electrically isolated posts. The blocks were clamped to the post support (Figure 3.19) so that stress could be applied whilst monitoring change in detector resistance. The red and black probes to the right-hand side of the photograph lead off to a digital multimeter.

As the stress was increased, it became apparent that a differential stress was being applied across the stack. Whilst resistance of channel C1 was maintained during the stressing procedure, and this was taken to indicate 50%, the resistance of the other channels in block C had fallen to 47% and 72% for channels C2 and C3 respectively.

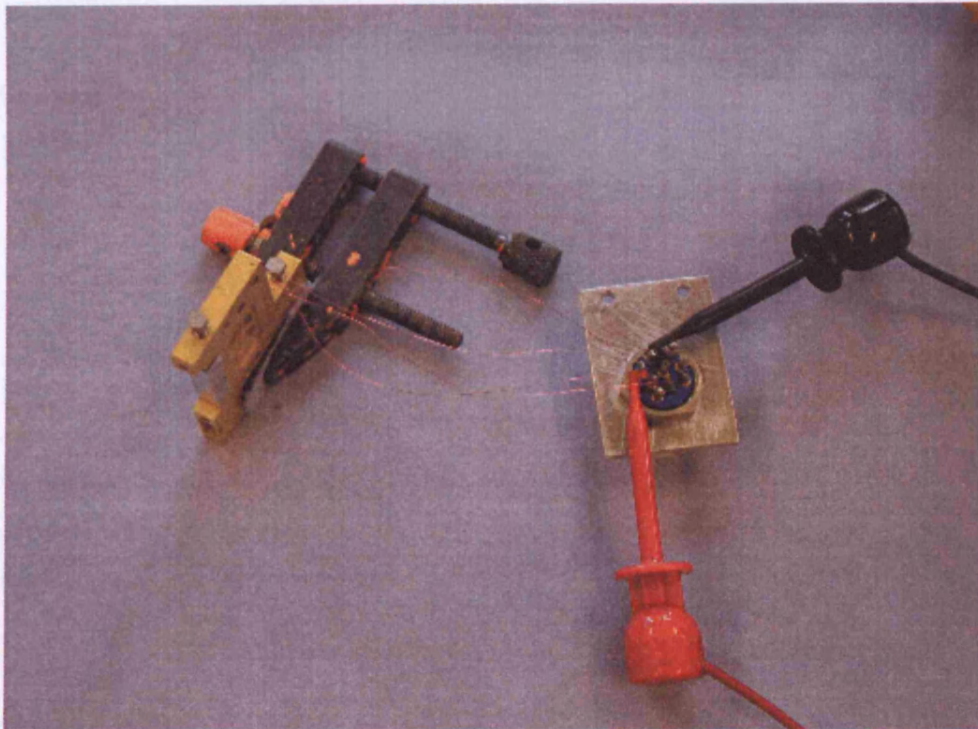


Figure 3.19. Detector block configuration for monitoring stress applied to detectors.

Mechanical stress is applied by tightening the screw, as shown in Figure 3.20. The screw has a non-standard pitch of 0.35 mm to enable a fine adjustment of stress. As the sample of Ge:Ga is stressed its resistance will decrease. If stress is applied such that resistance drops below 30% of the unstressed value then the crystal becomes highly likely to shatter. The value of cutoff wavelength varies very little between 40% and 30% of the unstressed resistance. In an attempt to limit dark current stress was applied to the detectors until resistance was 50% of the unstressed value. Stress is applied in small amounts. The resistance is monitored and allowed to rise whilst the brass contact pads extrude around the crystal. The process is further repeated with an ever-increasing application of stress.

The exception to the above was block C where it became apparent that a differential stress was being applied across the stack. Whilst resistance of channel CL was monitored during the stressing procedure, and this was taken to initially 56%, the resistance of the other channels in block C had fallen to 67% and 72% for channels CM and CU respectively.



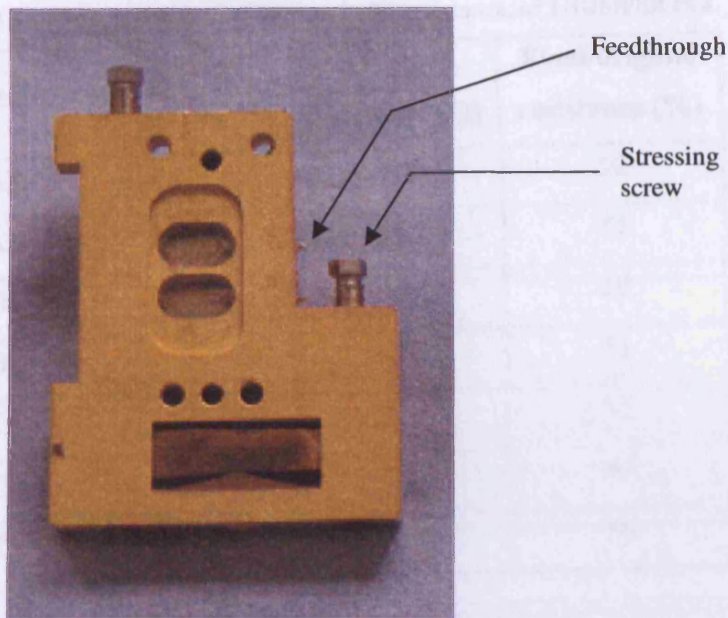


Figure 3.20. Resistance was monitored through the feedthroughs at the back of the detector block as the stressing screw was tightened.

Table 3.1 lists the final stress levels in terms of resistance for each channel at room temperature (RT). A stress of approximately  $60 \text{ kg/mm}^2$  would provide a fall to 35% unstressed resistance. Such a variation in unstressed resistance is common, even amongst crystals cut from the same wafer (Beeman, 2002). Variations can arise from a number of factors including imperfections in the contacts, non-uniformities in the crystal structure, non-uniform doping through the crystal wafer, imperfections in the metalised contacts, or an imperfectly cleaned electrical contact pad.

Table 3.1. Stress, monitored by changes in RT resistance, of THUMPER PCs.

<b>Detector</b>	<b>Original resistance (<math>\Omega</math>)</b>	<b>Final resistance (<math>\Omega</math>)</b>	<b>Final/original resistance (%)</b>
AL	633	317	50
AU	687	348	51
BL	518	271	52
BU	710	361	51
CL	597	210	35
CM	559	241	43
CU	537	270	50

### 3.6 Summary

For the THUMPER instrument PCs are the detectors of choice because at a wavelength  $\leq 200 \mu\text{m}$  they can provide photon noise limited (BLIP) sensitivity at unpumped LHe temperatures. Figures of merit for such devices have been defined and an appropriate noise model developed to aid with the optimisation of the THUMPER detectors.

Having reviewed the development of stressed PCs over the last three decades a method for constructing the THUMPER array was developed and successfully employed. A full description of the construction of the THUMPER stressed detector array has been presented.

### 3.7 References

- Arutyunyan, V.M., Gasparyan, F.V. & Melkonyan, S.V., 1989, *Theory of 1/f Noise in Medium and Far Infrared Photodetectors*, *Infrared. Phys.* **29**, (2-4), 243-250
- Beeman, J.W., 2000, Private Communication, Lawrence Berkeley National Laboratory, USA.
- Beeman, J.W., 2002, Private Communication, Lawrence Berkeley National Laboratory, USA.

- Boyd, R.W., 1982, *Photon Bunching and the Photon-Noise-Limited Performance of Infrared Detectors*, *Infrared Phys.*, **22**, (3), 157-162.
- Bratt, P.R., 1977, in *Semiconductors and Semimetals Vol. 12* (eds. Willardson, R.K. & Beer, A.C.) (Academic Press: New York).
- Church, S.E., Griffin, M.J., Price, M.C., Ade, P.A.R., Emery, R.J. & Swinyard, B.M., 1993, *Calibration and Performance of Doped-Ge Photoconductors for the ISO Long Wavelength Spectrometer*, *Infrared Phys.*, **34**, (4), 389-406.
- Dickinson, P.H., Carli, B, Ade, P.A.R., Nolt, I.G., Léotin, J. & Carlotti, M., 1995, *SAFIRE-A: an Airborne Far Infra-Red Limb Sounder*, *Proc. SPIE Global Process Monitoring and Remote Sensing of the Ocean and Sea Ice*, **2586**, 214-224.
- Haller, E.E., 1994, *Advanced Far-Infrared Detectors*, *Infrared Phys. Technol.*, **35**, (2-3), 127-146.
- Hiramoto, N., Itabe, T., Aruga, T., Okuda, H. & Matsuhara, H., 1989, *Stressed Ge:Ga Photoconductor with a Compact and Stable Stressing Assembly*, *Infrared Phys.*, **29**, (2-4), 255-259.
- Hiramoto, N., Saito, M. & Okuda, H., 1990, *Ge:Ga Far-Infrared Photoconductor with Low Compensation*, *Jpn. J. Appl. Phys.*, **29**, (9), 1739-1744.
- Hiramoto, N., Itabe, T., Shibai, H., Matsuhara, H., Nakagawa, T. & Okuda, H., 1992, *Three-Element Stressed Ge:Ga Photoconductor Array for the Infrared Telescope in Space*, *Appl. Opt.*, **31**, (4), 460-465.
- Kazanskii, A.G., Richards, P.L. & Haller, E.E., 1977, *Far-Infrared Photoconductivity of Uniaxially Stressed Germanium*, *Appl. Phys. Lett.*, **31**, (8), 496-497.
- Kraft, S., Frenzl, O., Charlier, O., Cronje, T., Katterloher, R.O., Rosenthal, D., Groezinger, U. & Beeman, J.W., 2000, *FIRST-PACS: design and performance of the sensor engineering models*, *Proc. SPIE, UV, Optical, and IR Space Telescopes and Instruments*, **4013**, 233-243.
- Laverny, C. *et al.*, 1987, Poster: *High Performance Stressed Ge:Ga Photoconductors*.
- Lee, C., 1997, *Far-Infrared Spectroscopic Measurements of HBr in the Lower Stratosphere*, PhD Thesis, Queen Mary & Westfield College, University of London.



- Lemke, D., Garzon, F., Gemuend, H., Groezinger, U., Heinrichsen, I., Klaas, U., Kraetschmer, W., Kreysa, Ernst., Luetzow-Wentzky, P., Schubert, J., Wells, M. & Wolf, J., 1994, *Far-Infrared Imaging, Polarimetry, and Spectrophotometry on the Infrared Space Observatory*, Opt. Eng., **33**, (1), 20-25.
- Léotin, J., Laverny, C., Goiran, M., Askenazy, S. & Birch, J.R., 1985, *A Stress Tunable Gallium Doped Germanium Infrared Detector System*, Internat. J. Infrared Millimeter Waves, **6**, (5), 323-337.
- Luinge, W., Wildeman, K.J. & van Duinen, R.J., 1980, *Evaluation of Si:As Photoconductive Detectors for Infrared Astronomy*, Infrared Phys., **20**, 39-52.
- Lutz, D., Lemke, D. & Wolf, J., 1986, *Stressed Ge:Ga Infrared Detectors - Performance and Operational Parameters*, App. Opt., **25**, (10), 1698-1700.
- Moore, W.J. & Shenker, H., 1965, *A High-Detectivity Gallium-Doped Germanium Detector for the 40-120 $\mu$ m Region*, Infrared Phys., **5**, 99-106.
- Pankove, J.I., 1971, *Optical Processes in Semiconductors*, Dover Publications, Inc., New York.
- Pollak, F.H., 1965, *Effect of Uniaxial Compression on Impurity Conduction in p-Germanium*, Phys. Rev., **138**, (2A), 618-631.
- Price, M.C., 1994, *Non-Linear Behaviour of Doped Germanium Photoconductors: Inherent and Ionising Radiation Induced Effects*, PhD Thesis, Queen Mary & Westfield College, University of London.
- Rabanus, D., Dotson, J.L., Erickson, E.F. & Wolf, J., 2000, *Design and Assembly of a Stressed Ge:Ga Photoconductor Array for AIREAS*, Proc. SPIE, Airborne Telescope Systems, **4014**, 148-155.
- Rosenthal, D., Beeman, J.W., Geis, N., Looney, L.W., Poglitsch, A., Park, W.K., Raab, W. & Urban, A., 2000, *16 x 25 Ge:Ga Detector Arrays for FIFI LS*, Proc. SPIE, Airborne Telescope Systems, **4014**, 156-163.
- Rieke, G.H., 1996, *Detection of Light: From the Ultraviolet to the Submillimeter*, (CUP, 2<sup>nd</sup> Edn.).
- Sibille, F., 1986, *Infrared Detection and Imaging*, Rep. Prog. Phys., **49**, (11), 1197-1242.

- Stacey, G.J., Geis, N., Genzel, R., Lugten, J.B., Poglitsch, A., Sternberg, A. & Townes, C.H., 1991, *The 158 Micron [C II] Line: a Measure of Global Star Formation Activity in Galaxies*, *Astrophys. J.*, **373**, (2), 423-444.
- Stacey, G.J., Beeman, J.W., Haller, E.E., Geis, N., Poglitsch, A. & Rumitz, M., 1992, *Stressed and Unstressed Ge:Ga Detector Arrays for Airborne Astronomy*, *Internat. J. Infrared Millimeter Waves*, **13**, (11), 1689-1707.
- Vincent, J.D., 1990, *Fundamentals of Infrared Detector Operation and Testing*, (John Wiley & Sons, New York).
- Wang, J.-Q., Richards, P.L., Beeman, J.W., Haegel, N.M. & Haller, E.E., 1986, *Optical Efficiency of Far-Infrared Photoconductors*, *Appl. Opt.*, **25**, (22), 4127-4134.
- Wang, J.-Q., Richards, P.L., Beeman, J.W. & Haller, E.E., 1987, *Stressed Photoconductive Detector for Far-Infrared Space Applications*, *Appl. Opt.*, **26**, (22), 4767-4771.
- Wolf, J., 1994, *Low-background Far-Infrared Detectors and Arrays*, *Opt. Eng.*, **33**, (5), 1492-1500.
- Wolf, J., Katterloher, R., Lemke, D., Grözinger, U., Hermans, L., Frenzl, O., Engemann, D., Beeman, J. & Fabbicotti, 1996, *Far-Infrared Stressed Ge:Ga Array for FIRST*, Proc. 30<sup>th</sup> ESLAB Symp., Submillimetre and Far-Infrared Space Instrumentation, **SP-388**, 25-28.

## Chapter 4 Instrument Design

### 4.1. Introduction

This chapter focuses on the basic design parameters of THUMPER. At the outset there were a number of issues to be addressed. THUMPER has to meet with the science sensitivity requirements when used on the JCMT. It also has to be integrated with the existing SCUBA optics with minimal impact on the performance of SCUBA. It has to be capable of observing simultaneously with SCUBA and use the same electronic scheme and hence analysis package, therefore it should look like add-on channels to SCUBA. These constraints limit the size of the array to the seven spare SCUBA channels in the electronics rack and have a severe impact on the optics feed chain and location of the system. These along with operational constraints, that the cryostat should require minimal servicing from the JCMT support team required critical consideration at the design stage. Here the design requirements are outlined and solutions are addressed for each of the main driving parameters leading to a detailed description of the key elements of the THUMPER photometer.

### 4.2. Instrument Requirements

The science drivers were outlined in Chapter 1 from which it is evident that ideally a multi-element array is needed with an angular resolution comparable to that achieved with SCUBA at  $450\ \mu\text{m}$ , and which is photon-noise limited. It also needs to observe simultaneously with SCUBA to reduce the effect of a changing atmospheric transmission. It has already been shown in Chapters 2 and 3 that PC detectors will meet with the BLIP condition and that the bandwidth and central wavelength of the photometric band have been defined. The practicalities of designing an instrument for the JCMT to fit with the other constraints above further serve to limit the design.

Figure 4.1 is a schematic of SCUBA and THUMPER at the telescope. First, the beam optics need to be integrated to the existing SCUBA optics with minimal impact on SCUBA itself. This is described in Section 4.3. A dichroic, which will transmit the submillimetre SCUBA bands at  $850$  and  $450\ \mu\text{m}$  and reflect the  $200\text{-}\mu\text{m}$  band, needs to be placed in the SCUBA beam to pick off the THUMPER input beam. The parameters

for the dichroic are discussed in Section 4.4 along with a description of the other optical components employed by THUMPER. The optimal point for effecting the pick off point required optical modelling with ZEMAX and are also described in this Section.

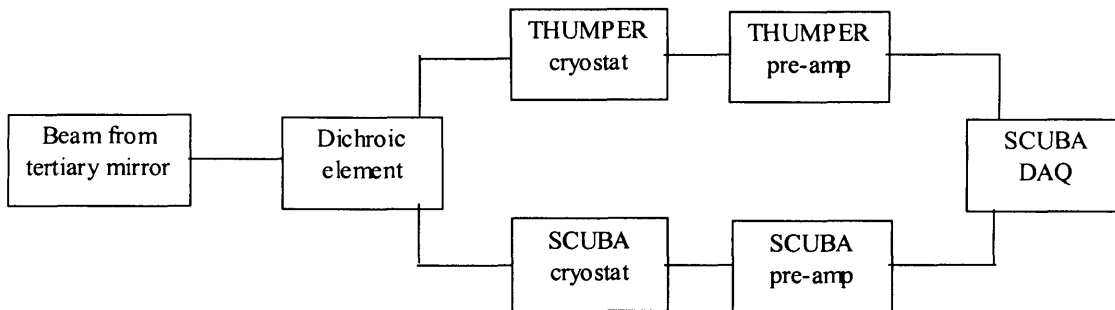


Figure 4.1. Schematic of THUMPER and SCUBA at the JCMT.

Following the dichroic the beam needs to be steered to the position where THUMPER will be mounted, near the Nasmyth focus next to SCUBA. The optical path taken is described in Section 4.3. Selection of the mounting position is described in Section 4.5, along with a description of the cryostat.

Taking on-board the operational constraints in terms of dewar servicing placed a severe limitation on the THUMPER window throughput so the optics design included a beam waist position at the dewar window. This, along with the need to re-focus the beam and limit stray light on the detectors, determined the design of the cold focal plane optics. A further consideration has to be given to poor surface quality of the JCMT for 200- $\mu\text{m}$  radiation. Calculations, based on the Ruze formula, and consideration of beam size compatibility with SCUBA at 450  $\mu\text{m}$  drive the final selection of the THUMPER beam size on the sky. All these considerations are detailed in Section 4.3.

Lastly, the readout needed to be integrated with the SCUBA electronics of which there are seven spare channels. Because of this and the need to limit the throughput to enhance cryogen hold time THUMPER is designed to be a seven-channel photometer. The electronic readout is detailed in Section 4.6.

### 4.3. Optical Configuration

The optical design for THUMPER was driven by the location of the cryostat. The location is described in Section 4.5.1. A fundamental requirement for THUMPER is that

it should observe in as similar a way to SCUBA as possible. The beam size for THUMPER has been matched to the 850- $\mu\text{m}$  channel of SCUBA at 14.3". Later modifications to the feedhorn entrance aperture will then match the angular resolution of THUMPER to the 450- $\mu\text{m}$  SCUBA channel.

#### 4.3.1. Telescope and SCUBA Optics

The beam from the JCMT is severely degraded by the surface accuracy of the primary mirror. When constructed the telescope was not envisaged for undertaking 200- $\mu\text{m}$  observations. The error caused by the JCMT primary mirror is negligible for a surface accuracy greater than  $\lambda/14$ . Such an accuracy provides a Strehl ratio of greater than 0.8, by convention considered diffraction limited (Schroeder, 1987). For 200- $\mu\text{m}$  observations this would necessitate the surface to be better than 14  $\mu\text{m}$ . However the accuracy is (as of April 2003) estimated to be good to around 17  $\mu\text{m}$  (Richer, 2003). Hence the ultimate aim for THUMPER in terms of spatial resolution is to match the diffraction limit of the 450- $\mu\text{m}$  channel of SCUBA.

The design of THUMPER's optics has been driven by the limitation imposed by cryostat placement availability. The first warm optical elements are the same as those used by SCUBA so a brief review of the SCUBA external optics is initially included. Holland *et al.* (1999) provide a more complete description. An image of the warm optics used by SCUBA is shown in Figure 4.2.

Light from the JCMT primary mirror is reflected up to the 60-cm diameter secondary, and then back through the primary hole to the tertiary mirror, located within the receiver cabin. The distance between the secondary and primary mirrors has been increased for SCUBA, a necessity in order to fit the beam through the Nasmyth bearing. After exiting the Nasmyth bearing the beam travels to the first SCUBA flat mirror, M1. This is followed by a powered mirror (M2), used as part of a Gaussian beam telescope (GBT) used to reduce the beam diameter entering the SCUBA cryostat window. A GBT is formed by two mirrors (or lenses) whose separation is equal to the sum of their focal lengths. The beam is then directed into the SCUBA cryostat by a further final flat (M3).

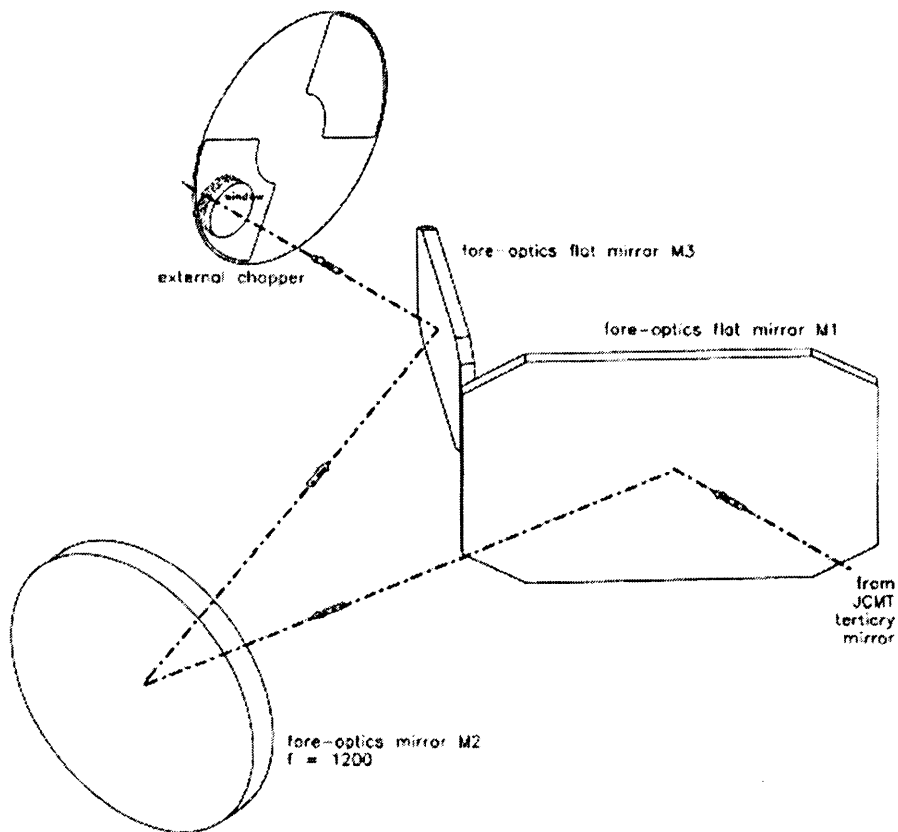


Figure 4.2. The optical path for the external SCUBA optics, from position approximately at top of THUMPER cryostat (from Holland *et al.*, 1999).

#### 4.3.2. THUMPER Optical Configuration

The optical design for THUMPER was optimised by P.C. Hargrave at Cardiff University using the optical design software package ZEMAX, based on an original optical design by S.A. Rinehart.

THUMPER's external optics are initiated prior to the final SCUBA flat mirror, M3. ZEMAX images of the warm optics used by THUMPER are shown in Figures 4.3 and 4.4. A dichroic is placed in front of this mirror and reflects the THUMPER beam downwards and back in the direction of the SCUBA powered mirror. The SCUBA beam passes through the dichroic onto M3. The dichroic is discussed in more detail in Section 4.4.3. Its placement is dictated by its limited physical size: at this location the SCUBA beam is at its smallest where a beamsplitting element can still be placed without interference to SCUBA optical components. Below M2 a correcting mirror, T1, used to

correct for aberrations caused by the JCMT primary mirror's defocus, is placed at the pupil. The position of T1 is the optimum position for a correcting element as it minimises any further increase in the magnitude of the aberrations.

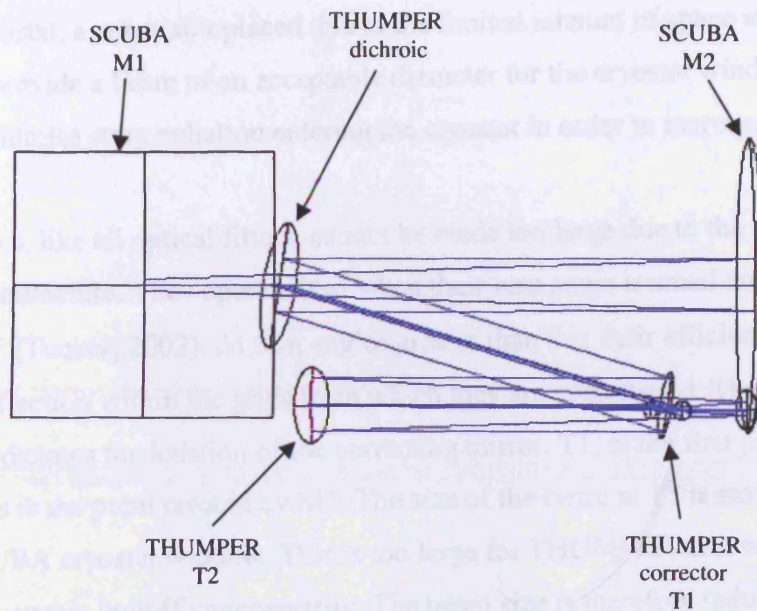


Figure 4.3. The optical path for the external THUMPER optics, as viewed from the side.

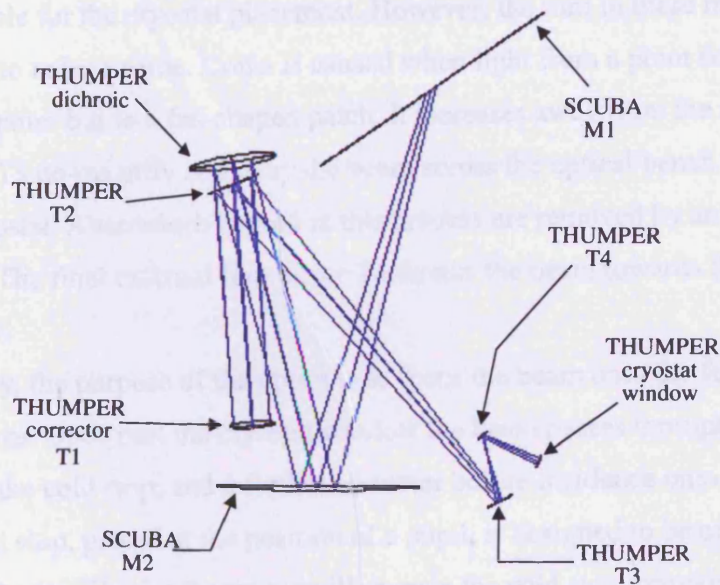


Figure 4.4. The optical path for the external THUMPER optics, as viewed from above.

T1 directs the beam to a plane parallel to and below SCUBA's beam. The THUMPER beam is 50 mm above the optical tabletop. The subsequent external optics serve two purposes. Firstly they guide the beam into the only acceptable location for the THUMPER cryostat, a constraint placed due to the limited amount of space at the JCMT. Secondly they provide a beam of an acceptable diameter for the cryostat window, necessary to minimise stray radiation entering the cryostat in order to increase cryogenic hold time.

Dichroics, like all optical filters, cannot be made too large due to the size of grid available in manufacture. They operate best when their turn angle is small and this must be less than  $22^\circ$  (Tucker, 2002). At turn angles greater than this their efficiency breaks down due to reflection within the grids from which they are constructed. The turn angle of the dichroic dictates the location of the correcting mirror, T1, at the first pupil after aberration. This is the pupil created by M2. The size of the beam at T1 is matched to the size of the SCUBA cryostat window. This is too large for THUMPER as it would increase the cryogenic boiloff unnecessarily. The beam size is therefore reduced by means of a GBT. The GBT has the added bonus of allowing the beam to be turned toward a direction suitable for the cryostat placement. However, the turn in these mirrors must be kept small so as to reduce coma. Coma is caused when light from a point source is imaged not to a point but to a fan-shaped patch. It increases away from the optical axis. Mirrors T2 and T3 de-magnify and relay the beam across the optical bench to the THUMPER cryostat. Aberrations caused in this process are removed by an internal corrector plate. The final external flat mirror T4 directs the beam towards the THUMPER cryostat window.

Internally, the purpose of the optics is to focus the beam onto the feedhorns' entrance apertures. Once past the cryostat window the beam passes through two filters on the LN<sub>2</sub> shield, the cold stop, and a further corrector before incidence onto a powered mirror. The cold stop, placed at the position of a pupil, is designed to be of the same diameter as the beam. The feedhorns over-illuminate the cold stop, providing an illumination profile that is of a flatter top than with no over-illumination. The main elements of the internal optics, as taken from ZEMAX, are shown in Figure 4.5 as viewed from above. The corrector plate eliminates aberrations in the beam introduced by the turn



angle of T2 and T3. The penultimate optical element T5 brings the beam to a focus at the entrance of the feedhorns. The final mirror of T6 turns the beam toward the direction of the focal plane.

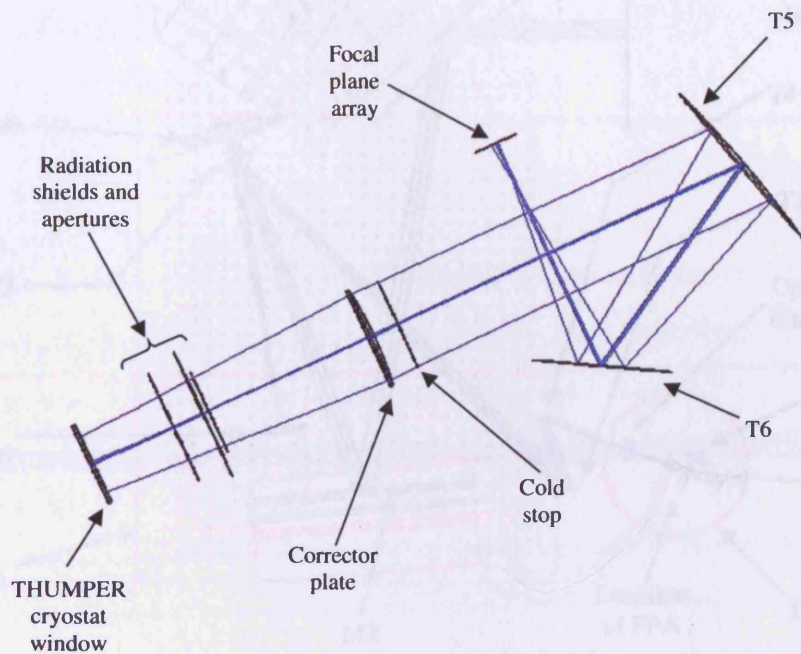


Figure 4.5. The layout of the internal THUMPER optics.

The overall configuration for the SCUBA and THUMPER optical components is shown in Figure 4.6 along with a schematic of the beam. The position of the centre of each of these components with respect to the centre of the Nasmyth bearing is shown in Table 4.1. The centre of the SCUBA beam is 240 mm above the optical table whilst that for THUMPER for all elements after the dichroic, is 50 mm.

Dichroic	-185	712
T1	-436	502
T2	-311	599
T3	-307	99
T4	-466	349
THUMPER window	57	27
THUMPER cryostat	281	-13

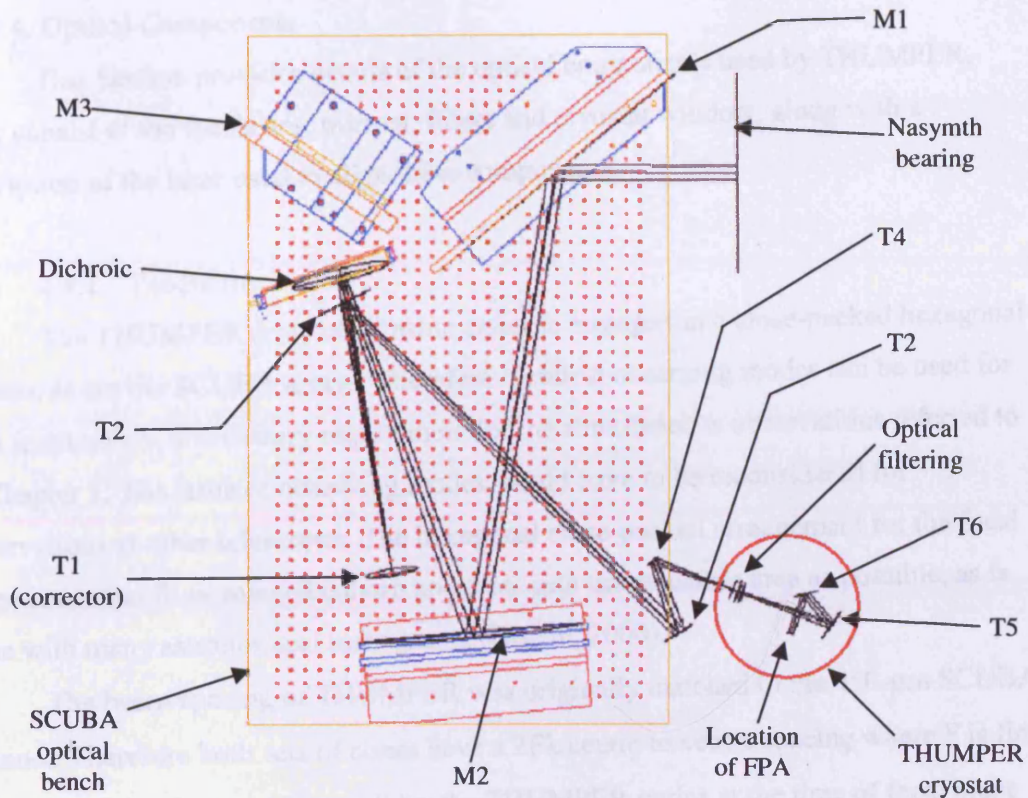


Figure 4.6. View of the optical table used for SCUBA and THUMPER.

Table 4.1. Coordinates of the external optical components used by THUMPER.

	x (mm)	y (mm)
Nasymth bearing	0	0
M1	0	324
M2	-843	472
Dichroic	-184	712
T1	-686	528
T2	-217	699
T3	-817	99
T4	-686	147
THUMPER window	-729	27
Centre cryostat	-781	-118

#### 4.4. Optical Components

This Section provides details of the optical components used by THUMPER. They consist of the feedhorns, mirrors, filters and cryostat window, along with a description of the laser used to align these components.

##### 4.4.1. Feedhorns

The THUMPER array of Winston cones is arranged in a close-packed hexagonal pattern, as are the SCUBA arrays. Therefore identical observing modes can be used for both instruments, a necessary requirement for the simultaneous observations referred to in Chapter 1. The issue of observing modes would have to be reconsidered for observations at other telescopes. The hexagonal close-packed arrangement for the focal plane is used to fit as many feedhorn apertures into the available area as possible, as is done with many astronomical instruments (Griffin, 2000).

The beam spacing of THUMPER was originally matched to the 450- $\mu\text{m}$  SCUBA channel. Therefore both sets of cones have a  $2F\lambda$  centre to centre spacing where  $F$  is final focal ratio.  $\lambda$  is taken as 450  $\mu\text{m}$ .  $F$  for the THUMPER optics at the time of focal plane design freeze was 5.75, leading to a centre-to-centre spacing of 5.18 mm. The spacing samples approximately twice the full-width half-maximum (FWHM) of the Airy disk pattern at 200  $\mu\text{m}$ . The THUMPER horns have wall thickness of 0.2 mm at their entrance aperture and an entrance diameter of 4.8 mm. This covers beyond the second dark ring of the Airy disk pattern at 200  $\mu\text{m}$ .

The horns are Winston shaped cones (Harper *et al.*, 1976). From a definition of entrance and exit diameters ( $d_1$  and  $d_2$  respectively), and acceptance angle  $\theta$ , Harper *et al.* derive the length to be

$$L = \frac{d_1 + d_2}{2 \tan \theta}. \quad (4.2)$$

The exit aperture was set to minimise loss from the detector integrating cavity without causing diffraction of 200- $\mu\text{m}$  radiation. Figure 4.7 shows the general shape of feedhorn, exit aperture and detector crystal. The exit aperture was countersunk to direct radiation towards the crystal since light is diffuse upon exiting the Winston cone.

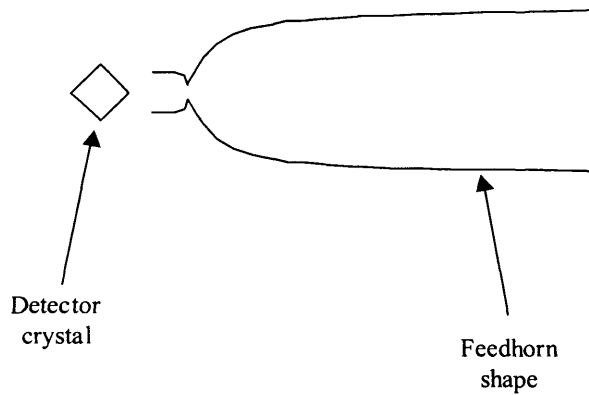


Figure 4.7. Schematic of a feedhorn.

#### 4.4.2. Mirrors

The mirror mounts, constructed from Al, are similar to those used in SAFIRE-A. The mirrors themselves are made from diamond turned Al. This is the preferred material for the manufacture of mirrors due to the relative softness of Cu.

Table 4.2 lists parameters for the THUMPER mirrors. These are the design diameter, radius of curvature, and conic constant. Design diameter is approximately 10 to 20% larger than a ray-tracing image size to allow for diffraction effects.

Table 4.2. Mirror parameters.

	Design diameter (mm)	Radius of curvature (mm)	Conic constant
T1	78	-752	+268
T2	100	+2026	-361
T3	55	-620	-1.26
T4	50	Flat	
T5	40	-308	-1
T6	32	Flat	



#### 4.4.3. Dichroic

The dichroic is the first THUMPER optic that the beam from the Nasmyth bearing will come into contact with. Because there exists a need for simultaneous SCUBA and THUMPER observations the dichroic will allow wavelengths above around 300  $\mu\text{m}$  to pass relatively unhindered to SCUBA whilst reflecting shorter wavelengths into the THUMPER optical system.

A folding down pickoff assembly is required for the dichroic in order that the SCUBA polarimeter can be accessed. The polarimeter attaches to the SCUBA cryostat window, physically very close to the location of the dichroic. The pickoff assembly is a motorised element that can be operated remotely. The assembly, shown in Figure 4.8, consists of a large ring into which the dichroic element can be placed and held by a retaining ring. The dichroic mount is connected to the base of the assembly by a sprung hinge. Rising from the base there are two roof top-shaped supports into which the main ring can recline, centring itself as it does so. Also attached to its base is a mount for THUMPER mirror T2. In order that the dichroic can be protected during technicians' access to the SCUBA polarimeter, a box fits over the top of the dichroic once the assembly has folded down to protect the dichroic element from accidental damage. The cover is designed in an 'L' shape in order to fully enclose all the dichroic and its mount, as well as the mirror T2, so that the beam into SCUBA is not vignetted if the cover is left in place.

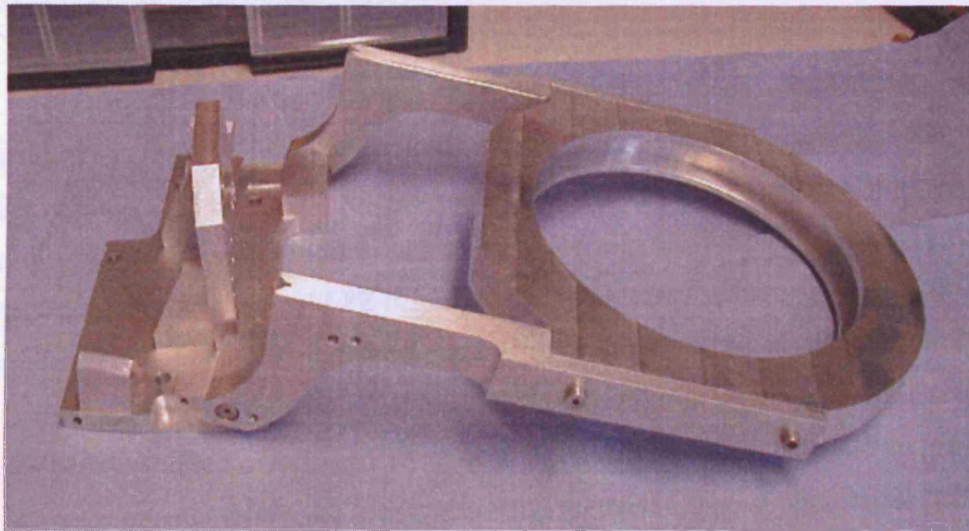


Figure 4.8. The dichroic mount.

#### 4.4.4. Filters

The technology for producing optical filters has existed for many years and been used with great success by instruments such as ISO (Griffin *et al.*, 1990) and SCUBA (Holland *et al.*, 1998). The filters are constructed using metallic meshes supported on Mylar substrate films. The spectral response of these filters are tuned by varying the period and geometry of the meshes, the type of metal used and the combination and spacing of the stacks of meshes (Lee, 1997).

Filters serve to define the spectral passband for the detectors. This severely diminishes the background power on the detectors, and hence considerably reduces the photon noise thus improving sensitivity. They also lower the thermal load falling onto the LHe can, lengthening LHe holdtime. Knowledge of the filters' spectral throughput is important for flux calculations during testing.

A low-pass edge (LPE) filter (B525) is located on the LN<sub>2</sub> temperature shield, allowing radiation lower than 60 cm<sup>-1</sup> to pass into the instrument whilst reflecting the higher frequency component. This is the lowest frequency LPE of the THUMPER optical system, placed in this location to limit LHe boiloff. It is beneficial to move this edge as close as possible to the atmospheric window, without actually impinging on the atmospheric window, in order to limit thermal loading on the cryostat and preserve a high LHe holdtime without reducing sensitivity. A second LPE of 65 cm<sup>-1</sup> (B523) is placed immediately next to the 60-cm<sup>-1</sup> LPE to reduce the effects of harmonic leaks in the 60-cm<sup>-1</sup> LPE. Harmonic leaks occur due to the Fabry-Perot nature of filters.

A further LPE filter, at 90 cm<sup>-1</sup>, is placed further down the optical chain immediately in front of the entrance to the feedhorns. Next to this final LPE is the bandpass filter. LPE filters are necessary at different temperature stages in order to maximise the cryogenic holdtime. Such a series also aids the out-of-band rejection of unwanted radiation. The final LPE is located at the feedhorns' entrance aperture to minimise stray light entering the feedhorns. All LPE filters are tuned to maximise 200- $\mu$ m transmission. Transmission of all the THUMPER cold filters has been measured using a Martin-Puplett polarising FTS (Martin & Puplett, 1970) and are shown in Figure 4.9. Also included in the Figure is that atmospheric transmission at 200  $\mu$ m for 0.25-mm PWV at Mauna Kea, as presented in Chapter 2.

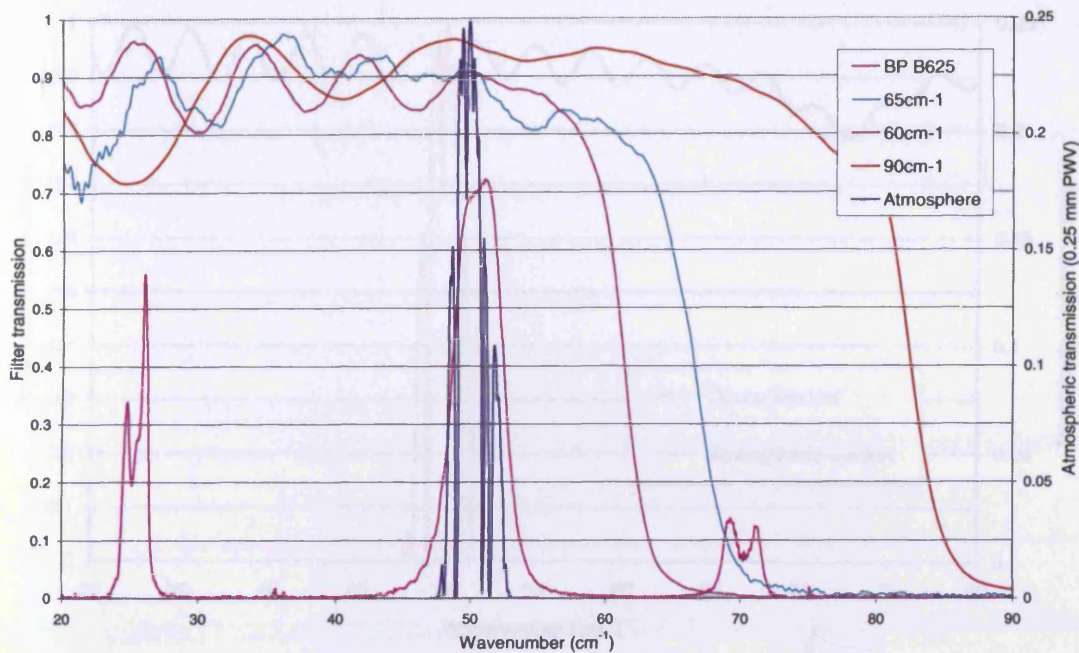


Figure 4.9. Transmission of THUMPER cold filters.

#### 4.4.5. Window

On the outer vacuum case (OVC) of the THUMPER cryostat is a window made of polyethylene. An anti-reflection coating was initially included on the window but was found to be porous to air at the point it met the OVC and 'O'-ring. Transmission of the THUMPER window has been measured and is shown in Figure 4.10.

#### 4.4.6. Alignment Laser

Accurate positioning of the THUMPER cryostat and optical components is of the utmost importance. It is therefore envisaged that optical alignment will take up a large amount of the initial commissioning time. In an effort to optimise the accuracy of the alignment process a laser and mount have been acquired.

The laser is a class IIIa 5-mW HeNe laser. It is mounted immediately above the THUMPER cryostat window with a mount that consists of a 45° fold-mirror to direct the beam through the warm THUMPER optical components. By positioning the image of the laser at the correct position on the JCMT tertiary mirror, individual optical elements can be aligned. For alignment of the external optics a reflector will be used in place of the



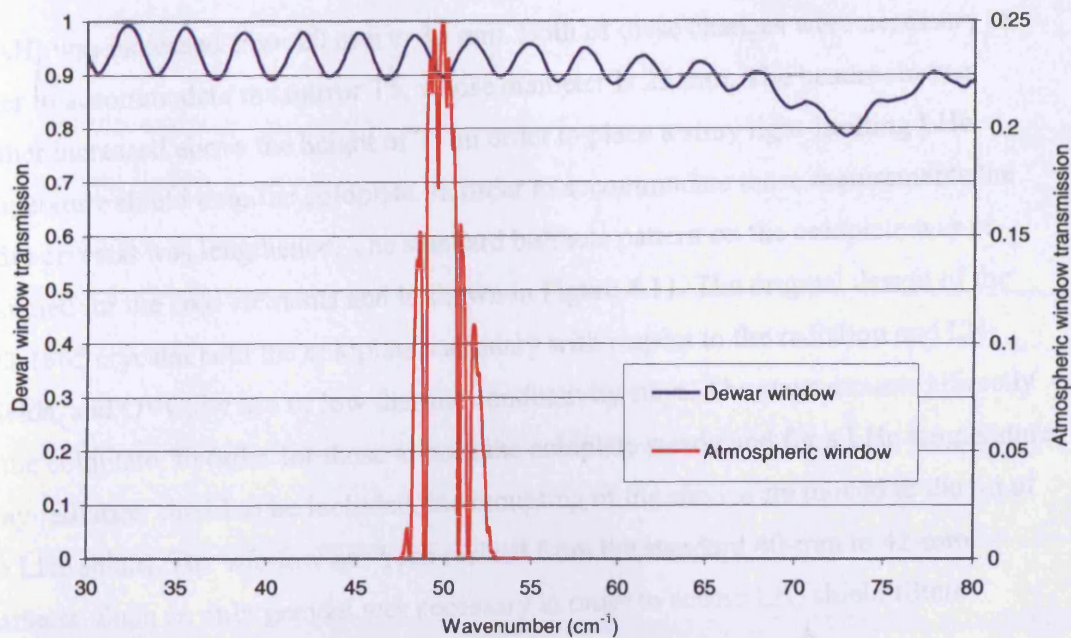


Figure 4.10. Transmission of the THUMPER window.

dichroic since the THUMPER dichroic is in transmittance in the visible part of the spectrum.

In terms of internal alignment, a mirror is placed to reflect the laser from outside the cryostat through the window aperture to the centre of the FPA. A cross-hair target is constructed for this purpose. The LN<sub>2</sub>, He boiloff gas and LHe cooled shields are held steady with the THUMPER cryostat transit plate whilst alignment of the internal optics is performed.

#### 4.5. Cryostat

The original design of the QMC Instruments Ltd TK-1865 cryostat, in which THUMPER will operate, has been modified to incorporate the necessary elements which comprise THUMPER's optics. The TK-1865 cryostat is based on the Oxford Instruments MD-1865 design. It consists of an Al OVC and LN<sub>2</sub> cooled shield with a stainless steel LHe reservoir and Cu coldplate. An extra Al radiation shield is fitted which is cooled from gas boiled off from the LHe reservoir. The headroom above the coldplate, to the vapour cooled shield, was increased from 60 mm to 95 mm. The optical axis height



(OAH) was increased from 20 mm to 30 mm. Both of these changes were necessary in order to accommodate the mirror T5, whose diameter is 25 mm. The headroom was further increased above the height of T5 in order to place a stray light-limiting LHe temperature shield onto the coldplate. In order to accommodate these requirements the entire cryostat was lengthened. The standard bolthole pattern on the coldplate was re-designed for the cold elements and is shown in Figure 4.11. The original design of the MD-1865 cryostat held the coldplate stationary with respect to the radiation and LN<sub>2</sub> shields, and OVC, by use of low thermal conductivity stays. The stays mounted directly to the coldplate. In order for these to hold the coldplate steady and for a LHe temperature stray-radiation shield to be included, the mounting of the stays were moved to the lid of the LHe shield. The window has been resized from the standard 40-mm to 42-mm diameter. Such an enlargement was necessary in order to access LN<sub>2</sub> shield filters externally.

The remaining dimensions of the cryostat are as follows. The coldplate has a diameter of 203 mm. The stray light shield on the coldplate limits the usable size of the coldplate surface to a diameter of 180 mm. The height of the cryostat is 670 mm, or 785 mm including cryogen-fill necks and valves, with an outer diameter of 290 mm.

Every effort is made to limit the power loading on the LHe temperature components of the cryostat. Two LPE filters are included on the LN<sub>2</sub> shield to minimise radiation incident onto the 4-K stage. There exists an option of including an additional high pass edge on the LN<sub>2</sub> shield at a later date. Wires feeding the focal plane components and JFET units are lengthened in order that they contribute a negligible load to the LHe boiloff.

The coldplate components are bolted directly to the coldplate, with an additional layer of thermal grease to ensure good thermal contact. A photograph of their location within the cryostat is shown in Figure 4.12. The use of a baseplate was considered but rejected due to previous experience in components not reaching cryogenic temperature due to the thermal impedance imposed by baseplates (Ade, 2001). The introduction of a thermal impedance would have serious consequences for stressed PCs at unpumped LHe temperatures due to the large amount of dark current present and its temperature

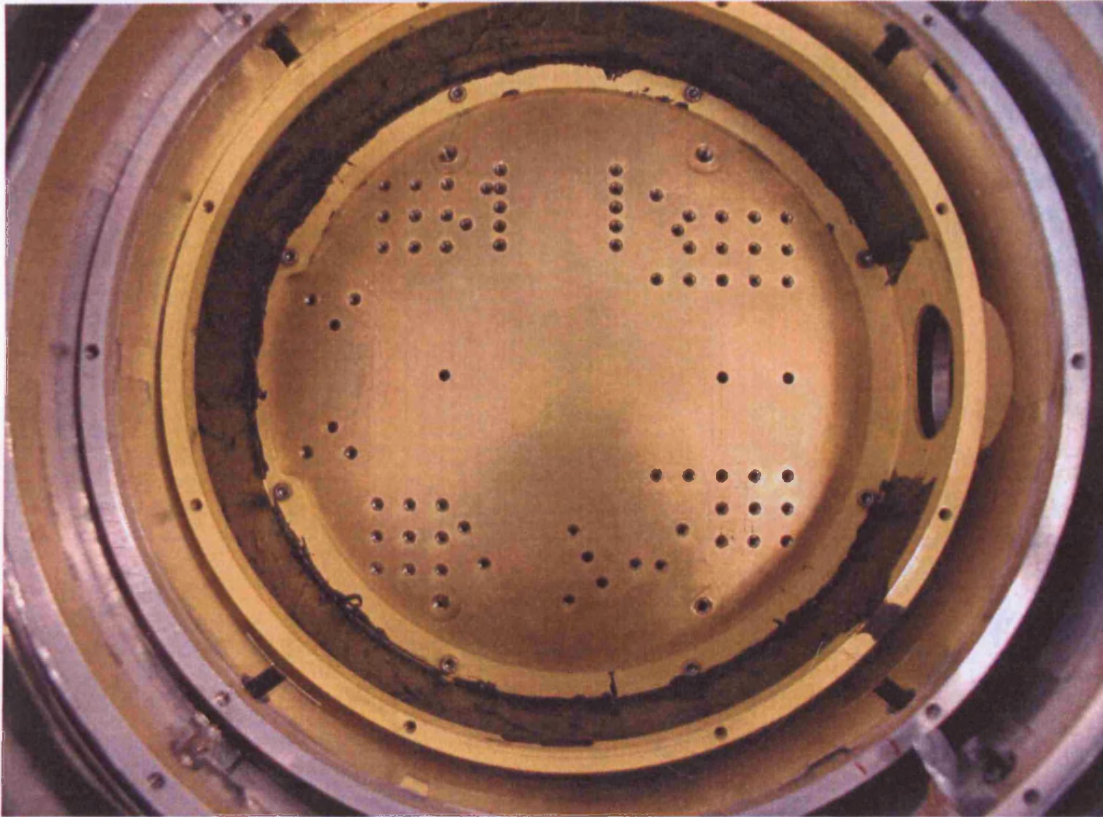


Figure 4.11. The bolthole pattern of the coldplate.

dependence. However, baseplates generally ease the alignment of the optics since adjustments can often be more easily made outside a cryostat than inside.

An optical coldstop is mounted directly onto the coldplate. A LHe temperature shield contains all elements on the coldplate. A baffle leads in from the entrance of this shield towards the centre of the coldplate to limit stray light. Further shields are used to limit cryogenic loss. These are a shield cooled by He gas at approximately 40 K, evaporated from the LHe reservoir, followed by a shield at LN<sub>2</sub> temperature.



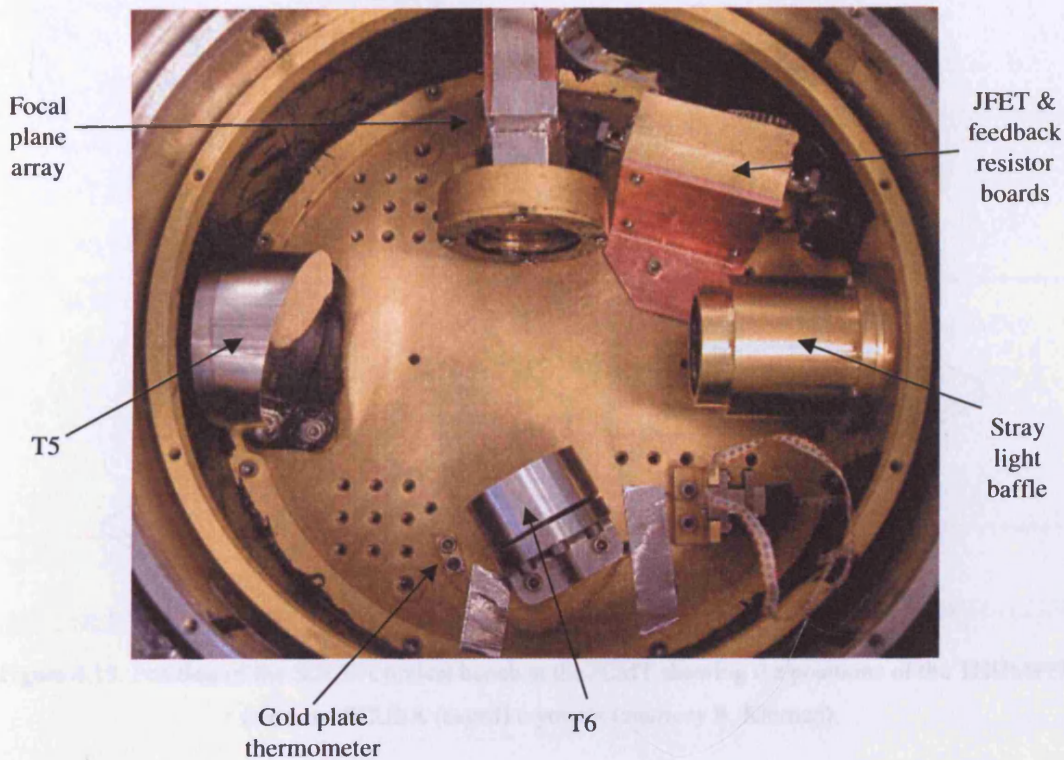


Figure 4.12. Internal components of THUMPER.

#### 4.5.1. Location

The location of the THUMPER cryostat has been the driving force behind the optical design. The cryostat will be placed on top of a bracket extruding from the A-frame of the telescope central bearing support. Due to the lack of available space around the SCUBA cryostat, THUMPER's location is the only one acceptable. Figure 4.13 is a schematic of the SCUBA optical bench showing the location of the SCUBA and THUMPER cryostats. A photograph of the THUMPER cryostat superimposed on an image of its position at the JCMT is shown in Figure 4.14.

The cryostat is mounted onto the side of the main telescope support A-frame. Due to the large weight of the THUMPER dewar when full (about 70 kg) the support is required to be very robust. Constructed from mild steel it joins the A-frame at five locations. Between this and the cryostat are two Al alloy plates. Adjustment can be made in horizontal-tilt directions, along with rotations about the long-axis of the cryostat.

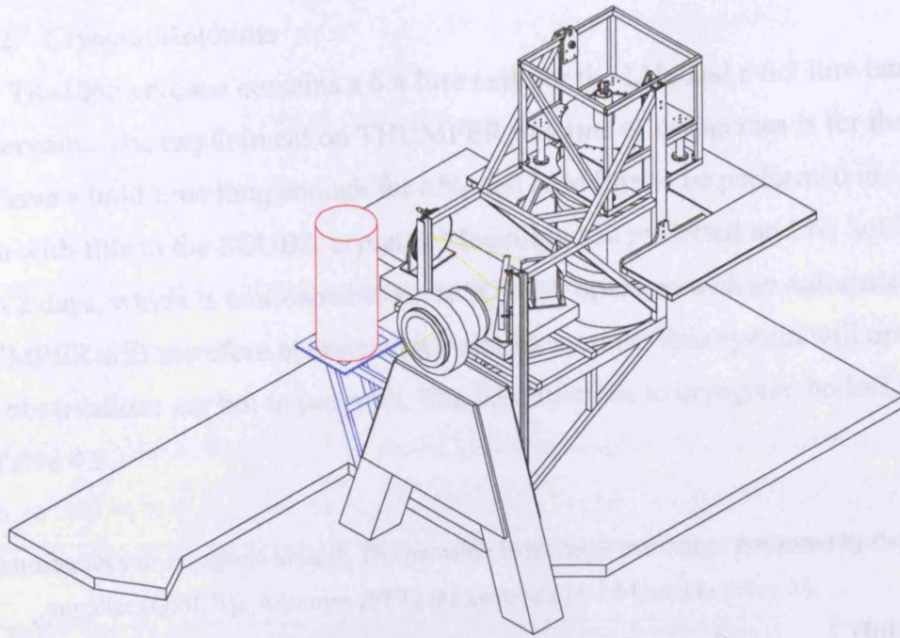


Figure 4.13. Position of the SCUBA optical bench at the JCMT showing the positions of the THUMPER (red) and SCUBA (caged) cryostats (courtesy B. Kiernan).

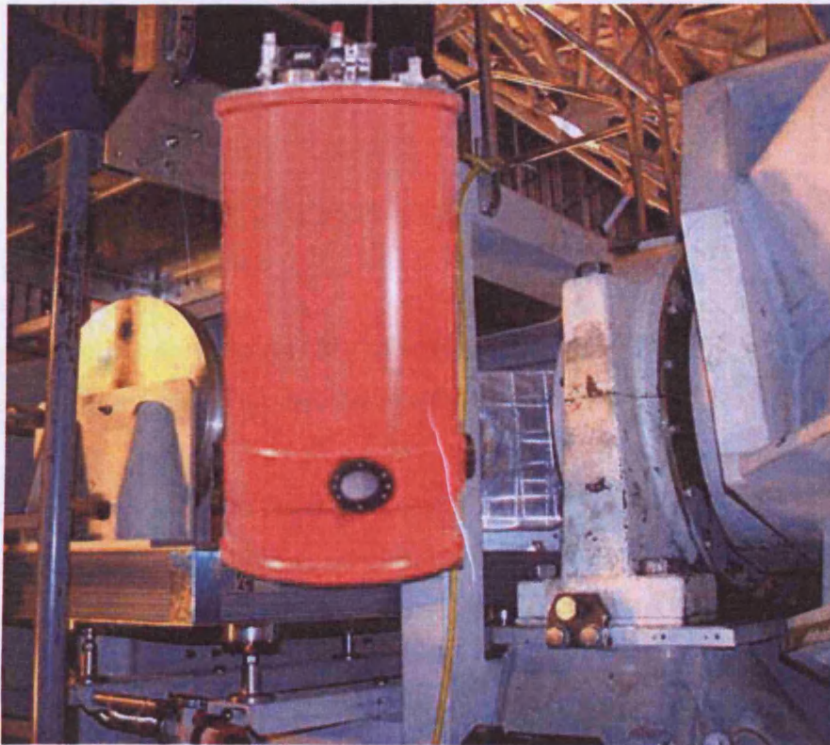


Figure 4.14. Position of the THUMPER cryostat at the JCMT.



#### 4.5.2. Cryogen Holdtime

The TK-1865 cryostat contains a 6.4 litre tank for the LHe and a 6.5 litre tank for the LN<sub>2</sub> reservoirs. The requirement on THUMPER in terms of cryogenics is for the cryostat to have a hold time long enough for LN<sub>2</sub> and LHe fills to be performed in conjunction with fills to the SCUBA cryostat. Modelling has predicted an LN<sub>2</sub> hold time of less than 2 days, which is unacceptable since SCUBA operates with an automated LN<sub>2</sub> filler. THUMPER will therefore operate with a similar system. This system will operate only when observations are not in progress. The contributions to cryogenic boiloff are shown in Table 4.3.

Table 4.3. Contributions to cryogenic boiloff. The parasitic loads are those values measured by the cryostat supplier (QMCIL). Assumes JFETs are switched on 24 hours in every 24.

Load	Parasitic	Radiation	Wiring	JFETs	Total	Hold time (days)
LHe boiloff (ml/day)	110	42	23	45	220	30
LN <sub>2</sub> boiloff (ml/day)	3100	Included in parasitic	5.3	nil	3100	2.1

#### 4.6. Electronic Readout

The electronics serve to derive a measurable voltage from the signal current, as produced by the detectors. They were designed and built in-house by R. Tucker and R. V. Sudiwala.

The signal current from the detectors is read out by TIAs. The first stage of amplification is provided by JFET units (Infrared Laboratories). The TIA circuit is described in general in Section 3.3. Those elements specific to THUMPER are discussed here.

The value of feedback resistor used for the THUMPER channels are 120 M $\Omega$  and are housed in "flatpack" units. Capacitors placed in parallel have values of 30 pF giving

the detector circuit a time constant of around 45 Hz. Higher frequency noise became apparent during multi-channel testing of THUMPER necessitating the need to use a feedback capacitor.

Since the JFET pairs are constructed with a small internal heater an original intention had been to mount the units on the LN<sub>2</sub> shield in order to maximise LHe holdtime. However the increased distance involved in mounting the JFETs on the LN<sub>2</sub> shield, with such a low current passing through such an increased length of wire, led to a large boost in noise.

The housekeeping comprises the thermometry and an illuminator. Two thermometers will be included inside the cryostat. These are supplied by Lake Shore Cryotronics, Inc. through the Joint Astronomy Centre, Hilo. One will be mounted on the detector coldplate whilst the other will be mounted on the LN<sub>2</sub> temperature shield lid. The illuminator will be placed on the cold stop. The power for this is provided by warm electronics supplied by Cochise Instruments with subsequent modification by R. Tucker at Cardiff University.

Sensitivity of stressed Ge:Ga generally varies very little around the optimum bias point (see, for example, Lee, 1997, Figs 4.11; Stacey *et al.*, 1992, Figs. 2 & 3; this thesis, Figure 5.12). However, bias supply for the THUMPER detectors has been designed so that each detector can be biased individually. Such a design ensures an absolute maximum sensitivity for each detector in terms of bias.

The initial stage of the warm amplifier is the operational amplifier section of the TIA circuit. The TIA circuit has been described in Section 3.3. Warm electronics are kept in an RF shielded box mounted onto the side of the THUMPER cryostat to eliminate excess noise.

The subsequent stage of the warm electronics is the pre-amplifier board. This filters the signal to provide the necessary bandwidth and gain for the THUMPER signal to be fed into the SCUBA DAQ. This is necessary since DAQ for THUMPER is performed by unused SCUBA DAQ channels. The SCUBA ADC has a  $\pm 10$ -V range. THUMPER pre-amps have therefore been designed with a  $10^4$  gain for the  $< 1$ -mV AC signal. SCUBA amplifiers have a 3-dB frequency response of 0.2 to 48 Hz and this has

been matched by THUMPER. In effect THUMPER has been constructed to appear as a third SCUBA array.

Power for the THUMPER pre-amp is by mains supplied charging batteries. Mains supply was a requirement placed upon the design of THUMPER in respect of its low maintenance capability. The use of batteries reduces any mains pickup. As designed the electronics will function for either 115 or 230 V at 60 or 50 Hz.

In addition, the warm electronics include power for the illuminator and provision for monitoring the thermometry. Electronics for this are in a dedicated box, also mounted on the THUMPER cryostat.

All wiring between the different temperature stages is polyester enamelled constantan of 44 SWG. Constantan has a far lower thermal conductivity than Cu (10.2 and  $715 \text{ W cm}^{-1}$  respectively, integrated between 4.2 and 77 K (Vincent, 1990)) so limits LHe boiloff. The enamel coating electrically isolates current carrying wires from other wires and from ground.

Housekeeping wiring is kept separate from signal wiring along their lengths from coldplate to room temperature electronics housings. A separation between the two sets of wiring is to minimise any possibility of pickup from the high impedance detector signal wires. Wires leading to the thermometry are twisted pairs, as are the wires supplying power to the illuminator.

For the JFET units, ground, heater supply and heater return are common for the seven units. Such a method of wiring reduces thermal conduction and increases cryogenic holdtime. Source wires use twisted pairs to minimise pickup. All wires are fed out from the cryostat's OVC by 55-pin hermetic connectors.

#### 4.6.1. Pinouts

In order to facilitate the straightforward removal of the coldplate items, namely the FPA and first-stage amplification box, the wiring between each of these items and the warm amplifier stage is separated by a series of MDM connectors. These connectors are bolted down to the cryostat coldplate by means of an 'L'-bracket. The routing through each of these MDMs, up to the external signal connector is shown schematically in Figure 4.15 and listed pin-to-pin in Table 4.4.

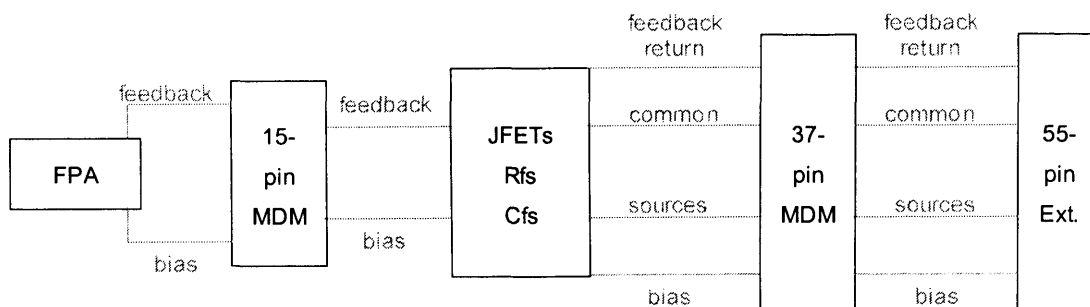


Figure 4.15. Schematic of wiring within THUMPER cryostat.

Housekeeping wires, for the illuminator and coldplate thermometer, are routed through a 9-pin MDM, mounted onto the coldplate through an L-shaped bracket. Similarly, the LN<sub>2</sub> thermometer is wired through a dedicated 9-pin MDM, attached to the LN<sub>2</sub> shield lid, to the housekeeping hermetic connector. The wiring plan for the housekeeping is shown in Table 4.5.

#### 4.8. Calibration

An internal illuminator will be used, shown in Figure 4.16, and is supplied by Haller-Beeman Associates, Inc. Mounted in an O<sub>2</sub>-free, high-conductivity Cu ring the emitting element is composed of sapphire with a thin NiCr coating. It is mounted on the coldplate, next to the coldstop.

#### 4.8. Summary

The THUMPER instrument has been fully presented within this chapter. The rationale behind the component level design has been explained.



Table 4.4. Wiring for the signal chain. Bias refers to bias voltage input, Feedback to line from detector to JFET gate and feedback resistor, Source 1 to non-inverting op-amp input, and Source 2 to inverting op-amp input.

Channel	Application	15-pin MDM pin	37-pin MDM pin	Hermetic pin
1 (Formerly AU)	Bias	8	23	a
	Feedback	15	22	E
	Source 1		2	F
	Source 2		1	b
2 (Formerly CU)	Bias	7	25	X
	Feedback	14	24	C
	Source 1		4	Y
	Source 2		3	r
3 (Formerly BU)	Bias	6	27	U
	Feedback	13	26	V
	Source 1		6	A
	Source 2		5	W
4 (Formerly CM)	Bias	5	29	k
	Feedback	12	28	S
	Source 1		8	T
	Source 2		7	m
5 (Formerly AL)	Bias	4	31	I
	Feedback	11	30	P
	Source 1		10	R
	Source 2		9	j
6 (Formerly CL)	Bias	3	33	L
	Feedback	10	32	M
	Source 1		12	h
	Source 2		11	g
7 (Formerly BL)	Bias	2	35	d
	Feedback	9	34	e
	Source 1		14	f
	Source 2		13	K
Common	Heater		16	c
	Drain		15	H
	Ground		17	J

Table 4.5. Wiring for the housekeeping chain.

	9-pin MDM pin	Hermetic pin	Application
4 K	1	H	Thermometer (I+)
	2	e	Thermometer (V+)
	3	spare	spare
	4	f	Illuminator (I+)
	5	K	Illuminator (V+)
	6	J	Thermometer (I-)
	7	d	Thermometer (V-)
	8	v	Illuminator (I-)
	9	L	Illuminator (V-)
77 K	1	W	Thermometer (I+)
	2	V	Thermometer (I-)
	6	X	Thermometer (V+)
	7	U	Thermometer (V-)

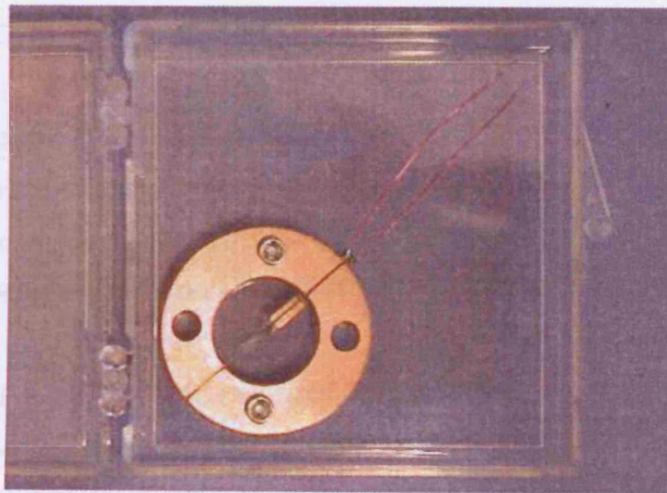


Figure 4.16. The internal illuminator.

#### 4.9. References

- Ade, P.A.R., 2001, Private Communication.
- Griffin, M.J., Ade, P.A.R., Church, S., Murray, A., Overhamm, M., Faymonville, R. & Wang, S.Y., 1990, *Performance Tests on Ge:Ga and Ge:Be Detectors for the ISO Long Wavelength Spectrometer*, In ESA, From Ground-Based to Space-Borne Sub-mm Astronomy, **SP-314**, 359-364.
- Griffin, M.J., 2000, *Bolometers for Far-Infrared and Submillimetre Astronomy*, Nucl. Instr. and Meth. A, **444**, (1-2), 397-403.
- Haller-Beeman Associates, Inc., 5020 Santa Rita Road, El Sobrante, CA 94803, USA.
- Harper, D.A., Hildebrand, R.H., Winston, R. & Stiening, R., 1976, *Heat Trap – An Optimized Far Infrared Field Optics System*, Appl. Opt., **15**, (1), 53-60.
- Holland, W.S., Cunningham, C.R., Gear, W.K., Jenness, T., Laidlaw, K., Lightfoot, J.F. & Robson, E. I., 1998, *SCUBA: A Submillimeter Camera Operating on the James Clerk Maxwell Telescope*, Proc. SPIE Advanced Technology MMW, Radio, and Terahertz Telescopes, **3357**, 305-318.
- Holland, W.S., Robson, E.I., Gear, W.K., Cunningham, C.R., Lightfoot, J.F., Jenness, T., Ivison, R.J., Stevens, J.A., Ade, P.A.R., Griffin, M.J., Duncan, W.D., Murphy, J.A. & Naylor, D.A., 1999, *SCUBA: a Common-User Submillimetre Camera Operating on the James Clerk Maxwell Telescope*, Mon. Not. R. Astron. Soc., **303**, (4), 659-672.
- Infrared Laboratories, 1808 E. 17<sup>th</sup> Street, Tucson, AZ 85719-6505, USA.
- Lake Shore Cryotronics, Inc. 575 McCorkle Blvd, Westerville, OH 43082, USA.
- Lee, C. 1997, *Far-Infrared Spectroscopic Measurements of HBr in the Lower Stratosphere*, PhD Thesis, Queen Mary & Westfield College, University of London.
- Martin, D.H. & Puplett, E., 1970, *Polarised Interferometric Spectrometry for the Millimetre and Submillimetre Spectrum*, Infrared Phys., **10**, (2), 105-109.
- Queen Mary College Instruments, Ltd, Department of Physics and Astronomy, Cardiff University, 5, The Parade, Cardiff, CF24 3YB, U.K.
- Richer, J., 2003, Private Communication.
- Rinehart, S.A., 1999, THUMPER proposal.

- Schroeder, D.J., 1987, *Astronomical Optics*, p191, Academic Press, Inc., San Diego.
- Stacey, G.J., Beeman, J.W., Haller, E.E., Geis, N., Poglitsch, A. & Rumitz, M., 1992, *Stressed and Unstressed Ge:Ga Detector Arrays for Airborne Astronomy*, *Internat. J. Infrared Millimeter Waves*, **13**, (11), 1689-1707.
- Tucker, C., 2002, Private Communication.
- Vincent, J.D., 1990, *Fundamentals of Infrared Detector Testing and Operation*, (John Wiley & Sons, New York).

## Chapter 5 Laboratory Testing and Modelling

### 5.1. Introduction

To determine the optimal configuration and operational parameters for the THUMPER PC detectors, measurements were first made on a number of prototypes. From these datasets the size and shape of the detector crystals, the applied stress, and the optimum doping for operation at 3.7 K were determined. These data were then used to define and construct the THUMPER detector arrays as described in Chapter 3.

This Chapter provides a description of the experimental arrangement for these laboratory measurements and a description of the THUMPER detector testing. Results are presented for both single element prototype detectors and the THUMPER PC arrays allowing comparisons to be made between them. Tests included spectral response, dark current, responsivity and noise measurements, all as a function of temperature. Models are presented drawing upon the general theory of PCs presented in Chapter 3, which are then compared to the experimental data.

### 5.2. First Prototype Detector Testing

The tests on the prototype detectors defined the parameters and configuration chosen for the THUMPER array. These detectors were constructed using a similar method to that described in Chapter 3.

Ge:Ga material was obtained from the LBNL in order that mounting and stressing procedures set out in Chapter 3 could be perfected in-house. The material selected was a 1.5×1.0×1.0-mm crystal of 102-13.6 Ge:Ga. As mentioned in Section 3.5.2 this refers to the 102<sup>nd</sup> crystal grown at LBNL with a wafer cut 13.6 cm from the seed end of the crystal. This was then mounted in a prototype SAFIRE-A, single element, stressing block with stress applied along the longest length of the crystal.

#### 5.2.1. Experimental Arrangement

For performance testing the stressed detectors were mounted as single units in an Infrared Labs HD-3 cryostat. A schematic of the HD-3 is shown in Figure 5.1. By

varying the vapour pressure above the LHe, tests could be performed at any temperature between 4.2 K (boiling point of He at 1 atmosphere) and 1.5 K (boiling point of He at a few mbar vapour pressure). This allowed for the characterisation tests to be performed around the expected He boiling point at the JCMT of 3.7 K (for a vapour pressure around 615 mbar). Tests performed on the detectors included spectral response, dark current and sensitivity determinations.

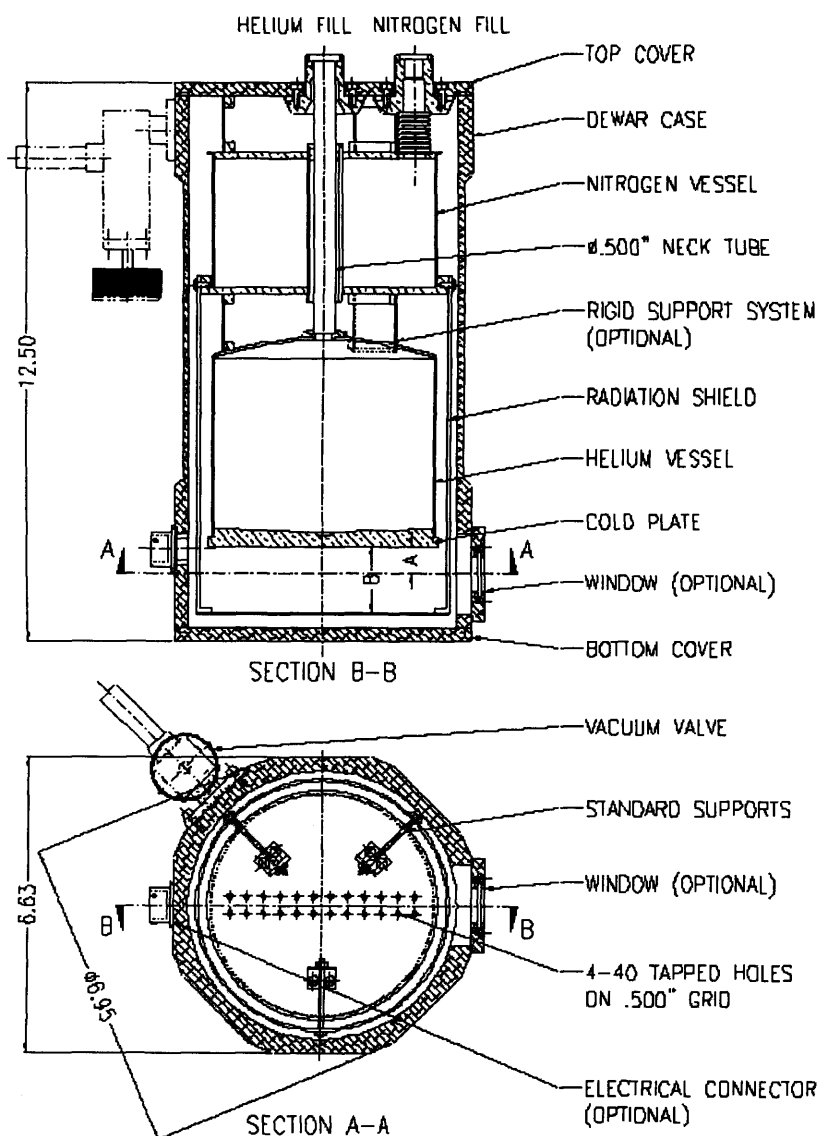


Figure 5.1. Schematic of an Infrared Labs HD-3 cryostat.

### 5.2.2. Spectral Response Measurements

One of the most important parameters of a Ge:Ga PC is the dependence of spectral response on applied stress. A requirement for THUMPER was to ensure that the detector responds well at 200  $\mu\text{m}$ . The best way of measuring this is a direct optical measurement obtained by using the detector with a spectrometer.

Signals were read out using a TIA pre-amplifier. Filtering within the cryostat consisted of a 150- $\text{cm}^{-1}$  LPE on the  $\text{LN}_2$  shield, and a 500- $\text{cm}^{-1}$  LPE within the snout at 4 K.

A polarising FTS (Martin & Puplett, 1970) was used to measure the spectral response of the detector. A schematic of the internal components of an FTS system is shown in Figure 5.2. Radiation from a mercury arc lamp source passes through a fixed polariser. This reflects half of the source power back to the source. The transmitted polarised beam continues on to a polarising beam splitter, which has its polarisation direction orientated at  $45^\circ$  with respect to the input polariser. The incident beam is therefore split into two orthogonally polarised beams one being reflected and the other transmitted. The transmitted component travels to a fixed roof top mirror orientated such that it rotates the polarised beam by  $90^\circ$  on reflection. The reflected component travels to a moving rooftop mirror, which also rotates the polarised beam by  $90^\circ$  on reflection. The different optical path traversed in this arm introduces a phase delay when the two beams recombined at the beamdivider. As the moving mirror traverses, each source frequency is modulated resulting in a characteristic cosine pattern being observed at the output. When white light is incident the output is the sum of all the monochromatic components, referred to as an interferogram. Performing a FT on the measured interferogram reduces it to the input spectrum hence the name FT spectrometer. A more complete description of the FTS can be found in other texts, e.g. Bell (1972) and Martin (1982).

The interferogram is measured directly by the detector. The output signal from the TIA readout is passed to a computer running LabVIEW software, and FTed to give the detector's relative spectral response.



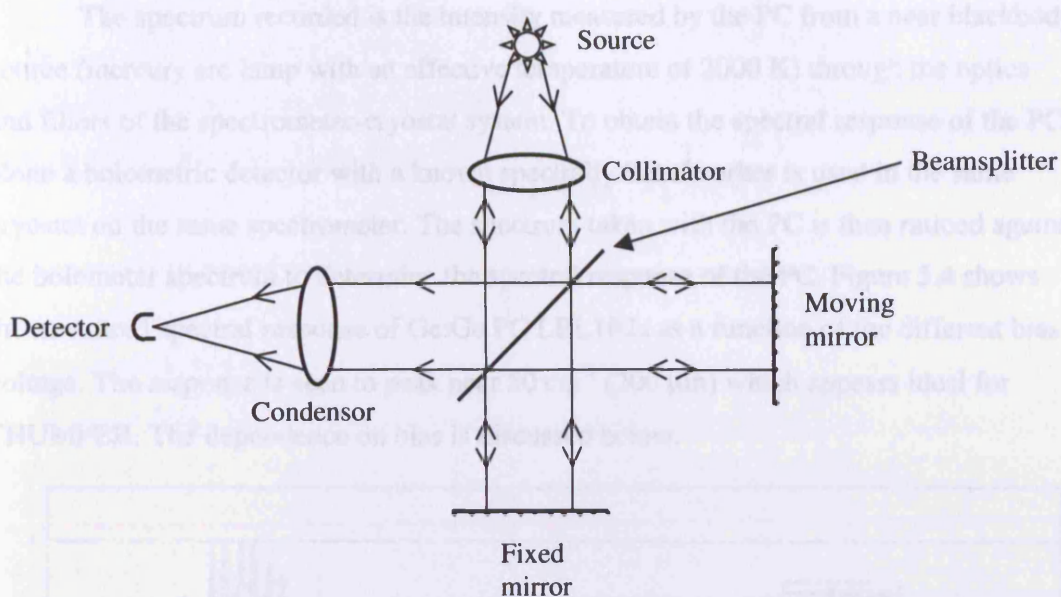


Figure 5.2. Schematic of the internal components of an FTS.

Figure 5.3 is a block diagram of the FTS system. The HD-3 was placed so that the cryostat window was sitting next to the exit port of the spectrometer. The inside of the spectrometer was evacuated, necessary to remove the absorption by atmospheric gases such as  $H_2O$  vapour and  $O_2$  in the optical path. The vacuum seal is effected directly onto the window of the HD-3 cryostat ensuring there is no air in the optical path.

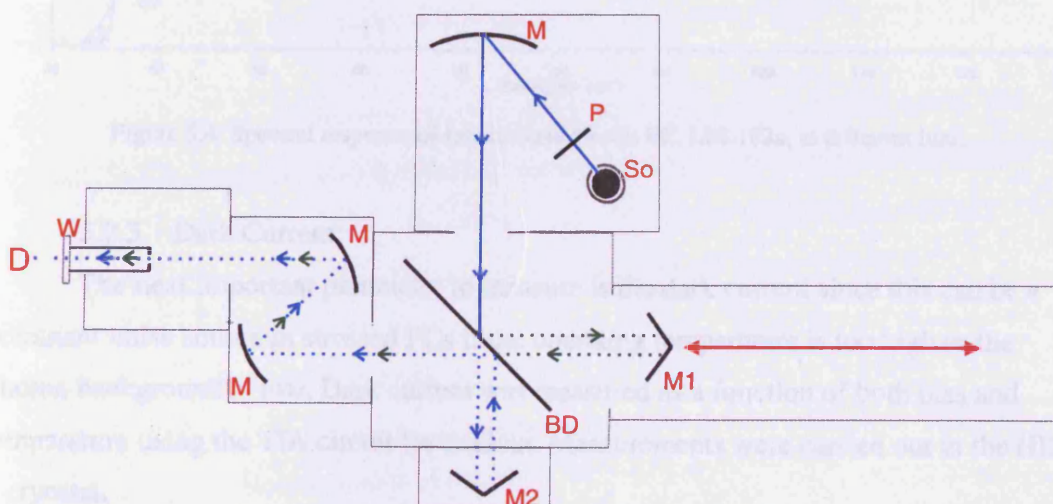


Figure 5.3. Block diagram of the FTS (courtesy C. Tucker).

The spectrum recorded is the intensity measured by the PC from a near blackbody source (mercury arc lamp with an effective temperature of 2000 K) through the optics and filters of the spectrometer-cryostat system. To obtain the spectral response of the PC alone a bolometric detector with a known spectrally flat absorber is used in the same cryostat on the same spectrometer. The spectrum taken with the PC is then ratioed against the bolometer spectrum to determine the spectral response of the PC. Figure 5.4 shows the measured spectral response of Ge:Ga PC LBL102a as a function of the different bias voltage. The response is seen to peak near  $50 \text{ cm}^{-1}$  ( $200 \mu\text{m}$ ) which appears ideal for THUMPER. The dependence on bias is discussed below.

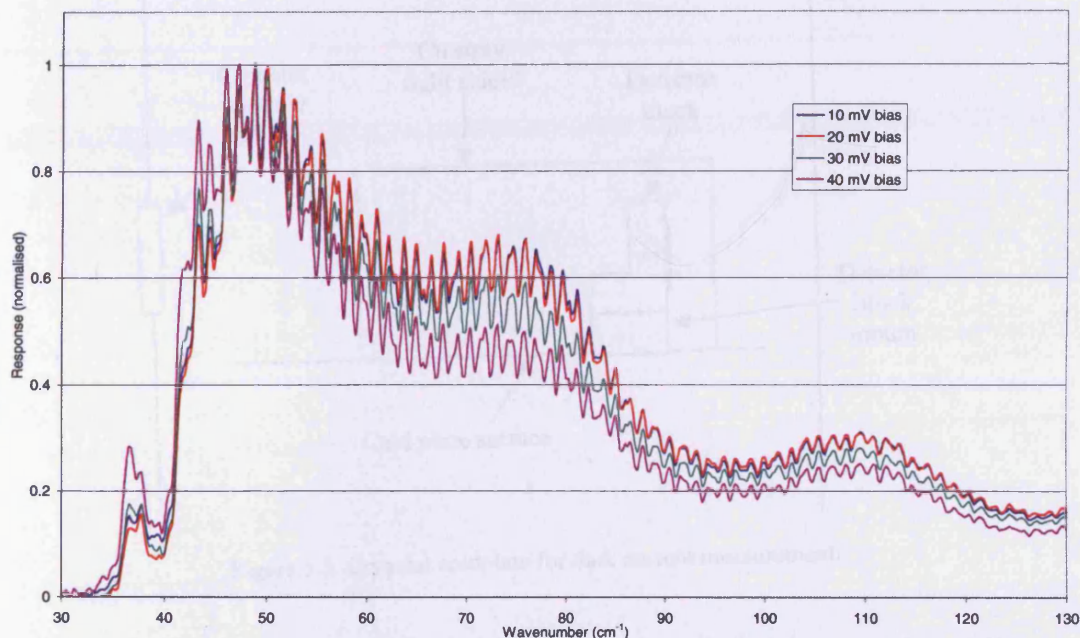


Figure 5.4. Spectral response of test stressed Ge:Ga PC, LBL102a, at different bias.

### 5.2.3. Dark Current

The next important parameter to measure is the dark current since this can be a dominant noise source in stressed PCs if the operating temperature is too high or the photon background is low. Dark current was measured as a function of both bias and temperature using the TIA circuit for readout. Measurements were carried out in the HD-3 cryostat.

A sketch of the cryostat coldplate showing the configuration for dark current measurements is shown in Figure 5.5. The entrance to the detector cavity was covered with Al tape. The detector blocks were placed on a mounting block that was attached to the cold surface with the detector facing away from the cryostat window. The additional mounting block was necessary due to the availability of tapped-hole positions on the dewar cold surface. A closed Cu shield was placed over the mounting block and screwed down directly onto the cold surface.

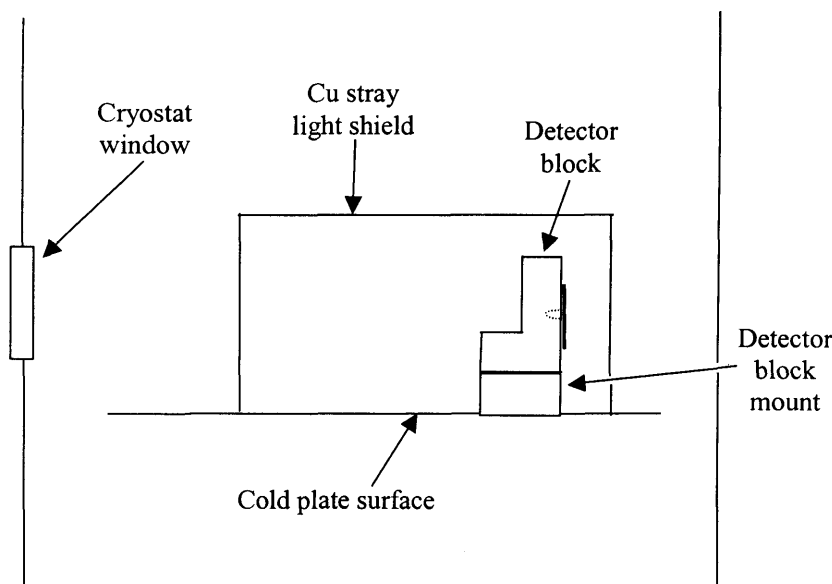


Figure 5.5. Cryostat coldplate for dark current measurement.

A pressure reduction valve was used to control a vacuum line pumping on the LHe and thus to control the temperature of the LHe reservoir. This eases the pumping process since it provides a stable pressure over several hours. Figure 5.6 shows a block diagram of the cryostat and vacuum pump used for reducing He vapour pressure.

At several different temperatures a series of output voltage measurements were recorded as a function of the detector bias level including the zero bias offset. An offset exists since the FETs are not perfectly matched. The value of offset voltage must be subtracted from the recorded voltage to obtain the true output. From the knowledge of feedback resistance, applied bias voltage and application of Ohm's law, detector resistance and dark current can then be determined at each bias. Figure 5.7 plots dark



current against reciprocal temperature at 30 mV bias. The overall shape of the plot agrees well with that expected through application of Equation 3.3.

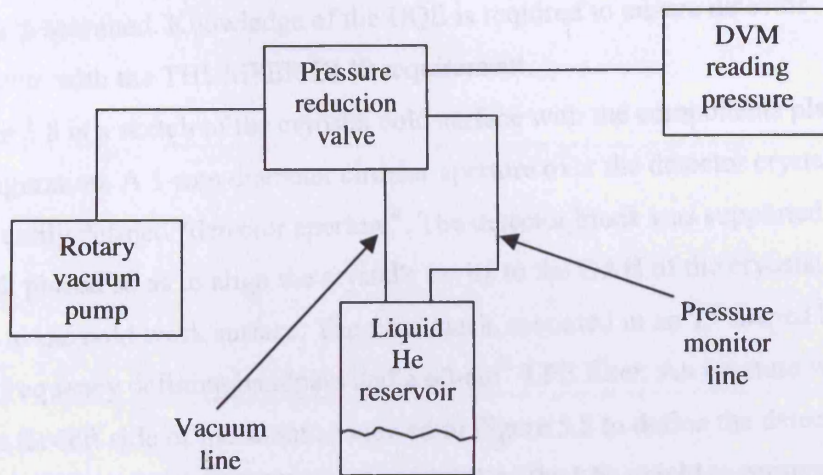


Figure 5.6. Block diagram showing apparatus used in the reduction of He vapour pressure within the HD-3 cryostat.

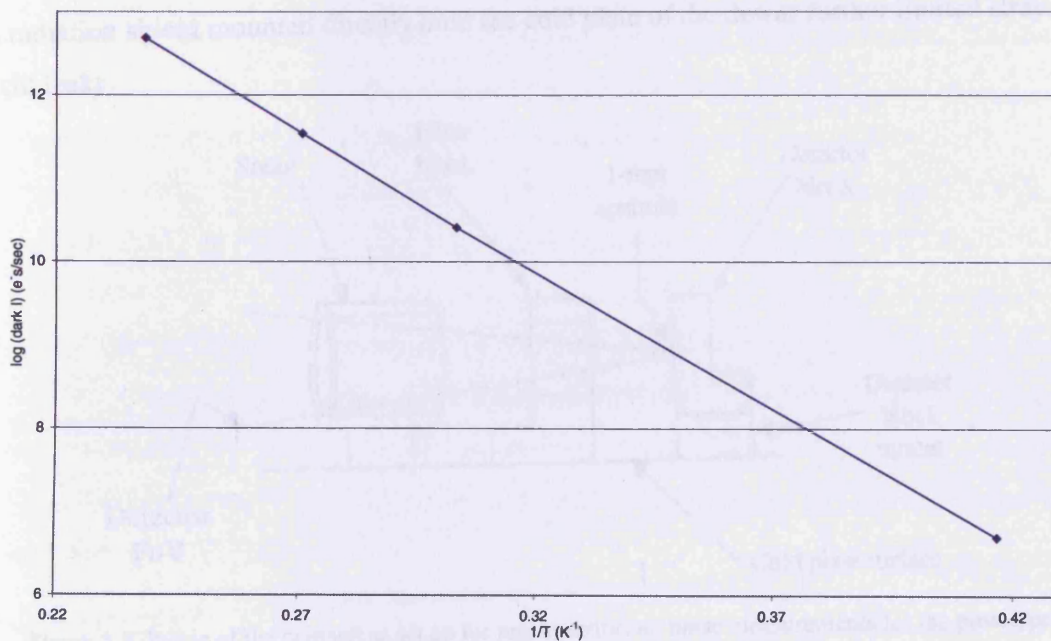


Figure 5.7. Dark current falling with temperature for detector LBL102a.

#### 5.2.4. Responsivity and Noise

Measurements of a detector's responsivity and noise allow the DQE of the detector to be determined. Knowledge of the DQE is required to ensure detector sensitivity meets with the THUMPER BLIP requirement.

Figure 5.8 is a sketch of the cryostat cold surface with the components placed in the test configuration. A 1-mm diameter circular aperture over the detector crystal cavity provided an easily defined "detector aperture". The detector block was supported by a spacing block placed so as to align the crystal's cavity to the OAH of the cryostat window with respect to the cold work surface. The filter stack, mounted in an 'L'-shaped block, contained a frequency defining bandpass and a  $60\text{-cm}^{-1}$  LPE filter. An aperture was placed in the far-left side of the snout as viewed in Figure 5.8 to define the detector's field of view. A further  $150\text{-cm}^{-1}$  LPE filter was mounted on the  $\text{LN}_2$  shield to preserve LHe holdtime by limiting the FIR power that radiates onto the LHe vessel. Figure 5.9 shows the transmission of these filters along with the transmission of the cryostat window. The gap between detector and filter blocks was covered with Cu tape to limit stray light leaks. A radiation shield mounted directly onto the cold plate of the dewar further limited stray light leaks.

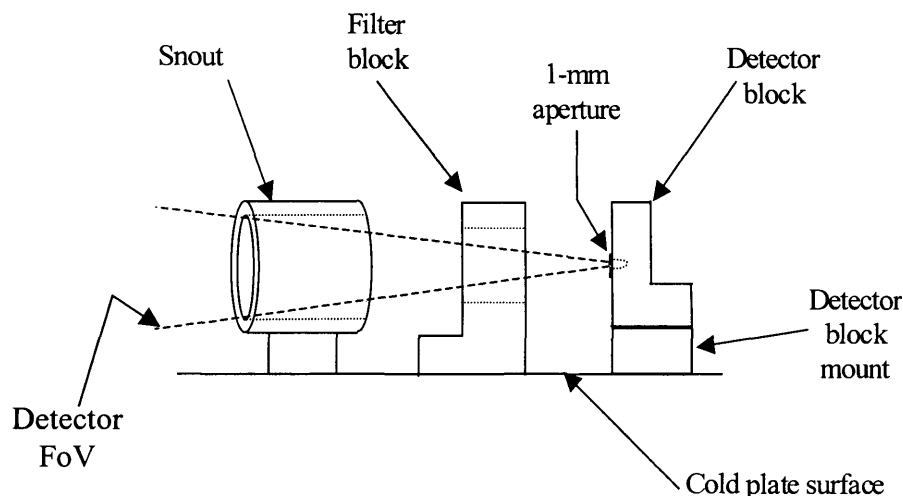


Figure 5.8. Inside of the cryostat as set up for responsivity and noise measurements for the prototype detectors.

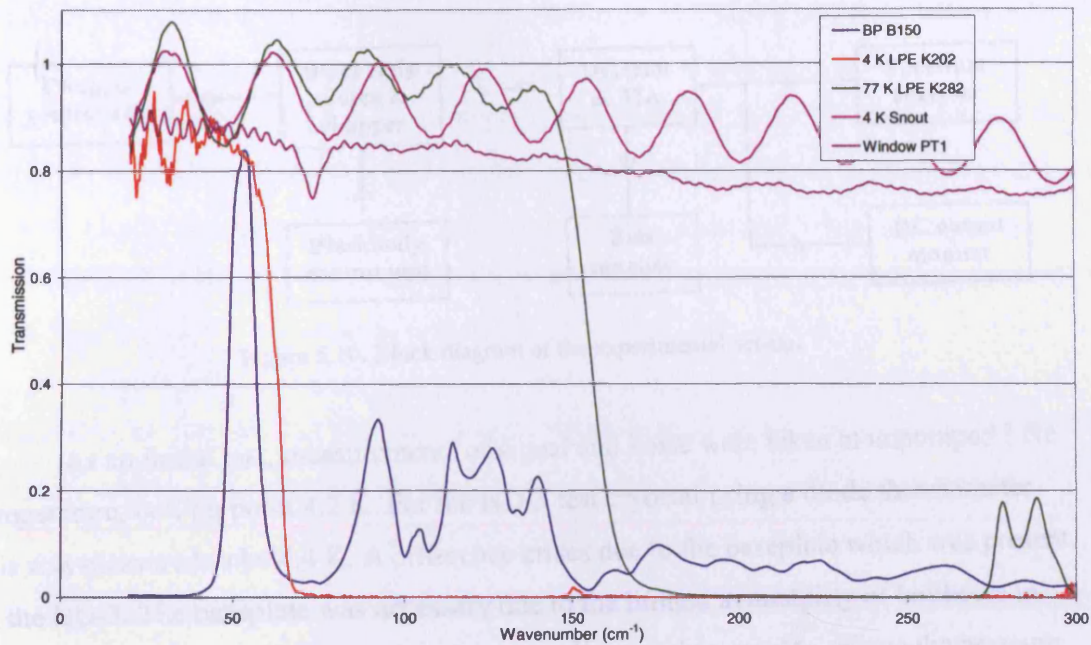


Figure 5.9. Transmission of test filters for prototype detectors.

Figure 5.10 shows a block diagram of the experimental set-up. For the purpose of responsivity measurements an Electro Optical Industries Inc. blackbody emitter (Model WS143), with temperature controller (Model 215B) calibrated for 800 K was used. A Brookdeal Light Chopper 9479 was connected to the blackbody emitter such that a chopped signal of approximately 8 Hz was emitted. Chopper blades were covered with Eccosorb AN74 to limit reflection of radiation from inside the cryostat. The 8 Hz chopping frequency was chosen to emulate the chop frequency of the JCMT secondary mirror. The output from the warm part of the TIA circuit was fed into a Hewlett Packard 35665A Dynamic Signal Analyser (DSA), and a Fluke 8842A multimeter for DC voltage measurements. The spectrum analyser returns the power spectrum of the original output signal from the detector and TIA, providing a plot of signal strength in a given frequency interval.

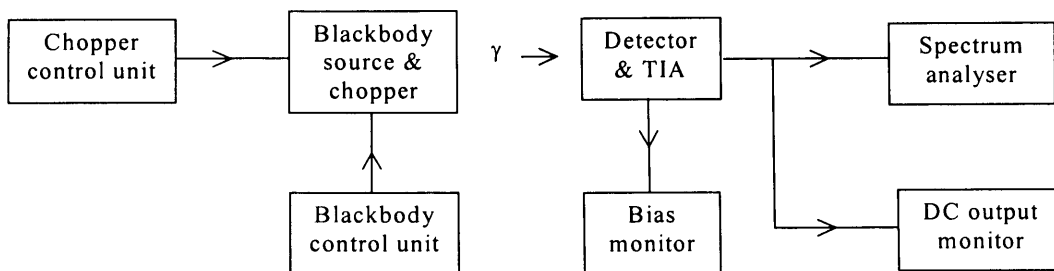


Figure 5.10. Block diagram of the experimental set-up.

As an initial test, measurements of signal and noise were taken at unpumped LHe temperature, boiling point 4.2 K. For the HD-3 test cryostat using a diode thermometer this was measured to be 4.4 K. A difference arises due to the baseplate which was present in the HD-3. The baseplate was necessary due to the limited availability of boltholes in the cold plate surface. The pressure reduction valve was then used to reduce the pressure on the LHe reservoir to obtain a cryostat cold plate temperature of 3.7 K.

For each of the responsivity tests the dewar was placed a known distance, approximately 40 mm, from the blackbody source. The detector's entrance aperture was aligned to the blackbody emitter aperture by moving the dewar and monitoring the DSA signal, in order to maximise the signal. To evaluate the significance of H<sub>2</sub>O vapour in the path between the detector and the blackbody source, N<sub>2</sub> gas was blown between the cryostat window and blackbody whilst signal measurements were recorded. As signal levels were within 1% of each other for both cases it can be assumed that no significant loss due to H<sub>2</sub>O vapour absorption was evident. Water vapour profiles (AFGL midlatitude summer) used in the atmospheric model presented in Chapter 2 predict 14 mm PWV in the lowest km of the atmosphere under the most pessimistic of weather conditions. This equates to a "PWV" of slightly greater than 0.5 μm in a distance of 40 mm at sea level, which is negligible.

The maximum bias that could be applied across the detector before breakdown was determined empirically by increasing the bias voltage whilst observing a corresponding increase in the output signal voltage until the output signal was lost. Over a range of voltages, from zero to just under the maximum, the bias was varied and the corresponding signal observed and averaged over ten measurements. The background



noise level was measured by placing a piece of Eccosorb in front of the cryostat window. The noise was measured over a frequency range of 0 to 100 Hz, averaged over ten samples. This number of averages was sufficient to reliably determine the power spectrum allowing an estimate of the noise voltage ( $\sqrt{\text{Hz}}$ ) at 8 Hz to be made with an accuracy of approximately  $\pm 10\%$ . The signal to noise ratio (SNR) was then calculated for each bias level at 8 Hz and thus the optimum bias voltage could be determined. From the SNR the DQE could then be calculated.

Figure 5.11 shows the responsivity and noise for detector LBL102a at a temperature of 3.7 K. The DQE is shown in Figure 5.12 and within this Figure a peak is clearly visible at 40 mV. This is the point of optimum operating bias for this PC.

Due to the large decrease in dark current, lower operating temperatures provide a detector with an improved DQE. However, at a particular temperature carrier mobility will be curtailed, leading to a falling DQE at temperatures below this point. Figure 5.13 plots DQE as a function of temperature. Each point is given at optimum operating bias for that temperature. Optimum bias increases slightly with decreasing temperature due to the decrease in carrier mobility with decreasing temperature.

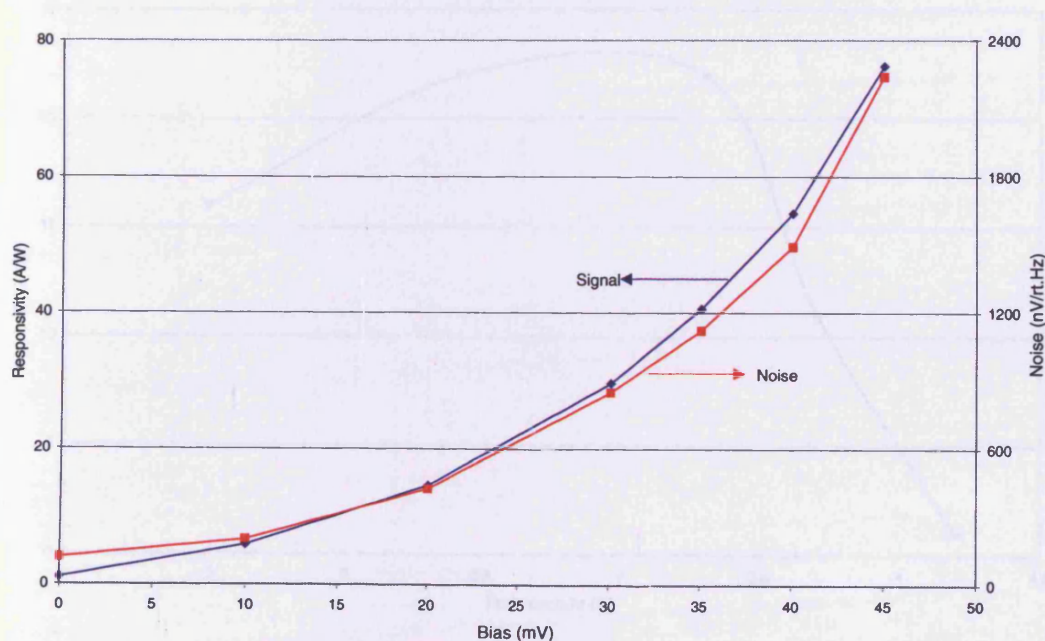


Figure 5.11. Increase of signal and noise with increasing bias for LBL102a. Detector temperature is 3.7 K.

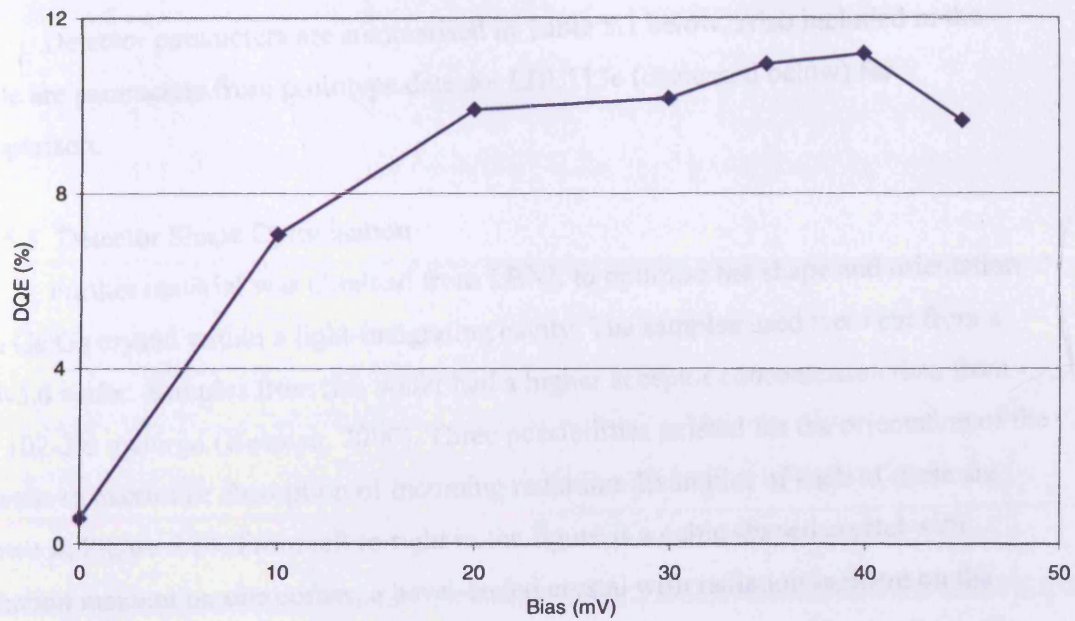


Figure 5.12. DQE of detector LBL102a vs. applied bias voltage. Detector temperature is 3.7 K. Operating bias is taken at the point of maximum DQE.

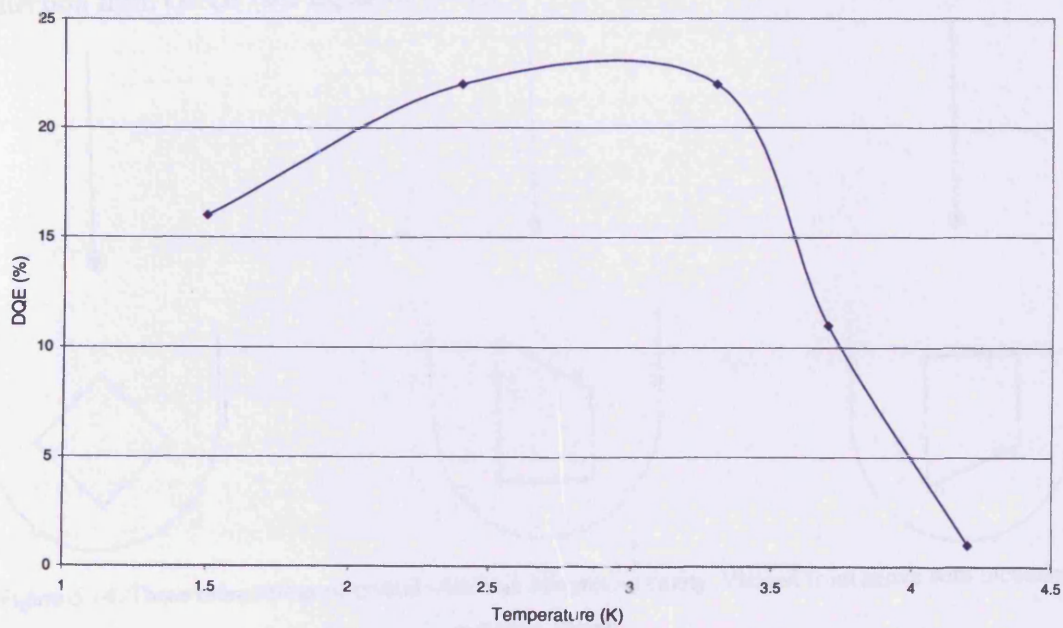


Figure 5.13. Variation of DQE with temperature measured for LBL102a.

Detector parameters are summarised in Table 5.1 below. Also included in the Table are parameters from prototype detector LBL113c (discussed below) for comparison.

### 5.3. Detector Shape Optimisation

Further material was obtained from LBNL to optimise the shape and orientation of a Ge:Ga crystal within a light-integrating cavity. The samples used were cut from a 113-3.6 wafer. Samples from this wafer had a higher acceptor concentration than from the 102-3.6 material (Beeman, 2000). Three possibilities existed for the orientation of the crystals to maximise absorption of incoming radiation. Examples of each of these are shown in Figure 5.14. From left to right in the figure is a cubic shaped crystal with radiation incident on one corner, a bevel-ended crystal with radiation incident on the bevel-end, and a bevel-ended crystal with radiation incident on the end opposite to the bevel-end. The option of using a cubic crystal with a flat face towards the incoming radiation was considered unlikely to yield a high absorption due to the high amount of reflection from Ge:Ga (see Equation 3.11).

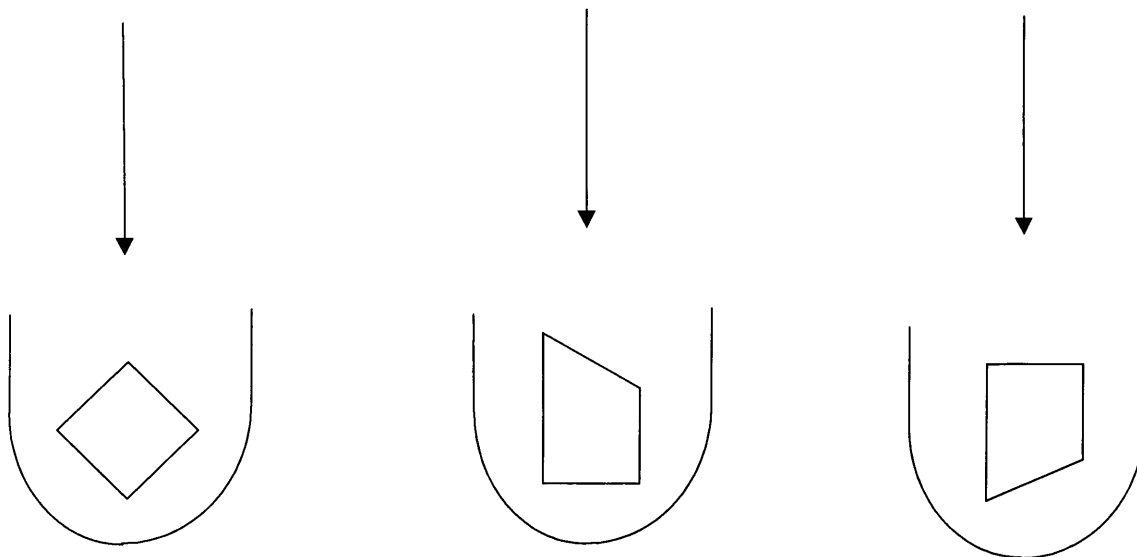


Figure 5.14. Three orientations of crystal within an integrating cavity. Viewed from above with incoming radiation shown.

The three orientations of crystal were each individually mounted, stressed and then tested within the same 4-mm diameter, Au-plated, Cu integrating cavity. Stress was



applied in a direction normal to the plane of the page as viewed in Figure 5.14. The mounting procedure followed that set out in Chapter 3. All crystals were stressed to 40% of their unstressed resistance values. Figure 5.15 shows spectral response measurements for each of the three detectors. The cutoff at  $70\text{ cm}^{-1}$  is due to optical filtering within the cryostat.

The use of a bevel-ended crystal increased the output signal over that of a cubic shaped crystal, with highest signal measured for radiation incident on the bevel-end. Figure 5.16 plots the measured output signal for each of the three orientations and shapes of crystal. However, the difference in signal of less than 10% was too small to attribute to any particular orientation or shape so no definite conclusions can be drawn. Table 5.1 includes some of the main parameters for a bevel-ended prototype crystal LBL113c.

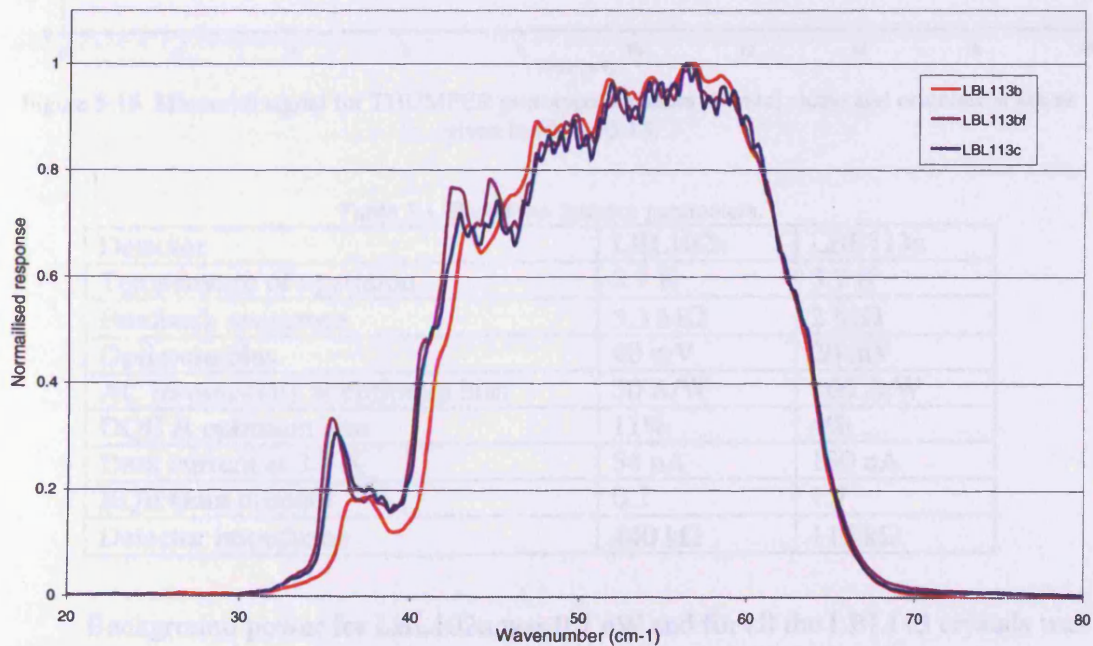


Figure 5.15. Spectral response measurements for THUMPER prototype detectors. The LBL113b refers to a bevel-ended crystal with radiation incident to its bevel-ended face. LBL113bf refers to the same crystal with radiation incident such that the bevel-end is at the back of the cavity. LBL113c is of the same orientation.

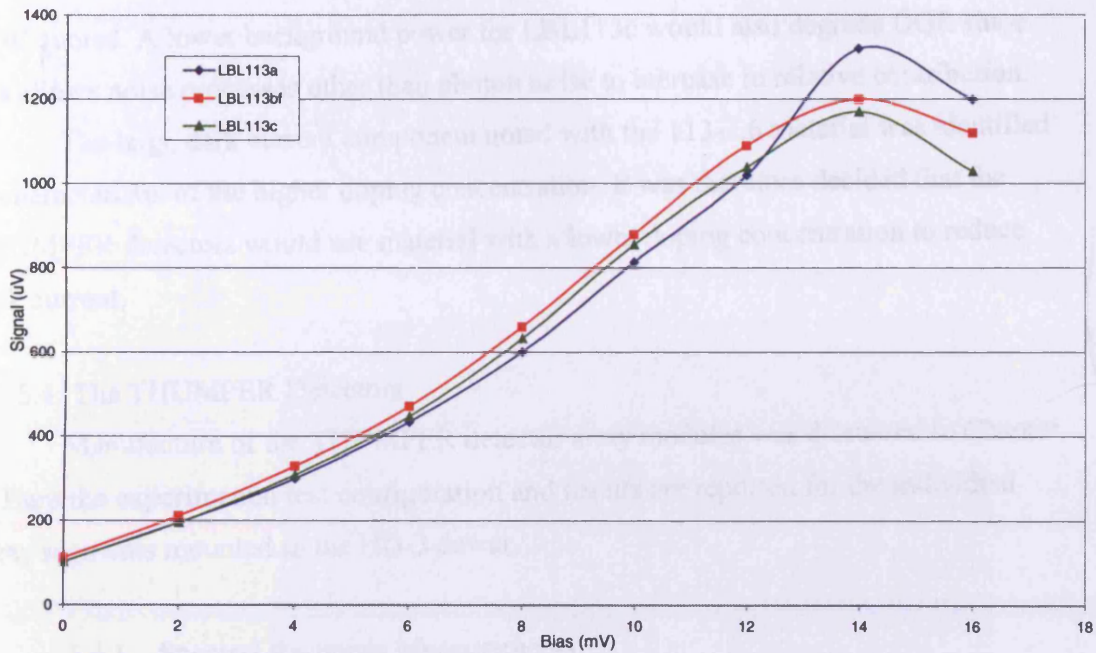


Figure 5.16. Measured signal for THUMPER prototype detectors. Crystal shape and orientation are as given in Figure 5.15.

Table 5.1. Prototype detector parameters.

Detector	LBL102a	LBL113c
Temperature of operation	3.7 K	3.7 K
Feedback resistance	3.3 M $\Omega$	2 M $\Omega$
Optimum bias	40 mV	20 mV
AC responsivity at optimum bias	30 A/W	260 A/W
DQE at optimum bias	11%	4%
Dark current at 3.7 K	54 nA	130 nA
RQE Gain product	0.2	1.7
Detector impedance	440 k $\Omega$	110 k $\Omega$

Background power for LBL102a was 0.7 nW and for all the LBL113 crystals was 0.3 nW, the difference arising due to the width of bandpass filter used. Responsivity was similar for all the LBL113 crystals. Increases in responsivity are large for stressed PCs, values over 100 A/W having been published (Wang *et al.*, 1987), but the values quoted here are greater. Such increases could possibly have been caused by a light leak in the test cryostat, although no such leak could be discerned at time of testing. In Table 5.1, the higher dark current for LBL113c is seen to be the significant factor resulting in the lower

DQE quoted. A lower background power for LBL113c would also degrade DQE since this allows noise processes other than photon noise to increase in relative contribution.

The large dark current component noted with the 113-3.6 material was identified as characteristic of the higher doping concentration. It was therefore decided that the THUMPER detectors would use material with a lower doping concentration to reduce dark current.

#### 5.4. The THUMPER Detectors

Manufacture of the THUMPER detector array modules was discussed in Chapter 3. Here the experimental test configuration and results are reported for the individual array segments mounted in the HD-3 dewar.

##### 5.4.1. Spectral Response Measurements

In order to be able to measure the spectral response of array segments they were stacked horizontally. For the  $1 \times 2$  arrays the two identical blocks were placed side by side. Figure 5.17 shows the position of the blocks in their test location. The snout, on the left-hand side of the image, acts to define the field of view of the detectors. Cu tape between the snout and detector block limits stray light falling on to the detectors. Figure 5.18 shows a schematic of the detectors' cavities, as viewed from the window side of the cryostat. The point equidistant from the centre of all four detector cavities was then aligned as near to the centre of the test dewar's OAH as was possible. A slight offset of up to 5 mm may have existed due to limited availability of mounting blocks and spacers, and in the location of cryostat baseplate holes. A mounting offset implies equal amounts of radiation may not have been incident on all detectors, causing variations in relative output signal responsivity during spectral response measurements.

Signals were read out using a TIA pre-amplifier. The warm part of the circuit had been altered so that bias could be applied to different detectors by operating a switch, instead of re-soldering the warm electronics. Re-soldering would have necessitated switching off the JFET supply voltage since they are prone to damage if soldering takes place whilst they are switched on. This enabled the spectral response of several detectors to be measured in a single cryostat cooldown with a single cold TIA module. Filtering



within the cryostat consisted of a  $320\text{-cm}^{-1}$  LPE on the  $\text{LN}_2$  shield, and a  $200\text{-cm}^{-1}$  LPE within the snout at 4 K. Such a high wavenumber LPE filter ensures the high frequency detector tail-off is discernible.

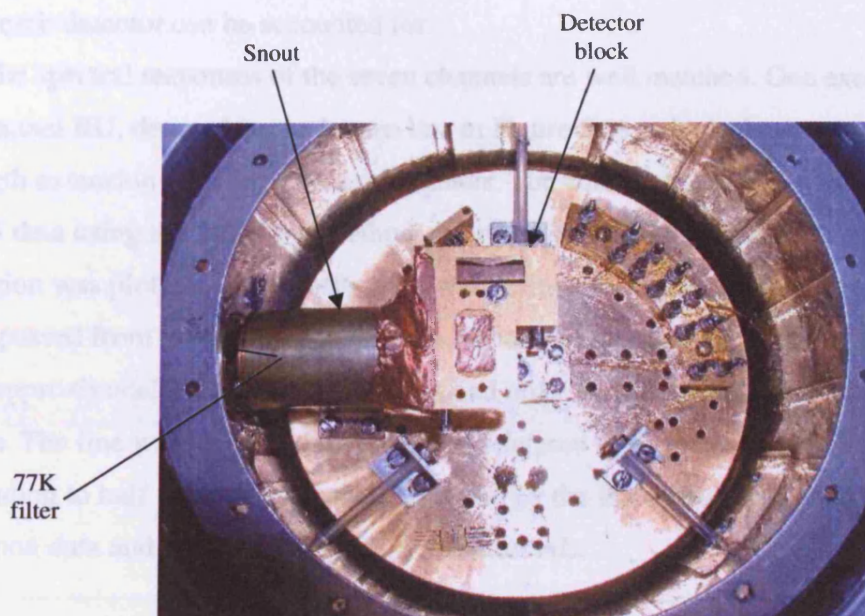


Figure 5.17. Photograph of the two THUMPER side arrays set up for spectral response measurement. Extra Cu tape limits light leaks whilst the snout, here seen on the left, provides the detectors' field of view.

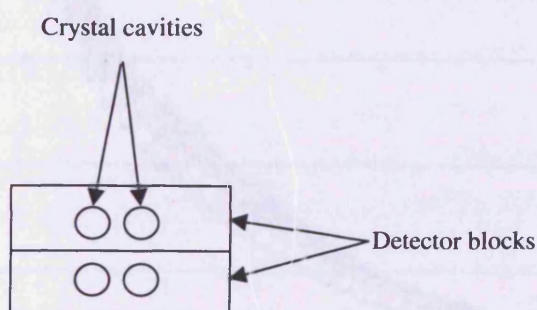


Figure 5.18. Schematic of the front view of the  $1 \times 2$  detector arrays, set up for spectral response measurement.

Figure 5.19 plots the spectral response of the THUMPER detectors, biased at 100 mV. The raw spectra are normally ratioed against background measurements made with a bolometric detector to remove instrumental effects as discussed above. However, for the

THUMPER detectors the spectral region of interest was limited to the narrow region near the long wavelength cutoff. For this reason the transformed data were not ratioed. Data in Figure 5.19 are normalised since it is only the cutoff wavelength that is being determined. Their relative response is best determined by photometric tests below where the physical offset of each detector can be accounted for.

The spectral responses of the seven channels are well matched. One exception to this is channel BU, denoted by the brown line in Figure 5.19, which shows a lower wavelength extension than the other six channels. The cutoff wavelength was determined from FTS data using the following method. A sample of the transformed data around the cutoff region was plotted. The cutoff region was defined to be that frequency in which the response passed from minimum to maximum response. For all seven detectors this was between approximately  $35$  and  $65\text{ cm}^{-1}$ . A second order polynomial line was fitted to these data. The line was examined and the cutoff defined to be that wavenumber corresponding to half maximum response as given by the line. Figure 5.20 plots the cutoff region data and fitted-polynomial for detector AL.

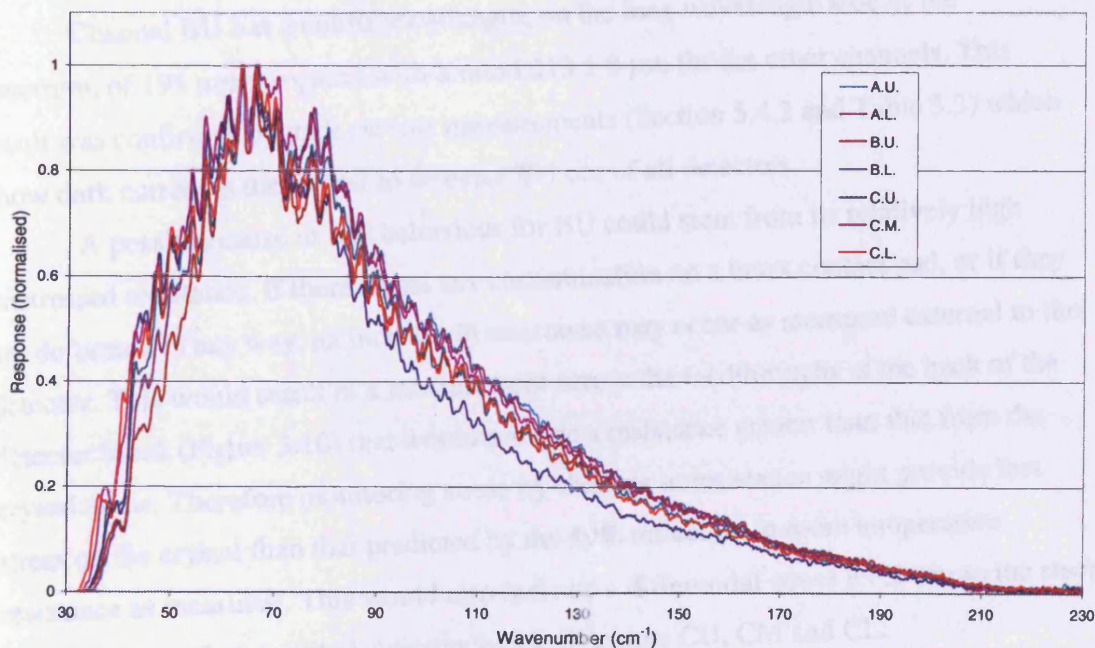


Figure 5.19. Spectral response of the THUMPER detectors.



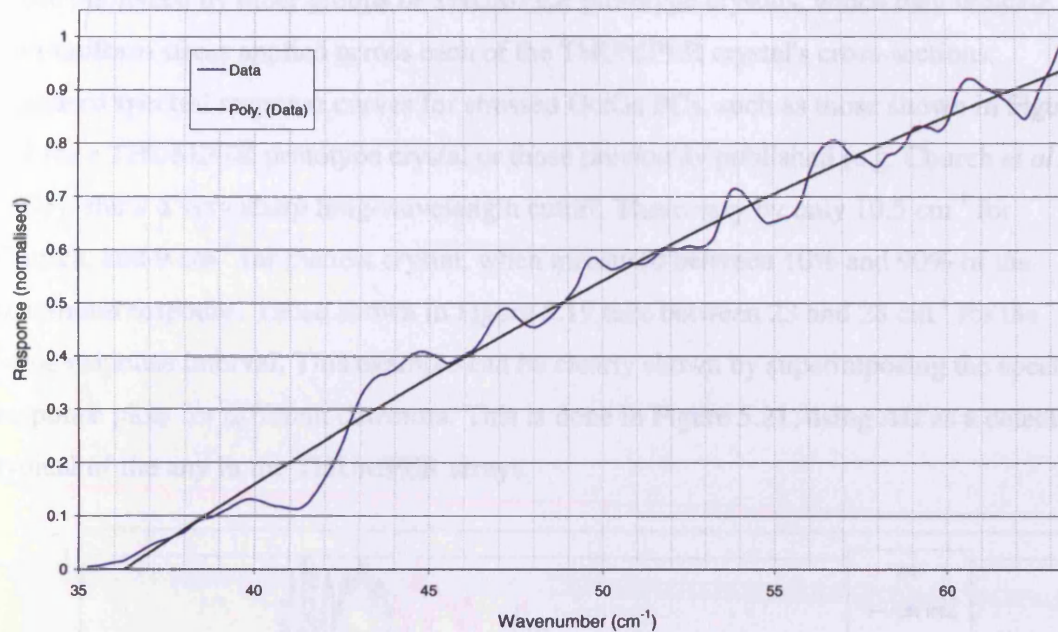


Figure 5.20. Cutoff region in spectrum of detector AL, with fitted polynomial.

Channel BU has a cutoff wavelength, on the long wavelength side of the spectrum, of  $195 \mu\text{m}$  compared with around  $213 \pm 8 \mu\text{m}$  for the other channels. This result was confirmed by dark current measurements (Section 5.4.2 and Table 5.3) which show dark current is the lowest in detector BU out of all detectors.

A possible cause of this behaviour for BU could stem from its relatively high unstressed resistance. If there exists any contamination on a brass contact pad, or if they are deformed in any way, an increase in resistance may occur as measured external to the detector. This would result in a measurement across the feedthroughs at the back of the detector block (Figure 3.10) that would provide a resistance greater than that from the crystal alone. Therefore monitoring stress by changes in resistance might provide less stress on the crystal than that predicted by the 49% reduction in room temperature resistance as measured. This would also indicate a differential stress level across the stack as is evident with the central stressing block, detectors CU, CM and CL.

The particular shape of the spectral response curves in Figure 5.19, at the long wavelength cutoff, suggests the possibility that stress inhomogeneities are present. The gradient around the long wavelength cutoff was less than expected when compared to

those published by other groups or THUMPER prototype crystals, which may indicate a non-uniform stress applied across each of the THUMPER crystal's cross-sections. Standard spectral response curves for stressed Ge:Ga PCs, such as those shown in Figure 5.4 for a THUMPER prototype crystal or those previously published (e.g. Church *et al.*, 1993), show a very sharp long-wavelength cutoff. These vary by only  $10.5 \text{ cm}^{-1}$  for Church, and  $9 \text{ cm}^{-1}$  for the test crystal, when measured between 10% and 90% of the maximum response. Those shown in Figure 5.19 take between 23 and  $28 \text{ cm}^{-1}$  for the same response interval. This example can be clearly shown by superimposing the spectral response plots for different detectors. This is done in Figure 5.21, using AU as a detector typical of the any in the THUMPER arrays.

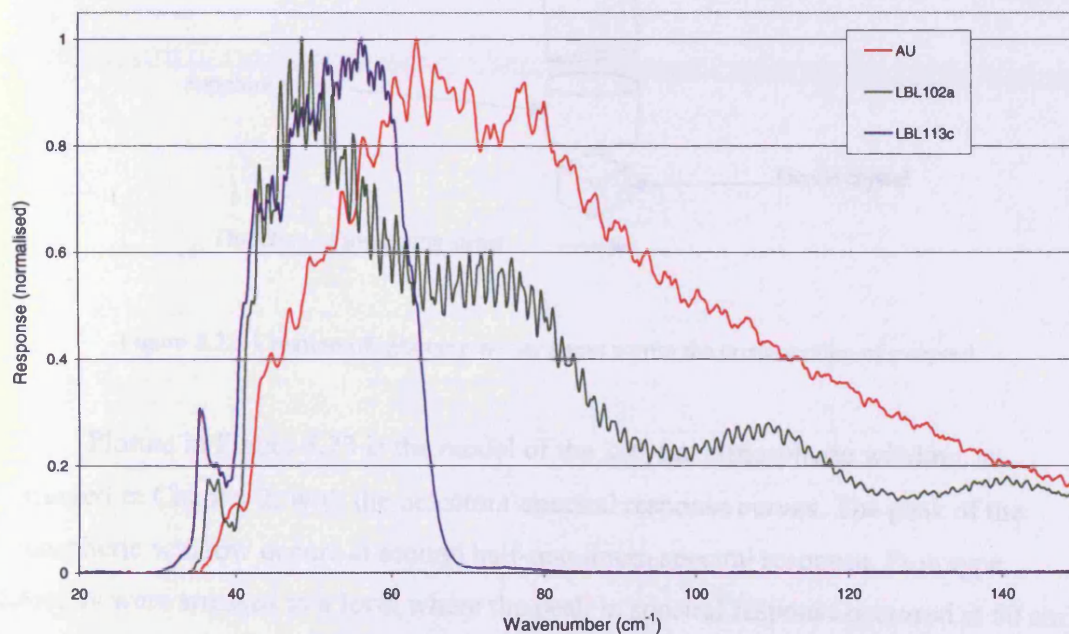


Figure 5.21. Comparison of the spectral responses of three PCs. LBL102a and LBL113c are prototypes, whereas AU is a THUMPER detector.

The stress inconsistency across the crystal cross-section could be caused by a less than perfect dowel finish, with a dowel end that was not perfectly perpendicular to the long-axis of the dowel. A method which overcomes this possible flaw was used in the construction of the PACS instrument for the Herschel mission (Kraft *et al.*, 2000), and is discussed in greater detail below. Alternatively some sticking may have occurred with the

block, for example, between the dowel rod and the stressing block body. If the dowel then rotates, a similarly inhomogeneous application of stress would result. This latter scenario may exist if the dowel rod is not perfectly matched in diameter to the cavity in which it sits. Figure 5.22 represents an image of how stress inhomogeneity would occur caused by a rotating dowel pin. If one end of the rod becomes embedded into the detector block, stress will not be able to pass down the length of the array, causing a differential stress on each of the crystals in one array, as is evident in the central THUMPER detector array.

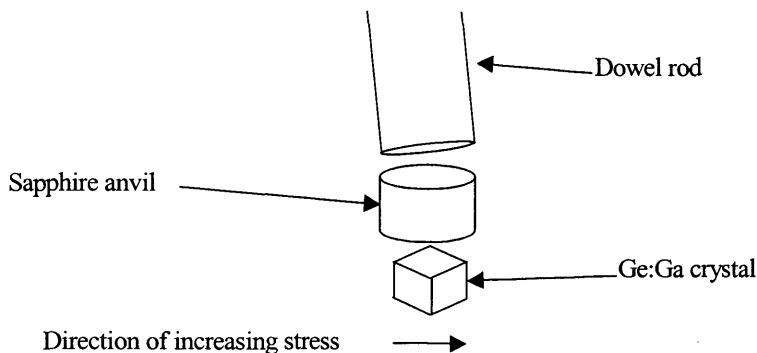


Figure 5.22. Creation of inhomogeneous stress across the cross-section of a crystal.

Plotted in Figure 5.23 is the model of the 200- $\mu\text{m}$  atmospheric window, as discussed in Chapter 2, with the detectors' spectral response curves. The peak of the atmospheric window occurs at around half-maximum spectral response. Prototype detectors were stressed to a level where the peak in spectral response occurred at  $50\text{ cm}^{-1}$ , but such a high stress gave rise to large values of dark current. Dark current accounted for 58% of the total noise of one prototype detector (LBL113c) under background power levels expected at the JCMT. In order to provide a detector with a lower dark current noise contribution, less stress was applied to the detectors for THUMPER compared to the prototypes. Dark current was between 50 and 100 times lower in THUMPER PCs than in the prototype detectors (130 nA for LBL113c). Responsivity was reduced by a factor of two due to the position of the atmospheric window with respect to the peak in spectral response.



Figure 5.24 gives the spectral response, as measured with the FTS, at two different bias levels for THUMPER detector CL. The spectrum recorded at the optimum bias level of around 100 mV is typical of all those measured for the seven THUMPER detector channels at unpumped LHe temperature. An extension of 5  $\mu\text{m}$  is evident in the cutoff wavelength at half-peak response when the bias is increased from 50 to 100 mV. This is in approximate agreement to the 10  $\mu\text{m}$  found by Church *et al.* (1993, Fig. 7) for the ISO highly stressed PC LW5 measured over a similar doubling of bias (measured at half-maximum response, interpolation of the Church *et al.* figure). The THUMPER prototype detectors, see LBL102a in Figure 5.4, also exhibit an increase in response of around 10  $\mu\text{m}$ .

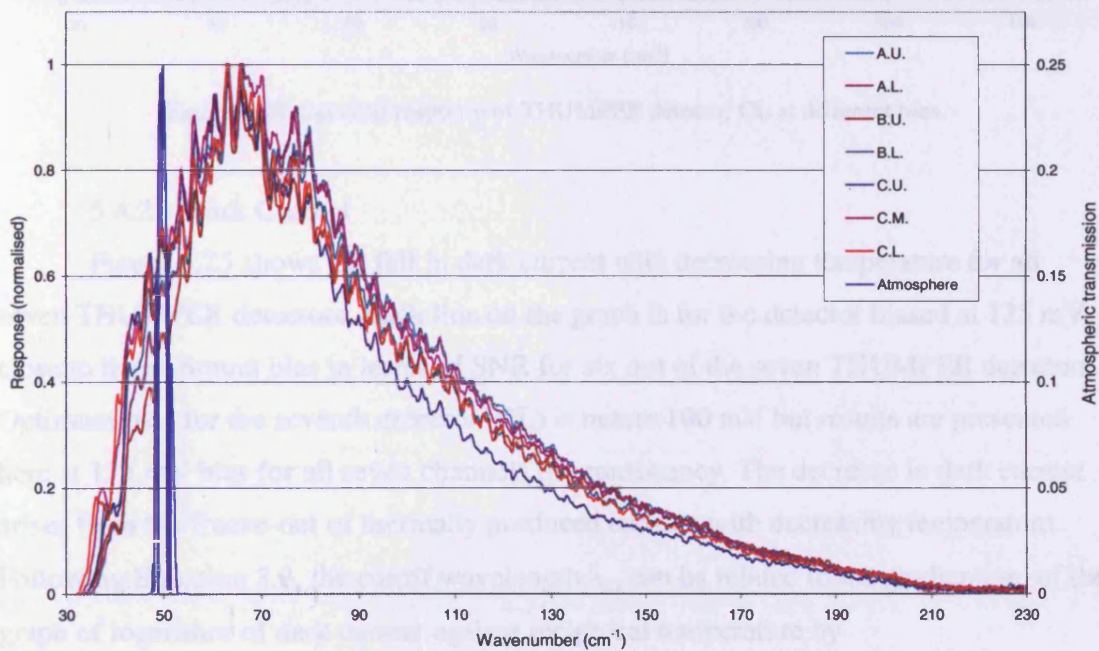


Figure 5.23. Spectral response of the THUMPER detectors as Figure 5.19. Also shown in this Figure is the model of atmospheric transmission, from Chapter 2, with low levels of PWV.



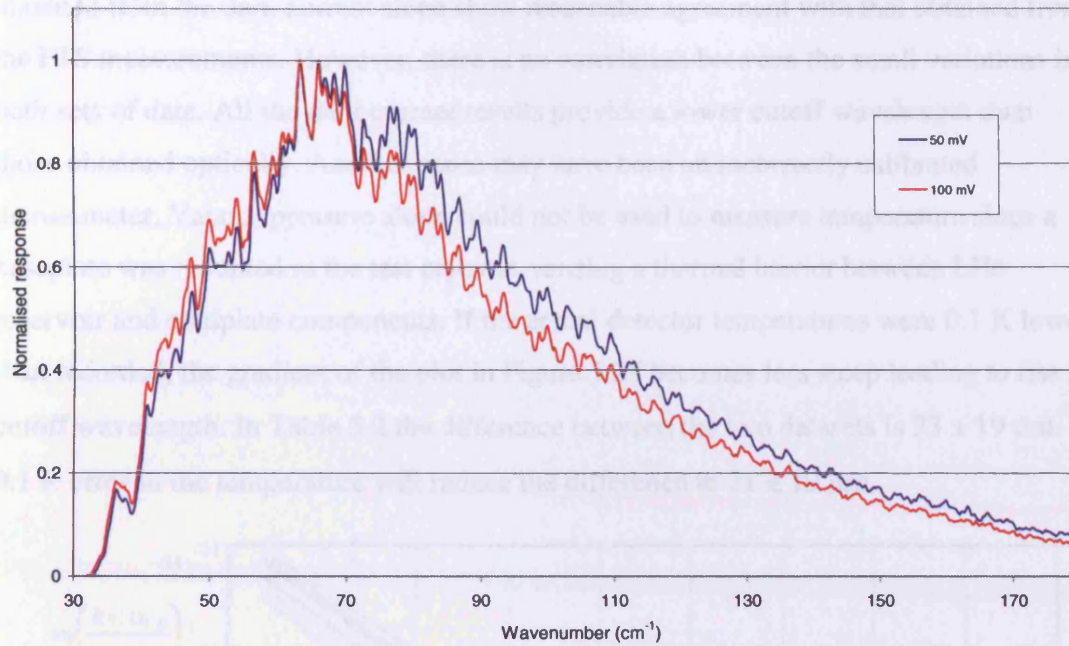


Figure 5.24. Spectral response of THUMPER detector CL at different bias.

#### 5.4.2. Dark Current

Figure 5.25 shows the fall in dark current with decreasing temperature for all seven THUMPER detectors. Each line on the graph is for the detector biased at 125 mV, close to the optimum bias in terms of SNR for six out of the seven THUMPER detectors. Optimum bias for the seventh detector (CL) is nearer 100 mV but results are presented here at 125 mV bias for all seven channels for consistency. The decrease in dark current arises from the freeze-out of thermally produced carriers with decreasing temperature. Following Equation 3.3, the cutoff wavelength  $\lambda_c$ , can be related to the gradient,  $m$ , of the graph of logarithm of dark current against reciprocal temperature by

$$m = \frac{1.24 \cdot q \cdot \log e}{k \cdot \lambda_c} \quad (5.1)$$

where  $q$  is the electronic charge on a free carrier and dark current is in electrons per second.

Table 5.2 compares cutoff wavelength of each of the detectors obtained by FTS with that obtained by dark current measurements. Cutoff wavelength was determined from FTS data following the method described above. Estimates of the cutoff wavelength

obtained from the dark current slope show reasonable agreement with that obtained from the FTS measurements. However, there is no correlation between the small variations in both sets of data. All the dark current results provide a lower cutoff wavelength than those obtained optically. Another cause may have been an incorrectly calibrated thermometer. Vapour pressure alone could not be used to measure temperature since a baseplate was mounted in the test cryostat, causing a thermal barrier between LHe reservoir and coldplate components. If the actual detector temperatures were 0.1 K lower than recorded, the gradient of the plot in Figure 5.25 becomes less steep leading to rise in cutoff wavelength. In Table 5.2 the difference between the two datasets is  $33 \pm 19 \mu\text{m}$ . A 0.1 K error in the temperature will reduce the difference to  $21 \pm 19 \mu\text{m}$ .

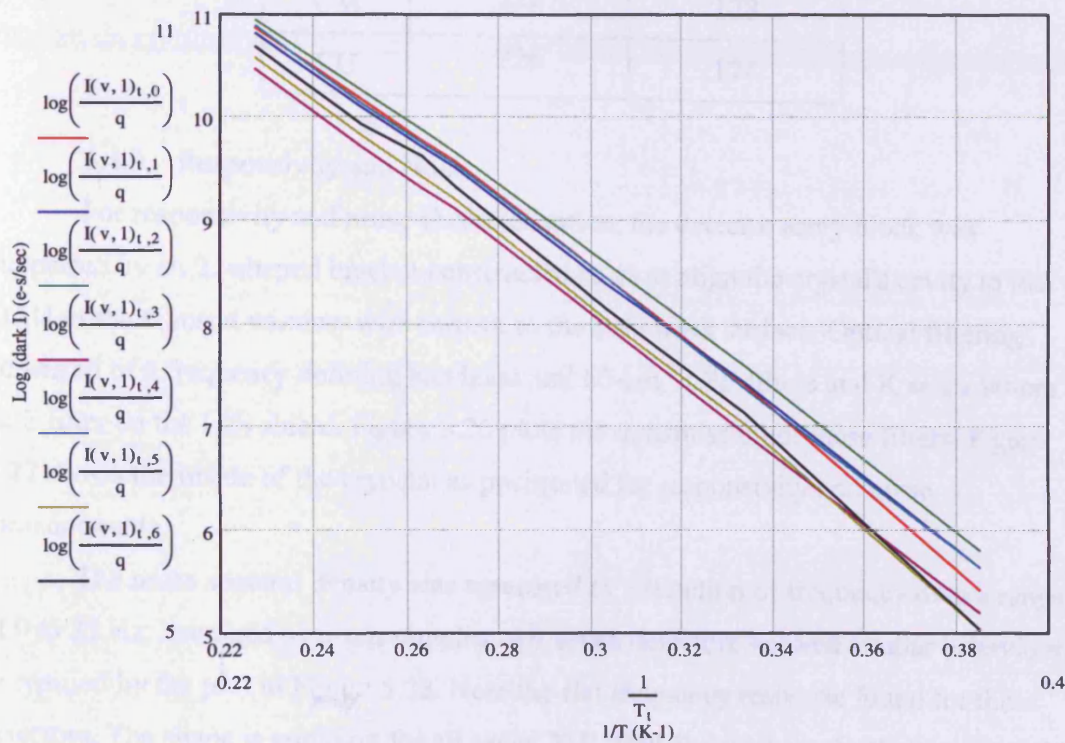


Figure 5.25. Fall in dark current with decreasing temperature.

Table 5.2. Cutoff wavelengths for the THUMPER PCs as determined by FTS and by dark current measurement.

<b>Detector</b>	<b>Cutoff <math>\lambda</math> (FTS)</b>	<b>Cutoff <math>\lambda</math> (dark I)</b>
AL	211	180
AU	222	189
BL	217	191
BU	200	186
CL	224	186
CM	222	178
CU	226	174

#### 5.4.3. Responsivity and Noise

For responsivity and noise characterisation, the detector array-block was supported by an 'L'-shaped bracket constructed so as to align the crystal's cavity to the OAH of the cryostat window with respect to the cold work surface. Optical filtering consisted of a frequency defining bandpass and 60-cm<sup>-1</sup> LPE filters at 4 K and a 90-cm<sup>-1</sup> LPE filter on the LN<sub>2</sub> shield. Figure 5.26 plots the transmission of these filters. Figure 5.27 shows the inside of the cryostat as positioned for responsivity and noise measurements.

The noise spectral density was measured as a function of frequency over a range of 0 to 25 Hz, averaged over ten samples. All seven detectors showed similar behaviour, as typified by the plot in Figure 5.28. Note the flat frequency response found for these detectors. The shape is common for all seven THUMPER detectors. As the electric field across the detector is increased the signal rises. This is non-linear due to responsivity increasing with both carrier mobility and carrier lifetime and both these quantities vary as electric field (Bratt, 1977). Noise increases in a similar manner until breakdown occurs at which point the noise increases dramatically due to impact ionisation of the charge carriers. DQE, proportional to the square of the SNR, peaks at optimum bias, around 125 mV for detector BL. Figures 5.29 and 5.30 show the signal and noise response, and DQE



as a function of bias for one of the THUMPER detectors.

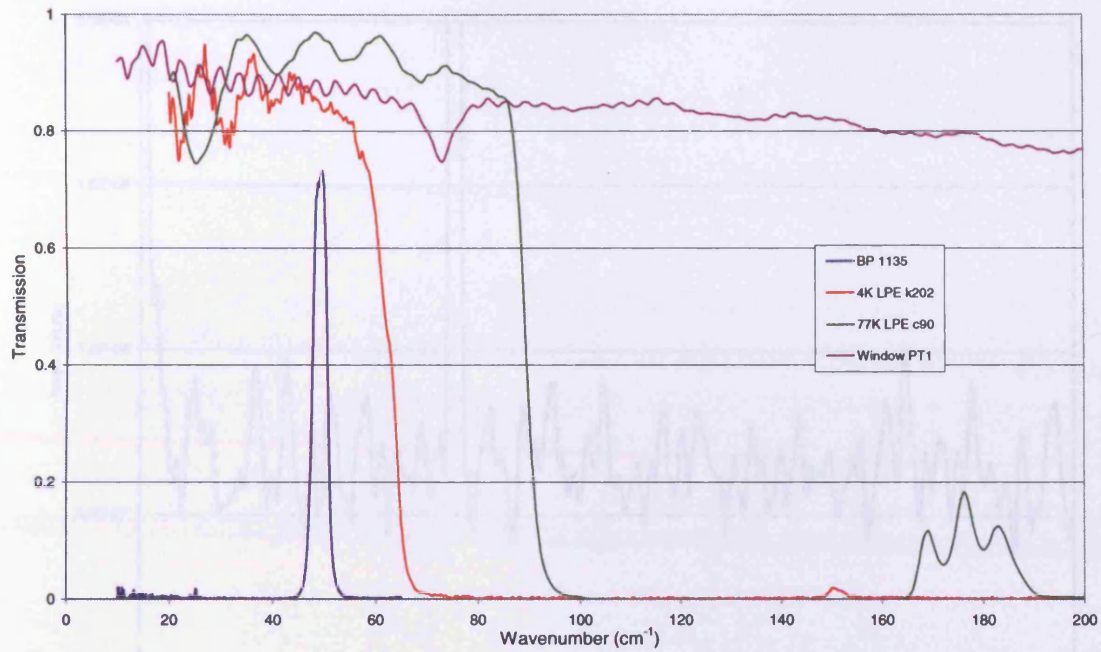


Figure 5.26. Transmission of test filters for THUMPER detectors.

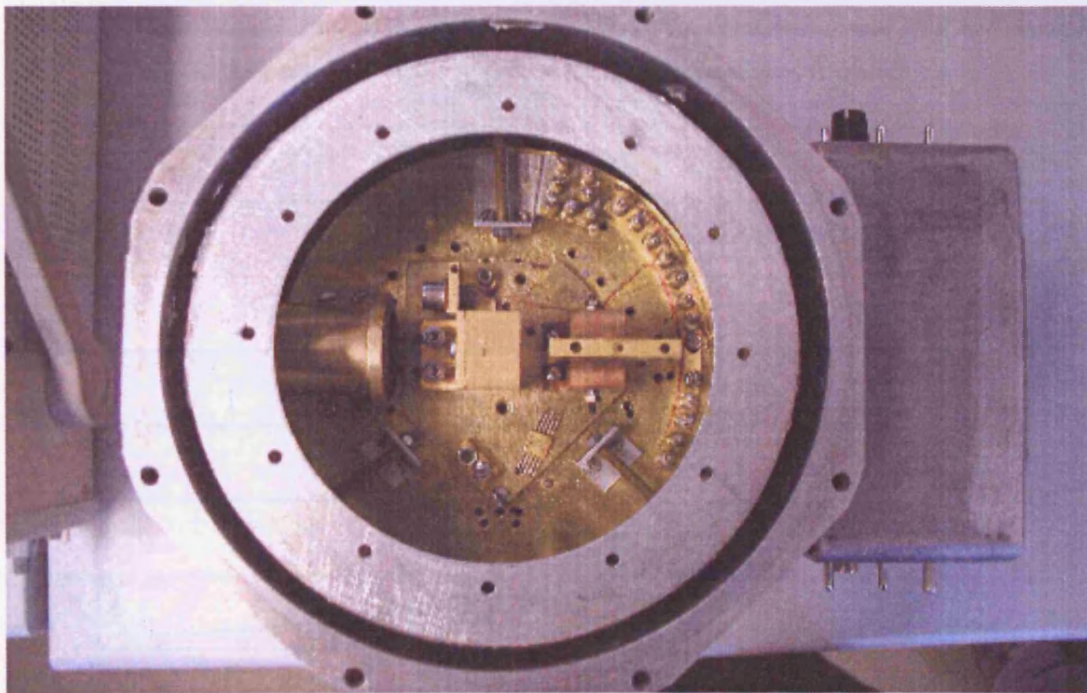


Figure 5.27. Inside of the cryostat as set up for responsivity and noise measurements for the THUMPER detectors.

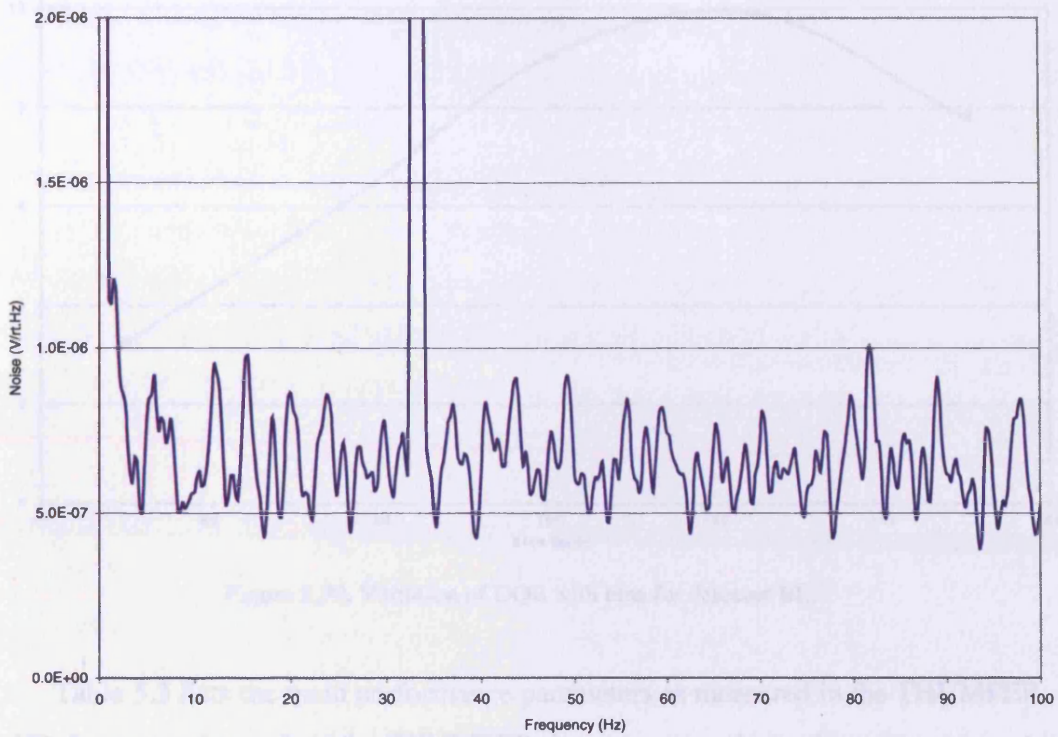


Figure 5.28. Noise spectral density for THUMPER PC AU. Detector temperature was 3.7 K and biased at the optimum level of 125 mV. Note the flat response at low frequency.

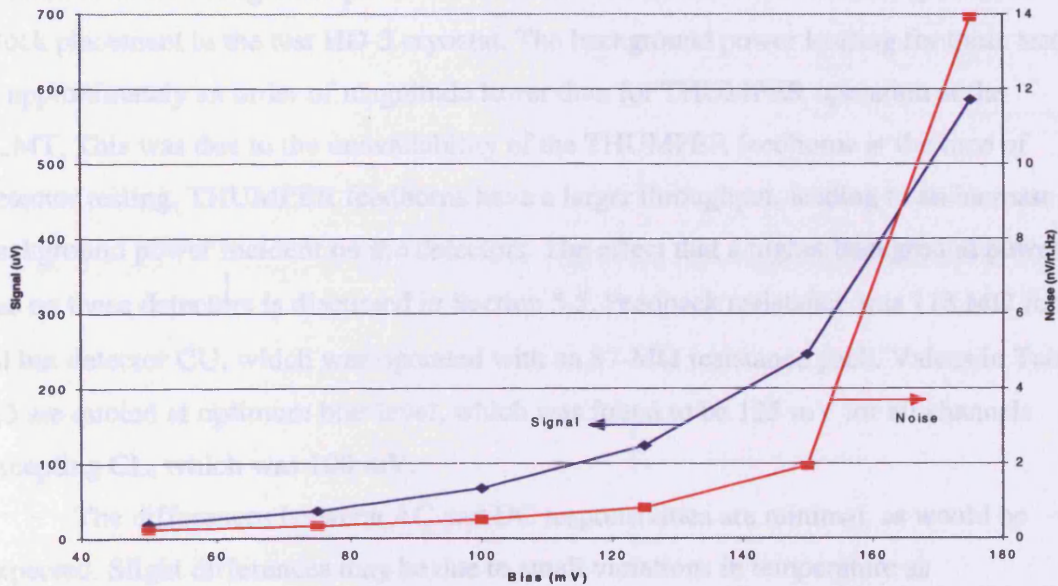


Figure 5.29. Increase of signal and noise with increasing bias for detector BL.



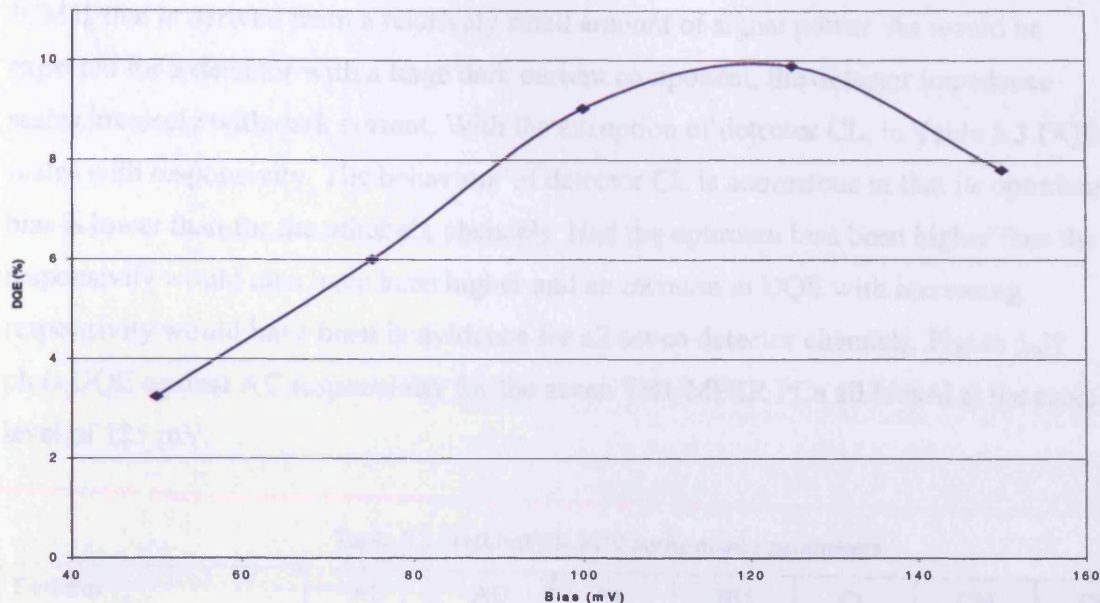


Figure 5.30. Variation of DQE with bias for detector BL.

Table 5.3 lists the main performance parameters as measured in the THUMPER test HD-3 cryostat for each of the THUMPER detectors, at optimum bias. The parameters for each of the tests referred to in the Table were as similar as possible. However, small variations in the background power incident on each detector were caused by detector block placement in the test HD-3 cryostat. The background power loading for these tests is approximately an order of magnitude lower than for THUMPER operation at the JCMT. This was due to the unavailability of the THUMPER feedhorns at the time of detector testing. THUMPER feedhorns have a larger throughput, leading to an increase in background power incident on the detectors. The effect that a higher background power has on these detectors is discussed in Section 5.5. Feedback resistance was  $118\text{ M}\Omega$  for all but detector CU, which was operated with an  $87\text{-M}\Omega$  resistance pack. Values in Table 5.3 are quoted at optimum bias level, which was found to be  $125\text{ mV}$  for all channels excepting CL, which was  $100\text{ mV}$ .

The differences between AC and DC responsivities are minimal, as would be expected. Slight differences may be due to small variations in temperature as measurements were taken. The more important figure of merit between the two is the AC responsivity since this is the quantity, as well as mirroring the secondary chop of the



JCMT, that is derived from a relatively small amount of signal power. As would be expected for a detector with a large dark current component, the detector impedance scales inversely with dark current. With the exception of detector CL, in Table 5.3 DQE scales with responsivity. The behaviour of detector CL is anomalous in that its optimum bias is lower than for the other six channels. Had the optimum bias been higher then the responsivity would also have been higher and an increase in DQE with increasing responsivity would have been in evidence for all seven detector channels. Figure 5.31 plots DQE against AC responsivity for the seven THUMPER PCs all biased at the same level of 125 mV.

Table 5.3. THUMPER PCs' performance parameters.

Detector	AL	AU	BL	BU	CL	CM	CU
DQE (%)	7.1	5.8	9.9	5.8	9.8	7.6	12
AC responsivity (A/W)	0.98	0.88	1.3	0.70	0.85	0.95	1.4
DC responsivity (A/W)	1.0	0.82	1.2	0.51	0.77	0.99	1.4
NEP (fW/ $\sqrt{\text{Hz}}$ )	6.6	6.6	5.4	6.6	5.7	6.6	5.4
Background power (pW)	270	220	250	220	280	290	310
Chopped signal power (fW)	800	730	780	730	730	740	850
Dark current (pA)	340	260	560	200	370	510	580
Background photocurrent (pA)	270	180	300	100	210	280	420
Impedance (M $\Omega$ )	210	290	150	410	170	160	130

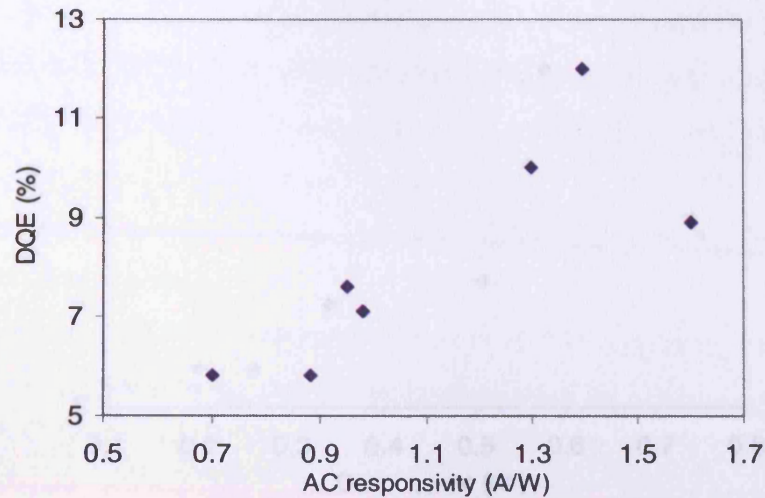


Figure 5.31. Scatter graph of DQE against AC responsivity.

DQE scales approximately with dark current for detectors biased at the same level, a scatter graph of which is plotted in Figure 5.32 for all detectors biased at 125 mV. The exception to this is again detector CL, the data point to the far right in Figure 5.32, which was stressed the most. A higher dark current is indicative of either a greater amount of stress on the crystal, or a higher impurity concentration. A greater amount of stress would lead to an increase in carrier mobility (Léotin *et al.*, 1985; Haller, 1994) since effective mass of the charge carrying holes is decreased with stress. However, a higher impurity concentration might lead to a higher amount of absorption by the crystal. Either, or both, of these scenarios would give a higher value of responsivity as is measured for the detectors with higher dark current.

The overall low values of responsivity are likely to be caused by the varying amount of stress over each of the crystals' cross-section. The variation has caused only a fraction of each of the crystals' volumes to be stressed to a level high enough for that part of the crystal to become responsive to 200- $\mu\text{m}$  radiation. This would also cause dark current values to be lower in the THUMPER detectors.

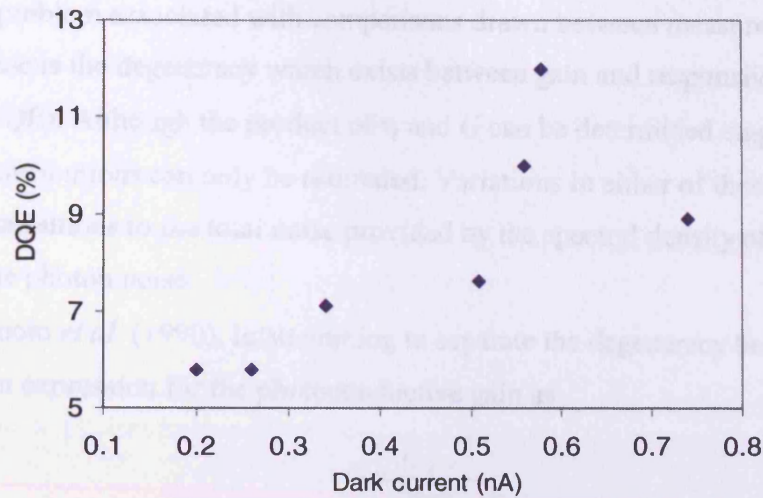


Figure 5.32. Scatter graph of DQE against dark current.

#### 5.4.4. Noise Performance

By modelling the sum of individual components of the noise, predictions can be made and comparisons drawn between measured and modelled noise. Measurements of the total noise of detector-and-associated electronics were therefore recorded.

A noise model has been developed and is applicable to all detectors. Contributions within the model are from the noise sources presented in Chapter 3. The total noise of the detector plus amplifier is given by

$$i_{n,T} = \sqrt{\left\{ \frac{e_{n(\text{FET})} [1 + j\omega R_f (C_f + C_d)]}{R_f} \right\}^2 + i_n^2 + \frac{4kT}{R_f} + \frac{4kT}{R_d} + \frac{4R_f^2 Ph\nu}{\eta} \left( 1 + \frac{\eta t_{fil}}{e^{\frac{h\nu}{kT}} - 1} \right)}. \quad (5.2)$$

Equation 5.2 is that noise modelled by Luinge *et al.* (1980) with the additional photon-wave and detector-Johnson noise terms.

Conditions are for one detector under test conditions as described above. Parameters have therefore been given as in the test set-up. Since the THUMPER detectors show very little evidence of  $\frac{1}{f}$  noise no term has been included to account for this particular noise source.

One problem associated with comparisons drawn between measured and modelled noise is the degeneracy which exists between gain and responsive quantum efficiency (RQE). Although the product of  $\eta$  and  $G$  can be determined empirically, their individual contributions can only be estimated. Variations in either of these parameters can alter contributions to the total noise provided by the spectral density of dark current and that of the photon noise.

Hiramoto *et al.* (1990), in attempting to separate the degeneracy between  $\eta$  and  $G$ , arrive at an expression for the photoconductive gain as

$$G = \frac{i_{n,g-r}^2}{4qI_d} . \quad (5.3)$$

The noise spectral density of current caused by generation-recombination of free charge carriers,  $i_{n,g-r}^2$ , can be determined by measuring the noise spectral density of detector plus electronics and subtracting from this the noise spectral density of the same system with zero bias applied. Thus Hiramoto's method relies purely on experimental method. One problem with this approach is that there must be absolutely no excess noise present when measurements are taken. Since there does appear to be a discrepancy between modelled and measured noise for the THUMPER detectors, whereby modelled noise is around 30% lower than that value measured, similar analysis cannot be performed here. The differences between measured and modelled values are discussed in greater detail below.

Table 5.4 shows the total value of noise measured at optimum bias for each of the seven THUMPER PCs. Also given are modelled values. The main assumption made in the model was that the RQE was twice the measured DQE. Such an assumption was necessary in order to match modelled with measured data as closely as possible. In the model both dark and photo-currents have a gain dependence whereas only the photo-current is a function of the RQE. For a lower value of RQE, gain must be greater in order for modelled current responsivity to match measured values. In this way the total noise, as modelled, is maximised thus matching modelled and measured data as closely as possible. Using the noise model developed in Chapter 3 it is possible to model a noise value for detector and amplifier to within 5% of the measured noise. However, in order to

match modelled and measured values the assumed RQE in the model must be given a value equal to the measured DQE. Since there exist noise terms comparable in magnitude to the photon noise, such as the thermal noise of the feedback resistor, it must be concluded that the DQE must be smaller than the RQE. The RQE is always greater than the DQE, since DQE accounts for photon absorption as well as other noise sources. Therefore there must exist an excess noise component unaccounted for in the model used here.

Table 5.4. Measured and modelled noise of THUMPER PCs at optimum bias.

Detector	Noise (nV/ $\sqrt{\text{Hz}}$ )	
	Measured	Modelled
AL	760	550
AU	690	490
BL	860	690
BU	540	400
CL	570	460
CM	720	600
CU	660	500

Taking detector AL as an example, if the RQE is made equal to the DQE (7%), then a modelled noise of 740 nV/ $\sqrt{\text{Hz}}$  is obtained. However, photon noise is only three times greater than the thermal noise of the feedback resistor in this case, the magnitude of which is important.

Figure 5.33 shows a breakdown of the total noise into its respective parts for THUMPER PC AU, again as modelled following the analysis of Luinge *et al.* (1980). Relative contributions to the total noise are typical for any of the THUMPER PCs. In addition to the modelled noise contributions a large component of extra noise exists in experimental measurements adding a further 25% to 40% to the modelled noise.



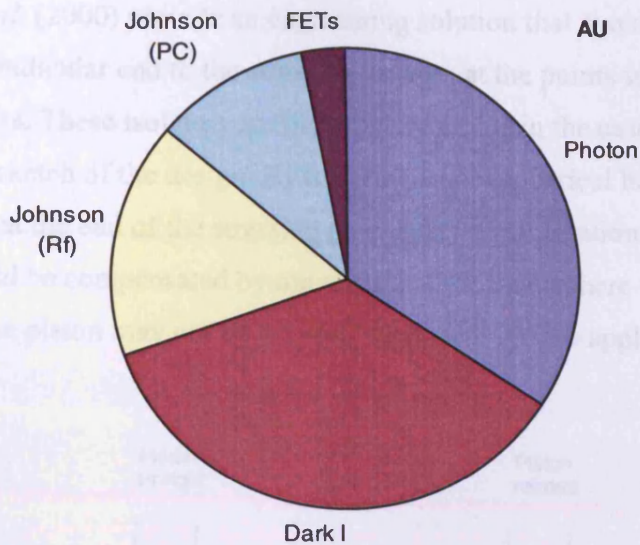


Figure 5.33. Pie chart of noise contributions.

### 5.5. Operation of Detectors in THUMPER Cryostat

Operation of the THUMPER detectors with feedhorns would be expected to improve detector performance due to the increased number of photons giving rise to a relatively larger photon noise contribution. Such a case diminishes the relative contribution to the total noise played by the dark current.

Background power for the initial THUMPER detector tests performed in the HD-3 cryostat was in the region 200 to 300 pW. Background for the detectors in the TK-1865 cryostat will be around 2 nW creating a boost in photon noise by a factor of around three, assuming identical bias values.

### 5.6. Detector Block Upgrades

As indicated in Section 5.4.1, improvements could be made to the components comprising the stressing assembly. The need for the improvements has been caused by the lack of uniformity in the stress applied across the cross-section of the Ge:Ga crystals. The most simple of changes would be in matching the size of stressing piston to exactly the same diameter as the cavity in which these pistons are housed. The, however slight, smaller piston diameter now in existence leaves open the risk of the piston rotating, as shown in Figure 5.21.



Kraft *et al.* (2000) provide an engineering solution that avoids the requirement of a perfectly perpendicular end to the stressing pistons, at the points where they meet the electrical isolators. These isolators are the sapphire anvils in the case of THUMPER. Figure 5.34 is a sketch of the design. By inserting a hemispherical bearing into a matching cavity at the end of the stressing piston, any small rotation of the piston about the vertical would be compensated by movement of the hemisphere within its cavity. Thus although the piston may not be vertical, stress will still be applied in a vertical direction.

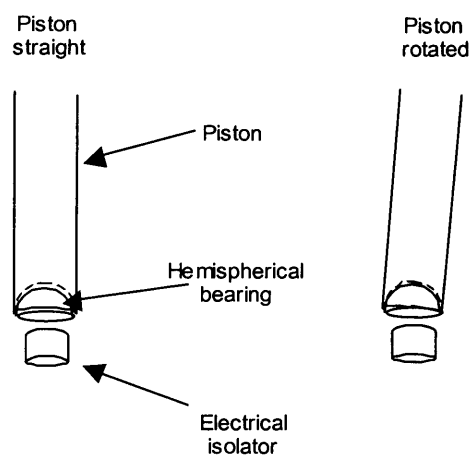


Figure 5.34. Alternative stressing piston for THUMPER.

The possibility exists that the low responsivity evident through testing of the THUMPER detectors is caused by the large feedthrough-holes, towards the rear of the crystal cavities. These were originally incorporated in the design as it was envisaged that larger feedthrough components would be used for electrical conductivity, as was incorporated in the SAFIRE-A prototype detector housings. If the design of the stressing blocks were to be revised, a boost in photon absorption could be made by narrowing the feedthrough-holes to more closely match the feedthrough-wire diameter. The benefit of constructing prototype detector housings cannot therefore be understated.

## 5.7. Summary

Two types of prototype crystal, and three arrays of detectors have been tested for spectral response, dark current, current responsivity and noise. Test results of the

prototypes have led to a definition of parameters for the arrays. Results of the arrays tests strongly imply there exists an inhomogeneous stress across the cross-section of each of the crystals. Although this results in a beneficial low measurement of dark current, an additional characteristic is the low responsivity. Noise of the detectors has been modelled and found to agree with measured values to within 30%.

#### 5.8. References

- Beeman, J.W., 2000, Private Communication, Lawrence Berkeley National Laboratory, USA.
- Bell, R.J., 1972, *Introductory Fourier Transform Spectroscopy*, Academic Press, New York.
- Bratt, P.R., 1977, in *Semiconductors and Semimetals Vol. 12* (eds. Willardson, R.K. & Beer, A.C.) (Academic Press: New York).
- Church, S.E., Griffin, M.J., Price, M.C., Ade, P.A.R., Emery, R.J. & Swinyard, B.M., 1993, *Calibration and Performance of Doped-Ge Photoconductors for the ISO Long Wavelength Spectrometer*, *Infrared Phys.*, **34**, (4), 389-406.
- Haller, E.E., 1994, *Advanced Far-Infrared Detectors*, *Infrared Phys. Technol.*, **35**, (2-3), 127-146.
- Hiromoto, N., Saito, M. & Okuda, H., 1990, *Ge:Ga Far-Infrared Photoconductor with Low Compensation*, *Jpn. J. Appl. Phys.*, **29**, (9), 1739-1744.
- Kraft, S., Frenzl, O., Charlier, O., Cronje, T., Katterloher, R.O., Rosenthal, D., Groezinger, U. & Beeman, J.W., 2000, *FIRST-PACS: design and performance of the sensor engineering models*, *Proc. SPIE, UV, Optical, and IR Space Telescopes and Instruments*, **4013**, 233-243.
- Léotin, J., Laverny, C., Goiran, M., Askenazy, S. & Birch, J.R., 1985, *A Stress Tunable Gallium Doped Germanium Infrared Detector System*, *Internat. J. Infrared Millimeter Waves*, **6**, (5), 323-337.
- Luinge, W., Wildeman, K.J. & van Duinen, R.J., 1980, *Evaluation of Si:As Photoconductive Detectors for Infrared Astronomy*, *Infrared Phys.*, **20**, 30-52.
- Martin, D.H., 1982, *Polarizing (Martin-Puplett) Interferometric Spectrometers for the*

*Near- and Submillimeter Spectra*, Infrared and Millimeter Waves, vol. 6,  
Academic Press.

Martin, D.H. & Puplett, E., 1970, *Polarised Interferometric Spectrometry for the  
Millimetre and Submillimetre Spectrum*, Infrared Phys., **10**, (2), 105-109.

Wang, J.-Q., Richards, P.L., Beeman, J.W. & Haller, E.E., 1987, *Stressed  
Photoconductive Detector for Far-Infrared Space Applications*, Appl. Opt., **26**,  
(22), 4767-4771.

## Chapter 6 THUMPER Commissioning

### 6.1. Introduction

Once commissioned, THUMPER will be used with SCUBA to provide 200- $\mu\text{m}$  imaging which will be coincident with the seven central pixels in the 450- $\mu\text{m}$  array. Therefore like SCUBA it will also become a common user instrument. The commencement of commissioning is due in 2004. Initially, instrument performance will be monitored to ensure THUMPER meets with the sensitivity requirements specified for the JCMT site. These tests will be performed during daylight shifts to ensure that prime observing time with SCUBA is not lost. Nighttime commissioning and observations can then begin.

This chapter provides an estimate of THUMPER's expected astronomical point source sensitivity at the JCMT and other FIR observing sites determined from atmospheric models and telescope efficiency assumptions. Attempts to correlate atmospheric opacity at 1500 GHz with that measured by the local sky opacity monitor at 225 GHz are also discussed. The key parameters to measure during the commissioning period are listed and appropriate calibration sources identified along with their availability at a given juncture.

### 6.2. SURF and Data Analysis

The SCUBA User Reduction Facility (SURF) (Jenness & Lightfoot, 2000) is a software package used for reducing SCUBA data. Its purpose is to remove instrument dependent effects, such as relative differences in pixel responsivity. THUMPER data will also be reduced using SURF. Since THUMPER operates using identical mapping modes to SCUBA, it will appear as a sub-instrument. The 450 and 850- $\mu\text{m}$  arrays of SCUBA already appear as sub-instruments. Some differences will arise in reducing THUMPER data, however, due to differences in beamshape and flat fielding values.

Privett *et al.* (1998) provide access to the brightness temperature of five of the planets: Mars, Jupiter, Saturn, Uranus and Neptune through the software package FLUXES. The primary calibrator is Mars with the brightness temperatures of all the other

planets being referenced to Mars. The Martian atmosphere is very tenuous and is nearly completely transparent throughout the FIR/submillimetre region. Its surface has a high emissivity with virtually no spectral structure. Apart from the occasional dust storm it is therefore a very predictable flux source at these wavelengths. Also listed in the FLUXES program are the positions of all planets, the Sun and the Moon. Flux densities and brightness temperatures are provided at the SCUBA wavelengths for the five above-mentioned planets.

SCUBA calibration can be performed with SURF using the FLUXES package. However, for the new channels at 200- $\mu\text{m}$  the beam parameters and telescope efficiency parameters will need to be determined experimentally before they can be input into SURF for each of the planets. Only once this has been done will THUMPER become a true common-user instrument. This Chapter describes the work to be done.

### 6.3. Modelled in-the-Field Performance of THUMPER

Observing sites have been chosen for use in FIR astronomy due to their superior atmospheric transmission, compared to other sites, in the wavelengths of interest. The three best ground based observing sites, in terms of atmospheric transmission at 200  $\mu\text{m}$ , are Mauna Kea, Hawaii; the Atacama plain in Northern Chile; and the South Pole. The transmission through the atmosphere of 200- $\mu\text{m}$  radiation with varying amounts of PWV has been fully discussed in Chapter 2. Here a description of how transmission through the atmosphere will affect the sensitivity of THUMPER is examined.

A photometric model has been developed to characterise the performance of THUMPER in terms of the NEFD at the JCMT and other sites. The NEFD is the incident flux density that would give unity SNR in a 1-Hz PDBW. It is calculated by dividing the detector NEP by the optical efficiency of the various factors between the detector and source. These consist of the optical filters and cryostat window transmissions, coupling of warm and cold optics, Ruze efficiency of the JCMT primary mirror as a function of its surface accuracy, transmission through the telescope's Gore-tex screen, and transmission through the atmosphere. Some of these factors are not accurately known, for example the rms surface accuracy of the JCMT primary mirror, and the atmospheric transmission. The photometric model is presented in full in Appendix A.

NEFD can be estimated as a function of both AM and of PWV, since both of these variables contribute an attenuation of atmospheric transmission. Table 6.1 presents modelled estimates of the NEFD for the JCMT if a JCMT-type system were present at each of the three top infrared observing sites. Results of modelling are presented for both zenith and 1.3 AM observations. Also included in Table 6.1 are the lower quartile measurements of PWV for the same three sites (Stark *et al.*, 2001, reference therein). The South Pole data comes from radiosonde measurements whilst Chajnantor and Mauna Kea data are computed from  $\tau_{225}$  data. Stark *et al.* (2001) point out that the PWV- $\tau_{225}$  relationship may overestimate PWV by about 12% at Mauna Kea and Chajnantor. This is due to a linear form relating  $\tau_{225}$  with PWV (Masson, 1994) for these sites whereas a 2<sup>nd</sup> order power law (Pardo *et al.*, 2001) is used for the South Pole resulting in a more realistic fit.

Table 6.1. Lower quartile measurements of PWV, and estimates of NEFD for a JCMT system under conditions of that value of PWV, at various FIR observing sites.

Site	PWV (mm)	Predicted NEFD for (Jy/ $\sqrt{\text{Hz}}$ )	
		Zenith	1.3 AM
Mauna Kea	1.05	520	3200
Chajnantor	0.68	84	300
South Pole	0.19	2.5	3.5

#### 6.4. Calibration

The target for absolute calibration is 30%. That is to say absolute flux values will be quoted to an accuracy of  $\pm 30\%$ . It may take up to the first year of observing, during which 50% or more of observing time is expected to be used for calibration, to achieve such accuracy.

Calibration at 200  $\mu\text{m}$  is expected to be extremely difficult because of sky noise. Sky noise is caused by spatial and temporal fluctuations in the emissivity of the atmosphere along the telescope's line of site (Jenness *et al.*, 1998). This is increased at



200  $\mu\text{m}$ , compared to the SCUBA windows, due to the lower transmission and hence higher emission at this shorter wavelength window. The strong correlation in opacity between the 450 and 850- $\mu\text{m}$  windows has already been established (Jenness *et al.*, 1998). Our model fitting with FTS data shows that this should extend to the 200- $\mu\text{m}$  waveband. Significant tracking of the planets will also be needed to calibrate the relation between sky opacity at 200  $\mu\text{m}$  and that at longer wavelengths. By the time THUMPER comes online, there will exist a water vapour radiometer operating at 183 GHz, working in the line-of-sight, running continuously. It is hoped that this can be used to correlate the 450 and 850- $\mu\text{m}$  channels of SCUBA with the 200- $\mu\text{m}$  channel of THUMPER.

Many of the initial observations made by THUMPER will be for calibration purposes. Sky dips are thought to be of little or no use at 200  $\mu\text{m}$  due to variations in sky temperature between zenith and horizon at this wavelength being too small to measure. Small variations are caused by the high emissivity at low atmospheric transmission windows.

Point sources, or extended sources smaller than 14", will only appear in only the central pixel of THUMPER. In such instances the outer pixels can be used to remove sky fluctuations. A similar system is in use with SCUBA (Jenness *et al.*, 1998).

#### 6.4.1. Planets as Calibrators

Planetary brightness temperatures are provided by observations carried out by Griffin *et al.* (1986), Orton *et al.* (1986) and Griffin & Orton (1993). The Martian brightness temperature is calculated based on the model developed by Wright (1976) but updated to provide flux estimates beyond JD 2450000.5 (19<sup>th</sup> October 1995) to within 1 K, or around 0.5%. Although brightness temperatures in FLUXES, as well as those quoted by Griffin & Orton (1993), are quoted only for the SCUBA observing bands of 350, 450, 600, 750 and 850  $\mu\text{m}$ , and 1.1, 1.4 and 2.0 mm, the original model of Wright (1976) provides brightness temperatures in the region 30 to 300  $\mu\text{m}$ . Thus the FLUXES data will be extrapolated in order to calculate the flux received at a wavelength of 200  $\mu\text{m}$ .

Table 6.2 presents data on the flux values for each of the primary calibration planets. Data were calculated from the FLUXES software (Privett *et al.*, 1998) for a

given date in late-2003. A brightness temperature at 200  $\mu\text{m}$  was extrapolated from values given at wavelengths from 350  $\mu\text{m}$  to 2 mm. Table 6.3 gives the brightness temperatures for each of the calibrator planets derived by this method. An example of the algorithm for the extrapolation of flux at 200  $\mu\text{m}$  is provided in Appendix C. Fluxes from Mars were determined by fitting a straight line to a temperature,  $T$ , vs. log wavelength,  $\lambda$  plot. Figure 6.1 shows the plot of  $T$  vs.  $\log\lambda$  for Mars. Griffin (1985) used a similar method to extrapolate the brightness temperature of Mars to wavelengths from 350  $\mu\text{m}$  to 3.3 mm. A similar method was used to derive the Jovian temperature in Table 6.3. Figure 6.2 shows the plot of  $T$  vs.  $\log\lambda$  for Jupiter. Although a spurious brightness temperature is returned by the FLUXES software at a position in the Jovian spectrum of just greater than  $\log\lambda \approx 3.1$  ( $\lambda \approx 1.2$  mm), the spectrum appears considerably smoother approaching wavelengths below this. An alternative method of determining brightness temperature at 200  $\mu\text{m}$  is to consider only the four lower-most wavelengths, leading to a linear plot of temperature against  $\log\lambda$ . The two methods lead to a difference of only 3% in brightness temperature at 200  $\mu\text{m}$ . Since the expected calibration for THUMPER data is 30% within the first year, errors in planetary flux of this value are negligible.

Table 6.2. Total flux and the flux in a 14" beam for each of the primary calibration sources at 200  $\mu\text{m}$ .

Shift start date (UT)	mid-shift time (UT)	Mars		Jupiter		Uranus		Neptune	
		Total flux (Jy)	Flux in beam (Jy)	Total flux (Jy)	Flux in beam (Jy)	Total flux (Jy)	Flux in beam (Jy)	Total flux (Jy)	Flux in beam (Jy)
12 10 03	8:30	74506	43039			342.9	335.1	135.6	134.4
15 10 03	8:30	69730	42943			342.9	335.1	135.6	134.4
19 10 03	8:30	63899	42831			342.9	335.1	135.6	134.4
01 11 03	8:30	47978	42471			335.3	327.9	133.3	132.1
08 11 03	16:30			139187	25142				
09 11 03	8:30	40350	29498			331.6	324.3	133.3	132.1
14 11 03	16:30			143273	25142				
18 11 03	8:30	33390	25662			324.1	317.2	130.9	129.8
18 11 03	16:30			146376	25142				
22 11 03	8:30	30817	24138			324.1	317.2	130.9	129.8
26 11 03	16:30			152860	25142				
30 11 03	16:30			156423	25142				
04 12 03	17:30			160208	25142				
09 12 03	17:30			164957	25142				
15 12 03	17:30			171085	25142				
21 12 03	17:30			177516	25142				
31 12 03	17:30			188562	25142				

Table 6.3. Brightness temperatures at 200  $\mu\text{m}$  for the calibrator planets.

Planet	Mars	Jupiter	Uranus	Neptune
Brightness temperature (K)	201 - 206	133	48.0	47.7

Uranus and Neptune have an empirically determined third order polynomial fit of  $T$  against  $\log \lambda$ , as described by Griffin & Orton (1993). Gaps in Table 6.2 are due to the unavailability of the planet during that commissioning period. The flux in the beam is derived from the total flux by one of two methods, depending on angle subtended by the source. For sources smaller than the beamsize a correction factor, CF, is used (Griffin, 1985; refs therein)

$$\text{CF} = \frac{x^2}{1 - e^{-x^2}} \quad (6.1)$$

where  $x$  is given by

$$x = \frac{d_s \sqrt{\ln 2}}{\text{FWHM}} \quad (6.2)$$

for source of diameter  $d_s$  and full width at half maximum is the beamwidth. For beamsizes larger than the source, flux is derived by taking the product of 14" beamsize and the Planck function for the particular source.

Errors in the brightness temperatures given in Table 6.3 are likely to be similar to those quoted by Griffin and Orton (1993) for the same planets. These are  $\pm 5\%$  for Mars, and less than  $\pm 2$  K. for Uranus and Neptune. Griffin *et al.* (1986), from whom the FLUXES calculations originate, quote an error for the Jovian brightness temperature of  $\pm 10\%$  over the wavelength range 350  $\mu\text{m}$  to 3.3 mm, which may be higher at 200  $\mu\text{m}$  due to atmospheric absorption, mentioned above.

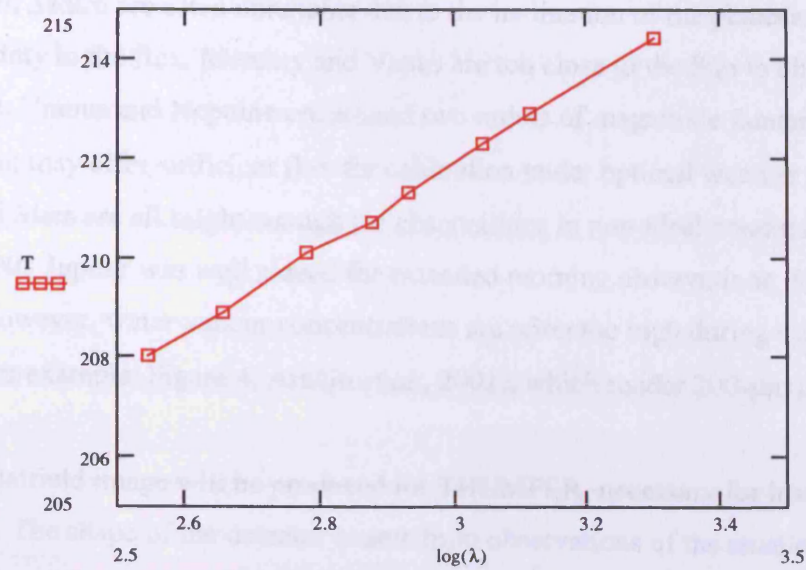


Figure 6.1.  $T$  vs.  $\log \lambda$  for Mars.

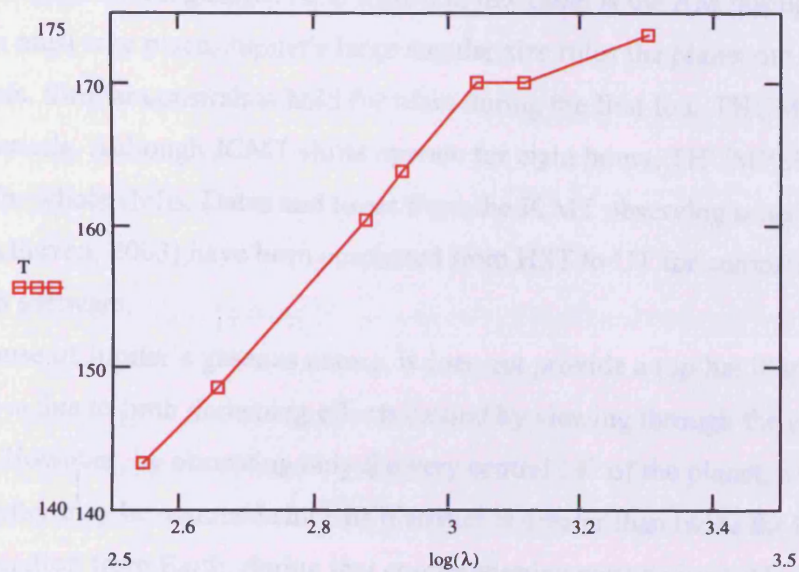


Figure 6.2.  $T$  vs.  $\log \lambda$  for Jupiter.

Mars is the preferential candidate for calibration, although Jupiter and possibly Uranus and Neptune also offer suitably bright fluxes. Mars is preferred because flux calculations from other planets refer back to the Martian brightness. This is due to the lack of Martian atmosphere, its solid surface, and its, usually, small angular size. Flux

values from Saturn are often unreliable due to the inclination of the planet's rings causing an uncertainty in the flux. Mercury and Venus are too close to the Sun to observe. Pluto is too faint. Uranus and Neptune are around two orders of magnitude fainter than Mars at 200  $\mu\text{m}$ , but may offer sufficient flux for calibration under optimal weather conditions. Jupiter and Mars are all bright enough for observations in non-ideal conditions. During October 2003 Jupiter was well placed for extended morning observations, from 9:30 am to noon. However, water vapour concentrations are often too high during this part of the day (see, for example, Figure 4, Araújo *et al.*, 2001), which render 200- $\mu\text{m}$  observations impossible.

A flatfield image will be produced for THUMPER, necessary for instrument calibration. The shape of the detector beams from observations of the smaller calibration sources, i.e. smaller than the THUMPER beamsize, will be performed. Table 6.4 shows the semi-diameter subtended by each of the source planets at a time of proposed THUMPER commissioning shifts. Also shown in the Table is the AM through which observations must take place. Jupiter's large angular size rules the planet out of beamsize measurements. Similar constraints hold for Mars during the first four THUMPER observing periods. Although JCMT shifts operate for eight hours, THUMPER's time is not always for whole shifts. Dates and times from the JCMT observing schedule (Moriarty-Schieven, 2003) have been converted from HST to UT for compatibility with the FLUXES software.

Because of Jupiter's gaseous nature, it does not provide a top-hat illumination profile. This is due to limb darkening effects caused by viewing through the planet's atmosphere. However, by observing only the very central 14" of the planet, a top-hat profile of Jupiter may be assumed since its diameter is greater than twice the beamsize at its furthest position from Earth, during that commissioning period given. Mars also appeared larger than the 14" beamsize during the first three THUMPER shifts, although the flux from Mars is less dependant on which part of the planet is observed.

Table 6.4. Angular size and AM of five planets during a period previously given for THUMPER's commissioning. Blanks in columns indicate the planet is unavailable for observations.

Shift start date (UT)	mid-shift time (UT)	Mars		Jupiter		Uranus		Neptune	
		Diameter (")	AM	Diameter (")	AM	Diameter (")	AM	Diameter (")	AM
12 10 03	8:30	18.42	1.272			3.60	1.272	2.28	1.722
15 10 03	8:30	17.84	1.285			3.60	1.303	2.28	1.785
19 10 03	8:30	17.10	1.306			3.60	1.352	2.28	1.934
01 11 03	8:30	14.88	1.383			3.56	1.605	2.26	2.786
08 11 03	16:30			32.94	1.141				
09 11 03	8:30	13.68	1.455			3.54	1.871	2.26	3.980
14 11 03	16:30			33.42	1.100				
18 11 03	8:30	12.48	1.54			3.50	2.369	2.24	7.946
18 11 03	16:30			33.78	1.078				
22 11 03	8:30	12.00	1.583			3.50	2.712	2.24	12.902
26 11 03	16:30			34.52	1.048				
30 11 03	16:30			34.92	1.038				
04 12 03	17:30			35.34	1.049				
09 12 03	17:30			35.86	1.068				
15 12 03	17:30			36.52	1.102				
21 12 03	17:30			37.20	1.150				
31 12 03	17:30			38.34	1.269				

## 6.5. Commissioning Plan

The commissioning of THUMPER will be carried out after integrated instrument testing within the laboratory. Knowledge of expected instrument performance at the JCMT will then be known, allowing estimates of NEFD to be gained.

The time spent preparing THUMPER for use at the JCMT should be kept to a minimum. A goal of THUMPER, from the outset, has been to cause a minimum of disruption to other instruments at the facility, such as SCUBA, whilst still enjoying simultaneous observations. This is in part due to the manner in which the instrument was funded. Such an ethos requires as much of the commissioning as possible to be accomplished in the daytime. In this way disruption to other instruments is minimised. In addition, there is no need to perform much of the commissioning process during night-time.

The primary task once THUMPER and associated team are at the JCMT is the need to install the system and prepare it for observing. Figure 6.3 is a schematic of the THUMPER cryostat and its warm components, and where these will interface into the existing JCMT infrastructure. By the time THUMPER arrives in Hawaii, the A-frame support will be in place, connected to the telescope central bearing. In addition, the pickoff assembly and associated driver motor, control switch and software flag will be



ready. Inherent to this is the interfacing of THUMPER to the SCUBA software, performed by Joint Astronomy Centre (JAC) staff.

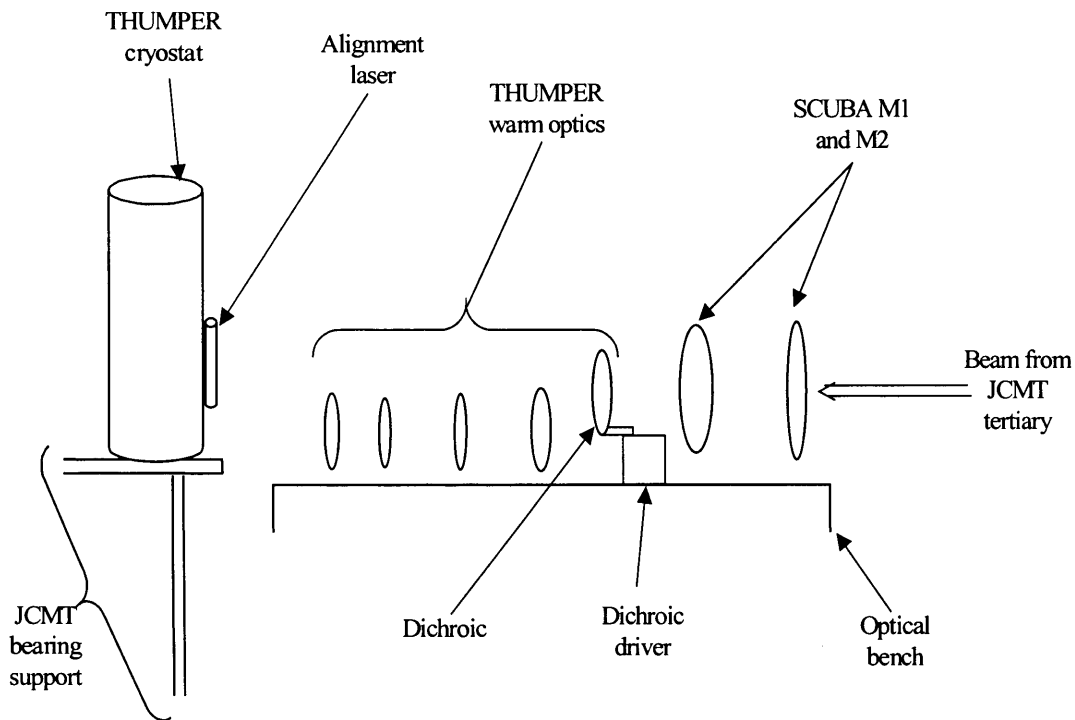


Figure 6.3. Schematic of THUMPER at the JCMT. Mirrors are depicted as lenses for clarity.

### 6.5.1. Daytime Commissioning

The first tests on THUMPER at the JCMT will be a visual inspection to ensure no damage has occurred in transit from Cardiff. In addition, the standard procedure of health checks, regularly performed during laboratory testing prior to cooldown, will be completed. Once amplification and power have been installed to the cryostat these checks can be performed. They include measurements of DC output voltage, and checks on bias supply, source voltages and JFET supply voltages. Checks are designed to ensure no problems have occurred due to, for example, disconnected wiring, detectors electrically shorting to ground or JFETs failing.

A check of the internal optical alignment will be carried out. This will be by use of a Melles Griot 5mW He-Ne laser. This is the same type of laser as used by SCUBA for alignment. The THUMPER laser will be placed vertically, above the THUMPER cryostat window.

The beam from the laser is reflected into the cryostat by means of a small mirror mounted at  $45^\circ$  to the vertical. To ensure that the beam is horizontal to the cryostat coldplate, two removable targets of identical height will be located on the coldplate. The targets have been constructed such that the beam is at a height of 30.0 mm above the surface. Once this has been verified the flat mirror T6 will be adjusted such that the laser falls upon the center of the central detector. A reflecting piece of mylar will then be placed over the feedhorn entrance apertures. The reflected beam can then be directed such that, at flat mirror T6, both beams are coincident. Indeed, the incoming and reflected beams will also be coincident at T5 and the  $45^\circ$  mirror of the laser.

The next stage of alignment concerns the shields. Due to the long holdtime of the THUMPER cryostat, the shields at temperatures of LHe and He vapour are only delicately attached to the OVC. This has the effect of providing a large amount of detrimental lateral movement. The shields must therefore be aligned such that the incoming beam, from either the alignment laser or from the JCMT/THUMPER external optics, is directed towards the central pixel of the FPA.

The LHe and He vapour cooled shields will be aligned with each other by means of a micrometer. The laser will be moved in a direction along the length of the cryostat towards the fill ports by approximately 1.7 mm, so that the laser beam will pass through the centre of the cryostat window aperture. The movement of the laser in that direction is due to thermal contraction of the inner cryostat shields upon instrument cooling. A cross-hair will be placed on the LHe temperature shield aperture. The inner components of the cryostat can then be centred with respect to the incoming laser beam.

After internal alignment, the instrument will then be cooled to operating temperature and the system checked to function as it did in the laboratory. Checks will be performed with the internal illuminator using the THUMPER dedicated PC running LabVIEW DAQ software.

Alignment of the external optics will be performed with THUMPER in position on the A-frame mount next to the SCUBA optical table. THUMPER optics must also be aligned to the SCUBA external optics. To some extent the warm optics can be installed on the SCUBA optical bench simultaneously to tasks discussed above. Mirrors T1 to T4 will be mounted on the optical bench and positioned as accurately as possible using ruler

and micrometer measurements. Each mirror is adjusted by use of 3-point adjusters to the rear of the mount. The 45° mirror on the THUMPER alignment laser will be oriented such that the laser beam will emanate as if from the centre of the cryostat window.

The THUMPER cryostat will be positioned on the A-frame mount and positioned, relative to the optical bench, by micrometer measurements. Accurate positioning in terms of the focus from the JCMT secondary mirror is discussed below. The rotational orientation of the cryostat will be adjusted until the beam emerging from the cryostat is incident on the centre of the flat mirror T4. Sequential adjustment to the orientation of each of the external THUMPER mirrors in turn will be made until the laser is incident on the centre of the dichroic mount. Due to the limited number of degrees of freedom available for movement of the dichroic mount, adjustments will have to be made to both the mount and to T1 to direct the laser beam onto the centre of M2. Since the dichroic is fully transmissive in the visible, a dummy "dichroic" of 50% reflectance in the visible will be mounted in the dichroic ring to provide reflection for the laser. As a check for simultaneous THUMPER/SCUBA alignment, the SCUBA laser will be used to verify coincidence of both lasers on M2. The coincidence should extend to the tertiary mirror.

THUMPER will then be connected to the DAQ system of SCUBA. Tasks relating to this will be performed by JAC staff.

Alignment of the THUMPER array will eventually coincide with the central bolometers of the SCUBA 450- $\mu\text{m}$  array. Due to the hexagonal pattern of both arrays, and the lack of knowledge as to the orientation of the SCUBA arrays, there exists the possibility of a misalignment of the THUMPER FPA by 30° to the SCUBA arrays. To check the rotational alignment of both arrays, 64-point jiggle maps will need to be made of one of the planets. A task such as this can be accomplished in a single daytime morning. Since rotating THUMPER's FPA would necessitate warming up the cryostat, this aspect of alignment is best suited to a scheduled warm-up. To prepare for this eventuality, the THUMPER FPA has been designed for rotation about its central pixel. Although such alignment is not an absolute necessity for simultaneous observations, it would ease direct pixel-to-pixel comparisons between THUMPER and SCUBA arrays.

### 6.5.2. Nighttime Commissioning

During nighttime commissioning THUMPER will repeatedly observe the planets through different quantities of AM. Planets suitable for this task, in terms of providing adequate flux, are Mars, Jupiter, and possibly Uranus and Neptune. Occasional periods will be spent observing during early morning if conditions are optimum. Results will provide answers to three main areas of interest. These are to map the beamshape of the detectors and feedhorns, to measure the electrical responsivity of the detectors, and to quantify atmospheric transmission as a function of water vapour. This latter quantity will provide values of sky opacity, and hence transmission, at 200  $\mu\text{m}$ .

Primary calibration will be by use of the planets and it is envisaged that THUMPER will spend long periods observing them. After observations of an astronomical source, THUMPER will observe a calibrator planet in order to provide a Jy per mV conversion factor from the well-known flux produced by that planet. It is beneficial to use the nearest planet to that portion of sky being observed in order to limit any changes that may be caused by changes in AM or spatial variations in atmospheric emissivity.

Whilst calibrating THUMPER, observing modes will use the standard 64-point jiggle-map mode (Lightfoot *et al.*, 1995). 64-point maps are needed since there is a need to observe simultaneously over the three wavebands of 200, 450 and 850  $\mu\text{m}$ . Due to the factor of two difference in horn spacing between the 450 and 850- $\mu\text{m}$  SCUBA arrays, the 16-point maps become insufficient for multi-channel observations (Cunningham, 1990). The telescope pointing-mode is also of limited value for THUMPER commissioning since there is a need to check that sky-pointing and alignment have stayed constant.

Changes in temperature at Mauna Kea lead to thermal contractions of the JCMT secondary mirror support. To correct for the change in focus caused by these contractions the secondary mirror is moved in a direction perpendicular to the primary mirror, and measurements made of flux values, by SCUBA, at different secondary mirror positions. A maximum in flux received by SCUBA occurs when SCUBA is focussed to the telescope. Focussing THUMPER will be by a similar method. THUMPER will be moved in the plane parallel to the beam entering the cryostat window, along the axis of the beam, until a maximum signal is measured by THUMPER. This will be performed when

SCUBA is focussed so that THUMPER will be simultaneously focussed to SCUBA and the telescope. Focus measurements can be made during the day and checked at the start of nighttime observations.

Tracking planets across different AM values will provide the knowledge of how the flatfield view and beam profile vary with sky elevation. This may occur due to deformation of the JCMT primary mirror as it tilts. Data from the flatfielding will be added to the DAQ for THUMPER.

In addition, the nighttime commissioning process will serve to measure the true loss, in terms of flux, to the SCUBA 450 and 850- $\mu\text{m}$  channels caused by the inclusion of the dichroic into the SCUBA beam.

## 6.6. Sky Calibration

For the flux  $F_0$  from an astronomical source incident on the top of the atmosphere, an amount  $F_G$  will be incident on the Earth's surface, as given by

$$F_G = F_0 e^{-\tau_0 \sec z} . \quad (6.3)$$

for zenith opacity  $\tau_0$ . By measuring the flux from a planet as a function of AM, and hence  $z$ , and with knowledge of the planet's flux before atmospheric attenuation, a secant plot, of  $\ln F_G$  against  $\sec z$ , provides a gradient of the atmospheric opacity at the wavelength of which observations have been made. For  $\ln F_G$  plotted in terms of the signal voltage, the intercept with the ordinate axis,  $\ln F_0$ , will provide the Volt to Jansky responsivity. Planet observations will be performed using the 64-point jiggle map mode of observation, and repeated over a wide range of AMs. These will be interspersed with SCUBA skydips every half-hour, or hour if the sky is more stable. Skydips involve measuring the sky emission as a function of AM and provide a measure of opacity at the wavelength of observation.

The CSO, 160 m from the JCMT, and the WVM (Wiedner, 1998), working along the line of sight of the JCMT, provide the sky opacity at 225 GHz and the integrated strength of the water line at 183 GHz respectively. These data can be used to infer the water vapour content in the atmosphere above the site at Mauna Kea.

Combining SCUBA skydip data with CSO  $\tau_{225}$  and secant plots will enable comparisons to be drawn between  $\tau_{1500}$  and  $\tau_{225}$ . Similarly, the SCUBA skydips will be

combined with secant plots to build up an empirical relationship of atmospheric transmission at 200  $\mu\text{m}$  with that at 450 and 850  $\mu\text{m}$ . Previous studies (Archibald *et al.*, 2000) have correlated opacity at 450  $\mu\text{m}$  with that at 850  $\mu\text{m}$ . Correlation is especially close for  $\tau < \sim 0.2$  ( $\cong 3.5$  mm PWV). If opacity at 450 and 850  $\mu\text{m}$  correlates well with that at 200  $\mu\text{m}$  then no additional overhead would be included for calibration of the atmosphere at 200  $\mu\text{m}$ .

By calibrating observations from the CSO and WVM with the secant plots it will be possible to correlate atmospheric transmission at 200  $\mu\text{m}$  with the amount of water vapour in the atmosphere. This will provide a quantitative measure by which suitable conditions for THUMPER can be determined by water vapour concentrations in the atmosphere. WVM data is preferred since this works in the line of sight of the JCMT, whereas the CSO operates at fixed azimuth.

Opacity at any given frequency,  $\tau(\nu)$ , is related to atmospheric transmission at that frequency,  $t(\nu)$ , by Equation 2.8

$$t(\nu) = e^{-\tau(\nu)}. \quad (2.8)$$

Values of PWV, obtained from CSO and WVM measurements, can be used to evaluate the atmospheric model developed in Chapter 2.

Because the 200- $\mu\text{m}$  window is generally of low transmission THUMPER needs to operate in Band 1 weather. Definitions of the various weather bands at use at the JCMT are given in Table 6.5.  $\tau_{225}$ -derived values of PWV are obtained using Equation 2.20 (Davis *et al.*, 1997).

Observations at 450  $\mu\text{m}$  lead to anomalous refraction effects due to the instability of the atmosphere (Zylka *et al.*, 1995). These manifest themselves as an image of a point source which appears extended, and blurred around the edges. Such effects can lead to random changes in telescope pointing of up to 60" in extreme cases for the 350 and 450- $\mu\text{m}$  windows (Duncan *et al.*, 1990). There is a need to ascertain whether these effects are



Table 6.5. Definition of weather bands used at the JCMT (Jenness, 1998).

<b>Band</b>	<b>Definition</b>	<b>CSO <math>\tau_{225}</math></b>	<b>PWV (mm)</b>
1	Very dry	< 0.05	< 0.68
2	Dry	0.05 – 0.08	0.68 – 1.28
3	Medium	0.08 – 0.12	1.28 – 2.1
4	Wet	0.12 – 0.2	2.1 – 3.7
5	Very wet	> 0.2	> 3.7

present at 200  $\mu\text{m}$ . Since calibration planets are not point sources it will be necessary to use the secondary calibrators (see below) for this purpose.

Because the atmosphere changes over a period of weeks, it is beneficial that THUMPER's commissioning is spread out over almost three months. This will enable one set of observations to be taken before the weather will provide a different set of atmospheric conditions. A range of observations during different weather conditions is advantageous in producing a database of atmospheric transmission during different PWV levels.

Since THUMPER is an array, it has the ability to observe some sources, those smaller than the beamsize, with the central pixel only. The surrounding outer pixels can then be used to calculate sky fluctuations, as SCUBA operations allow (Archibald *et al.*, 2002). Furthermore, if sky fluctuations correlate across wavelengths, for sources within the THUMPER field of view, but not within that of the outer pixels of SCUBA, the possibility exists of removing sky noise by use of the outer SCUBA pixels.

Following the procedure detailed above, secondary calibrators will then be observed. These are a number of ultracompact HII regions, as listed by Sandell (1994), whose fluxes are determined relative to Mars. Brightnesses of the secondary calibrators are listed for all SCUBA channels (Sandell, 1998), and will also be useful for THUMPER when primary calibrators are either unavailable or too large.

Figure 6.4 summarises the observations that will be undertaken during night-time commissioning of THUMPER.

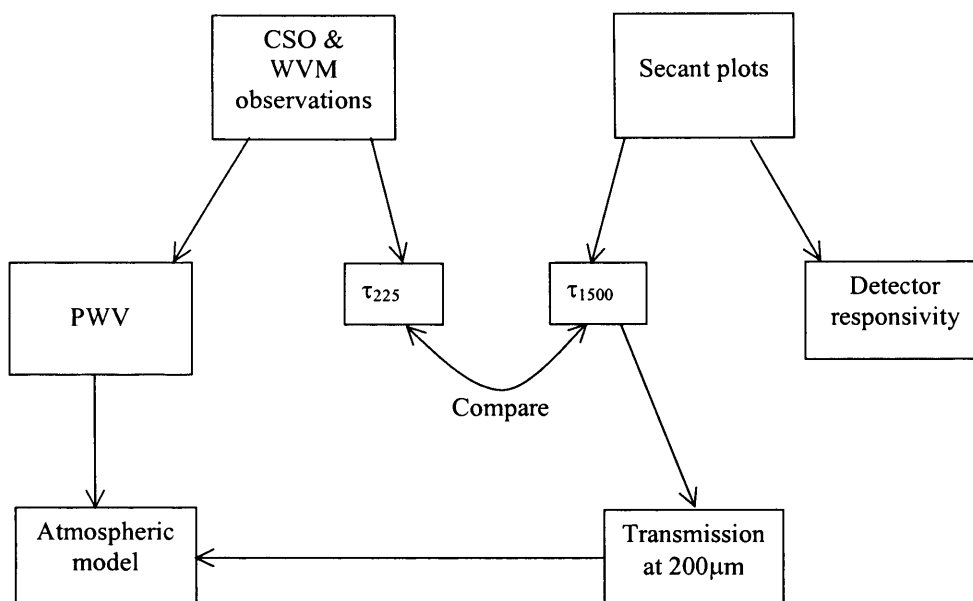


Figure 6.4. Diagram of THUMPER observations during commissioning.

### 6.7. Previous Results

Matsushita *et al.* (1999) attempted to correlate the opacity at the frequencies of the FIR windows with that at 225 GHz for the Chilean site of Pampa la Bola. The relevant results of that analysis are summarised here.

Using an FTS, atmospheric transmission was measured in the spectral range 150 to 1600 GHz. Data were plotted of the opacity at 225 GHz against that of the frequencies at which other windows open up. One such window is at 1500 GHz. Matsushita *et al.* quote a fit to the data, reproduced in Figure 6.5, of

$$\tau_{1500} = (105 \pm 32) \cdot \tau_{225} \quad (6.4)$$

The Figure implies that there exists a non-zero offset between the two opacities, which has not been included by Matsushita. Analysis of this data can therefore be improved. The non-zero offset could arise from far-wing absorption of, for example, O<sub>2</sub> or O<sub>3</sub>. A quantitative study of this zero-τ<sub>225</sub> offset would require further measurements at very low water vapour levels.

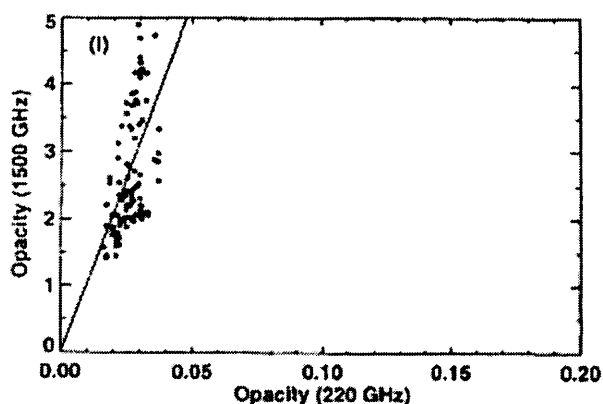


Figure 6.5. Correlation between  $\tau_{1500}$  and  $\tau_{225}$  (Matsushita *et al.*, 1999).

### 6.8. Decommissioning

Decommissioning of THUMPER is expected to occur late in 2005, in conjunction with SCUBA. This is due to telescope preparation for the next generation SCUBA-2.

Such a juncture would provide an ideal time to commission THUMPER at other locations. By late-2005 the South Pole Submillimeter Telescope (SPST) (NRC, 2001) should be fully operational at a location providing optimum atmospheric conditions for 200- $\mu\text{m}$  astronomy.

### 6.9. Summary

A model has been applied to THUMPER at the JCMT and an indication given as to the relative merits of three different astronomical observing sites, for such a system, in terms of NEFD. Calibration will be challenging, due to lack of knowledge of the behaviour of the sky at 200  $\mu\text{m}$ . An indication has been provided as to how this will be achieved.

The basic arrangement for undertaking commissioning has been described. Data on flux values in a 14" beam for planets at the times of scheduled commissioning periods have been presented. The AM and angular size of these sources have also been given. Although  $\tau_{1500}$  and  $\tau_{225}$  correlation has been attempted, this can be improved. The time when THUMPER will be decommissioned will provide an ideal opportunity to install the instrument at an alternative observing site.

## 6.10. References

- Araújo, H.M., Walker, R.J., Rinehart, S.A., Griffin, M.J. & Ade, P.A.R., 2001, *Assessment of the 200- $\mu$ m Atmospheric Window for Ground-Based Astronomy*, *Internat. J. Infrared Millimeter Waves*, **22**, (7), 965-982.
- Archibald, E.N., Wagg, J.W. & Jenness, T., 2000, *Calculating Sky Opacities: a Re-Analysis for SCUBA Data*, SCD System Note 2.2.
- Archibald, E.N., Jenness, T., Holland, W.S., Coulson, I.M., Jessop, N.E., Stevens, J.A., Robson, E.I., Tilanus, R.P.J., Duncan, W.D. & Lightfoot, J.F., 2002, *On the Atmospheric Limitations of Ground-Based Submillimetre Astronomy using Array Receivers*, *Mon. Not. R. Astron. Soc.*, **336**, (1), 1-13.
- Cunningham, C.R. & Gear, W.K., 1990, *SCUBA - Submillimetre Common-User Bolometer Array for the James Clerk Maxwell Telescope*, *Proc. SPIE, Instrumentation in Astronomy VII*, **1235**, 515-523.
- Davis, G.R., Naylor, D.A., Griffin, M.J., Clark, T.A. & Holland, W. S., 1997, *Broadband Submillimetre Spectroscopy of HCN, NH<sub>3</sub>, and PH<sub>3</sub> in the Troposphere of Jupiter*, *Icarus*, **130**, (2), 387-403.
- Duncan, W.D., Sandell, G., Robson, E.I., Ade, P.A.R. & Griffin, M.J., 1990, *A Millimetre/Submillimetre Common User Photometer for the James Clerk Maxwell Telescope*, *Mon. Not. R. Astron. Soc.*, **243**, (1), 126-132.
- Griffin, M.J., 1985, *A Helium-3 Cooled Submillimetre Photometer: Design, Performance and Planetary Observations*, PhD Thesis, Queen Mary College, University of London.
- Griffin, M.J., Ade, P.A.R., Orton, G.S., Robson, E.I., Gear, W.K., Nolt, I.G. & Radostitz, J.V., 1986, *Submillimetre and Millimetre Observations of Jupiter*, *Icarus*, **65**, (2-3), 244-256.
- Griffin, M.J. & Orton, G.S., 1993, *The Near-Millimetre Brightness Temperature Spectra of Uranus and Neptune*, *Icarus*, **105**, (2), 537-547.
- Jenness, T., 1998, <http://www.jach.hawaii.edu/JACpublic/JCMT/software/scuba/obsguide/node29.html>
- Jenness, T. & Lightfoot, J.F., 2000, *Starlink User Note 216*, Starlink Project, CLRC.

- Matsushita, S., Matsuo, H., Pardo, J.R. & Radford, S.J.E., 1999, *FTS Measurements of Submillimeter-Wave Atmospheric Opacity at Pampa la Bola II: Supra-Terahertz Windows and Model Fitting*, Publ. Astron. Soc. Japan, **51**, (5), 603-610 and Plate 24.
- Moriarty-Schieven, G., 2003, [http://www.jach.hawaii.edu/JACpublic/JCMT/Observing\\_info/Schedule/schedule.html](http://www.jach.hawaii.edu/JACpublic/JCMT/Observing_info/Schedule/schedule.html)
- NRC, 2001, *Astronomy and Astrophysics in the New Millennium*, p131 (National Academic Press): <http://books.nap.edu/books/0309070317/html/131.html>
- Masson, C.R., 1994, *Atmospheric Effects and Calibrations*, ASP Conference Series, Astronomy with Millimeter and Submillimeter Wave Interferometry, **59**, 87-95.
- Orton, G.S., Griffin, M.J., Ade, P.A.R., Nolt, I.G., Radostitz, J.V., Robson, E.I. & Gear, W.L., 1986, *Submillimeter and Millimeter Observations of Uranus and Neptune*, Icarus, **67**, (2), 289-304.
- Pardo, J. R., Serabyn, E. & Cernicharo, J., 2001, *Submillimeter Atmospheric Transmission Measurements on Mauna Kea during Extremely Dry El Nino Conditions: Implications for Broadband Opacity Contributions*, J. Quant. Spectrosc. Radiat. Transfer, **68**, (4), 419-433.
- Privett, G., Jenness, T. & Matthews, H., 1998, FLUXES JCMT Position and Flux Density Calibration, Version 1.1, User's Manual.
- Sandell, G., 1994, *Secondary Calibrators at Submillimeter Wavelengths*, Mon. Not. R. Astron. Soc., **271**, (1), 75-80
- Sandell, G., 1998, [http://www.jach.hawaii.edu/JACpublic/JCMT/Continuum\\_observing/SCUBA/astronomy/calibration/calibrators\\_2.html](http://www.jach.hawaii.edu/JACpublic/JCMT/Continuum_observing/SCUBA/astronomy/calibration/calibrators_2.html)
- Stark, A.A. *et al.*, 2001, *The Antarctic Submillimeter Telescope and Remote Observatory (AST/RO)*, Publ. Astron. Soc. Pacific, **113**, (783), 567-585.
- Ward-Thompson, D. *et al.*, 2003, *THUMPER Engineering and Commissioning Request*, Supplied to JACH.
- Wiedner, M.C., 1998, *Atmospheric Water Vapour and Astronomical Millimetre Interferometry*, PhD Thesis, Mullard Radio Astronomy Observatory and Gonville & Caius College, Cambridge.

Wright, E.L., 1976, *Recalibration of the Far-Infrared Brightness Temperatures of the Planets*, *Astrophys. J.*, **210**, (1), 250-253.

Zylka, R., Mezger, P.G., Ward-Thompson, D., Duschl, W.J. & Lesch, H., 1995, *Anatomy of the Sagittarius A Complex. 4: SGR A\* and the Central Cavity Revisited*, *Astron. Astrophys.*, **297**, (1), 83-97.



## Chapter 7 Conclusions

### 7.1 Thesis Overview

From the limited number of spectroscopic measurements that have been taken at various FIR astronomical observing sites it has been possible to verify a radiative transfer model created for the emission and transmission through the atmosphere. Although none of these measurements have been taken at 200  $\mu\text{m}$  from Mauna Kea, they are useful for THUMPER in that they provide an indication of atmospheric emission under certain conditions. In addition, with knowledge of such conditions the atmosphere can be accurately modelled in order to predict transmission at Mauna Kea under varying amounts of PWV.

Mauna Kea does not provide the only ground-based site suitable for 200- $\mu\text{m}$  astronomical observations. Chajnantor and the South Pole are superior locations due to an increased occurrence of low amounts of PWV at these sites.

For the THUMPER instrument, PCs are the detectors of choice because at wavelengths of less than 200  $\mu\text{m}$  they can provide photon noise limited sensitivity at the relatively convenient temperature of unpumped LHe. Figures of merit for such devices have been defined and an appropriate noise model developed to aid with the optimisation of the THUMPER detectors. The development of stressed PCs over the last three decades has been briefly considered with a view to optimising the construction of a stressed array for the THUMPER PCs. A full description of the construction of the THUMPER stressed detector array has also been provided.

The THUMPER instrument has been fully introduced within Chapter 4. The rationale behind the component level design has been explained.

Prototype PCs along with the three arrays of THUMPER detectors have been tested for spectral response, dark current, current responsivity and noise. Test results strongly imply there exists an inhomogeneous stress across the cross-section of each of the THUMPER crystals. Although this results in a beneficially low measurement of dark current, an additional characteristic is the low responsivity. Noise of the detectors has been modelled and found to agree with measured values of noise to within 30%.

A photometric model has been applied to THUMPER at the JCMT and an indication given as to the relative merits of the three different astronomical observing sites of Mauna Kea, Atacama and the South Pole, for a THUMPER-type system, in terms of NEFD. It is appreciated that calibration will be challenging, due to lack of knowledge of the behaviour of the sky at 200  $\mu\text{m}$ . An indication has been provided as to how this will be achieved. The basic arrangement for undertaking commissioning has been described. Data on flux values in a 14" beam for planets at a time of commissioning have been presented. The AM and angular size of these sources have also been specified. Although  $\tau_{1500}$  and  $\tau_{225}$  correlation has been attempted, only a limited number of measurements have been taken, and analysis can be improved upon. The time when THUMPER will be decommissioned, in conjunction with that of SCUBA, will provide an ideal opportunity to install the instrument at an alternative observing site.

## 7.2 Instrument Improvements

Having demonstrated that there exist certain complications within THUMPER, it is apparent that upgrades can be made to the detector blocks. These should have the benefit of increasing detector responsivity and hence DQE. Some possible improvements are given below.

As mentioned in Chapter 5, improvements could be made to the components comprising the stressing assembly. The need for the improvements has been caused by the lack of uniformity in the stress applied across the cross-section of the Ge:Ga crystals. The most simple of changes would be in matching the size of stressing piston to exactly the same diameter as the cavity in which these pistons are housed. The, however slight, smaller piston diameter now in existence leaves open the risk of the piston rotating, as shown in Figure 5.21.

The engineering solution provided by Kraft *et al.* (2000) and discussed in Section 5.6 would avoid the requirement of a perfectly perpendicular end to the stressing pistons, at the points where they meet the electrical isolators. By inserting a hemispherical bearing into a matching cavity at the end of the stressing piston, any small rotation of the piston about the vertical would be compensated by movement of the hemisphere within its

cavity. Thus although the piston may not be vertical, stress will still be applied in a vertical direction.

The possibility exists that the low responsivity evident through testing of the THUMPER detectors is caused, at least in part, by the large feedthrough holes, towards the rear of the crystal cavities. These were originally incorporated in the design as it was envisaged that larger feedthrough components would be used for electrical conductivity, as was incorporated in the SAFIRE-A prototype detector housings. If the design of the stressing blocks were to be revised, a boost in photon absorption could be made by narrowing the feedthrough-holes to more closely match the feedthrough-wire diameter. The advantage of constructing prototype detector housings would therefore have been most beneficial for the THUMPER arrays.

It can be seen though the modelling presented in Chapter 2 that an atmospheric window exists centred at 230  $\mu\text{m}$  with a transmission slightly superior to that at 200  $\mu\text{m}$ . By using highly stressed Ge:Ga PCs, or alternatives such as GaAs PCs or bolometers, observations could be undertaken through this window at the same time as those taken at 200  $\mu\text{m}$ . It should be noted that the alternative detectors mentioned above would require operational temperatures lower than that of the unpumped LHe temperature of THUMPER, a luxury unavailable to THUMPER.

### 7.3 References

Kraft, S., Frenzl, O., Charlier, O., Cronje, T., Katterloher, R.O., Rosenthal, D., Groezinger, U. & Beeman, J.W., 2000, *FIRST-PACS: design and performance of the sensor engineering models*, Proc. SPIE, UV, Optical, and IR Space Telescopes and Instruments, **4013**, 233-243.

## Abbreviations

ADC	Analogue to Digital Converter
AFGL	Air Force Geophysical Laboratory
AIRES	Airborne InfraRed Echelle Spectrometer
AM	Air Mass
APEX	Atacama Pathfinder EXperiment
AST/RO	Antarctic Submillimetre Telescope and Remote Observatory
ATM	Atmospheric Transmission at Microwaves
BIRT	Balloon borne InfraRed Telescope
BLIP	Background Limited Infrared Photoconductor
CSO	Caltech Submillimeter Observatory
DAQ	Data AcQuisition
DQE	Detective Quantum Efficiency
DSA	Dynamic Spectrum Analyser
FIFI	Far Infrared Fabry-Perot Interferometer
FIR	Far InfraRed
FIRST	Far InfraRed Space Telescope
FIS	Far-Infrared Surveyor
FPA	Focal Plane Array
FTS	Fourier Transform Spectrometer
FWHM	Full-Width Half-Maximum
GBT	Gaussian Beam Telescope
g-r	Generation-Recombination
HAWC	High-resolution Airborne Wideband Camera
HAWKS	HITRAN Atmospheric WorKStation
HITRAN	High-TRANsmission
HST	Hawaiian Standard Time
IBEX	Infrared Balloon EXperiment

IRAS	InfraRed Astronomical Satellite
IRIS	InfraRed Imaging Surveyor
IRTS	Infrared Telescope in Space
ISO	Infrared Space Observatory
JAC	Joint Astronomy Centre
JFET	Junction Field Effect Transistor
KAO	Kuiper Airborne Observatory
LBNL	Lawrence Berkeley National Laboratory
LHe	Liquid Helium
LN <sub>2</sub>	Liquid Nitrogen
LPE	Low-Pass Edge
LWS	Long Wavelength Spectrometer
MIPS	Multiband Imaging Photometer for Spitzer
MIR	Mid-InfraRed
NEFD	Noise Equivalent Flux Density
NEP	Noise Equivalent Power
OAH	Optical Axis Height
OVC	Outer Vacuum Case
PACS	Photoconductor Array Camera and Spectrometer
PC	Photoconductor
PWV	Precipitable Water Vapour
RQE	Responsive Quantum Efficiency
SAFIRE-A	Spectroscopy of the Atmosphere by using Far InfraRed Emission - Airborne
SCUBA	Submillimetre Common-User Bolometer Array
SED	Spectral Energy Distribution
SIRTF	Space InfraRed Telescope Facility
SNR	Signal-to-Noise Ratio
SOFIA	Stratospheric Observatory For Infrared Astronomy
SPST	South Pole Submillimetre Telescope
SURF	SCUBA User Reduction Facility

THUMPER	Two HUndred Micron PhotometER
JCMT	James Clerk Maxwell Telescope
TIA	Trans-Impedance Amplifier
UT	Universal Time
UV	Ultra Violet
VVW	Van Vleck and Weisskopf
WVM	Water Vapour Monitor
ZN	Zhevakin-Naumov



## Appendix A

Photometric model: throughput from source to detector for THUMPER at JCMT.  
Based in part on earlier model by H. Araujo.  
Units are SI.

Define constants:

$$k_b := 1.381 \cdot 10^{-23} \quad c := 2.998 \cdot 10^8 \quad h := 6.626 \cdot 10^{-34}$$

Planck function: 
$$B(\nu, T) := \frac{2 \cdot h \cdot \nu^3}{c^2 e^{k_b \cdot T}} \frac{h \cdot \nu}{e^{k_b \cdot T}}$$

Wavelength & frequency of operation: 
$$\lambda_{op} := 200 \cdot 10^{-6} \quad \nu_{op} := \frac{c}{\lambda_{op}}$$

Frequency range of interest: 
$$\nu := 1360 \cdot 10^9, 1361 \cdot 10^9 \dots 1640 \cdot 10^9$$

**Atmosphere:**

Temperature:  $T_{atm} := 269$  (see Paine et al., 2000)

Read in atmospheric transmission at 0.1, 0.25, 0.5 & 1.0 mm PWV at 1 AM:

$$i := 1, 2, \dots, 4 \quad \begin{pmatrix} \nu_a \\ t_{a1} \\ t_{a2} \\ t_{a3} \\ t_{a4} \end{pmatrix} = \begin{matrix} \text{[Data Table]} \end{matrix}$$

$$f_i := \text{cspline}(\nu_a, t_{a_i}) \quad t_{atm}(\nu, i) := \text{interp}(f_i, \nu_a, t_{a_i}, \nu)$$

$$T_{sky}(\nu, i) := T_{atm} \cdot (1 - t_{atm}(\nu, i))$$

**JCMT:**

GORE-TEX @ 200um, transmission as measured (PARA):

$$t_{GT} := 0.65 \quad \epsilon_{GT} := 0.35 \quad T_{GT} := 280$$

Telescope temperature:  $T_T := 280$

Emissivity:  $\epsilon_T := 0.1$

Beamsize of 850um channel:

$$\text{HPBW} := 1.22 \cdot \left( \frac{850 \cdot 10^{-6}}{15} \right) \quad \text{HPBW} = 6.913 \times 10^{-5} \quad (\text{rad})$$

$$\text{HPBW} \cdot \frac{180}{\pi} \cdot 3600 = 14.26 \quad (\text{arcsec})$$

Solid angle viewed by JCMT

Telescope aperture

$$\Omega_{\text{beam}} := \left[ \left( \frac{14.26}{3600 \cdot 2} \right) \frac{\pi}{180} \right]^2 \cdot \pi$$

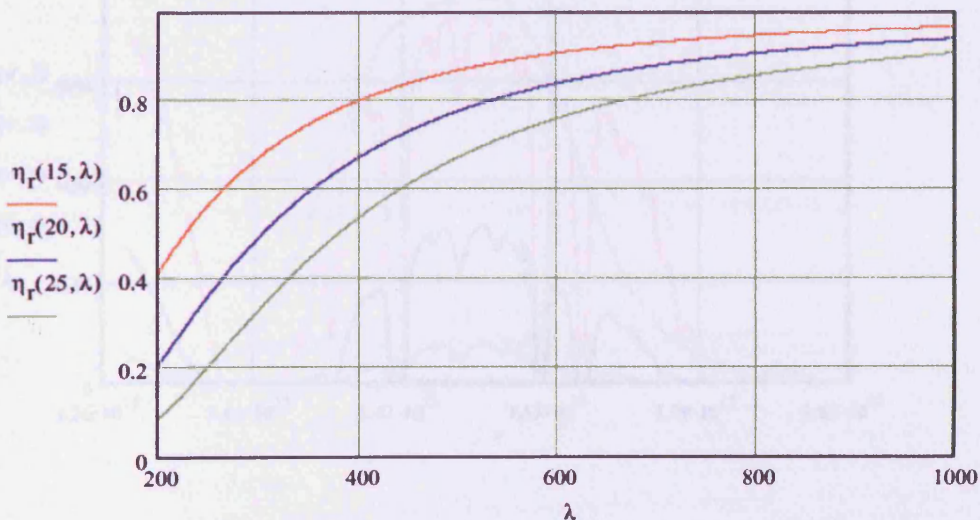
$$A_T := \left( \frac{15}{2} \right)^2 \cdot \pi$$

$$\Omega_{\text{beam}} = 3.754 \times 10^{-9}$$

$$A_T \cdot \Omega_{\text{beam}} = 6.634 \times 10^{-7}$$

Ruze efficiency is a function of surface error  $\epsilon$  of primary and of wavelength  $\lambda$

Ruze efficiency:  $\eta_r(\epsilon, \lambda) := e^{-\left( \frac{4 \cdot \pi \cdot \epsilon}{\lambda} \right)^2}$



Take  $\epsilon_s := 17 \cdot 10^{-6}$  s.t.  $\eta_R := \eta_r(\epsilon_s, \lambda_{op})$  then  $\eta_R = 0.32$

Chopping factor:  $\eta_{ch} := \frac{\sqrt{2}}{\pi}$

Coupling of warm optics:  $\eta_{wo} := 1$

**THUMPER cryostat:**

Temperature of window:  $T_w := 280$

Assume even transmission of window over frequency range of interest:  $t_w := 0.9$

Emissivity of window  $\epsilon_w := 1 - t_w$

Coupling of cold optics:  $\eta_{co} := 1$

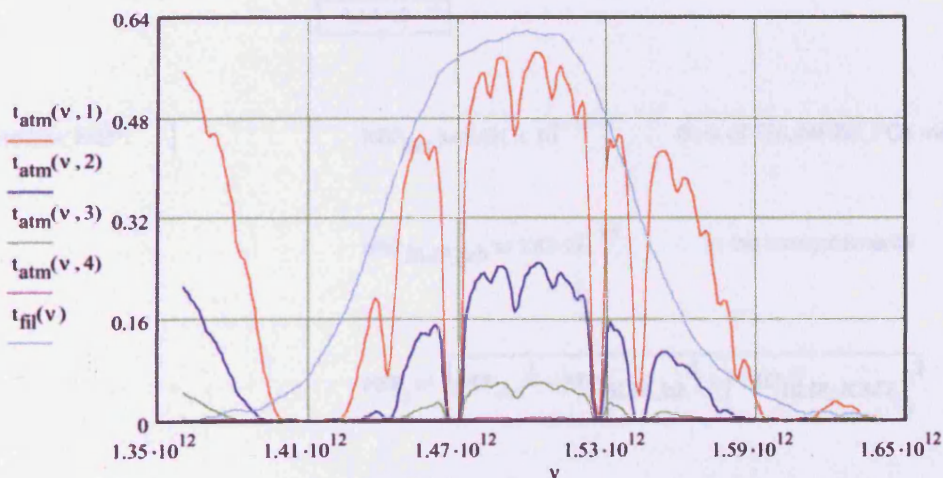
Read in filter profile of cold filters:

$$\begin{pmatrix} v_f \\ t_f \end{pmatrix} = \begin{matrix} \text{[Data Table]} \end{matrix}$$

$$f_f := \text{cspline}(v_f, t_f)$$

$$t_{fil}(v) := \text{interp}(f_f, v_f, t_f, v)$$

Plot atmosphere (0.1, 0.25, 0.5 & 1.0 mm PWV) and filters:





**FEEDHORNS:**

Feedhorn coupling efficiency: assume unity

$$\eta_h := 1$$

**Background power at feedhorn entrance:**

$$P(\nu, i) := A_T \cdot \Omega_{\text{beam}} \cdot t_{\text{fil}}(\nu) \cdot \eta_{\text{co}} \left[ \eta_{\text{wo}} \cdot t_{\text{w}} \left( t_{\text{GT}} B(\nu, T_{\text{sky}}(\nu, i)) + \epsilon_{\text{GT}} B(\nu, T_{\text{GT}}) + \epsilon_T B(\nu, T_T) \right) + \epsilon_w \cdot B(\nu, T_w) \right]$$

$$\int_{1.35 \cdot 10^{12}}^{1.65 \cdot 10^{12}} P(\nu, i) d\nu =$$

1.725 · 10 <sup>-9</sup>
1.846 · 10 <sup>-9</sup>
1.879 · 10 <sup>-9</sup>
1.886 · 10 <sup>-9</sup>

For 0.1, 0.25, 0.5 & 1.0 mm PWV

**JCMT photon limited NEP:**

$$\text{NEP}_{\text{BLIP\_JCMT}_i} := 2 \sqrt{h \cdot \nu_{\text{op}} \cdot \int_{1.35 \cdot 10^{12}}^{1.65 \cdot 10^{12}} P(\nu, i) d\nu \cdot \left( 1 + \frac{t_{\text{fil}}(\nu_{\text{op}})}{\frac{h \cdot \nu_{\text{op}}}{e^{k_b \cdot T_{\text{sky}}(\nu_{\text{op}, i)} - 1}} \right)}$$

$$\text{NEP}_{\text{BLIP\_JCMT}_i} =$$

3.413 · 10 <sup>-15</sup>
4.236 · 10 <sup>-15</sup>
4.629 · 10 <sup>-15</sup>
4.74 · 10 <sup>-15</sup>

**Detector NEP:**

$$\text{NEP}_{\text{det}} := 5.431 \times 10^{-15}$$

Best of THUMPER PCs measured in lab

$$\text{NEP}_{\text{BLIP\_lab}} := 1.87 \cdot 10^{-15}$$

In lab measurements

$$\text{NEP}_i := \sqrt{\text{NEP}_{\text{det}}^2 - \text{NEP}_{\text{BLIP\_lab}}^2 + \left( \text{NEP}_{\text{BLIP\_JCMT}_i} \right)^2}$$

**POINT SOURCE OBSERVATIONS:**

Noise equivalent flux density:  $NEFD_i := \frac{NEP_i \cdot 10^{26}}{\eta_R \cdot \eta_{co} \cdot \eta_{wo} \cdot \eta_{ch} \cdot A_T \int_{1.35 \cdot 10^{12}}^{1.65 \cdot 10^{12}} t_{fil}(v) \cdot t_{atm}(v, i) \, dv \cdot t_{GT} \cdot t_w}$

NEFD<sub>i</sub> =

1.65
5.003
24.952
520.04

$\left( \frac{Jy}{\sqrt{Hz}} \right)$

For 0.1, 0.25, 0.5 & 1.0 mm PWV

## Appendix B


Scaling water vapour concentration to 0.25 mm pwv above Mauna Kea

Boltzmann's constant:  $k := 1.381 \cdot 10^{-23}$

Define altitude resolution:  $r := 1$

and minima & maxima:  $alt := 0, r.. 119$

Read in H2O concentration profile. This is AFGL profile for tropical H2O.

$\begin{pmatrix} h_{ppm} \\ ppm \end{pmatrix} :=$  

Read in temperature profile:

$\begin{pmatrix} h_T \\ T \end{pmatrix} :=$   (K)

This is AFGL temperature profile. File located at  
/Personal/thesis/atmos/MK/MK\_T.xls

Read in pressure profile:

$\begin{pmatrix} h_P \\ P \end{pmatrix} :=$   (mbar)

This is AFGL pressure profile. File located at  
/Personal/thesis/atmos/MK/MK\_P.xls

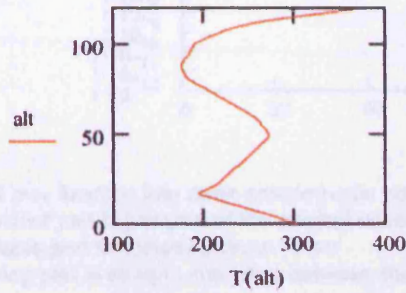
New water concentration profile, interpolated from empirical data:

$m := \text{cspline}(h_{ppm}, ppm)$        $PPM(alt) := \text{interp}(m, h_{ppm}, ppm, alt)$



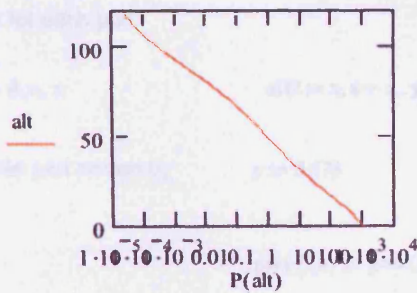
New temperature profile, interpolated from empirical data:

$$t := \text{cspline}(h_T, T) \quad T(\text{alt}) := \text{interp}(t, h_T, T, \text{alt})$$



New pressure profile, interpolated from empirical data:

$$p := \text{cspline}(h_p, P) \quad P(\text{alt}) := \text{interp}(p, h_p, P, \text{alt})$$



Total number of molecules per unit volume (assume  $PV=nkT$ )

$$\text{totN}(\text{alt}) := \frac{P(\text{alt}) \cdot 100}{k \cdot T(\text{alt})} \quad (\text{m}^{-3})$$

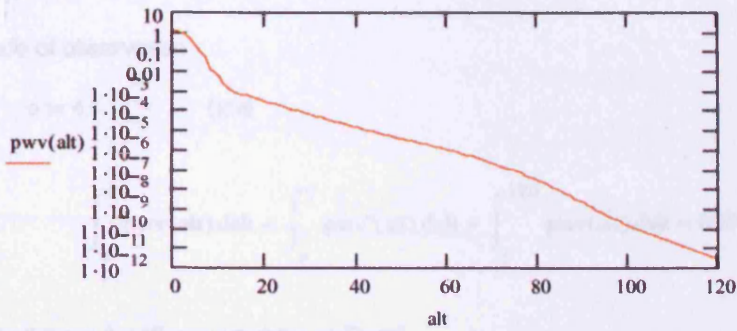
Number of H<sub>2</sub>O molecules per unit volume

$$\text{h2oN}(\text{alt}) := \text{totN}(\text{alt}) \cdot \frac{\text{PPM}(\text{alt})}{10^6} \quad (\text{m}^{-3})$$

pwv as a function of altitude

$$\text{pwv}(\text{alt}) := \frac{\text{h2oN}(\text{alt})}{3.34 \cdot 10^{22}}$$

1mm pwv is equivalent to column density  
3.34e21 cm<sup>-2</sup>



Split pwv function into three components: constant, variable and linking sections  
 Constant part is just part of the original concentration above altitude of tropopause.  
 Variable part is scaled by given factor  
 Linking part is straight line fitted between the two

Define maximum of variable part  $x := 11$  This point chosen fairly arbitrarily - s.t. profile looks smooth

Define minimum of constant part  $y := 17$  Tropopause at 17km altitude, since  $T(alt)$  has local minimum here and from shape of H<sub>2</sub>O profile

Altitude for each part

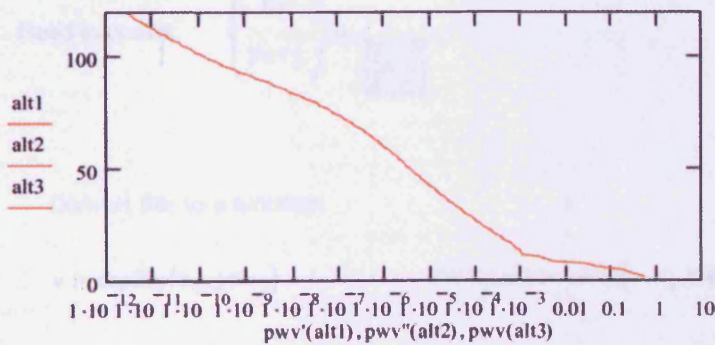
$alt1 := 0, r.. x$                        $alt2 := x, x + r.. y$                        $alt3 := y, y + r.. 119$

Variable part scaled by  $s := 0.478$

$$pwv'(alt) := pwv(alt) \cdot s$$

Set equation of line for linking section

$$n := \frac{pwv(x) - pwv(y)}{x - y} \quad c := pwv(y) - n \cdot y \quad pwv''(alt3) := n \cdot alt3 + c$$



Altitude of observation

$o := 4.1$  (km)

$$\int_o^x \text{pwv}'(\text{alt}) \, \text{dalt} + \int_x^y \text{pwv}''(\text{alt}) \, \text{dalt} + \int_y^{120} \text{pwv}(\text{alt}) \, \text{dalt} = 0.2500$$

Export three functions, combine in Excel

$\text{pwv}'(\text{alt}1) =$

0.492
0.515
0.414
0.305
0.187
0.092
0.046
0.026
$5.296 \cdot 10^{-3}$
$4.165 \cdot 10^{-3}$
$2.501 \cdot 10^{-3}$
$1.112 \cdot 10^{-3}$


$\text{pwv}''(\text{alt}2) =$

$1.112 \cdot 10^{-3}$
$1.008 \cdot 10^{-3}$
$9.032 \cdot 10^{-4}$
$7.987 \cdot 10^{-4}$
$6.941 \cdot 10^{-4}$
$5.895 \cdot 10^{-4}$
$4.849 \cdot 10^{-4}$

$\text{pwv}(\text{alt}3) =$

$4.849 \cdot 10^{-4}$
$4.044 \cdot 10^{-4}$
$3.384 \cdot 10^{-4}$
$2.845 \cdot 10^{-4}$
$2.395 \cdot 10^{-4}$
$2.025 \cdot 10^{-4}$
$1.731 \cdot 10^{-4}$
$1.484 \cdot 10^{-4}$
$1.258 \cdot 10^{-4}$
$1.068 \cdot 10^{-4}$
$9.109 \cdot 10^{-5}$
$7.782 \cdot 10^{-5}$
$6.652 \cdot 10^{-5}$
$5.693 \cdot 10^{-5}$
$4.88 \cdot 10^{-5}$
$4.19 \cdot 10^{-5}$

Scale back to ppm density:

Read in profile:  $\begin{pmatrix} h_1 \\ \text{pwv}_1 \end{pmatrix} =$  

Convert this to a function:

$v := \text{cspline}(h_1, \text{pwv}_1)$

$\text{PWV}_1(\text{alt}) := \text{interp}(v, h_1, \text{pwv}_1, \text{alt})$

Number H2O molecules per unit volume:

$\text{h2oN}_1(\text{alt}) := \text{PWV}_1(\text{alt}) \cdot 3.34 \cdot 10^{22} \quad (\text{m}^{-3})$



Water concentration profile:

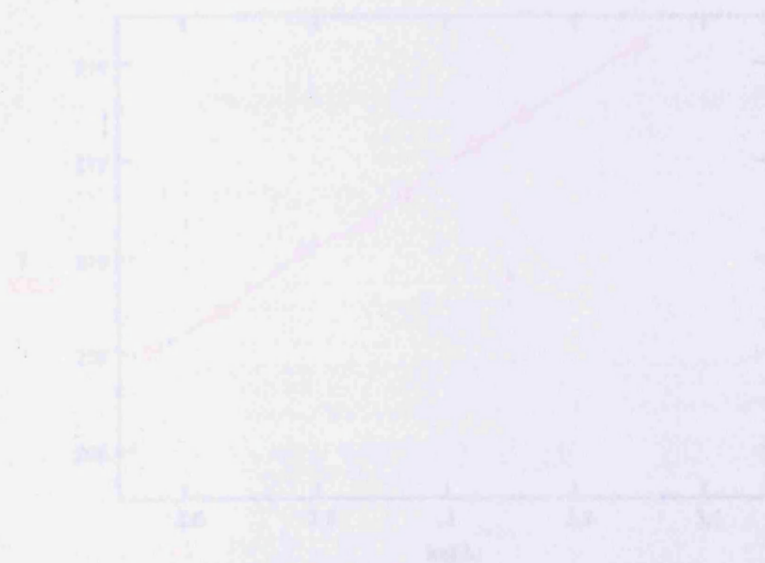
$$\text{PPM}_1(\text{alt}) := \frac{\text{h2oN}_1(\text{alt}) \cdot 10^6}{\text{totN}(\text{alt})}$$

alt := 0, 1.. 119

PPM<sub>1</sub>(alt) =

671.402
771.761
682.471
558.204
377.449
205.193
113.678
71.345
16.175
14.224
9.56
4.778
4.881
4.967
4.966
4.941

Result formatted as table display,  
exported to .xls sheet. Add altitude  
Sheet saved as txt



## Appendix C

Worksheet to calculate equivalent blackbody temperature and flux at 200  $\mu\text{m}$  from source planet, extrapolated from data in range 350  $\mu\text{m}$  to 2 mm

Constants:  $h := 6.626 \cdot 10^{-34}$        $k_b := 1.381 \cdot 10^{-23}$        $c := 2.998 \cdot 10^8$

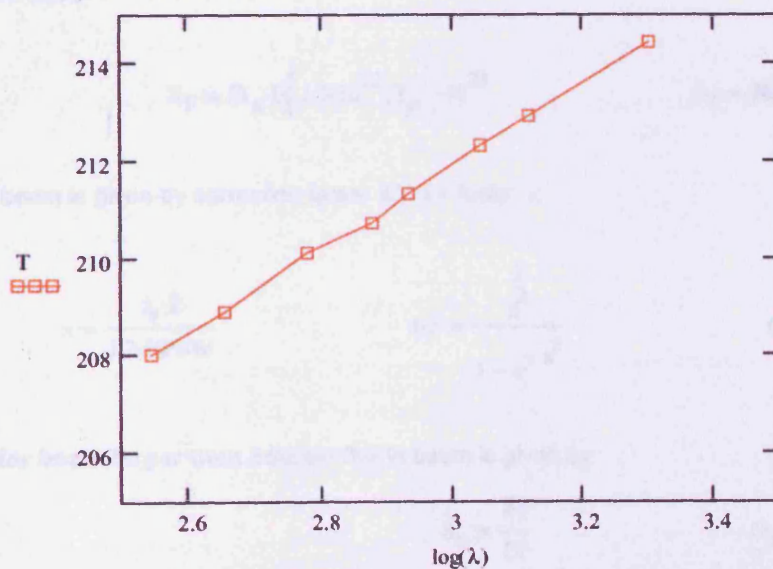
Planck function: 
$$B(\nu, T) := \frac{2 \cdot h \cdot \nu^3}{c^2 \left( e^{\left( \frac{h \cdot \nu}{k_b \cdot T} \right)} - 1 \right)}$$

Wavelength of THUMPER  $\lambda_T := 200$  ( $\mu\text{m}$ )

Read in wavelength and temperature data  $\begin{pmatrix} \lambda \\ T \end{pmatrix} := \begin{pmatrix} \mu\text{m} \\ \text{K} \end{pmatrix}$

Read in planet semi-diameter  $r_s := 9.21$

obtained from FLUXES for Mars on 12 10 03 @ 08:30:00 (UT)



Assume straight line fit of form  $y = mx + c$

$$\text{slope}(T, \log(\lambda)) = 0.117 \quad \text{intercept}(T, \log(\lambda)) = -21.865$$

Then equivalent temperature at 200um will be given by

$$T_p := \frac{\log(200) - \text{intercept}(T, \log(\lambda))}{\text{slope}(T, \log(\lambda))} \quad T_p = 205.932$$

Planet subtends a semi-diameter  $r_s = 9.21$  (arcsec)

Which gives solid angle  $\Omega_s := \left( \frac{r_s}{3600} \cdot \frac{\pi}{180} \right)^2 \cdot \pi$

HPBW for 850um as given in FLUXES  $\text{HPBW} := 14$  (arcsec)

Which gives solid angle  $\Omega_b := \left( \frac{\text{HPBW}}{3600} \cdot \frac{\pi}{180} \right)^2 \cdot \pi$

Total flux (Jy) [ $10^{-26}$  W/m<sup>2</sup>/Hz] is

$$S_T := \Omega_s \cdot B(1.5 \cdot 10^{12}, T_p) \cdot 10^{26} \quad S_T = 74506 \quad (\text{Jy})$$

Flux in beam is given by correction factor CF, for factor  $x$

$$x := \frac{r_s \cdot 2}{1.2 \cdot \text{HPBW}} \quad \text{CF} := \frac{x^2}{1 - e^{-x^2}} \quad \text{CF} = 1.719$$

Then for beam larger than source flux in beam is given by

$$S_b := \frac{S_T}{\text{CF}} \quad S_b = 43350$$



For extrapolated brightness temperature  $T_p = 205.9$

For source larger than beam flux in beam is given by

$$S_b := \Omega_b \cdot B(1.5 \cdot 10^{12}, T_p) \cdot 10^{26} \quad S_b = 43039$$

